Very High Energy Gamma Rays from the Binary Pulsar PSR B1259−63

DISSERTATION

zur Erlangung des akademischen Grades
doctor rerum naturalium
(Dr. rer. nat.)
im Fach Physik

eingereicht an der
Mathematisch-Naturwissenschaftlichen Fakultät I
Humboldt-Universität zu Berlin

von
Herr Dipl.-Phys. Stefan Schlenker
geboren am 31.3.1977 in Berlin

Präsident der Humboldt-Universität zu Berlin:
Prof. Dr. Jürgen Mlynek

Dekan der Mathematisch-Naturwissenschaftlichen Fakultät I:
Prof. Thomas Buckhout, PhD

Gutachter:

1. Prof. Dr. Werner Hofmann
2. Prof. Dr. Thomas Lohse
3. Prof. Dr. Hermann Kolanoski

eingereicht am:	20. April 2005
Tag der mündlichen Prüfung:	12. Juli 2005

Abstract

This work reports on the discovery of very high energy (VHE) γ-ray emission of the binary system PSR B1259−63 / SS 2883, consisting of a radio pulsar orbiting a massive, luminous star in a highly eccentric orbit. The observations of the binary system in the first half of 2004 were performed with the High Energy Stereoscopic System (H.E.S.S.), a system of imaging atmospheric Cherenkov telescopes, recently installed in Namibia and in full operation since December 2003. The instrument collects the Cherenkov light emitted by air showers which are induced by the interaction of cosmic γ-rays with the upper atmosphere. This technique allows to detect γ-rays with energies ranging from 10^{11} to 10^{14} electron Volts, and to reconstruct their direction and energy with an angular resolution of less than 0.1° and energy resolution of better than 20%, respectively.

Prior to the detection of VHE γ-rays from PSR B1259−63 / SS 2883, the system served as a candidate for the acceleration of particles to TeV energies. The acceleration is believed to take place in plasma shocks produced by the interaction of the relativistic pulsar wind with the massive stellar winds of the companion star. The VHE γ-ray signal from the binary system was detected with a total significance above $13\,\sigma$. This detection provides the first unambiguous evidence for particle acceleration to multi-TeV energies in this binary system. The measured time-averaged energy spectrum can be described by a power law $\mathrm{d}N/\mathrm{d}E \propto E^{-\Gamma}$ with a photon index $\Gamma = 2.7 \pm 0.2_{\mathrm{stat}} \pm 0.2_{\mathrm{sys}}$ suggesting that the emission is produced by inverse Compton scattering of shock-accelerated electrons and positrons on the thermal photons emitted by SS 2883. The γ-ray flux was found to vary significantly on timescales of days which makes PSR B1259-63 the first variable galactic source of VHE γ-rays observed so far and gives valuable insights into the dynamics of pulsar winds interacting with a changing environment.

Keywords:

Gamma-rays: observations, Pulsars: individual: PSR B1259−63, Instrumentation: Cherenkov telescopes, Instrumentation: Data acquisition

Zusammenfassung

Diese Arbeit beschreibt die Entdeckung von hochenergetischer Gammastrahlung aus Richtung des Binärsystems PSR B1259−63 / SS 2883. Die Beobachtungen dieses Systems von einem Radio-Pulsar, der sich auf einer stark exzentrischen Umlaufbahn um einen schweren und hellen Stern befindet, wurden mit dem High Energy Stereoscopic System (H.E.S.S.) in der ersten Hälfte des Jahres 2004 durchgeführt. H.E.S.S. ist ein System von abbildenden atmosphärischen Cherenkov-Teleskopen in Namibia, das im Dezember 2003 vollständig in Betrieb genommen wurde. Die Wechselwirkung der kosmischen Gammastrahlen mit der oberen Atmosphäre erzeugt Luftschauer von relativistischen Sekundärteilchen, deren Cherenkov-Emission von den Teleskopen des Systems nachgewiesen wird. Mit dieser Methode kann die Richtung einzelner Gammaquanten mit Energien zwischen 0.1 und 100 TeV (10^{12} Elektronenvolt) mit einer Winkelauflösung von weniger als 0.1° und die Energie mit einer Auflösung von besser als 20% bestimmt werden.

Vor der Entdeckung von TeV-Gammastrahlung aus Richtung von PSR B1259−63 / SS 2883 galt dieses System als ein aussichtsreicher Kandidat für die Beschleunigung von geladenen Teilchen auf Energien oberhalb von 1 TeV. Es wurde angenommen, dass die Wechselwirkung des relativistischen Pulsarwindes mit dem Sternenwind des Begleitsterns massive Plasmaschocks erzeugt, in denen die Beschleunigung erfolgt. Durch die H.E.S.S. Beobachtungen wurde ein Signal von Photonen im TeV-Bereich mit einer statistischen Signifikanz von über $13\,\sigma$ gemessen und somit wurde die Beschleunigung von Teilchen auf TeV-Energien innerhalb des Binärsystems erstmalig zweifelsfrei nachgewiesen. Das gemessene Energiespektrum kann im zeitlichen Mittel mit einem Potenzgesetz $\mathrm{d}N/\mathrm{d}E \propto E^{-\Gamma}$ mit dem Photonenindex $\Gamma = 2.7 \pm 0.2_{\mathrm{stat}} \pm 0.2_{\mathrm{sys}}$ beschrieben werden. Diese Form des Spektrums weist auf eine Erzeugung der Gammastrahlung durch inverse Compton-Streuung von schock-beschleunigten Elektronen und Positronen mit den Photonen der thermischen Strahlung von SS 2883 hin. Die gemessene Variation des Flusses der Gammastrahlung auf einer Zeitskala von Tagen ist bisher einmalig für eine galaktische Quelle von TeV Photonen und ermöglicht erstmalig Einblicke in die Dynamik der Wechselwirkung eines Pulsarwindes mit einer sich ändernden Umgebung.

Schlagwörter:
Gammastrahlung: Beobachtung, Pulsare: individuell: PSR B1259−63, Detektoren: Cherenkov-Teleskope, Detektoren: Datennahmesystem

Contents

List of Figures

List of Tables

Chapter 1

Introduction

The discovery of cosmic rays – charged particles of cosmic origin – in the beginning of the last century by Victor Hess [Hess, 1913] marked the beginning of a new era in physics. Many discoveries were made by the investigation of these highly energetic cosmic particles and lead to the development of modern elementary particle physics. The energy spectrum of cosmic ray particles was found to extend to 10^{20} electron volts and beyond, an energy which will not be accessible by terrestrial accelerators in the near future. Furthermore, the energy density of cosmic rays represents a significant contribution to the total energy density of the universe, since it is comparable to that of the cosmic microwave background or integrated star light at optical wavelengths. This provides sufficient motivation for the search of the sources of cosmic rays by studying plausible candidates.

The origin of the cosmic rays – although their existence is known since nearly hundred years – is still largely unknown. The acceleration of cosmic ray particles to the observed energies has to result from high energy processes on astrophysical scales. Up to the present date, there are only hints about the nature, location, and type of the cosmic accelerators which are able to produce the high energy particles.

Twenty-five years after the discovery of cosmic rays, Enrico Fermi proposed a mechanism for the acceleration of charged particles: particles can gain energy by magnetic reflection in plasma clouds [Fermi, 1949]. However, this process was found to be too inefficient to account for the energies reached by the observed cosmic rays because of energy losses of the accelerated particles. Later, this idea was applied to shock fronts, allowing the particles to gain energy by being repeatedly reflected by magnetic mirrors in the plasma on both sides of the shock [Bell, 1978, Blandford and Ostriker, 1978]. This process – called first order Fermi acceleration – was fast enough to produce particles with sufficiently high energies. Furthermore, the particle energy spectrum resulting from this process is similar to that observed for cosmic rays after considering the energy losses on their way to Earth. Strong shocks can be produced by the most violent astrophysical processes, like the explosion of dying stars, called supernova, or in collimated outflows – jets – produced near compact and very massive objects such as supermassive black holes in the core of distant galaxies (active galactic nuclei, AGN).

But also other phenomena turned out to account for particle acceleration to very high energies: Supernovae were proposed to leave behind the collapsed core of the exploding star, compressed by its own gravity and only kept stable by the degeneration of state of neutrons – a neutron star – which is highly magnetized and rotates at periods of the order of 1 second. In the late 60's of the last century, an object emitting very regular radio pulses with this period was discovered [Hewish et al., 1968] – called pulsar – and it is well established today that pulsars are actually neutron stars. Such a rapidly spinning compact object with a strong magnetic field gives rise to a strong electric field which is capable to accelerate particles to energies of the order of 1 TeV.

The largest fraction of cosmic rays observed at Earth is represented by protons and heavier nuclei which are deflected by varying interstellar and intergalactic magnetic fields and thus these particles which have energies below $\approx 10^{15}$ eV have lost all directional information about their origin since the corresponding gyro-radius is small compared to galactic distances. Nevertheless, the energy loss of cosmic rays by interaction with their environment is very likely to produce photons of various energies with the highest density close to the cosmic ray production sites. Since photons are not bent by magnetic fields, they serve as an excellent probe for the high energy universe allowing to trace the cosmic accelerators. Especially photons with energies above several MeV (10^6 eV) – γ-rays – should be associatively produced in the vicinity of cosmic ray sources of highly relativistic particles. The investigation of cosmic γ-rays lead to the development of a new field of research – *γ-ray astronomy* – probing the non-thermal universe.

Since the Earth atmosphere is opaque for photons above 10 eV, detectors on board of satellites had to be used to detect the γ-rays. The various instruments operating in space from the early 70's to the late 90's gave a comprehensive picture of the γ-ray sky for photon energies up to several GeV. They detected diffuse γ-ray emission from all over the sky but significantly enhanced within the galactic plane dominating at energies around 100 MeV. The morphology corresponds to the matter density distribution in our galaxy interpreted to result from the interaction of cosmic rays with galactic material. At γ-ray energies above 1 GeV, the emission is dominated by point sources of galactic and extra-galactic origin.

Basically three classes of objects with counterparts at other photon energies could be identified to represent the majority of the γ-ray sources: Galaxies containing an AGN, supernova remnants, and pulsars. The multi-wavelength photon spectra of these objects are often characterized by a two-component structure of non-thermal radiation, a low-energy part ranging from radio up to GeV γ-ray energies, and a high-energy part at higher γ-ray energies. The low energy emission is commonly attributed to the synchrotron emission of plasmas containing electrons and positrons accelerated to relativistic energies. The second, high energy part can originate from the same leptons which emit the synchrotron radiation by transferring most of their energy to ambient photons in the process of inverse Compton scattering. However, accelerated hadrons interacting with ambient matter by deep inelastic scattering can also produce γ-rays by the decay of secondary neutral π-mesons. This ambiguity can only be resolved by detailed studies of the high energy component of the source photon spectra.

For most of the sources, the measured spectra indicated that the main energy release in the high-energy part had to be expected at γ-ray energies higher than that accessible by the γ-ray satellites. In particular, one of the strongest known stable sources of γ-rays – the Crab Nebula – has a particle flux in the order of $10^{-11}\,\mathrm{cm}^{-2}\,\mathrm{s}^{-1}$ at energies above 1 TeV. In order to detect such rare particles at reasonable rates of the order of $1\,\mathrm{min}^{-1}$, one needs detectors with collection areas of more than $10^5\,\mathrm{m}^2$ exceeding the limits of space-borne instruments by many orders of magnitudes. Since high-energy particles interact with the upper atmosphere creating extensive air showers of secondary particles, large amounts of primary particles can be detected by collecting the Cherenkov emission of the showers on the ground with dedicated detectors.

The most successful ground based instruments are imaging atmospheric Cherenkov telescopes (IACTs) which estimate the characteristics of the the primary γ-ray from images of its air shower Cherenkov emission and allow to explore the sky in very high energy (VHE) γ-rays between several 10 GeV and 100 TeV. The first and second generations of these instruments were able to detect a few sources of TeV γ-rays, nearly all of them belonging to one of the three categories mentioned above and confirming that these objects are able to accelerate particles to TeV energies and beyond. However, it was not yet possible to unambiguously identify an accelerator of hadronic cosmic rays. On the contrary, the emission of most of these sources is consistent to be produced by accelerated electrons and positrons. A comprehensive review of γ-ray astronomy in the last century can be found in Hoffman et al. [1999].

In the beginning of this century, the third generation of IACT projects becomes operational providing a much better sensitivity in order to find new sources of high energy radiation and to improve the accuracy of the energy spectrum measurements. With the first of these instruments which became operational, the *High Energy Stereoscopic System* (H.E.S.S.), it was possible to more than double the number of known sources of TeV γ-ray sources in its first year of operation, opening a new era of high energy γ-ray astronomy.

The best studied example of a cosmic accelerator of electrons is the Crab Nebula, a remnant of a supernova which happened roughly thousand years ago containing a very energetic pulsar. In contrast to the pulsed radiation emitted from the direct vicinity of the rotating neutron star and extending up to several GeV of photon energy, the emission of the Crab Nebula has a strong component of continuous non-thermal radiation. The energy spectrum of this component has been measured over 20 orders of magnitude in photon energy and extends up to 100 TeV. The radiation is thought to be powered by the pulsar which converts a significant fraction of its rotational energy into a wind of relativistic particles. This pulsar wind is terminated by a strong shock in the surrounding material of the supernova remnant, filling the resulting pulsar wind nebula (PWN) with a plasma containing shock-accelerated particles which emit the observed non-thermal radiation. Many of such PWNs have been found at X-ray energies by detecting the synchrotron emission of the accelerated electrons, but only a few of them have been identified as TeV γ-ray emitters. This may be related to the fact that the presence of the γ-ray component produced by inverse Compton scattering of electrons strongly depends on the density of target photons in the radiating plasma. In the Crab Nebula, the low density of target photons is mainly compensated by the exceptional energy output of the pulsar.

In pulsar binary systems, where a pulsar is gravitationally bound with a normal star, the companion naturally provides an extremely dense photon field. Roughly one hundred binary pulsars are known today and many more are believed to exist [for a review see Stairs, 2004]. However, their detection remains a difficult task mainly since the stellar winds of the companion stars distort the pulsed emission at radio energies. The binary system PSR B1259−63 / SS 2883, consisting of a radio pulsar in an eccentric orbit around a luminous, massive star, represents a very good candidate for VHE γ-ray emission. In fact, the system was found to emit variable non-thermal radiation, in particular at X-ray energies, which was interpreted to originate from the varying interaction of the pulsar and stellar winds, similar to the situation in PWNs around isolated neutron stars.

This work reports on the discovery of VHE γ-ray emission from PSR B1259−63 / SS 2883 with the H.E.S.S. instrument. The detection of this emission establishes a new type of object for VHE γ-ray astronomy, where a pulsar wind interacts with a changing environment allowing to study the dynamics of shock-acceleration. In fact, PSR B1259−63 turns out to be the first galactic source of variable VHE γ-rays ever observed.

Chapter 1 gives an introduction on neutron star formation, pulsar winds and their associated nebulae, and the non-thermal radiation of the Crab Nebula which serves as the best known example of a PWN around an isolated pulsar. The known facts about the binary system of PSR B1259−63 are reviewed with emphasis to the high energy emission and their theoretical interpretation, and the expectations of VHE γ-ray emission from the system are discussed in the context of theoretical models in order to provide the motivation for the H.E.S.S. observations. Chapter 2 introduces the H.E.S.S. instrument, beginning with the principles of the imaging atmospheric Cherenkov technique, followed by a detailed description of the detector components. The data recorded by the telescope system had to be calibrated and selected according to quality criteria. Subsequently, the properties of the primary γ-rays had to be reconstructed and cleaned from the huge background of cosmic ray induced air showers. These calibration and data reduction routines are described in Chapter 3. The data analysis procedures used for the determination of the properties of the γ-ray signal, such as position, energy spectrum, and the flux light curve, are described and the results are presented in Chapter 4. Finally, in the last chapter, these results are discussed in the context of the theoretical framework introduced in Chapter 1.

Chapter 2

High Energy Phenomena in the Binary System of PSR B1259−63 / SS 2883

The binary system of PSR B1259−63 and its companion SS 2883 resemble a, so far, unique combination of a pulsar orbiting a very luminous main sequence star. The system was discovered by the pulsed radio emission of the PSR B1259−63 which was found to be in a highly eccentric orbit around its companion.

In general, neutron stars are believed to loose their rotational energy in the form of relativistic winds of charged particles forming pulsar wind nebulae (PWN) observable by its non-thermal emission of radiation. So far, PWN are well studied for the case of isolated neutron stars like the Crab Nebula. In fact, the system of PSR B1259−63 was detected to emit variable non-thermal X-rays possibly originating from ultra- relativistic electrons with energies of the order of 1 TeV. However, the non-thermal X-ray emission may originate from several different astrophysical mechanisms, and only the detection of VHE γ-ray emission would clearly prove the acceleration of particles to such high energies in this object. Furthermore, the temporal characteristics of such an emission would give valuable insights into the dynamics of pulsar winds interacting with a changing environment.

First in this chapter, the basics of particle acceleration in pulsars and their wind nebulae and the corresponding radiation mechanisms are reviewed. Subsequently, the binary system of PSR B1259−63 is described in detail based on the knowledge obtained by the numerous observations at various wavelengths. Special emphasis is given to the high energy emission at X-ray wavelengths and its origin, corresponding directly to the expectations on the VHE γ-ray emission from PSR B1259−63, which are finally discussed in order to motivate the H.E.S.S. observations of the system.

2.1 Pulsars and Pulsar Wind Nebulae

The Crab Nebula is the most famous example of a pulsar powering a nebula containing ultra-relativistic particles with energies of more than 1 PeV. Many objects of similar type are known, but the energy release of the Crab in form of high-energy radiation is exceptionally high compared to other galactic objects, which allowed to probe and understand the mechanisms of particle acceleration in great detail. The theoretical modeling of the Crab PWN plays an important role in the understanding of the high energy phenomena occurring in the system of

PSR B1259−63. Thus, first in this section, the formation and physics of the central engine of a PWN – the neutron star – is briefly introduced, and subsequently its interaction with the environment and the resulting non-thermal radiation is discussed with special emphasis given to the Crab Nebula.

2.1.1 Neutron Star Formation

Neutron stars are believed to be formed by supernova explosions at the end of the life cycle of stars. Common to all different types of supernovae, depending on the environment and the mass of the exploding star, is the collapse of the stars core due to its own gravitational force overcoming the pressure resulting from the degeneration of state of electrons. The type of the remaining object depends on the mass of the progenitor star. For progenitor masses $2M_\odot \lesssim M \lesssim 25M_\odot$ the remaining core is stabilized by the pressure of the degeneration of state from neutrons balancing the gravitational force and thus forming a *neutron star*. For greater masses, no known force can prevent the further collapse to a black hole. The typical radius for a stable neutron star consisting of non-relativistic neutrons under Newtonian gravity is of the order of 10^4 m with densities around 10^{13} g/cm^3. The huge amount of gravitational energy released in the core collapse process,

$$\Delta E_\mathrm{G} = O\left(\mathcal{G}M^2\left[\frac{1}{R'} - \frac{1}{R}\right]\right),$$

with M as the mass of the star and R/R' as the radius of the star before/after the collapse is exhausted in a catastrophic explosion – the supernova. If the final state of the collapse is a neutron star, the energy released in the supernova is of the order of 10^{53} erg (10^{46} J), which is mainly carried away by neutrinos.

Since the magnetic field of a progenitor star is frozen within its nearly ideally conducting plasma, the magnetic field is strongly compressed during the collapse while the total energy of the magnetic field is almost conserved. Therefore the field strength increases according to

$$B' = B\left(\frac{R'}{R}\right)^2 .$$

For an initial field of $B = 100\,\mathrm{G}$ of a sun-like star this would yield an extreme magnetic field strength of $B' = 10^{12}\,\mathrm{G}$. The corresponding, at least partial conservation of angular momentum, $L \propto R^2/P$ with P as the rotation period of the star, would require the neutron star to rotate rapidly with periods P' of several milliseconds.

Such a strong rotating magnet radiates magnetic dipole radiation and in the case of a *non-aligned rotator*, i.e. if the rotation axis differs from the magnetic field orientation, the radiation is emitted in a lighthouse-like effect. For an observer on Earth, this would result in a periodic signal of electromagnetic radiation. Indeed, in the middle of the last century, objects with a very regular periodic radio emission were detected, called *pulsars*, and later on identified to be neutrons stars, opening the complete new field of pulsar research [see e.g. Lyne and Graham-Smith, 1998].

2.1.2 Pulsar Magnetosphere

The simple picture of radiation emerging from a rotating dipole above only holds for a neutron star surrounded by vacuum. In fact, when treating the neutron star as an ideal conducting sphere rotating in a static magnetic field [Goldreich and Julian, 1969], a strong electric field is induced which has a component perpendicular to the neutron star surface, especially near the magnetic poles, which can be strong enough to pull out charged particles. For example, the typical electric force acting on a proton at the neutron star surface is 10^9 times larger than the counteracting gravitational force. Assuming that charged particles exist on the surface, the exterior of the neutron star will be filled with a flow of particles which are accelerated to relativistic energies. Unfortunately, the structure of a neutron star surface is quite uncertain because of the extreme conditions involved, i.e. especially the strong magnetic field is expected to have a strong effect on the distribution of matter on the surface. Up to now, the process of particle emission from the surface is not completely understood. However, the existence of a single "lost" electron or positron outside of the neutron star is sufficient to fill the exterior with an e^+e^- plasma, since it will produce synchrotron radiation in the magnetic field leading to a cascade of pair production in the strong electric field.

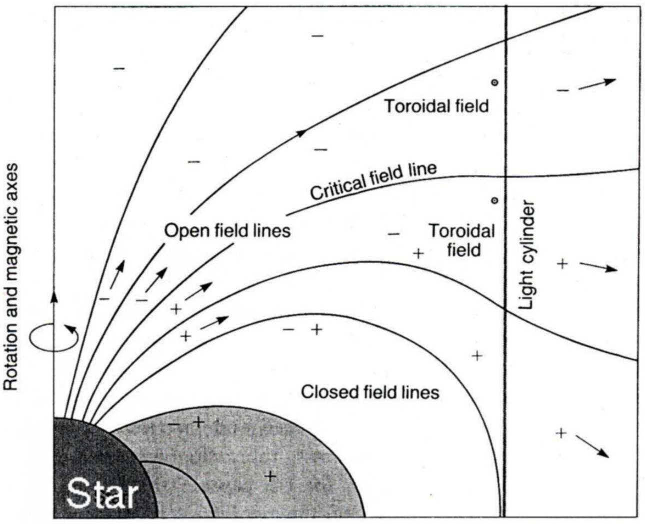

Figure 2.1: *Pulsar magnetosphere of an aligned rotator according to Goldreich and Julian [1969].*

Figure 2.1 shows the schematic structure of a neutron star *magnetosphere* for the example of an aligned rotator, where the magnetic field orientation matches the rotation axis, $\vec{\Omega}||\vec{B}$. The emitted/produced plasma particles which are bound to the magnetic field "lines", travel along curved trajectories. The orientation of the electric field with respect to the neutron star surface causes a charge separation – negative charges are found close to the magnetic poles while positive charges reside at the equatorial regions of the neutron star. The particles co-rotate with the magnetic field inside the *light cylinder*, which is determined by the volume within which the field lines have a rotation velocity equal to or less than the speed of light, $v \leq c$. The field lines which are closed within this cylinder keep their bound particles within the magnetosphere. At the edge and outside of the light cylinder, relativistic effects prevent the plasma from co-rotation and the magnetic field lines are wrapped around the light cylinder flowing away from the neutron star. These "open field lines" allow the particles of the enclosed plasma to escape from the magnetosphere. Hence, there exists a flow of particles bound to the open field lines even inside the light cylinder close to the magnetic poles of the neutron star.

The Lorentz factor γ of electrons ($e^{\pm}$) accelerated within the magnetosphere for the simplified example of the aligned rotator is given by [Padmanabhan, 2001]:

$$\gamma = 10^7 \frac{B}{10^{12}\,\mathrm{G}} \left(\frac{P}{1\,\mathrm{s}}\right)^{-2},$$

with B as the magnetic field strength, assuming acceleration over a distance in the order of the neutron star radius. This Lorentz factor corresponds to electron energies greater than 1 TeV for a neutron star with a typical magnetic field of 10^{12} G and a rotation period of less than 1 s. However, the electrons are likely to decelerate due to the processes of curvature radiation and associated pair production on their way out of the magnetosphere.

A variety of electromagnetic radiation was observed to emerge from the magnetosphere of pulsars, ranging from the radio emission originating from regions close to the magnetic poles, which led to the discovery of pulsars, to the emission of γ-rays with GeV energies produced in the outer magnetosphere [see e.g. Lyne and Graham-Smith, 1998].

The energy contained in the emitted pulsed radiation from the magnetosphere and the energy of the outflow of the relativistic plasma results in a continuous slowdown of the pulsars rotation. This loss of rotational energy, called *spin-down luminosity*, can be estimated according to

$$\frac{\mathrm{d}E}{\mathrm{d}t} = \dot{E} = I\Omega\dot{\Omega},$$

with I as the moment of inertia of the neutron star and its magnetosphere, and $\dot{\Omega}$ as the decrease of angular frequency which can be measured very precisely for radio pulsars.

For example in the case of the Crab Nebula, this corresponds to an enormous spin-down luminosity of $\dot{E} \approx 4.4 \times 10^{38}\,\mathrm{erg\,s^{-1}}$ which is observed to be converted into pulsed radiation originating from the magnetosphere to a small extent ($< 1\%$). Thus, the missing energy must be carried away from the pulsar by other means.

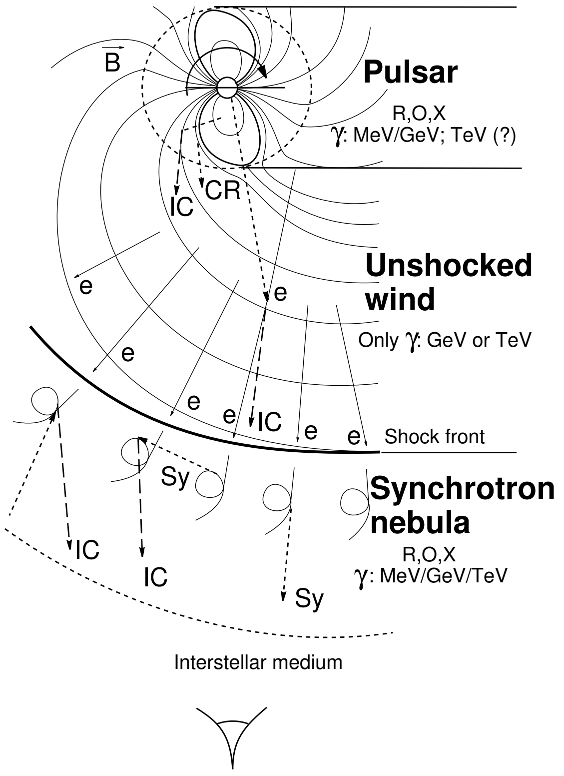

Figure 2.2: *Electromagnetic radiation from pulsars and their pulsar wind nebulae [from Aharonian and Bogovalov, 2003].*

2.1.3 Pulsar Winds and Associated Nebulae

Figure 2.2 schematically illustrates the current understanding of the interaction of a pulsar with its surroundings. The relativistic outflow of magnetospheric e^+e^- plasma beyond the light cylinder is called *pulsar wind*, flowing radially away from the central engine. The wind is considered to be thermodynamically "cold", since the particles are bound to the magnetic field, and is characterized by its

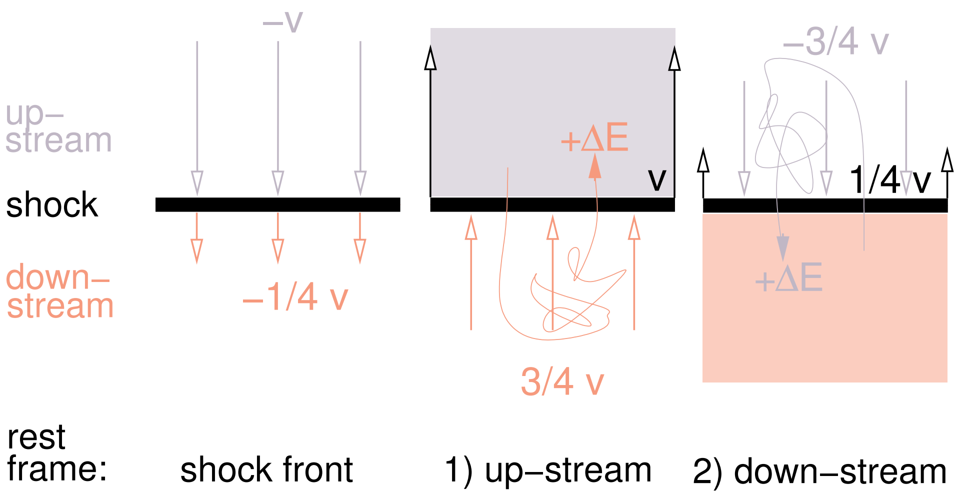

Figure 2.3: *First order Fermi acceleration.*

Lorentz factor γ and the ratio between the energy density of the magnetic field and the kinetic energy density of the plasma particles, σ. Both values are quite uncertain and depend on the rate of pair production within the magnetosphere. However, from recent modeling of the observed pulsed radiation, values of $\gamma > 10^5$ up to the theoretical limit mentioned above, and an electromagnetically dominated wind with $\sigma \gg 1$ are favoured.

The wind is thought to terminate in a standing reverse shock induced by the wind interacting with the interstellar medium around the wind zone, heating the plasma and accelerating the relativistic wind particles via shock acceleration.

Particle Acceleration in a Shock Front

The simplest mechanism for an effective particle acceleration in a shock front is represented by the *first order Fermi acceleration* [for a quantitative analysis see e.g. Padmanabhan, 2001]. The general principle is illustrated in Fig. 2.3. A plasma flow with a Mach number $M \gg 1$ containing relativistic charged particles is considered to slam into a cloud of interstellar material at rest producing a shock front moving at a certain speed, $\vec{v}$, leaving the shocked material to follow at $\frac{3}{4}v$ (case 1). The latter velocity can be derived considering the cloud to be an ideal mono-atomic gas. The shock induces a high level of plasma turbulence in both regions, *up-* and *down-stream*, causing any charged particle crossing the shock to be randomly magnetically reflected without loosing kinetic energy, but effectively getting isotropised within its environment. Considering the process in the rest frame of the region the particle originates from, either up- or down-stream, it gains additional energy by adapting to the flow speed of the new environment. This process might be recurrent and since the situation is symmetric on both sides of the shock front, the acceleration continues until the particle can escape from the shock region.

The net energy gain for a relativistic particle

$$\left\langle \frac{\Delta\epsilon}{\epsilon} \right\rangle = \frac{2}{3}\frac{v}{c},$$

depends on its energy ϵ, and therefore for example an initially mono-energetic particle energy spectrum degenerates to a power law

$$\frac{\mathrm{d}N}{\mathrm{d}\epsilon} \propto \epsilon^{-\alpha},$$

with $\alpha = 2$.

For shocks of pulsar winds with its specific shock geometry regarding flow direction and magnetic field orientation, a more recent and detailed model of Hoshino et al. [1992] is often referred to in the literature and results as well in a power law particle energy distribution with $\alpha \sim 2$. However, within this model, the pulsar wind must contain a significant fraction of heavy ions for which neither the origin is yet understood nor observational evidence was yet found.

Radiation Spectra of PWN Particles

Behind the shock front, the shocked plasma adiabatically expands into the *synchrotron nebula* with a non-relativistic speed. The accelerated, isotropised plasma particles with the power law injection spectrum (index α^{inj}) loose energy mainly via

- ▹ synchrotron radiation of electrons induced by the magnetic field,
- ▹ Bremsstrahlung of electrons within ambient gas,
- ▹ inverse Compton (IC) scattering of electrons with ambient photon fields,
- ▹ and the adiabatic expansion itself since the particles can be removed from regions where radiation processes occur and which renders them invisible to the observer.

Each of these mechanisms leads to a change of the energy distribution of accelerated electrons compared to the power law injection spectrum $\alpha_{\mathrm{e}}^{\mathrm{inj}} \to \alpha_{\mathrm{e}}(\epsilon_{\mathrm{e}})$. The adiabatic expansion just reduces the energy density and therefore leaves the spectral index unchanged while the radiation mechanisms significantly change the primary acceleration spectrum.

For the case of electron synchrotron radiation, the emitted differential photon spectrum is given by [see Blumenthal and Gould, 1970]:

$$n_{\mathrm{sy}}(E) = n_0 E^{-\Gamma_{\mathrm{sy}}} \propto B^{\frac{1}{2}(\alpha_{\mathrm{e}}+1)}\ \epsilon_{\mathrm{e}}^{\frac{1}{2}(\alpha_{\mathrm{e}}+1)},$$

where ϵ_{e} is the kinetic energy of the electrons, B the magnetic field in the plasma, E the photon energy, Γ the *photon index*, i.e. $\Gamma_{\mathrm{sy}} = \frac{1}{2}(\alpha_{\mathrm{e}}+1)$, while for Bremsstrahlung the photon index is equal to the spectral index of the parent electron distribution.

The spectrum of inverse Compton scattered photons [see Blumenthal and Gould, 1970], where the parent electron transfers a significant amount of its kinetic energy to an ambient photon of low energy, depends on the energies of the involved electrons. The value of the parameter

$$b = 4\frac{\epsilon_{\mathrm{e}}\, h\nu}{(m_{\mathrm{e}}c^2)^2}, \tag{2.1}$$

with $h\nu$ as the energy of the initial photon, distinguishes between the Thompson ($b \ll 1$) and the Klein-Nishina ($b \gg 1$) regime and a corresponding radiation spectrum with $\Gamma_{\mathrm{IC}} = \frac{1}{2}(\alpha_{\mathrm{e}}+1)$ and $\Gamma_{\mathrm{IC}} = \alpha_{\mathrm{e}}+1$, respectively.

In case of synchrotron losses, the characteristic lifetime of an electron is given by

$$t_{\mathrm{sy}} = \frac{\epsilon_{\mathrm{e}}}{\dot{\epsilon}_{\mathrm{e}}} \propto \frac{1}{B^2\,\epsilon_{\mathrm{e}}},$$

where $\dot{\epsilon}_e$ is the energy loss rate of the electrons. The electron spectrum steepens continually with increasing distance from the primary injection region at the shock. Therefore, the nebula should feature a correspondingly steepening overall synchrotron spectrum, which is indeed observed in case of the Crab Nebula as explained in the next section.

2.1.4 The Non-Thermal Emission of the Crab Nebula

The Crab Nebula (see Fig. 2.4) represents the prime example of a pulsar wind nebula. It contains a young pulsar with a large spin-down luminosity within the supernova remnant, created in 1056 A.D. Since the nebula is visible in nearly all electromagnetic wavelengths with high luminosity of pulsed and unpulsed non-thermal radiation, the Crab was the subject of many experimental and theoretical studies, especially at γ-ray energies and it became the standard candle of γ-ray astronomy. For a more detailed overview see e.g. Aharonian [2004b].

The inner regions of the Crab Nebula, i.e. near the pulsar position, exhibit a very strong emission of continuous unpulsed non-thermal radiation, ranging from radio to γ-ray energies and with a total luminosity of the same order of magnitude as the pulsar spin-down luminosity. In the unshocked pulsar wind region itself the broad band electromagnetic radiation is unlikely be produced and therefore it was proposed by Rees and Gunn [1974] that the relativistic pulsar wind plasma is confined within the surrounding material of the supernova remnant. The remnant material propagates at non-relativistic speeds and thus the pulsar wind is terminated by a strong shock.

Figure 2.4: *Optical image of the Crab Nebula (VLT ESO PR Photo 40f/99) with a width of 6.8′.*

The idea was adapted by Kennel and Coroniti [1984] which developed a self-consistent spherically symmetric model of the Crab PWN, using detailed magneto-hydrodynamic (MHD) calculations of the plasma flow near the shock front. In order to meet boundary conditions set by observations, several model parameters were constrained. The shock was calculated to occur at a distance 3×10^{17} cm from the pulsar with a Lorentz factor of the wind of $\gamma \sim 10^6 \dots 10^7$. The magnetic field within the nebula was estimated to be 2×10^{-4} G under the assumption that the energy density of the magnetic field matches the energy density of the plasma particles (the *equipartition condition*). The wind energy density was found to be dominated by the kinetic energy of the wind particles near the shock, i.e. $\sigma < 10^{-2}$ (see Sec. 2.1.3). This contradicts the predictions on the characteristics of the injected wind near the magnetosphere with $\sigma \gg 1$, requiring that either the pair production in the magnetosphere is far more efficient than expected, or the electromagnetic energy of the wind is converted into kinetic energy within the wind zone after the injection. The latter case could be realised by considering magnetic reconnection of the striped magnetic field of the unshocked wind [Coroniti, 1990, Kirk and Skjæraasen, 2003].

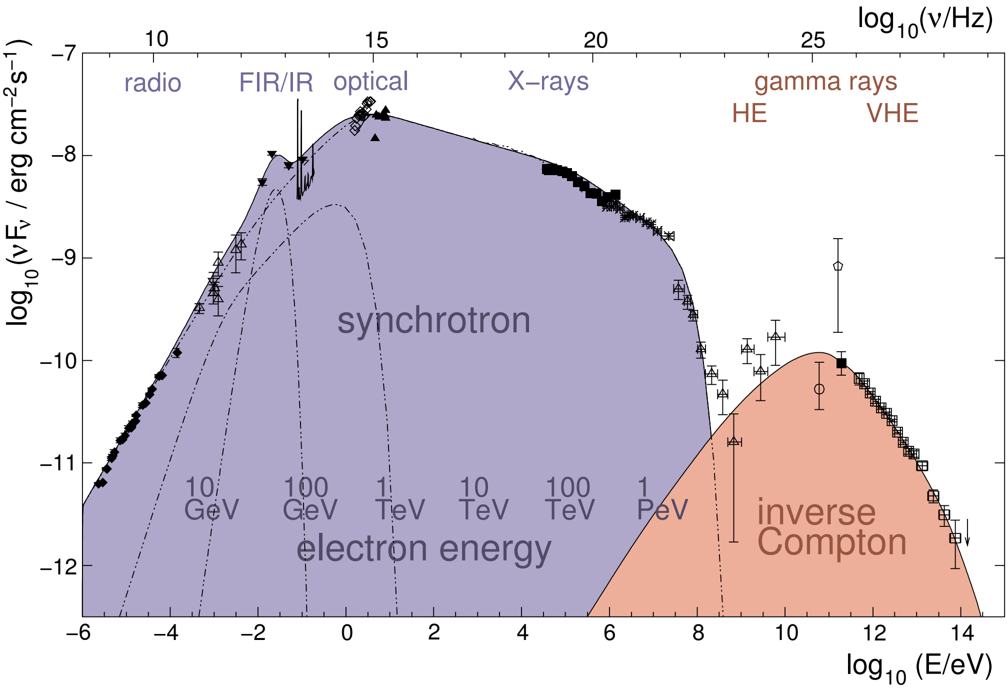

Figure 2.5: *Broad-band spectral energy distribution (SED) of continuous radiation from the Crab Nebula [compiled in HEGRA collaboration, 2004]. The solid lines represent a fit to the model considering the synchrotron and inverse Compton emission of shock-accelerated electrons within the PWN.*

Spectrum of the Non-Thermal Continuum

Figure 2.5 shows the broad-band spectral energy distribution (SED) of the continuum radiation observed from direction of the Crab Nebula using the most up-to-date data from various observatories, compiled by the HEGRA collaboration [2004]. The SED represents the energy flux of emitted photons per unit $\ln E$

$$E^2 \mathrm{d}N/\mathrm{d}E \equiv EF_E \equiv \nu F_\nu ,$$

where $E = h\nu$ is the photon energy, and $\mathrm{d}N/\mathrm{d}E$ is the photon flux per unit energy interval. The integral over this distribution corresponds to the total energy flux in form of radiation.

The data ranging from radio up-to soft γ-rays can be explained as synchrotron emission of accelerated electrons according to the model of a shocked MHD wind originating from the pulsar. Considering all implications of the observed radiation spectrum onto the underlying electron spectrum, the injection spectrum of shock-accelerated electrons can be estimated to have a power law index of $\alpha_\mathrm{e}^\mathrm{inj} \approx 2.4$ [Aharonian, 2004b]. The shock-accelerated electrons are responsible for the synchrotron radiation for electron energies greater than the kinetic energy of the unshocked wind particles, i.e. $\epsilon_\mathrm{e} > 1\,\mathrm{TeV}$. These energies correspond to the observed spectrum above photon energies in the optical band with a photon index $\Gamma_\mathrm{sy} = \frac{1}{2}(2.4 + 1) = 1.7$. The synchrotron component below these energies probably originates from electrons which already lost energy via the different radiation processes.

The γ-ray emission at energies above several GeV until nearly 100 TeV can be explained by inverse Compton scattering of the same shock-accelerated electron population as responsible for the synchrotron emission. The ambient photon field needed for the process is domi-

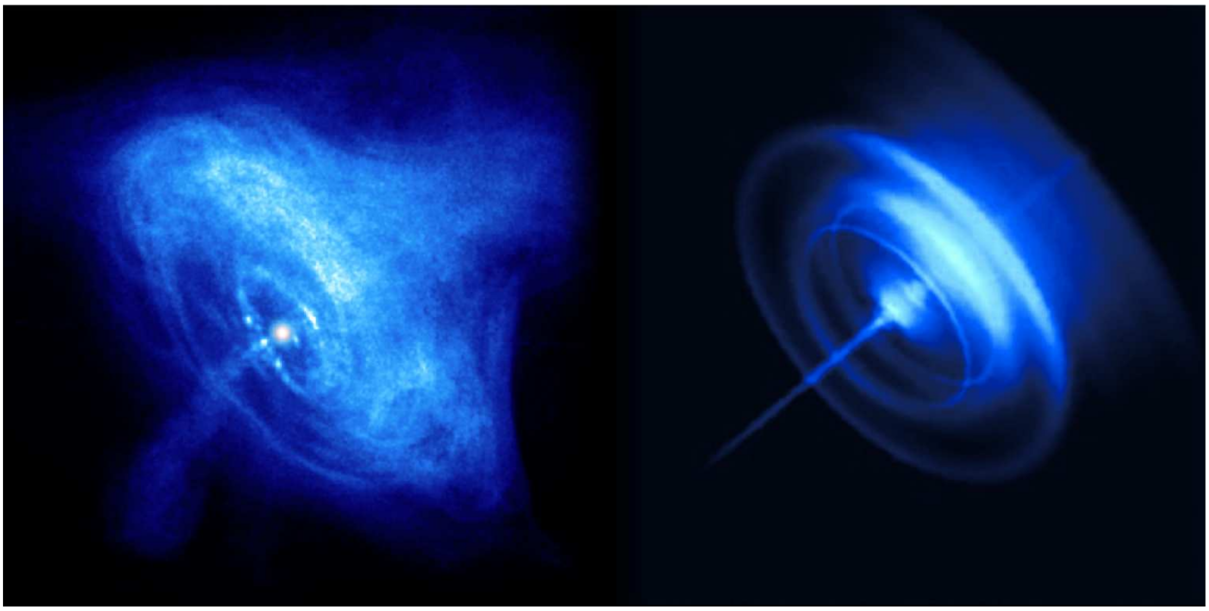

Figure 2.6: **L**eft: *Sky-map showing the continuous X-ray emission of the Crab Nebula at keV photon energies (1.6′, NASA/CXC/ASU/J. Hester et al.).* **R**ight: *Corresponding distribution of X-ray brightness as calculated in the MHD model of Komissarov and Lyubarsky [2003].*

nantly supplied by the synchrotron photons produced inside the nebula by these electrons itself (*synchrotron self Compton* (SSC) model). The shape of the IC spectrum is the result of the combination of the shape of the parent electron and synchrotron photon spectrum, additionally steepened due to the transition from the Thompson to the relativistic Klein-Nishina regime, where the up-scattering takes place. Since the luminosity of the observed synchrotron radiation strongly depends on the magnetic field strength within the nebula, the IC component furthermore allows to independently estimate the magnetic field by relating the observed synchrotron and IC flux. The obtained value of 1.6×10^{-4} G agrees pretty well with the value derived from the MHD model above.

Morphology of the Nebula Radiation

Since the synchrotron lifetime of the accelerated electrons decreases with increasing electron energy, the compactness of the synchrotron nebula is expected to scale with the energy of the observed synchrotron photons. Indeed, the nebula appears to be quite extended at radio to optical wavelengths, up to $3' = 5 \times 10^{18}$ cm, while at soft X-ray energies, the nebula has a size of roughly half of this value. At higher energies, the extension cannot be resolved anymore because of the bad angular resolution of the instruments. E.g. for the VHE γ-ray IC emission, only a limit on the size can be obtained, recently determined to be $\approx 1'$ at 3 TeV γ-ray energy using all data obtained with the HEGRA detector [HEGRA collaboration, 2004].

The morphology of the synchrotron nebula around the Crab pulsar was impressively resolved by the *CHANDRA* X-ray satellite [Hester et al., 2002] revealing a detailed non spherically, but axis-symmetric X-ray emission shown in Fig. 2.6 (left). The "underluminous" region around the central spot corresponding to the pulsar position is interpreted as the pulsar wind region, surrounded by a toroidal structure, the synchrotron nebula. Interestingly, the underluminous region is enclosed by a bright ring of $\approx 14''$ projected radius, corresponding to a distance of 4×10^{17} cm which is consistent with the distance of the pulsar wind shock calculated within the MHD model of Kennel and Coroniti [1984]. However, the data also show that the structure is much more complex than implied by the simple model above. More recent axis-symmetric MHD model calculations of the wind, its shocks, and the synchrotron nebula [e.g. Komissarov and Lyubarsky, 2003, Fig. 2.6, right] are able to reproduce the observed emission at a quite detailed level, illustrating the current understanding of the high energy processes within the Crab Nebula.

2.2 The Binary System of PSR B1259−63 / SS 2883

The system of PSR B1259−63 / SS 2883 was initially discovered by the pulsed radio emission of PSR B1259−63 which was found to be eclipsed at a short time period along its orbit. Neutron stars within binary systems are a quite common phenomenon, since they represent a late stage of stellar evolution which basically also applies for stars in a bound state. However, the binary system PSR B1259−63 / SS 2883 represents a – so far – unique case where a young radio pulsar with a moderate spin-down luminosity is situated in a highly eccentric orbit around a massive Be-type companion star with strong stellar winds.

In this section, first a short review about the evolution of binary systems with regard to the system of PSR B1259−63 is given, followed by some basic facts about the properties of Be-stars. Subsequently, the characteristics of the system obtained from various observations at radio and optical wavelengths are introduced in detail.

2.2.1 Binary System Evolution

In fact, a large fraction of all known stars are formed in a bound state of two stars forming a binary system as it is the case for PSR B1259−63 / SS 2883. The stellar evolution in binary systems is significantly modified because of the interaction of the stars by means of tidal effects and – in the case of a small separation – even mass transfer. As for isolated stars, the stars can undergo a supernova explosion (SN) possibly leaving behind a neutron star and influencing the orbit of the bound state which can even result in the separation of the system. A general overview of binary pulsar evolution can be found in Stairs [2004].

A Keplerian binary orbit of point-masses is characterized by five force-free Lagrange points, with the equipotential surface forming the *Roche-lobe*. For a young star, this lobe is well outside the stars surface, but as the star evolves, it grows and reaches the red-giant phase. The star material starts to fill the Roche-lobe and a *Roche-lobe-overflow* occurs leading to a matter transfer to its companion and accelerating its own evolution. The mass transfer induces large friction forces reducing the orbital separation, circularising the orbit, and causing an alignment of the rotation axes of both stars.

The star which lost a significant part of its mass will have its life span strongly reduced and rapidly evolve into a white dwarf or explode in a SN of type I leaving behind a neutron star or even a black hole. The SN is likely to disrupt the binary depending on the mass loss or a possible asymmetry in the explosion. Additionally, among other factors, the mass of the companion and the eccentricity of the initial orbit are important. The system is guaranteed to remain bound if the exploding star has a mass of less than 20% of its companion or ejects < 20% of its mass.

If the binary stays bound, in any case the SN event significantly changes the binary orbit to an elliptic form. In case of a symmetric explosion, the eccentricity e is defined by:

$$M_{\mathrm{pre}} = (1+e)(M_{\mathrm{comp}} + M_{\mathrm{ns}}) - M_{\mathrm{comp}},$$

with M_{pre}, M_{comp}, and M_{ns} as the mass of the SN-progenitor, the companion, and the neutron star, respectively [Gott, 1972]. However, the resulting values of e are rather low, since a large mass of the progenitor increases the probability of the system to be disrupted.

A higher eccentricity can be reached in case of an asymmetric SN giving rise to a natal kick of the neutron star [Podsiadlowski et al., 2004]. Note, that in the latter case the rotation axes of both stars become misaligned, an important fact for the case of PSR B1259−63. Figure 2.7 shows an example for the evolution of a binary system of two massive stars with a different separation finally leading to an asymmetric or an almost symmetric SN and thus a rather elliptical or circular orbit, respectively [Podsiadlowski et al., 2004]. The evolution of the system with the larger separation with almost no mass transfer results in a pre-collapse Helium core with a mass similar to the case of an isolated star, while the small separation produces a smaller core because of the mass loss to the companion. Since in the collapse of the heavier core more material is ejected, the natal kick of the neutron star is much larger than in the other case.

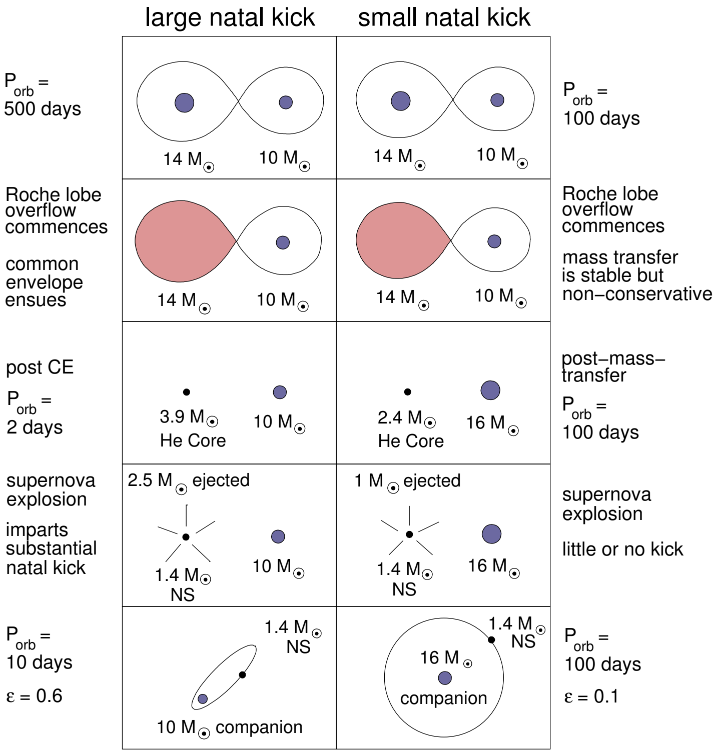

Figure 2.7: *Two extreme examples for the evolution of neutron star binaries leading to a large (left) and small (right) natal kick of the neutron star [from Podsiadlowski et al., 2004].*

After the SN, the companion star evolves and may initiate a mass transfer onto the compact remainder of the SN in the form an accretion disk. This stage of evolution is called X-ray binary. The process of accretion can transfer a significant amount of angular momentum to the neutron star, leading to the observed phenomenon of *millisecond pulsars* with $P \sim 10^{-3}$ s. X-ray binaries are divided into low mass (LMXB) and high mass (HMXB) systems depending on the mass of the companion of the neutron star. Stars of high mass often feature strong stellar winds which lead to the absorption of the pulsed emission of the neutron star. Therefore, HMXB with pulsars are a quite rare phenomenon and the known examples have strong elliptical orbits leading to the phenomenon of an eclipsing binary for which the radio pulse is eclipsed when the pulsar is near the point of minimal distance to its companion (*periastron*).

2.2.2 Be Stars

Be stars are massive stars of the spectral type B with a typical mass of $\sim 10\,M_\odot$, radii of $\sim 6R_\odot$, and additionally characteristic, often double peaked emission lines [see Waters et al., 1988, and references therein] emerging from a circumstellar equatorial disk composed of hot stellar gas. The disk is thought to result from mass transfer in binary systems consisting of two massive stars, forming an accretion disk in a Keplerian orbit because of the rather rapid rotation of the accreting massive star which prevents co-rotation of the disk. Additionally, B and thus Be stars are known to have strong stellar winds originating from their poles.

A study of the cataloged Be stars shows that the polar wind is quite hot at $\sim 10^5$–10^6 K with speeds of 1500 km s^{-1} and densities of less than 10^{-11} g cm^{-3}. The disks were found to be rather cold ($\sim 10^4$ K), more than ten times denser than the polar wind, and the disk material to be on a Keplerian orbit around the star. The disk geometry can be modeled to have a half opening angle between 5–10° and an extension up to 20 stellar radii where the gas is still visible to emit optical Hα radiation. The density profile can be modeled in the form

$$\rho(R) = \rho_0 \left(\frac{R}{R_\star}\right)^{-n},$$

with $R_\star$ being the star radius and with an “outflow exponent” n, typically in the range $2 < n < 4$. The radial velocity profile is then $v(R) \propto (R/R_\star)^{n-2}$ resulting in a radial outflow pressure $P(R) = \rho(R)v(R)^2 \propto (R/R_\star)^{n-4}$.

2.2.3 PSR B1259−63 and its Companion SS 2883

PSR B1259−63 was discovered in a high-frequency pulsar survey of the southern galactic plane using the *Parkes* radio telescopes in Australia [Johnston et al., 1992a,b]. In the following, the basic properties of the system derived from various measurements are reviewed and the discussed characteristic quantities are listed in Table 2.1.

PSR B1259−63 Radio Timing Measurements

The pulse profile was found to be similar to that of the Crab pulsar and the period P was immediately determined to be $P \simeq 47.7$ ms. However, only subsequent observations allowed to determine the period derivative $\dot{P} \simeq 2.3 \times 10^{-15}$ [Johnston et al., 1994]. Thus, the pulsar was calculated to have a characteristic magnetic field at the neutron star surface of $B \simeq 3.3 \times 10^{11}$ G, and a characteristic age of 3.3×10^5 y – a rather young pulsar.

An analysis of the pulse timing differences revealed a signature typical for binary systems and allowed to determine the five basic parameters for a Keplerian orbit

- the orbital period P_{orb},
- the projected semi-major axis x,
- the eccentricity e,
- and the longitude ω and
- epoch τ of periastron.

The data were consistent with an orbital period of $P_{\mathrm{orb}} \simeq 1237\,\mathrm{d} = 3.4\,\mathrm{y}$. Furthermore the orbit was found to be highly eccentric with $e \simeq 0.87$, which represented the highest eccentricity of a binary pulsar ever observed. The mass of both stars M_{ns} and M_{comp}, as well as the inclination angle i (with $x = a \sin i$, where a is the semi-major axis) of the orbital plane relative to the plane of the sky remain unknown but are related by the mass function

$$f_{\mathrm{M}} = \frac{(M_{\mathrm{comp}} \sin i)^3}{(M_{\mathrm{ns}} + M_{\mathrm{comp}})^2} = x^3 \left(\frac{2\pi}{P_{\mathrm{orb}}}\right)^2 \frac{1}{\mathcal{G}}, \tag{2.2}$$

which was found to be $f_{\mathrm{M}} = 1.53\,M_\odot$. Assuming the typical neutron star mass $M_{\mathrm{ns}} = 1.4\,M_\odot$, this yields a lower limit $M_{\mathrm{comp}} = 3.5\,M_\odot$ for $i = 90°$.

Properties of SS 2883

The search for a possible companion immediately brought attention to a Be-type star found in the catalog of Stephenson and Sanduleak [1971] which showed excellent positional agreement with PSR B1259−63. According to the catalog, the stars colour and magnitude put it in the category of B2e stars, with the –2– indicating the stage of stellar evolution.

Further dedicated spectrometric measurements [Johnston et al., 1994] at optical wavelengths showed the typical emission lines $\mathrm{H}\alpha \ldots H\zeta, HeI$ etc. to originate from the equatorial disk, confirming the type of SS 2883 to be B2e. Using the typical mass $M_{\mathrm{Be}} = 10\,M_\odot$ of Be stars and assuming $M_{\mathrm{n}s} = 1.4\,M_\odot$, the inclination angle was determined to $i = 36°$ according to Eq. (2.2). This would place PSR B1259−63 at a distance of only 25 stellar radii $R_\star = 6\,R_\odot$ at periastron, comparable to the disk extension. The measured blue-shift of the $\mathrm{H}\alpha$ line indicates a velocity of the binary system of $\sim 80\,\mathrm{km\,s^{-1}}$ providing evidence for a large natal kick due to the supernova explosion, since the majority of the known Be stars have speeds of less than $\sim 35\,\mathrm{km\,s^{-1}}$. Additionally, the $\mathrm{H}\alpha$ line is slightly asymmetric which was interpreted to result from radial and tidal disruptions of the disk induced by interactions with the pulsar.

System Distance

The distance to the system was estimated by two independent methods [Johnston et al., 1994]. The first method takes advantage of dispersion effects on the radio pulses by the interstellar medium within the line of sight. A model of the density of the interstellar medium [Lyne et al., 1985] was used in order to obtain a distance estimate from the *dispersion measure* (DM) to be $d \approx 2.3\,\mathrm{kpc}$, although with large uncertainties. Secondly, assuming that the system originates from one of the galactic arms within the line of sight, there are two possibilities, $d \approx 1.5\,\mathrm{kpc}$ (within the “Carina”-arm) and $d \approx 5.5\,\mathrm{kpc}$. In the latter case the measured magnitude of SS 2883 would imply that it has a completely different stellar type and would be among the class of O supergiants, which is in contradiction with the distance obtained with the dispersion measure and various spectral properties typical for Be-stars seen in the optical measurements. Therefore further on, the distance was assumed to be $d \approx 1.5\,\mathrm{kpc}$.

Pulsar Eclipse and Equatorial Disk Models

The pulsed emission originating from PSR B1259−63 was found to be eclipsed for several days before and after the periastron passage [Johnston et al., 1994]. Figure 2.8 shows the system

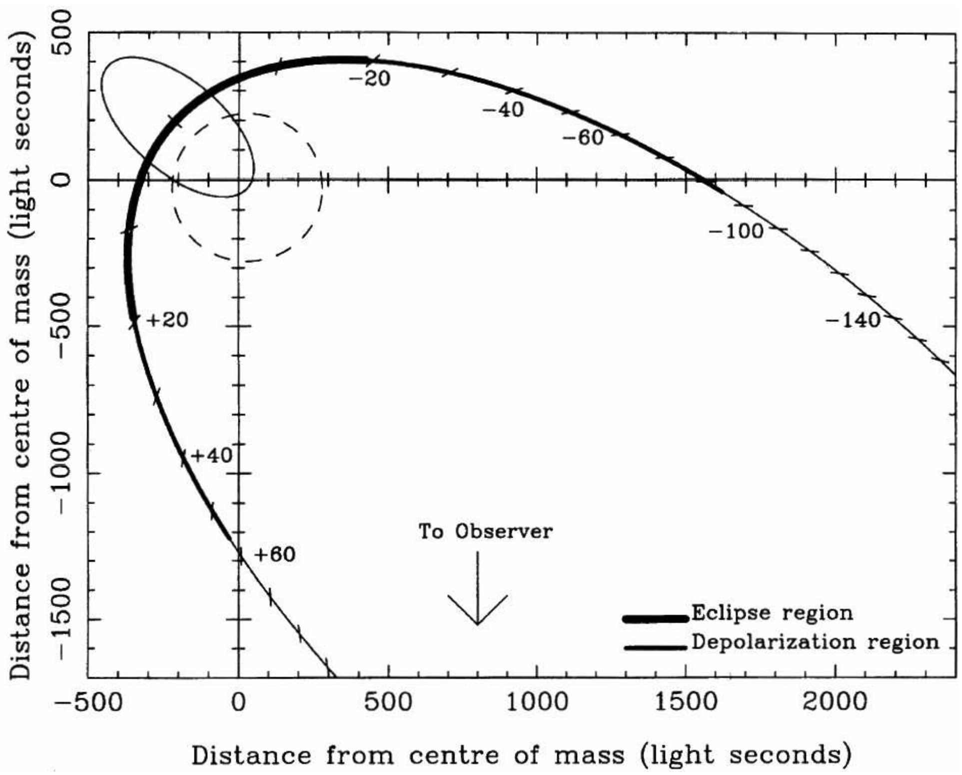

Figure 2.8: *Spatial scales of the pulsar and Be star orbit around the centre of mass [from Johnston et al., 1994]. The tick marks along the pulsar orbit represent time steps of 10 days. On the part of the orbit marked by the thick line near periastron the pulsed radio emission of PSR B1259−63 is eclipsed.*

orbit in the coordinate system of the orbital plane near the periastron passage (epoch τ) with the region of the eclipse marked as bold line. Furthermore, between $-100\,\mathrm{d} \lesssim \tau \lesssim +100\,\mathrm{d}$, the pulsed emission is seen to slowly loose its characteristic polarisation, in contrast to the rather abrupt eclipse. The depolarisation behaviour can be easily explained by scattering of the pulsed radiation within the stellar wind of SS 2883 increasing towards periastron, but the eclipse could originate from absorption of the radiation by the stellar disk material, requiring a significant inclination of the disk with respect to the orbital plane. The epochs of the eclipse were consistent for all four periastron passages observed so far [Johnston et al., 2005], and the dates of pulse (dis)-appearance vary only on the level of a few days. If the eclipse mechanism is absorption on the material of a tilted disk, its opening angle is constrained to be <10° [Johnston et al., 1999].

Using the dispersion and rotation measure (DM and RM) obtained from the pulsed emission, a comprehensive model of the Be star wind and disk geometry was obtained by Melatos et al. [1995]. Therein it was found that the rapid rise in DM can only be explained by the dense disk material and thus

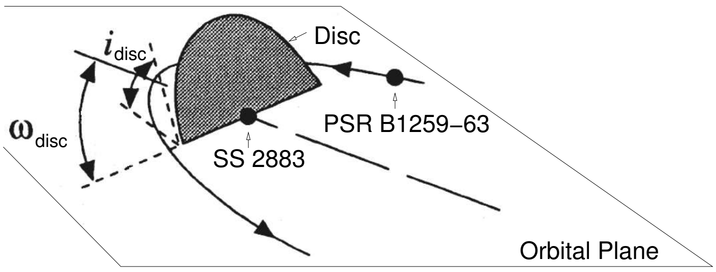

Figure 2.9: *System geometry [Melatos et al., 1995].*

requiring the disk to be inclined at angles $30^\circ < i_{\rm disk} < 40^\circ$, as illustrated in Fig. 2.9.

Up to now, the binary orbit is still not uniquely determined from the pulsar radio timing measurements, mainly because the pulsar is eclipsed near periastron. Wex et al. [1998] provided several timing solutions which tried to model the observed irregularities and timing jumps occurring near periastron and favoured a solution where significant spin-orbit coupling is considered. They interpreted this resulting from higher gravitational moments of the Be star and provided a possible explanation to be a significant inclination of the stars equator and its disk with respect to the orbit, i.e. $i_{disk} > 0^\circ$. However, the most recent timing analyses [Wang et al., 2004, Johnston et al., 2005] provide the best fit to the data without considering such an effect. Thus, the conclusion of an orbital inclination could neither be confirmed nor ruled out. Additionally, the best fit solution found by Wang et al. [2004] includes jumps of the pulsar orbit of $|x| = \mathcal{O}(10)$ light seconds (ls) at every periastron passage with changing sign, for which no obvious explanation could be found, but they speculated about tidal and Be star oscillation effects resulting from the orbital inclination.

2.3 Non-Thermal Emission of PSR B1259−63 / SS 2883

At the times of the pulsar eclipse close to the periastron passage, a continuous non-thermal radio emission was observed. This transient component was found to be variable with respect to the pulsar position along its orbit, probably resulting from the interaction of the stellar winds with the neutron star. Furthermore, observations at X-ray energies revealed a clearly non-thermal emission indicating the presence of high energy phenomena leading to particle acceleration. Similarly to the radio continuum emission, the measured flux of X-rays varied with the orbital phase but being detectable throughout the whole orbit. Several possibilities were considered in order to explain this emission and it turned out that shock acceleration in the interaction region of the stellar and pulsar winds is the most likely scenario. In fact, the situation is quite similar to that of the Crab Nebula discussed in Sec. 2.1.3, where the pulsar wind terminates within the remaining supernova ejecta and the interstellar medium. In the case of PSR B1259−63, the mass outflow of the companion star is responsible for the wind termination instead. Additionally, the eccentricity of the pulsar orbit provides an unique opportunity to study the dynamics of the interaction.

First in this section, the observational constraints from the radio, X-ray, and γ-ray measurements are introduced, followed by the description of the theoretical models found in the literature explaining the observed emission.

2.3.1 Transient Unpulsed Radio Emission

The radio observations near the periastron passage revealed a strong unpulsed emission [Johnston et al., 1999], roughly starting at the time when the pulsed emission disappears, and being detectable far beyond periastron. Figure 2.10 shows the corresponding light curve for the four periastron passages covered by observations so far [Johnston et al., 2005]. The times of the pulsar eclipse are indicated as double-arrow and were found to be persistent within 1–2 days in all four epochs. The flux rises steeply, beginning at $\approx \tau{-}20$ days and rapidly exceeds the flux level of the pulsed component (≈ 3 mJy) until a first maximum is reached at $\approx \tau{-}5$ d, then

Parameter		**V**alue	**R**eference
Pulsar PSR B1259−63			
Position	RA (J2000)	$13^{\mathrm{h}}2^{\mathrm{m}}47\overset{\mathrm{s}}{.}65(1)$	A
	Dec (J2000)	$-63^{\circ}50'8\overset{\prime\prime}{.}7(1)$	A
Period	P	47.762053919(4) ms	B
Period derivative	$\dot{P}$	$2.2793(4) \times 10^{-15}$	B
Spin-down luminosity	$\dot{E}$	9×10^{35} erg s^{-1}	B
Surface magnetic field	B	3.3×10^{11} G	B
Characteristic age	Δt_{SN}	3.3×10^{15} y	B
Mass	M_{ns}	$1.4\,M_{\odot}$	B
Be star SS 2883			
Mass	M_{comp}	$10\,M_{\odot}$	B
Radius	$R_{\star}$	$6\,R_{\odot} = 4.17 \times 10^{10}$ cm	B
Disk radius	R_{disk}	$> 20\,R_{\star}$	B
Disk inclination angle	$i_{\mathrm{disk}}{}^{*}$	$30 \ldots 40^{\circ}$	C
Disk orientation angle	$\omega_{\mathrm{disk}}{}^{*}$	$\approx 90^{\circ}$, $\approx 120^{\circ}$	C,E
Disk opening angle	θ_{disk}	$< 10^{\circ}$	D
Disk outflow index	n	≈ 2.5	E
System			
Projected semi-major axis	x	1296.272(5) ls	A
Eccentricity	e	0.8698872(9)	A
Epoch of periastron	τ	48124.34911(9) MJD	A
Orbital period	P_{orb}	1236.72432(2) d	A
Longitude of periastron	ω	$138.6659(1)^{\circ}$	A
Orbital inclination	i	36°	A
Separation at periastron	D_{p}	$23\,R_{\star}$	A
Separation at apastron	D_{a}	$331\,R_{\star}$	A
Distance	d	1.5 kpc	B

* highly uncertain

Table 2.1: *Properties of the PSR B1259−63/SS 2883 system. The references A,B,C,D,E correspond to Wang et al. [2004], Johnston et al. [1994], Melatos et al. [1995], Johnston et al. [1999], Tavani and Arons [1997], respectively. The numbers in brackets denote the 90% CL error on the last digit.*

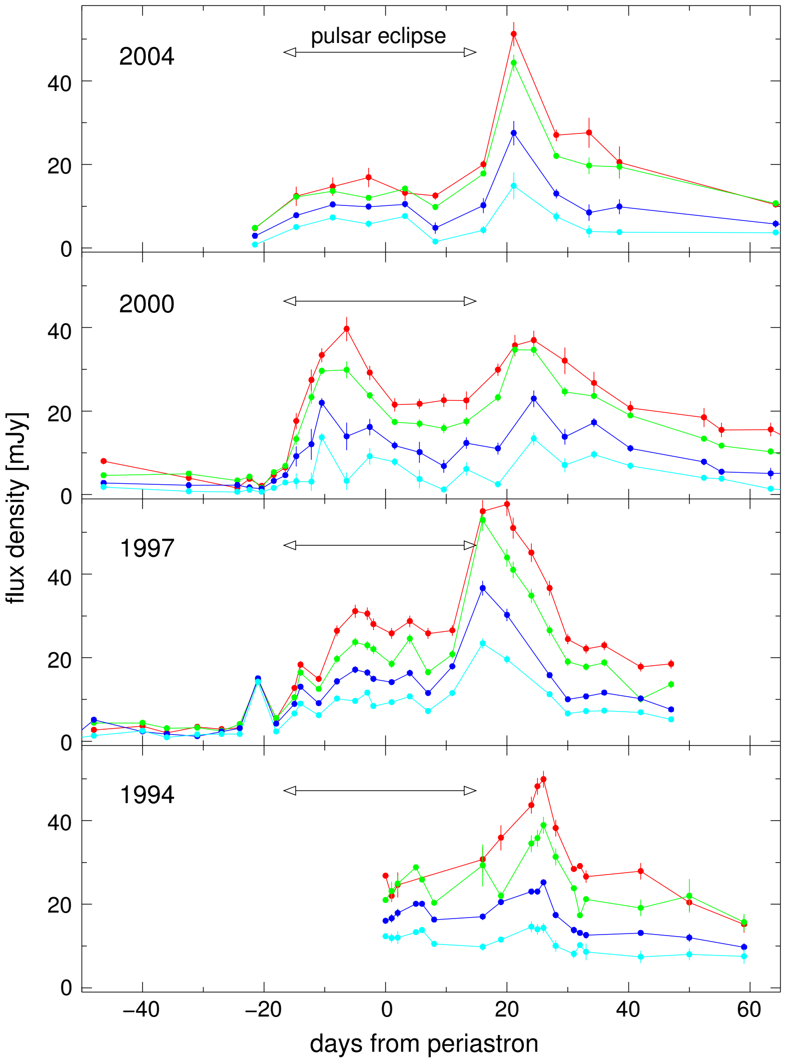

Figure 2.10: *Light curve of the non-thermal radio continuum [based on Johnston et al., 2005, Fig. 3]. The colors represent different radio frequencies at 1.4, 2.5, 4.8, and 8.6 GHz (from top to bottom). The arrows represent the pulsar eclipse period.*

declines slowly until it rises again steeply towards the second, more pronounced maximum at $\approx\tau+20$ d, and finally decays slowly, often still detectable at $\approx\tau+100$ d. This flux variability pattern is roughly consistent for all periastron passages observed so far. However, there are differences visible in the behaviour between the different periastron passages, especially in the 2000 passage.

The differential energy spectrum of the continuum emission is consistent with a power law with photon index Γ_{radio} ranging from 1.4 to 1.7, indicating a non-thermal origin. Such a non-thermal spectrum was also observed from other massive, early-type stars which was interpreted as synchrotron emission of relativistic electrons, accelerated in shocks induced by stellar wind turbulences [Johnston et al., 1999, and references therein]. However, in the case of PSR B1259−63, the transient character of the emission indicates an interaction of the stellar outflow and the pulsar.

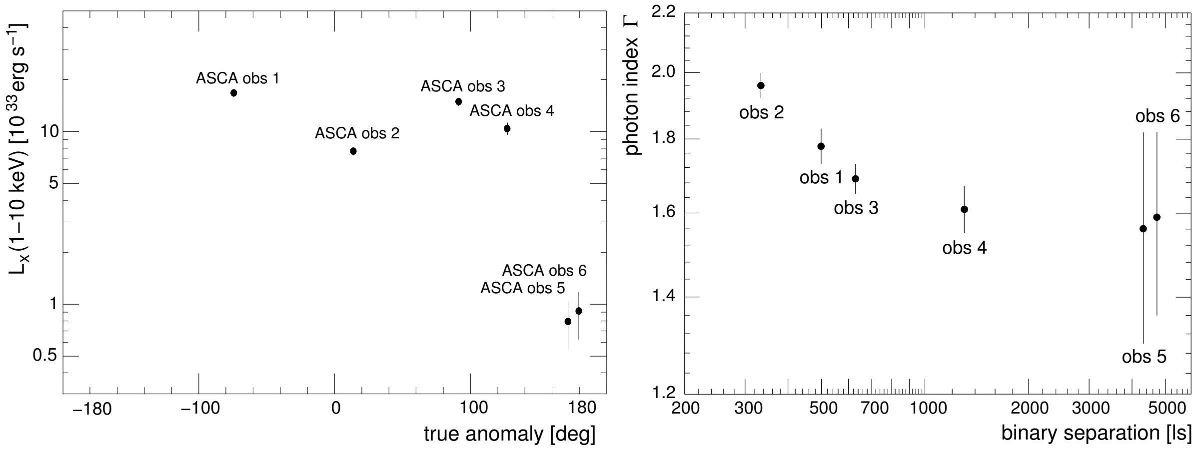

Figure 2.12: *X-ray light curve and photon index from ASCA observations according to Fig. 2.13 [E_X=1–10 keV, Hirayama et al., 1999].* **L**eft: *X-ray luminosity as a function of the true anomaly, ω.* **R**ight: *Photon index Γ_X of a power law fit to the differential photon spectrum as a function of the distance between the pulsar and its companion.*

2.3.2 Observations at X- and Soft γ-Ray Energies

The system of PSR B1259−63 was subject of several X- and γ-ray observations within the last 10 years, especially near periastron where the pulsar was expected to strongly interact with the stellar mass outflows.

The most sensitive observations at X-ray wavelengths were obtained by the *ASCA* satellite [Kaspi et al., 1995, Hirayama et al., 1996, 1999] and the *OSSE* detector on-board the *CGRO* satellite [Grove et al., 1995] leading to the detection of unpulsed non-thermal emission in the photon energy range of 1–10 keV and 50–200 keV, respectively. Figure 2.11 shows the orbital phases of the observations close to the epoch of periastron in 1994.

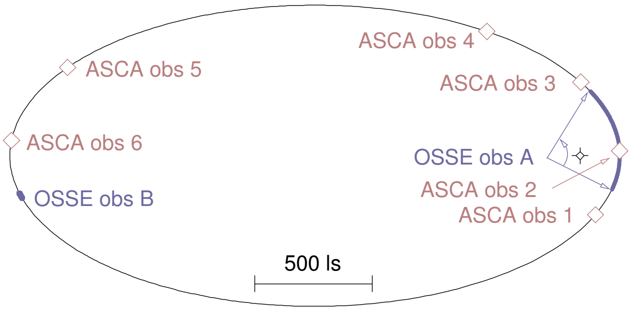

Figure 2.11: *Epochs of X-ray observations around the 1994 periastron [from Hirayama et al., 1999].*

In the energy range 1–10 keV, the coverage along the orbit was rather poor compared to the radio observations. However, PSR B1259−63 was detected with a high significance in every single exposure allowing for the determination of an energy spectrum. Figure 2.12 (left) shows the evolution of the X-ray luminosity as a function of the orbital phase. The highest flux was detected for the two observations where the pulsar is thought to cross the stellar disk, while the flux close to the periastron passage was somewhat lower. The observations near apastron yielded a flux roughly a factor of ten lower than at periastron. The measured spectrum follows a power law and is rather hard at apastron with $\Gamma \approx 1.6$ and steepens with decreasing distance between the pulsar and the Be star reaching $\Gamma \approx 2$ at periastron (see Fig. 2.12, right). A search for a pulsed component of the detected radiation was performed yielding an upper limit of $\approx 10^{33}$ erg s^{-1} [Hirayama et al., 1996].

At higher X-ray energies of 50–200 keV, the source was detected by *OSSE* during the observations near periastron and the data was found to follow a power law with index $\Gamma = 1.8 \pm 0.6$, similar to that of the softer X-rays. The other instruments of *CGRO* were not able to detect a significant flux and upper limits were derived. Figure 2.13 shows a broadband spectrum of the non-thermal radiation of PSR B1259−63 for the data obtained near the 1994 periastron in the energy range between 1 keV and 10 GeV.

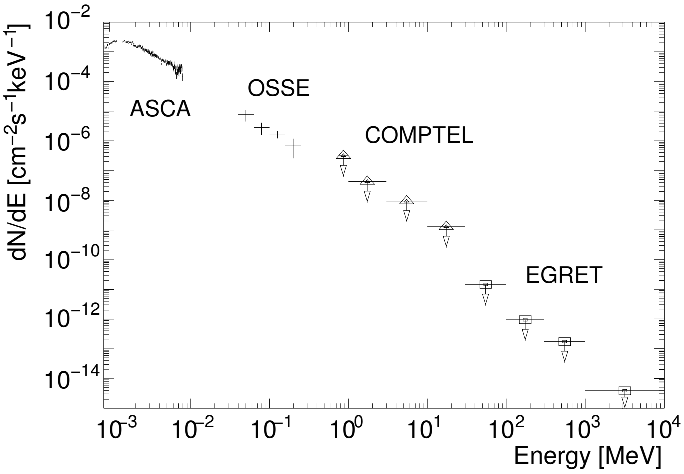

Figure 2.13: *Differential energy spectrum* $\mathrm{d}N/\mathrm{d}E$ *of X-rays from PSR B1259−63 at the periastron passage of 1994 [from Tavani and Arons, 1997].*

2.3.3 Shock Acceleration of Electrons

The non-thermal radiation emitted by the system indicates particle acceleration to relativistic energies which can result from a variety of mechanisms. For example, several other binary systems containing neutron stars feature non-thermal X-ray emission (X-ray binaries) which is attributed to accretion of stellar matter onto the neutron star surface. Other mechanisms include interaction of stellar material with the pulsar magnetosphere, Be star coronal emission, and Bremsstrahlung of heated gas in the stellar outflow. However, Tavani and Arons [1997] discussed the latter cases and found, that the observational data is not compatible with these scenarios and consider shock acceleration of electrons to be the most likely effect.

In the following, the characteristics of the Be star and pulsar wind interaction and the implications are discussed with respect to the observational data.

Be Star – Pulsar Wind Interaction

Figure 2.14 illustrates the basic properties of the interaction of the pulsar wind with the stellar outflows [see also Melatos et al., 1995, Tavani and Arons, 1997]. At a given distance from the pulsar, the momentum flux of the pulsar wind matches that of the stellar outflow (contact discontinuity) resulting in reverse shocks to be formed – the stellar outflow and the pulsar wind termination shock. The shock surface is bent in the direction of the star or the pulsar, depending on the strength of the wind, forming a *bow-shock* with its apex on the line between the pulsar and the star, in contrast to the spherically symmetric shock in the case of the Crab Nebula. Therefore, the plasma in the down-stream region between the contact and the shock surface expands in the direction away from the apex and a flow component parallel to the shock surface is established, different from the axial symmetric situation in the Crab synchrotron nebula, influencing the energy loss mechanisms of shock-accelerated particles in these regions.

Since the density of the stellar outflow is enhanced within the equatorial disk, a “comet-like” situation arises when the pulsar approaches periastron and enters the disk, such that the shocks appear close to the pulsar and the stellar material flows around the pulsar. As the shock geometry changes with the orbital phase, the non-thermal processes, which are expected to occur near the shocks, can produce a variability of non-thermal radiation emitted from the interaction region on a timescale of a few weeks in case the disk lies in the orbital plane. In the contrary case of an orbital inclination, the pulsar passes the equatorial disk two times close to periastron, at τ_1 and τ_2, significantly changing the shock geometry on an even shorter timescale of a few days. Figure 2.15 illustrates this scenario with respect to an observer at earth, assuming the most likely disk geometry (see also Table 2.1).

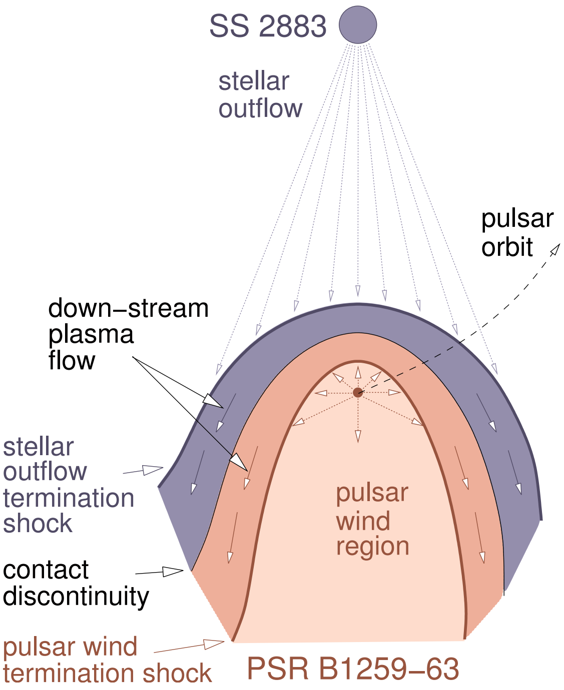

Figure 2.14: *Schematic view of the interaction between the stellar outflow and the pulsar wind.*

The two shocks can produce two different populations of shock-accelerated particles, originating from the stellar outflow and the pulsar wind, respectively. Both shock regions should have different properties such as particle energy spectrum and density, depending on the initial pre-shock attributes of the plasma like the mean kinetic energy of the particles, and the magnetic field strength within the plasma.

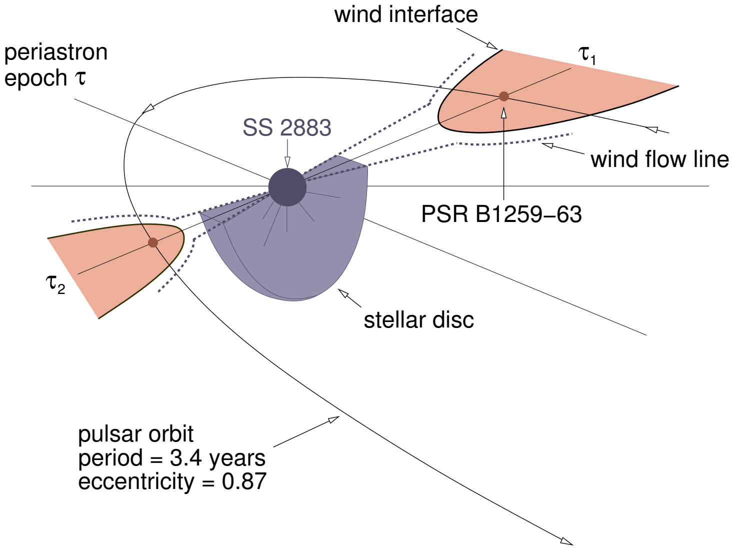

Figure 2.15: *Sketch of the orbit of PSR B1259−63 with respect to the line of sight. The pulsar approaches the equatorial disk prior to periastron (τ_1) while it is “behind” the companion star and turns towards the observer before it crosses the disk the second time (τ_2) after periastron [based on Johnston et al., 1999, Fig. 3]. During the interaction of the disk of the Be star and the pulsar, a more comet-like bow shock is formed.*

Be Star Electrons

Within the above picture of colliding winds, the transient non-thermal radio emission (see Sec. 2.3.1) was explained by Ball et al. [1999] as synchrotron emission of electrons accelerated in the Be star shock and evolving in the corresponding down-stream region. Therein, two arguments are given, showing that the electrons originate from the Be star and not from the pulsar wind. Firstly, the low energy of the synchrotron photons indicates a parent spectrum of low energy electrons, which would imply, if the electrons originate from the pulsar, that the pulsar wind has a Lorentz factor of $\gamma \approx 10$, five orders of magnitude lower than that assumed to be the case for young pulsars. Since the electrons from the unshocked Be star outflow are expected to be not highly relativistic, they could easily produce the observed synchrotron spectrum in the post-shock region. Secondly, the electron number density expected for the shocked pulsar wind is far from being sufficient in order to explain the observed flux level.

Furthermore, it was shown, that the observed flux is associated with the shock induced by the equatorial disk outflow rather than that from the polar wind, since the ratio of the fluxes observed at periastron and apastron is more than an order of magnitude higher than expected for the interaction with the polar wind only.

The observed light curves around periastron can be qualitatively reproduced with a model, where the pulsar wind interacts at a limited time interval with the disk material, and leaving behind a "synchrotron bubble" which evolves at timescales of weeks by synchrotron emission only, allowing to explain the slow decay of the observed flux. Possible adiabatic losses were neglected because the bubble was considered to expand very slowly. This naturally explains the evolution of the two flux maxima and provides further evidence for a significant disk inclination. In the model, the disk crossings were assumed to occur at the times indicated by the pulsar eclipse.

It is also important to note, that the maximum flux of the unpulsed emission occurs some days later than the assumed disk crossing times, which is explained in the model by an accumulation of accelerated electrons implying a fast acceleration compared to the timescale of energy losses through synchrotron radiation. However, no good explanation is found for the different flux levels of the maxima for different periastron passages (see Fig. 2.10) but it was speculated about inhomogeneities of the stellar outflow causing a varying pressure onto the pulsar wind [Connors et al., 2002]. The time evolution of the synchrotron spectrum allows a rough estimate of the magnetic field strength in the vicinity of the radiating plasma, and it was determined from the 2000 periastron passage data to be $\approx 1.6\,\mathrm{G}$ [Connors et al., 2002].

Pulsar Wind Electrons

The acceleration of electrons originating from the Be star disk cannot easily account for the observed X-ray emission of PSR B1259−63 since the typical acceleration timescale is much larger than the timescale of synchrotron losses. In contrast, the pulsar wind electrons have already got a high kinetic energy before being shock-accelerated, provided that the wind properties are similar to that of the Crab Nebula with a Lorentz factor of the wind of $\gamma_{\mathrm{wind}} > 10^5$, i.e. resulting in an injection spectrum starting above several GeV. The observed X-rays then result from synchrotron radiation in the magnetic field within the down-stream region of the pulsar wind shock.

In Tavani and Arons [1997], a complete MHD treatment of the pulsar wind termination shock was performed according to the model of Kennel and Coroniti [1984], developed for the Crab Nebula (see Sec. 2.1.4), but adapted to the environment of the system of PSR B1259−63. The calculations fit best for pulsar wind parameters $\gamma_{\mathrm{wind}} = 10^6$ and $\sigma = 0.02$ at the distance of the termination shock. The fact that the magnetisation parameter σ is much higher than for the Crab pulsar is explained by the much smaller distance of the shock to the pulsar magnetosphere such that less magnetic energy was converted into kinetic energy.

In order to reproduce the observed X-ray spectra and light curve, Tavani and Arons [1997] computed the shock characteristics for different stellar outflow parameters and for both, an inclined and coplanar disk. They fitted the model to the *ASCA* X-ray data obtained around the 1994 periastron. Figure 2.16 shows the X-ray luminosity L_X (top) and photon index Γ_X (bottom) in the energy range 1–10 keV as a function of the orbital phase ω for the best model fit to the data. The model clearly favours a disk inclination, with a rather big opening angle $\theta_{\rm disk} = 30°$ and, more interestingly, a disk orientation angle $\omega_{\rm disk} = 120°$ slightly deviating from the estimate deduced from radio observations and predicting a flux minimum to occur slightly later than periastron.

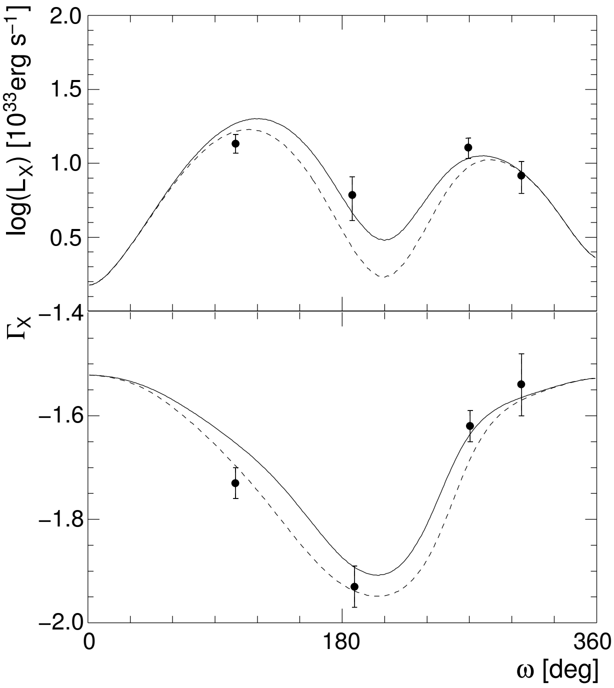

Figure 2.16: *X-ray luminosity (top) and photon index (bottom) as a function of orbital phase together with the best fit solution of a detailed MHD model of the pulsar wind shock by Tavani and Arons [1997].*

In Figure 2.17 (left, middle), the shock characteristics corresponding to the best fit model are displayed: the magnetic field strength in the down-stream region of the pulsar wind shock B_2 and the distance of the shock from the pulsar r_s, showing that the interaction with the disk outflow strongly confines the pulsar wind, resulting in a local minimum of r_s and a corresponding maximum of B_2 near the disk crossings at $\omega \approx 120°$ and 300°. However, the model assumption of a spherical shock geometry does not consider any asymmetric flow effects, as indicated in Fig. 2.14, which might be important.

Figure 2.17 (right) shows the characteristic timescales $t = \epsilon/\dot{\epsilon}$ relevant for the acceleration and evolution of the radiating electrons, in particular:

- $t_{\rm acc}$ as the acceleration time,
- $t_{\rm sy}$ as the synchrotron radiation timescale in the down-stream magnetic field,
- $t_{\rm IC,Th}$, $t_{\rm IC,KN}$ as the timescales on which the electrons undergo inverse Compton scattering with thermal photons emitted by the star, either in the non-relativistic Thompson or relativistic Klein-Nishina regime, respectively,
- $t_{\rm ad}$ as the timescale on which adiabatic losses proceed by removing the electrons from the region where acceleration or radiation processes can occur.

Clearly, the acceleration process has the shortest timescale, thus producing a power-law injection spectrum with index $\alpha_{\rm e}^{\rm inj}$ and Lorentz factors between γ_1 and $\gamma_2 > \gamma_1$ for the relativistic electrons accelerated in the shock and injected into the down-stream region. The lower end of the spectrum is determined by the Lorentz factor of the pulsar wind, $\gamma_1 = \gamma_{\rm wind} \approx 10^6$ while the upper end remains unknown but is constrained by observations to be $\gamma_2 \leq 10^4\gamma_1$, since the extrapolated power law synchrotron spectrum (see Fig. 2.13) is violated by the limits on the

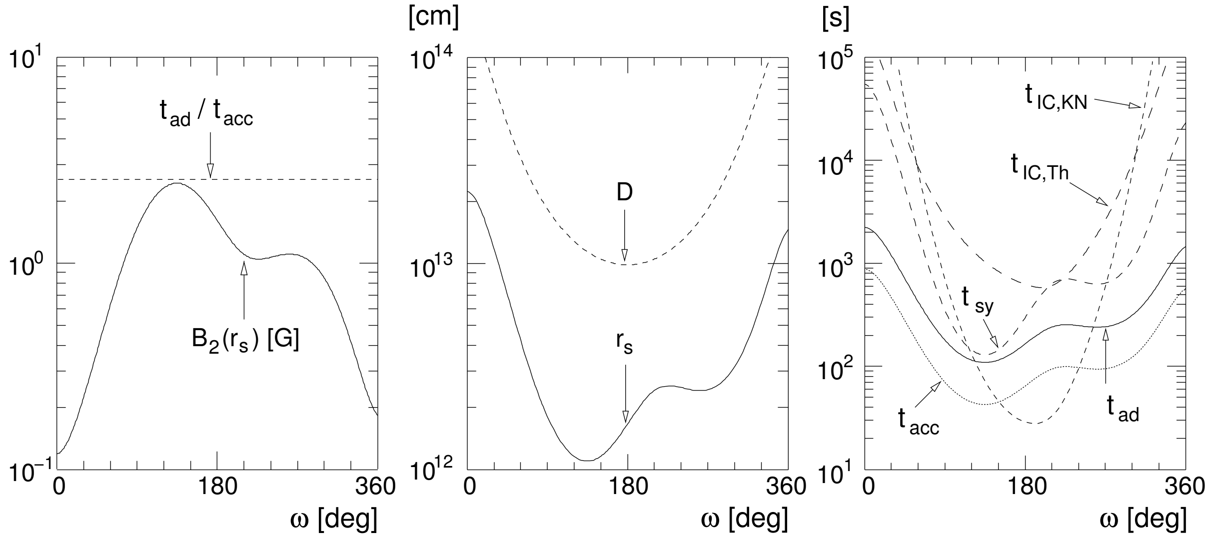

Figure 2.17: *Best fit model for the pulsar wind termination shock [Tavani and Arons, 1997]. Shown are the shock distance from the pulsar r_s, the distance between the pulsar and the Be star D (both middle panel), the down-stream magnetic field strength $B_2(r_s)$ (left panel), and the acceleration and energy loss timescales for electrons (right panel, see text) as a function of the orbital phase ω.*

soft γ-ray emission found by *EGRET* (20 MeV–10 GeV). The power-law index α_e of the radiating electrons, which could be different from the injection index since the population evolves in time, is given by $\alpha_e = 2\Gamma_X - 1 \approx 2.4$ (see Sec. 2.1.3). According to Fig. 2.17, adiabatic expansion seems to be the dominant energy loss mechanism over a wide range of the pulsar orbit, which would indicate a spectrum with $\alpha_e^{inj} = \alpha_e$. Since the magnetic field strength is enhanced near the disk crossings, synchrotron losses become comparable to the adiabatic losses for the first disk crossing, shortly prior to periastron. The timescale which applies for inverse Compton losses of the electrons lies somewhere in between $t_{IC,Th}$ and $t_{IC,KN}$ because the scattering takes place in the transition region of both regimes, highly depending on the energy of the electrons (see also Sec. 6.2.1). The maximum of IC scattering near periastron is a direct consequence of the small distance between the pulsar and its companion, where the density of thermal photons originating from the star reaches its maximum. The local minimum of the X-ray flux at periastron can be explained if the corresponding IC timescale becomes shorter than that of the adiabatic losses and especially synchrotron losses which result in the X-ray radiation. Additionally, the dominant IC losses lead to a softer electron and therefore softer X-ray emission spectrum, because the scattering cross section increases with the electron energy, consistent with actual observations (see Fig. 2.16).

It is important to note that the radiated photons resulting from IC losses would have a minimum energy $E_{IC} \sim \epsilon_e^{min} = \gamma_1 m_e \approx 5.11 \times 10^{11}$ eV = 0.511 TeV because in the scattering process the electrons transfers their momentum almost completely to the soft photon. Thus, the IC radiation would be VHE γ-rays, with a flux maximum at periastron.

2.4 VHE γ-Rays from PSR B1259−63 / SS 2883?

VHE γ-rays can be produced by various mechanisms, but in the case of non-thermal astrophysical processes, the existence of particles with kinetic energies higher than the energy of the produced γ-ray photons is required, i.e. with energies above ≈ 1 TeV. The spin-down luminosity of PSR B1259−63 is sufficiently high to create such particle populations, either electrons or hadrons, which can be contained in the pulsar wind itself or produced by acceleration in the wind termination shock as described above. Additionally, particles may be accelerated in the shock on the Be star side and produce γ-rays via Bremsstrahlung and π^0 decay induced by proton-proton interactions.

In this section, the above possibilities are described in detail on the basis of model calculations found in the literature, and the implications for an observer are discussed. Finally, previous observations of PSR B1259−63 at VHE γ-ray energies are shortly reviewed.

2.4.1 Inverse Compton Emission of Ultra-Relativistic Electrons

The synchrotron origin of the detected X-rays, discussed in the last section, implies electron acceleration to TeV energies. However, this represents only an indirect evidence and it cannot be firmly excluded that the non-thermal emission can be produced by other mechanisms. The detection of the IC component of the accelerated electron population would provide more direct evidence for the acceleration of electrons to TeV energies.

Unshocked Pulsar Wind Electrons

The cold, highly relativistic pulsar wind of the Crab Nebula remains unseen so far at all radiation wavelengths. However, in the case of PSR B1259−63, the companion star provides a very high-density photon field causing the pulsar wind electrons to undergo IC scattering leading to an observable flux of γ-rays [Ball and Kirk, 2000, Ball and Dodd, 2001]. The scattering cross section depends highly on the angle between the electron flow direction and that of the target photons, with its main contribution if they are oriented head on towards each other, and the scattered photons are emitted in the direction of the initial electron directions. Thus, the flux of γ-rays observable on Earth is maximal, if the angle between the line of sight and the line between both stars is minimal $\theta_{\mathrm{p}} = 90^\circ - i = 55^\circ$ when the pulsar is "behind" the star shortly prior to periastron (compare with Fig. 2.15), in contrast to the case when the pulsar is in "front" of the star with $\theta_{\mathrm{p}} = 125^\circ$ post-periastron.

Figure 2.18 (left) shows the expected spectral energy distribution of γ-rays, $E^2 \mathrm{d}N/\mathrm{d}E = EF_E$, for a minimal and maximal θ_{p} and for two values of the pulsar wind Lorentz factor, $\gamma_{\mathrm{wind}} = 10^6, 10^7$ (solid and dashed line, respectively). The Lorentz factor γ_{wind} determines the maximum energy a photon can obtain from the up-scattering. In fact, at the considered energies, the IC process takes place in the deep relativistic Klein-Nishina regime, resulting in a line-type spectrum of γ-rays since the electron transfers nearly all its momentum to the photon in the rest frame of the observer.

Figure 2.18 (right) shows the light curve for an orbital time range of 200 days around periastron. The overall shape of the light curve is dominated by the scaling of the target photon density with the separation between pulsar and companion, $n_{\mathrm{star}} \propto (D/R_\star)^{-2}$, resulting in a maximum

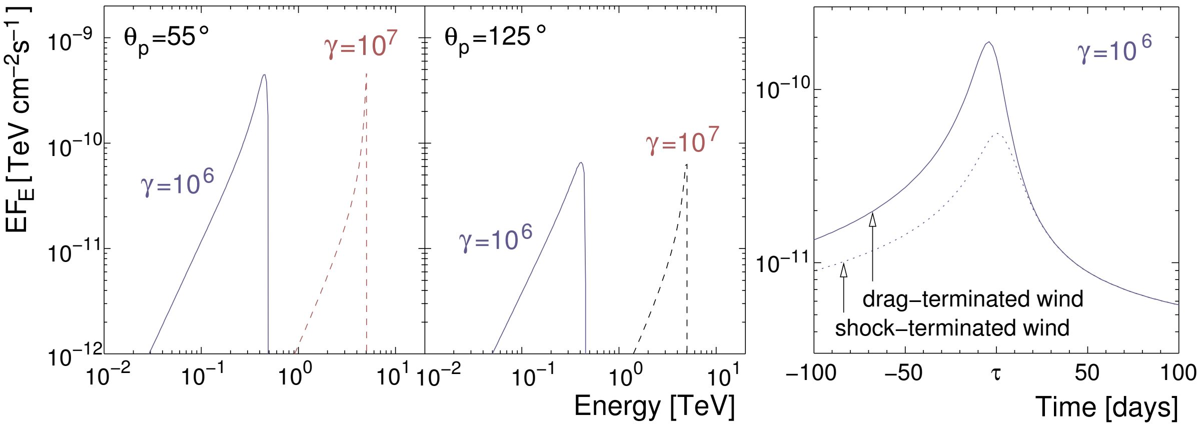

Figure 2.18: *Spectra and light curve for IC γ-ray emission from the unshocked pulsar wind of PSR B1259−63.* ***L****eft: Spectral energy distribution EF_E of γ-rays for $\theta_\mathrm{p} = 55°, 125°$ and wind Lorentz factors of $\gamma_\mathrm{wind} = 10^6, 10^7$ [solid and dashed lines Ball and Kirk, 2000].* ***R****ight: Integrated energy flux of VHE γ-rays as a function of time with respect to periastron for a wind Lorentz factor of $\gamma_\mathrm{wind} = 10^6$ [Ball and Dodd, 2001]. The solid and dashed lines correspond to a confinement of the pulsar wind by IC losses (drag) or by a termination shock, respectively.*

flux at periastron. The dependence on θ_p introduces an asymmetry with respect to periastron since the corresponding modulation of the light curve is symmetrical to $\theta_\mathrm{p} = 55°$, several days prior to periastron. Additionally, the absolute flux of IC photons depends on the size of the unshocked pulsar wind region. Most likely, the wind is terminated by a shock induced by the dense Be star outflow. However, if the pressure of this outflow onto the pulsar wind is weak, the wind particles may have lost most of its energy due to the IC scattering (*IC drag*) and the wind is decelerated to subsonic speeds and remains unshocked. These two cases correspond to the dotted and solid line in Fig. 2.18 (right).

Shock-Accelerated Pulsar Wind Electrons

The scenario in which pulsar wind electrons are accelerated by the wind termination shock was intensively discussed in Sec. 2.3.3. Kirk et al. [1999] calculated the resulting IC emission of the accelerated electrons in a – compared to the detailed modeling by Tavani and Arons [1997] – simplified approach and derived spectra and light curves considering different energy loss mechanisms.

In the model by Kirk et al. [1999], it was assumed that the shock is spherically symmetric, and that the ratio of the energy densities of the magnetic field and the stars photon field is constant which determines the shock position to scale with the orbital separation. The latter assumption implies an isotropic stellar outflow and requires the ram pressures of both winds to have the same radial dependence, which might be the case considering the uncertainties of recent Be star wind models, i.e. for a stellar outflow with a constant velocity profile with $n = 2$ (see Table 2.1).

The radiation spectra of shock-accelerated electrons were determined for the following parameters:

- ▹ the power-law index α_e^inj of the electron injection spectrum, produced by the acceleration process,

- the magnetic field strength B within the radiating plasma in the down-stream region of the shock,
- the pulsar wind Lorentz factor γ_1, and the corresponding upper cutoff of the acceleration spectrum, assumed to be $\gamma_2 = 100\,\gamma_1$.

The model parameters were tuned such that the computed spectra of synchrotron radiation match the *ASCA* and *OSSE* X-ray data (see Sec. 2.3.2).

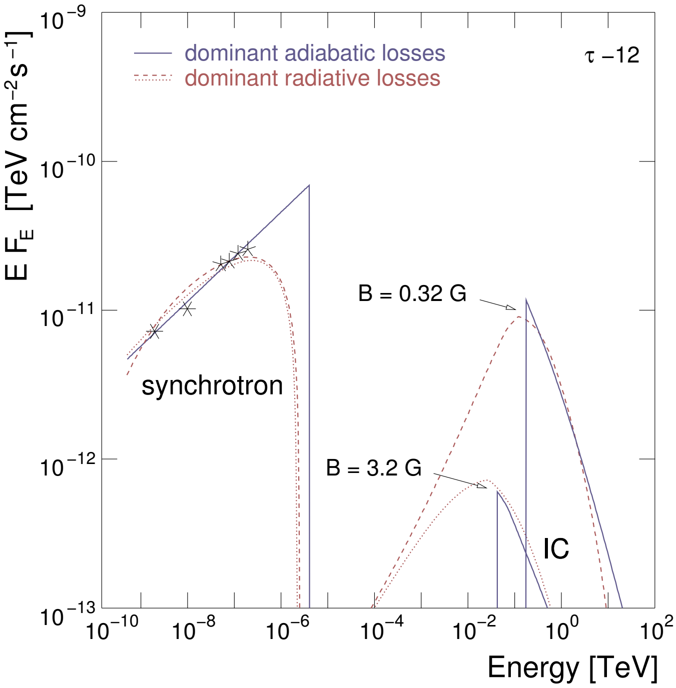

Figure 2.19: *Spectral energy distributions for synchrotron and IC emission of shock-accelerated electrons [based on Kirk et al., 1999, Fig. 2, 4, 6] for different energy loss mechanisms (see text).*

Figure 2.19 shows the best fit spectral energy distributions for the resulting synchrotron (X-ray) and IC (γ-ray) radiation component at an orbital phase 12 days prior to periastron, where the maximum IC flux is expected (see below).

For the case of dominant energy loss by plasma expansion (adiabatic losses, solid lines), the radiating electrons follow an energy spectrum with an index identical to the injection index $\alpha_\mathrm{e} = \alpha_\mathrm{e}^\mathrm{inj}$. From the measured synchrotron spectrum follows an injection spectrum with $\alpha_\mathrm{e} = 2\Gamma_\mathrm{X} - 1 \approx 2.4 = \alpha_\mathrm{e}^\mathrm{inj}$. The ratio of synchrotron and IC energy flux is determined by the magnetic field strength – an increasing magnetic field strength results in stronger synchrotron losses $\dot{n}_\mathrm{e} \propto B^2$ and therefore reduces the number of electrons n_e available for inverse Compton emission and vice versa. Since the synchrotron component is fixed by observations, a variation of B results in a different flux level of expected IC γ-rays. The chosen values of $B = 0.32$ G and 3.2 G were justified by the MHD calculations of Tavani and Arons [1997, see Fig. 2.17] and the estimate from the unpulsed radio emission near periastron (see Sec. 2.3.1). The spectrum of the IC component slightly deviates from a power law, since the scattering takes place in the transition region between the Thompson and Klein-Nishina regime (see also Sec. 6.2.1), with a corresponding γ-ray photon index of $\frac{1}{2}(\alpha_\mathrm{e} + 1) < \Gamma_\gamma < \alpha_\mathrm{e} + 1$. The sharp cutoff in the spectra is an artifact resulting from considering only accelerated electrons in a discrete energy range.

If the plasma expansion proceeds on a larger timescale than on which radiative energy losses of the electrons can occur, the initial injection spectrum gets significantly curved. Two cases were considered, dominant synchrotron losses for $B = 3.2$ G and dominant IC losses for $B = 0.32$ G, requiring injection spectra with $\alpha_\mathrm{e}^\mathrm{inj,sy} = 1.2$ and $\alpha_\mathrm{e}^\mathrm{inj,IC} = 1.4$, respectively. Note that such hard injection spectra may be difficult to produce with common shock-acceleration

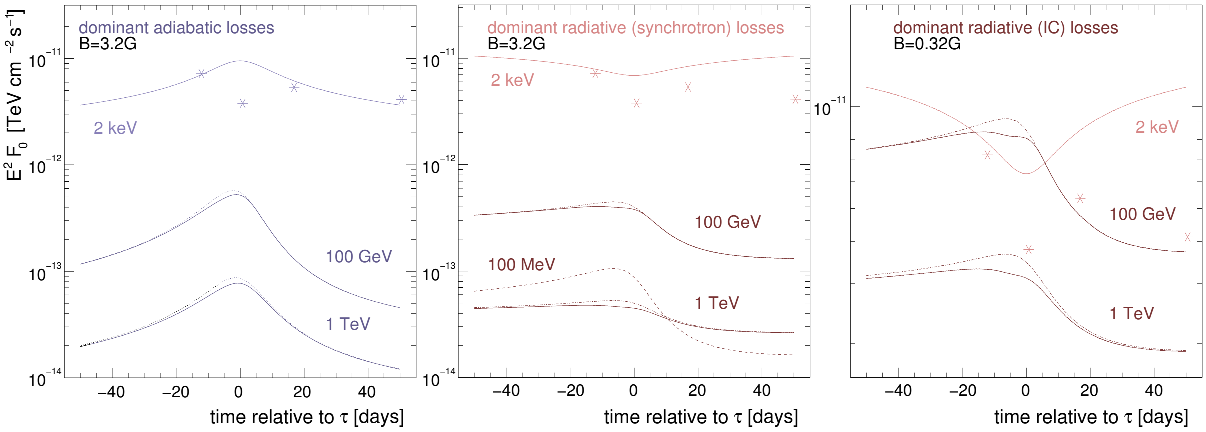

Figure 2.20: *Energy flux of synchrotron and IC radiation of shock-accelerated electrons as a function of time at orbital phases around periastron. The light curves are shown for dominant adiabatic (left) and synchrotron (middle) losses for $B = 3.2$ G, and dominant IC losses for $B = 0.32$ G (right).*

processes.

Within the model, the two loss mechanisms produce quite similar spectra in the VHE γ-ray energy range, making it difficult to distinguish between them. However, the radiative losses strongly depend on the magnetic field strength and the ambient photon field density and are thus expected to strongly vary with the phase of the pulsar orbit, producing a characteristic temporal behaviour of the flux and maybe even a variable spectral shape in case of competing radiative and adiabatic energy losses. Figure 2.20 shows the model light curves – the energy flux for radiation at X- and γ-ray energies as a function of time – for the three cases of dominant adiabatic (left), synchrotron (middle), and IC (right) losses together with the measured X-ray flux (asterisks). The light curves at γ-ray energies show an asymmetry with respect to periastron which is a result of the asymmetry of the IC scattering as discussed for the unshocked wind emission. However, since the shock-accelerated electrons are isotropically distributed and only the target photons have a preferred direction, the effect is less dominant. Furthermore, the γ-ray flux should be noticeably reduced shortly pre-periastron due to the effect of photon-photon pair production by interaction with the soft photons after the IC scattering took place (dotted vs. solid lines).

For dominant adiabatic losses (Fig. 2.20, left), the shape of the electron spectrum remains the same throughout the orbit and the orbital flux modulation is dominated by the confinement of the pulsar wind by the stellar outflow, which was assumed to be isotropic, resulting in a maximum at periastron for both, the synchrotron and IC emission, in contradiction with the X-ray data. For radiative losses, the electron spectrum index and norm varies with orbital phase, resulting in a minimum of the synchrotron emission at periastron for a given photon energy. The dominance of one of the two competing radiation mechanisms – synchrotron and IC cooling – is determined by the magnetic field strength. For a magnetic field of $B = 3.2$ G, synchrotron losses dominate, and the main energy is released in form of X-rays, while for $B = 0.32$ G IC losses are dominant and the maximum energy is contained in VHE γ-rays (see Fig. 2.20, middle and right, respectively). The evolution of the X-ray flux is not correctly reproduced in any of the three scenarios, which could be avoided if one considers adiabatic losses to be dominant for most of the orbit, but being suppressed by radiative losses near periastron, as already suggested by Tavani and Arons [1997].

In any case, the inverse Compton emission of highly relativistic electrons accelerated within the PSR B1259−63 system results in an unambiguous characteristic shape of the light curve.

2.4.2 Shock Acceleration of Stellar Wind Particles

In the model of [Kawachi et al., 2004], shock-acceleration of the stellar outflow material is considered to produce VHE γ-rays via IC and Bremsstrahlung processes of electrons and π^0-decay resulting from proton-proton interactions in the down-stream disk material. They assumed an acceleration efficiency (the fraction of wind particles to be accelerated) for protons to be 0.1 and – more importantly – a factor of 100 higher than the efficiency for the acceleration of electrons (10^{-3}), justified by the ratio of protons and electrons of all observed cosmic rays at Earth, thus implying that this ratio is somewhat natural for all cosmic accelerators. The stellar outflow was considered to consist of an equatorial disk and a polar component with its momentum flux, x, as a free parameter such that $x_{\rm disk} = 10\, x_{\rm polar}$ and the γ-ray flux was found to scale with x^2. The spectrum of shock-accelerated particles was assumed to be a power law with constant index $\alpha^{\rm inj}_{\rm e,p} = 2$, and any energy losses of the particles were neglected to occur such that the index of the particles producing the radiation remains the same, $\alpha_{\rm e,p} = \alpha^{\rm inj}_{\rm e,p}$. However, it might be questionable if this simplification is easily justified for the case of electrons, since already the high magnetic field strength suggests severe synchrotron losses on timescales of less than 1 hour.

Figure 2.21 (right) shows the computed differential spectrum of γ-rays (solid line) at periastron for an aligned disk, with components from electron Bremsstrahlung and IC scattering (dotted lines), and from π^0-decay (dashed line) representing the dominant contribution. The outflow parameter was chosen such that the calculated spectrum does not violate the upper limits from observational data.

Figure 2.21 (left) displays the model light curves for the flux of γ-rays with energies above 1 TeV in the time range of 400 days around periastron for three different cases of pulsar-disk interaction (i–iii). In model (i), the disk was considered to lie in the orbital plane, as for the γ-ray spectrum above. For model (i) and (ii), the pulsar wind was assumed to interact with the disk for a rather long period of $\tau - 100 < \tau < \tau + 100$ days and for two short periods ($\tau - 18$ to $\tau - 8$ and $\tau + 12$ to $\tau + 22$ days), respectively. Similarly to the model of Ball et al. [1999] for the unpulsed radio emission, a pulsar wind bubble was assumed to remain inside the disk flow, considering the accelerated protons to loose energy by p-p interactions only, resulting in a rather slow decay of the γ-ray emission on a timescale of weeks.

2.4.3 Previous Observations in VHE γ-Rays

The *CANGAROO* collaboration, operating imaging atmospheric Cherenkov telescopes in Australia, observed the system of PSR B1259−63 in the years 2000/2001 with their *CANGAROO II* 10 m telescope [Kawachi et al., 2004]. The observations were performed at $\tau + 47$ and $\tau + 157$ days (see Fig. 2.22), at energy thresholds of 0.78 and 3.6 TeV, and for exposure times of 3.4

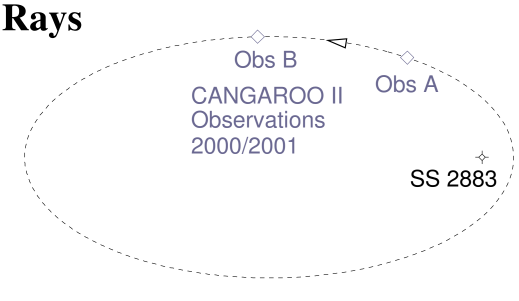

Figure 2.22: *Epochs of CANGAROO observations in 2000/2001 [Kawachi et al., 2004].*

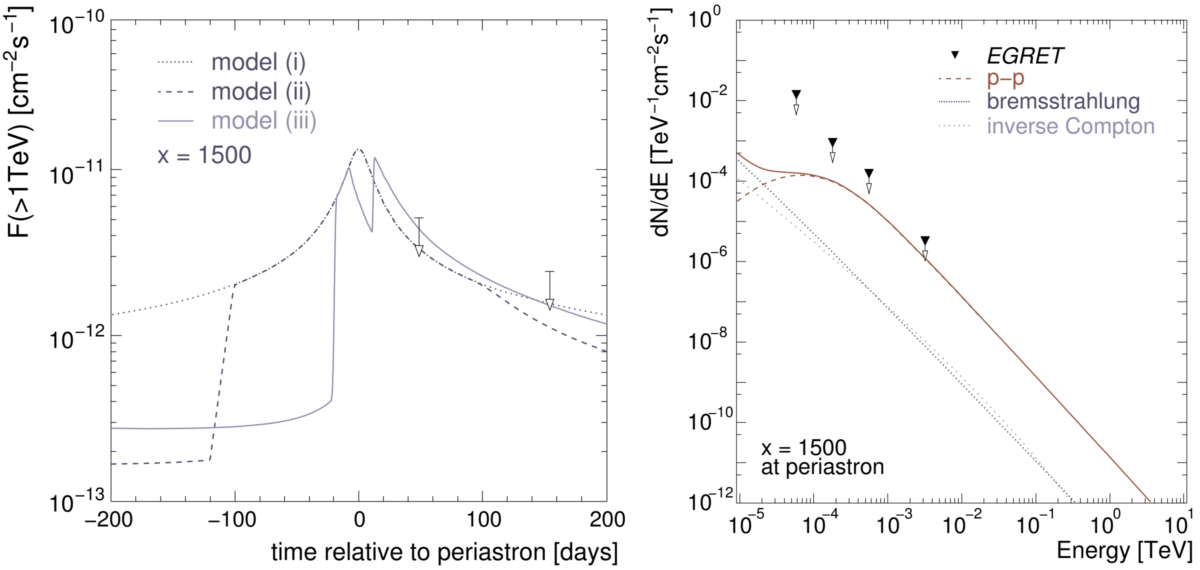

Figure 2.21: *Model light curves and spectrum for γ-rays produced by shock accelerated particles of stellar outflow material.* ***L****eft: Integral flux above 1 TeV as a function of time relative to the periastron passage for different periods of disk–pulsar wind interaction (see text). The upper limits result from observations with the* CANGAROO II *telescope in 2000/2001 (see Sec. 2.4.3).* ***R****ight: Corresponding differential spectrum of γ-rays for the case of an aligned disk. The main contribution results from the π^0-decay of p-p interactions (dashed line).*

and 18.0 hours, respectively. No significant γ-ray signal was detected and upper limits were derived at 54% (Obs A) and 13% (Obs B) of the flux of the Crab Nebula, also indicated in the model light curve in Fig. 2.21 (left).

The results of these observations imply a sensitivity for an integrated flux above 1 TeV of γ-ray energy of roughly 4×10^{-12} cm^{-2} s^{-1} for 10 hours of observations. The H.E.S.S. array, one of the new generation imaging atmospheric Cherenkov detectors, has a sensitivity which is better by more than one magnitude [$F(>1\,\mathrm{TeV}) \approx 3\times10^{-13}\,cm^{-2}\,s^{-1}$, Benbow, W. for the H.E.S.S. collaboration, 2004] and is therefore capable of significantly constraining all models of γ-ray emission of PSR B1259−63 discussed in this section. This provided sufficient motivation for H.E.S.S. observations of this unique binary system.

Chapter 3

The High Energy Stereoscopic System

The **H**igh **E**nergy **S**tereoscopic **S**ystem (H.E.S.S.) is an array of four imaging atmospheric Cherenkov telescopes located in Namibia, southern Africa. H.E.S.S. is run by an international collaboration of more than 90 physicists from over 20 institutions. It was completed in the year 2003 and is currently the most sensitive instrument for the detection of γ-rays in the energy band between 100 GeV and 100 TeV. Figure 3.1 shows a photograph of the array taken in January 2004.

The system provides a large field of view of 5° diameter, an angular resolution for individual γ-rays of better than 0.1°, an energy resolution of better than 20%, and a sensitivity to detect a γ-ray source with 1% of the flux of the Crab Nebula at $5\,\sigma$ significance within 25 hours of observations. These characteristics allowed H.E.S.S. to more than double the number of known TeV γ-ray sources in the first year of full operation [H.E.S.S. collaboration, 2005a]. Furthermore, a VHE γ-ray signal of the innermost part of our galaxy, the galactic centre, was detected and the excess location was found to be consistent with the central super-massive black hole [H.E.S.S. collaboration, 2004c]. Finally, H.E.S.S. produced the first resolved image of a shell-type supernova remnant in VHE γ-rays [H.E.S.S. collaboration, 2004b] marking the beginning of a new era in ground based γ-ray astronomy.

This chapter gives an overview of the imaging atmospheric Cherenkov technique, describes the detector setup and components, and introduces the shower and detector simulations which are essential for the understanding of the instrument.

Figure 3.1: *The complete H.E.S.S. array in January 2004.*

3.1 Imaging Atmospheric Cherenkov Technique

Since high energy γ-rays do not penetrate the atmosphere, they can only be directly detected by instruments on board of satellites. However, the particle flux of even the strongest known γ-ray sources at photon energies above several 10 GeV cannot be detected with collection areas of the order of 1 m^2 on reasonable timescales. Nevertheless, photons with higher energies can be detected by using the atmosphere as a calorimeter and measuring the Cherenkov emission of air showers induced by these photons. Imaging atmospheric Cherenkov telescopes are today the most successful detectors exploiting this principle and reach collection areas of the order of $10^6\,m^2$ and thus allow to access the VHE γ-ray universe.

In this section, the characteristics of air showers and their Cherenkov emission are briefly described, followed by a description of the principles of the detection technique.

3.1.1 Air Showers

Whenever a high energy particle interacts with the air molecules of the upper atmosphere, it induces a cascade of secondary particles – an extended air shower. A shower induced by primary photons, electrons, or positrons is dominated by electromagnetic interactions. Hadronic particles additionally undergo strong and weak interactions with electromagnetic sub-cascades.

Electromagnetic Showers

Air showers dominated by electromagnetic interactions are produced by high energy γ-rays or electrons and positrons (further on referred to as electrons). The main interaction processes for production and energy loss of secondary particles within the atmosphere are

- ▹ photon e^+e^- pair production and
- ▹ electron bremsstrahlung within electric fields of air constituents,
- ▹ ionization.

These processes determine the longitudinal development of the shower. The lateral distribution is dominated by multiple-scattering of the shower particles in the air. Bremsstrahlung and pair production processes during the particle propagation in air increase the number of particles in the shower, while the average energy per particle $\langle E \rangle$ decreases exponentially:

$$\langle E \rangle = E_0\, e^{-\frac{X}{X_\mathrm{r}}},$$

with E_0 as the initial energy and X the atmospheric depth, while X_r is a characteristic length, after which the energy is reduced by the factor $1/e$. The atmospheric depth is given in units of $\mathrm{g/cm^2}$, which corresponds to an atmospheric height h according to

$$X(h) = X_0\, e^{-\frac{h}{h_0}},$$

with $h_0 \approx 8\,\mathrm{km}$. Thus, the maximum atmospheric depth of a shower is related to the energy of the primary particle by $X_{\mathrm{m}ax} \propto \ln E$.

With increasing shower “age”, the ionization of air atoms, mostly nitrogen and oxygen, becomes important resulting in the absorption of the shower particles. At the critical energy E_c, for which the absorption begins to dominate over the production processes, the shower starts to run out of particles. Within air, this critical energy is $E_c \approx 81\,\mathrm{MeV}$. The typical timescale on which a complete electromagnetic shower develops is in the order of several microseconds.

A detailed analytic model of the longitudinal development of air showers and an approximation of the lateral shower development was developed by Greisen [1956], Katama and Nishimura [1958]. Therein it was shown, that any deviation of shower particles from the direction of the primary photon is dominated by elastic collisions with air molecules – multi-scattering – where the lateral extension is characterized by the Molière-radius $X_M \approx 9.6\,\mathrm{g/cm^2}$. Accordingly, the shower describes a cone around the shower axis, which would have, neglecting absorption, a radius of approximately 80 m at sea level including 90% of the energy of the shower particles at that height. The contribution to the lateral spread of the shower from bremsstrahlung and pair production is given by the average opening angle θ between the momentum of the produced particle and the shower axis, which is related to the energy E of the shower particle by

$$\langle\theta\rangle = \frac{m_e c^2}{E}.$$

Thus, except for very low energy particles with $E \ll E_c$, this contribution can be neglected.

Hadronic Showers

The first interaction of a cosmic ray nucleus in the atmosphere is typically strong inelastic scattering with an air nucleus. Such a collision results in fragmentation of the nuclei into a jet-like cascade of nucleonic fragments and mesons, mainly pions. For the excited nuclei, this process is repeated. The pions have significant transverse momenta, resulting in a larger lateral development of the hadronic shower compared to an electromagnetic shower. Pions decay either into photons (π^0-decay), inducing an electromagnetic sub-cascade, or muons and neutrinos ($\pi^\pm$-decay) often reaching the ground level without significant energy loss. The mean fraction of π^0s, created in the first interaction is $\sim 1/3$, creating an electromagnetic sub-cascade similar to that of a photon of $\sim 1/3$ of the primary particle energy.

In conclusion, a hadronic shower has a much wider lateral distribution compared to an electromagnetic cascade and typically has a significantly asymmetric sub-structure. Figure 3.2 gives examples of the longitudinal shower development for a simulated 300 GeV photon and a 1 TeV proton.

3.1.2 Cherenkov Emission of Air Showers

Most of the secondary particles in an extended air shower have relativistic energies since the shower only grows for particle energies greater than $E_c = 81\,\mathrm{MeV}$. Therefore, for the majority of particles, their velocity exceeds the speed of light in the medium air and the charged particles emit Cherenkov light [Jelley, 1958]. The Cherenkov emission leads to a characteristic Cherenkov photon distribution of an air shower on the ground.

A charged particle with a velocity v exceeding the speed of light c_n in air, polarizes the surrounding medium and induces constructive interference of electromagnetic waves. This creates a cone of light emission with the characteristic angle θ_C between the direction of the radiation

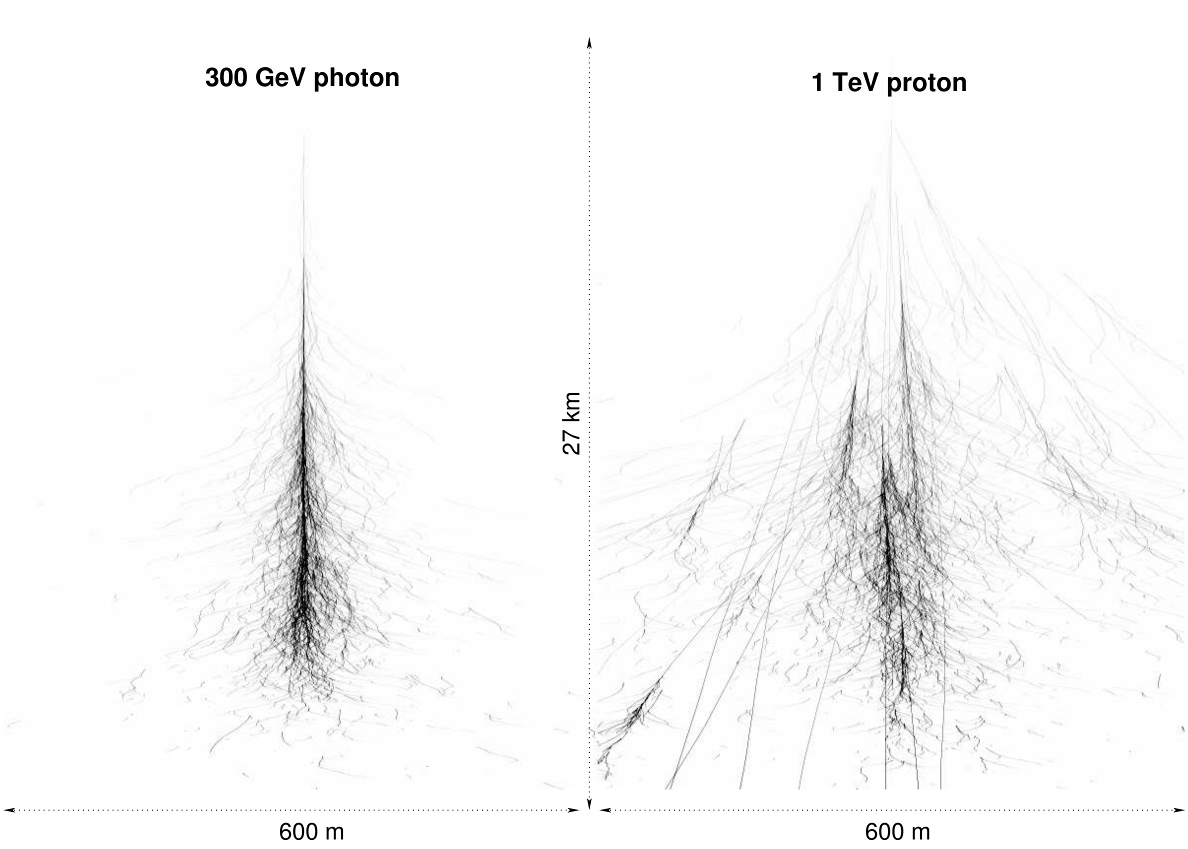

Figure 3.2: *Longitudinal shower development for a simulated 300 GeV photon and 1 TeV proton. Shown are the shower particle trajectories [Bernlöhr, 2000].*

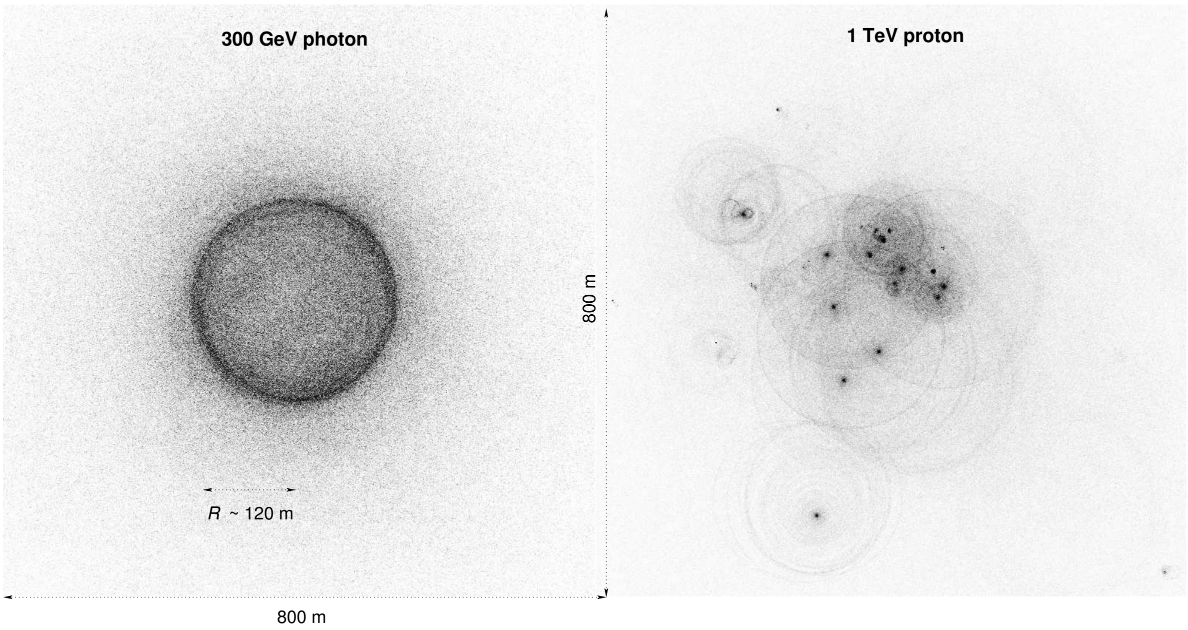

Figure 3.3: *Simulated lateral Cherenkov light density of a vertical shower from a primary 300 GeV photon and 1 TeV proton 1800 m asl. [Bernlöhr, 2000].*

and the particle track:

$$\cos\theta_\mathrm{C} = \frac{c_n}{v} = \frac{c}{nv} = \frac{1}{n\beta} \tag{3.1}$$

with n as the refraction index of air, neglecting dispersion effects. The velocity $\beta = v/c$ must exceed a threshold $\beta_\mathrm{min} = 1/n$, in order to satisfy (3.1). This corresponds to a threshold energy E_min of the radiating particle:

$$E = \gamma\, m_0 c^2 \Rightarrow E_\mathrm{min} = \sqrt{\frac{1}{1-\beta^2_\mathrm{min}}}\, m_0 c^2 = \sqrt{\frac{1}{1-\frac{1}{n^2}}}\, m_0 c^2.$$

Therefore, low mass particles such as electrons dominate the Cherenkov emission. Because the refractive index n is not constant within the atmosphere the threshold energy and the emission angle depend on the atmospheric altitude h. The Cherenkov angle θ_C varies between 0.5° and 1.4° within 15 km altitude above sea level. The wavelength λ of the emitted Cherenkov radiation is roughly 250 and 700 nm (blue to ultraviolet) with a spectrum $\propto 1/\lambda^2$.

The peak Cherenkov emission occurs at the shower maximum, which is between 7 and 10 km altitude for a primary photon with energies between 100 GeV to 10 TeV [Hillas, 1996]. For electromagnetic showers, the superimposed light of all contributing particles results in a light front, 2–3 ns "thick", producing an almost symmetric ring of light on the ground, and developing within timescales of the order of 10 ns. The Cherenkov emission of hadronic showers is dominated by their electromagnetic sub-cascades and is characterized by an heterogeneous and asymmetric Cherenkov photon distribution (see Fig. 3.3). The differences between the characteristics of the Cherenkov emission of primary photons and cosmic rays are used by ground based atmospheric Cherenkov detectors to distinguish between the primary particle types.

Cherenkov Emission for Inclined Showers

The average atmospheric depth of the first interaction of the primary particle is constant for a given primary energy. Therefore the distance between the shower maximum and the ground increases with rising inclination (given by the zenith angle Θ) of the shower direction. Correspondingly, the extinction of the emitted Cherenkov light is enhanced, and the lateral distribution on the ground is expanded. In addition to the dependence on the zenith angle, the Cherenkov emission depends on the azimuth of the shower direction because the orientation of the shower to the Earth's magnetic field has an effect on the trajectories of the charged shower particles and thus their Cherenkov emission. Both effects must be considered in the design and data analysis of Cherenkov detectors.

3.1.3 Detection Principle

Since the radial Cherenkov photon density on the ground is nearly constant within the Cherenkov ring of approximately 120 m distance from the shower axis and drops slowly towards higher values, the Cherenkov emission can be detected by any highly light-sensitive detector inside this "light pool". In order to be able to reconstruct the shower direction with a proper accuracy and suppress the hadronic background it is necessary to use an imaging instrument which is able to resolve the morphology of the Cherenkov emission. Both requirements are met by imaging atmospheric Cherenkov telescopes.

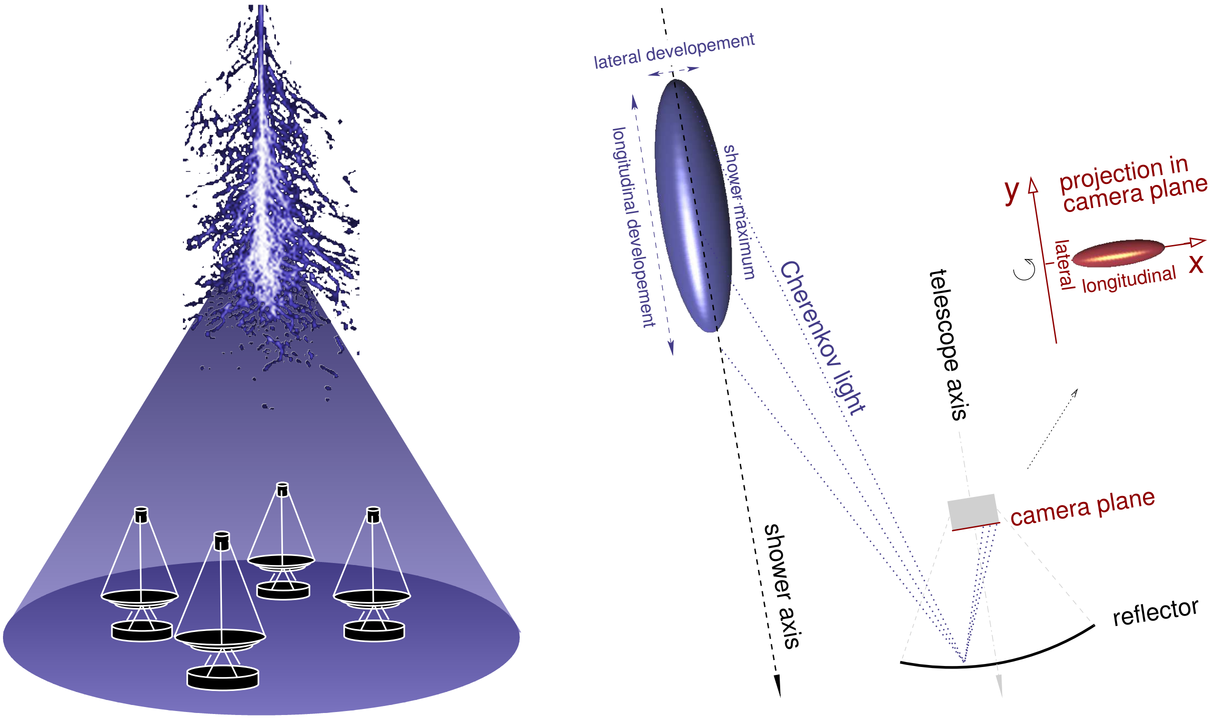

Figure 3.4: *Schematic principle of the optical imaging of Cherenkov emission from air showers.* ***L****eft: Cone of Cherenkov emission of an air shower illuminating several telescopes.* ***R****ight: Optical imaging of the shower with an imaging atmospheric Cherenkov telescope. The camera plane was magnified and rotated, in order to illustrate the image shape.*

Figure 3.4 illustrates the general principle of such imaging atmospheric Cherenkov telescopes. An optical reflector projects the Cherenkov emission of an electromagnetic shower onto a camera mounted in the focal plane of the telescope. For a shower of a primary photon of 1 TeV, the typical yield of Cherenkov photons is $\sim 100\,\mathrm{m}^{-2}$ at about 2 km height a.s.l.

The recorded image can be parametrised by an ellipse which allows to derive the properties of the primary particle: the orientation of the ellipse determines the direction and the amount of detected Cherenkov light is roughly proportional to the energy. For the purpose of an accurate shower energy reconstruction and background estimation, detailed Monte Carlo simulations of the Cherenkov emission of air showers and the detector response are essential.

In the case of a stereoscopic system of more than one telescope, the shower emission is recorded under different viewing angles. This allows an improved reconstruction of the shower geometry significantly enhancing the angular resolution of the instrument compared to the reconstruction using a single image only. Additionally, by requiring the telescopes to trigger simultaneously on timescales of several nanoseconds, non-air-shower background, such as random coincidences caused by night sky background (NSB) or single muons directly hitting the telescope, can be rejected.

The characteristics of the Cherenkov emission of air showers determine the requirements on an imaging atmospheric Cherenkov detector:

- ▹ **I**maging camera. The typical Cherenkov light photon density of roughly hundred photons per m^2 necessitates the use of sensitive photo-detectors which must also provide a sufficiently fine pixelisation in order to resolve shower images. Additionally, the faint Cherenkov light of the shower evolving on timescales of nanoseconds requires very short exposures to avoid the dominance of night sky background. This can only be accomplished by using very fast trigger and readout electronics.

- **R**eflector. The total amount of Cherenkov light the detector is able to collect, determines the total collection area and sensitivity for low energy showers. Therefore the reflector must provide a large area and good reflectivity. Additionally, the size of the optical point spread function should be ideally less than the extent of a single camera element. The support structure of the reflector must be rigid enough to avoid strong deformations.
- **T**racking system. Like conventional astronomical telescopes, the instrument has to be able to follow an astronomical object on the sky with sufficient accuracy on the level of arcseconds.
- **S**tereoscopy. The arrangement of an array of multiple telescopes must be chosen such that a sufficient number of telescopes are located within the typical extent of the Cherenkov light pool of an air shower on the ground, and at the same time, that the total area covered by the array is maximal.

3.2 The H.E.S.S. Instrument

The following section introduces the observation site and the individual hardware and software components of the H.E.S.S. instrument.

3.2.1 Site Location

The H.E.S.S. site lies in Namibia, at latitude 23° 16′ 18″ south, longitude 16° 30′ 00″ east, and 1800 m above sea level (see Fig. 3.5) in the Khomas Highland. The Khomas Highland region is known for its excellent optical quality for astronomical purposes [Wiedner, 1998]. In particular meteorological studies showed that 57% of the moonless dark time of 1600 hours per year, usable for observations with Cherenkov telescopes, were absolutely cloud-free. In 94% of the nights the relative humidity was below 90% and the average wind velocity of $3.5\,\mathrm{m\,s^{-1}}$ is rather low.

Furthermore, the location of H.E.S.S. in the southern hemisphere allows to observe the inner galactic plane at high elevations where the instrument is most sensitive for γ-ray energies below 1 TeV.

Figure 3.5: *Map of the Republic of Namibia showing the location of the H.E.S.S. site in red.*

3.2.2 Telescope Mechanics and Tracking System

The four telescopes are placed on the corners of a square with edges of 120 m length, where the diagonals are aligned in north-south and east-west direction. The spacing was optimised by simulations for a high sensitivity over the whole energy range between 100 GeV and 100 TeV.

Each telescope [Bernlöhr et al., 2003] has a reflector dish of 13 m diameter mounted in a rotating base-frame on a circular rail for movement in azimuth direction. Rotation in altitude is possible around the central elevation axis of the dish. Figure 3.6 shows a technical drawing of one of the telescopes. The complete steel structure has a mass of more than 50 tons.

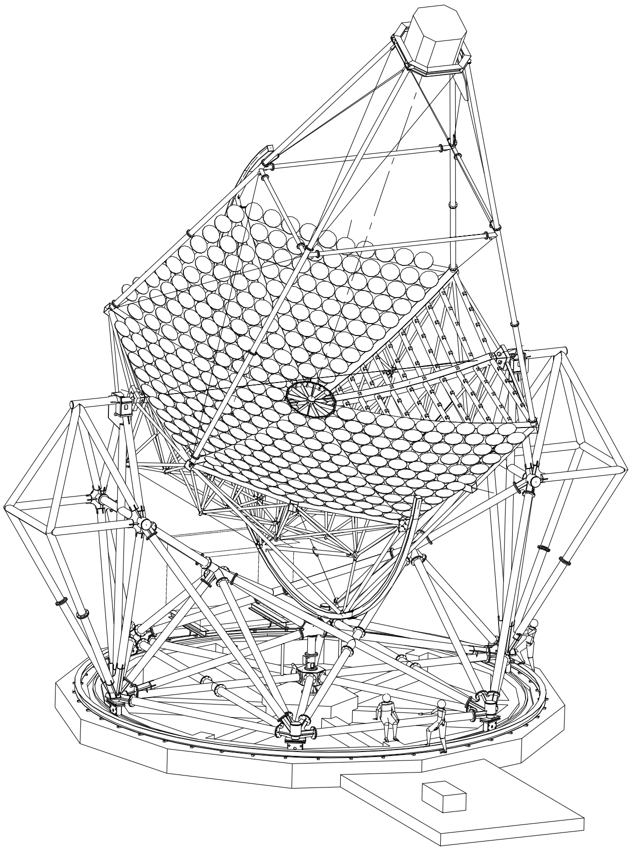

Figure 3.6: *Technical drawing of the H.E.S.S. telescope structure.*

Both in azimuth and elevation, the telescope is driven by friction drives acting on special 15.0 m diameter drive rails. The large lever arm reduces the drive forces and the requirements on the reduction gears. For both axes, the telescope can reach an angular velocity of $100^\circ\,\mathrm{min}^{-1}$. The pointing position is measured by shaft encoders with a digital step size of $10''$. Figure 3.7 shows that the accuracy of the drive system for the tracking of astronomical sources is better than $3''$ for normal observations. For a detailed description of the drive system see Bolz [2004b]. However, the pointing precision and therefore the resolution for γ-ray source location has other systematic uncertainties introduced by effects such as deformations of the dish and the camera arms. These issues are related to the calibration of the detector and will be addressed in Sec. 4.2.4.

3.2.3 Optics

The reflector of a H.E.S.S. telescope is segmented into 380 mirror facets with 60 cm diameter and an average reflectivity of 80% providing a total reflecting area of $107\,\mathrm{m}^2$. The layout follows that of Davies and Cotton [1957], arranging the small spherical mirrors with focal length $f = 15\,\mathrm{m}$ on a spherical shaped dish with radius f, being very cost-effective compared to a single spherical mirror surface and reducing spherical aberrations. However, the spherical dish introduces a spread in the arrival times of the Cherenkov photons from a shower uniformly distributed over 5 ns.

Each mirror facet is mounted on a motor-controlled support unit allowing them to be moved by remote control. The alignment was performed in an automatic procedure proceeding as

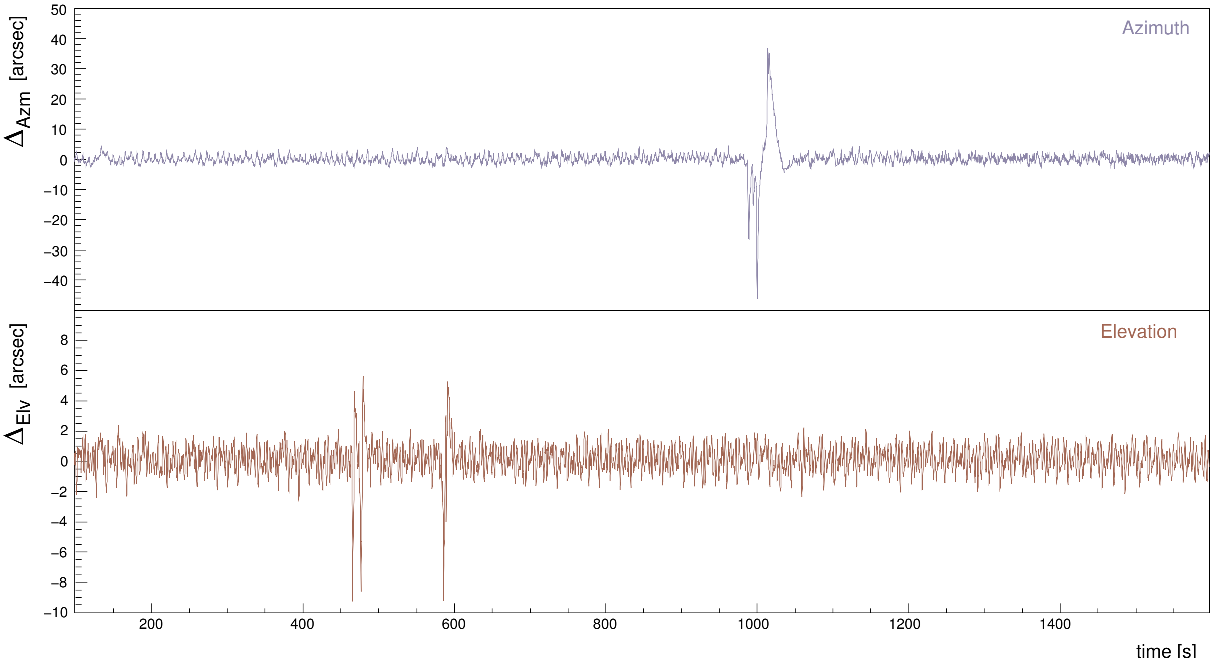

Figure 3.7: *Deviations from the nominal tracking position during an observation run of 28 minutes duration. The spikes originate from transitions between two parts of the azimuth rail (upper panel) or a welding seam on the elevation drive rail (lower panel).*

follows: A bright star is tracked with the telescope and its image in the focal plane is recorded with a CCD camera mounted in the centre of the dish. Each mirror spot is identified separately and moved to its nominal position in the centre of the field of view. The resulting optical point spread function (PSF), defined by the radius of a circle enclosing 80% of the spot intensity, $r_{80\%}$, varies with the angle to the optical axis θ due to the spherical aberrations of the reflector, and depends on the elevation α due to deformations of the dish structure (see Fig. 3.8). The PSF is well contained in a camera pixel of 2.8 mrad size and well within initial specifications for all combinations of θ and α. Furthermore, after two years of operation, the point spread function has degraded by less than 10%. A more detailed description of the optical system of the H.E.S.S. telescopes can be found in Bernlöhr et al. [2003] and Cornils et al. [2003].

3.2.4 Camera

The camera of each telescope is a highly light-sensitive device containing 960 photo-multiplier tubes (PMT or pixel). The camera body of 1.4 m diameter and 1 m depth contains the whole trigger and readout electronics (see Fig. 3.9), which allows to record Cherenkov images at a rate of ~250 Hz while keeping the dead time below 10%. For a detailed description of the camera electronics see Vincent et al. [2003].

Photo-multipliers

The individual pixels have an angular size of 0.16° and are arranged in the focal plane of the reflector, providing a total field of view of 5° in diameter. Since the window of each PMT has a

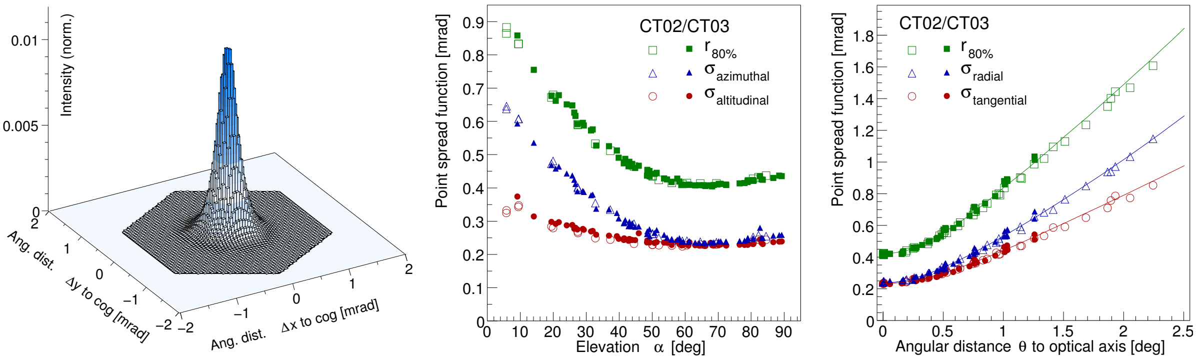

Figure 3.8: ***L**eft: Image of a star on the camera lid of CT3. The hexagonal border indicates the size of a camera pixel. **M**iddle, Right: Width of the point spread function as a function of elevation and angular distance to the optical axis, respectively [taken from Cornils et al., 2003].*

circular shape, hexagonal shaped light guides are used to close the gaps between neighbouring pixels, decreasing Cherenkov photons losses. Individual photons are detected by the PMTs with a maximum quantum efficiency of $\approx 30\%$. The analogue PMT response signal is fed into three different channels, one for the trigger and two for the acquisition system with different gains. The use of a high gain (HG) and a low gain (LG) channel extends the PMT response to be linear over a dynamic range from 1 to 1600 photo-electrons. This allows to resolve single photo-electrons from low energy showers without suffering from saturation at high Cherenkov photon densities originating from high energy showers. The high voltage, trigger, and amplification electronics are directly attached to the back of the PMTs. The pixels are grouped into *drawers* of 16 PMTs each allowing for easy maintenance and replacability.

Readout System

The amplified analog signals of the two acquisition channels of a PMT are continually digitized by a 1 GHz analog ring sampler (ARS). Upon a trigger signal, the sampling of all ARS units stops and the integrated charge of a 16 ns window is stored in the memory of each drawer and sent to dedicated FIFO cards in a compactPCI rack. Each camera has a CPU which reads out these FIFOs and sends the event data to the central data processing farm (see Sec. 3.2.7). The whole readout process takes $\approx 400\,\mu$s, during which the camera cannot respond to further trigger signals, the so called *dead time*, which limits the maximum acquisition rate to 2.5 kHz with 100% dead time.

3.2.5 Trigger

Camera Trigger

The trigger system has to provide a fast recognition of Cherenkov shower images and avoid the readout of images containing noise only. In order to achieve this, the camera is divided into 38 overlapping trigger sectors containing 64 or less pixels. A trigger decision is formed, if the illumination of a certain number of pixels in any one of these sectors exceeds a given threshold intensity within a time window of 2 ns. This defines the PMT and sector threshold,

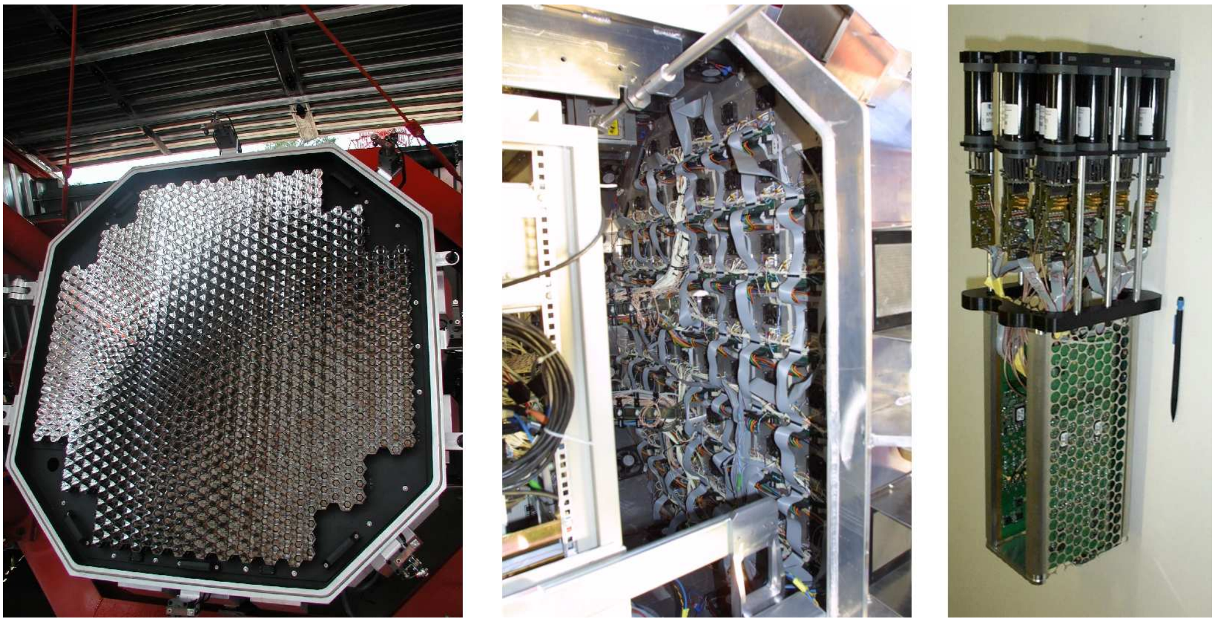

Figure 3.9: ***L**eft: Camera with open lid while the telescope is in parking position showing the array of photomultipliers with attached front plate of Winston cones. **M**iddle: Back ends of the drawers in the camera interior. **R**ight: One single drawer containing 16 PMTs, high voltage supplies and readout electronics.*

which are imposed at the hardware level using comparators superimposing the number of photoelectron equivalents (q) on the PMT level and the number of triggering pixels (p) for a trigger sector, respectively. Once a camera trigger signal is raised, the camera starts the readout and simultaneously sends a message to the central trigger system (see below). The optimal camera trigger configuration (p, q) was estimated by simulation studies [see e.g. Schlenker, 2001] and then refined using measurements of the trigger rate.

Central Trigger

In addition to the triggers induced by the Cherenkov emission of air showers, random coincidences due to night sky background, and the Cherenkov emission of single muons near the telescope represent a large fraction of the single telescope trigger rate. The central trigger system [Funk et al., 2004] reduces this background on the hardware level by checking for coincidences of several telescope triggers, significantly reducing the dead time of the cameras. This allows the camera trigger thresholds (p, q) to be decreased, thus lowering the energy threshold of the instrument.

Attached to each camera, a local interface module transfers the camera trigger signal to a central coincidence module, which requires that trigger pulses of n of the telescopes are coincident within in a gate of 80 ns, taking into account delays between the pulses due to the arrival time differences of the Cherenkov light for inclined showers. In case a coincidence is found, the module sends a confirmation signal together with a global event number back to the cameras which have triggered, and these cameras continue with the readout of the event. If no coincidence is found, the current readout process is interrupted in order to be ready for the next trigger. In case a camera triggers while it is still processing data, a “busy” signal is sent back to the central trigger station which can be used to directly measure the dead time of the system (see Sec. 4.2.5).

Figure 3.10 illustrates the rejection capabilities of the system by comparing the distribution of the image parameter Length/Size (see Sec. 4.4.1) for which muons can be seen as pronounced peak in single telescope data. This peak vanishes if a telescope multiplicity of $n = 2$ is required. The peak coincides with the expected distribution for single muons reaching the ground level.

In all observations discussed later, a standard trigger configuration ($n = 2$ telescopes, $p = 4$ pixels, $q = 5$ p.e.) was used, resulting in a typical trigger rate of 1 kHz for a single camera and a system rate of ~ 400 Hz at elevations near zenith.

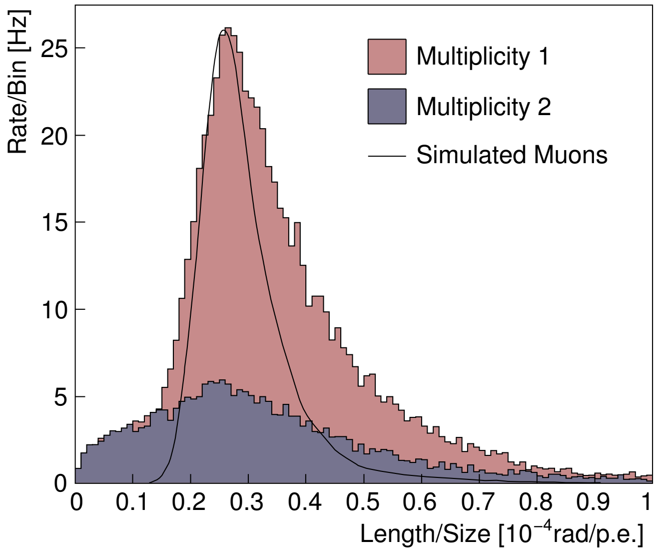

Figure 3.10: *Distribution of the ratio between length and total image brightness of camera images for telescope multiplicity 1 and 2. The solid line represents the corresponding distribution for simulated single muons [Funk et al., 2004].*

3.2.6 Atmospheric Monitoring

Atmospheric variations have a significant influence on the absorption of Cherenkov light on the way from the shower maximum to the detector and thus affect the absolute calibration of the instrument. Therefore, the atmospheric conditions have to be monitored during observations in order to at least select data according to some quality criteria (see Sec. 4.3.1). For an accurate energy calibration of the instrument it is desirable to model the atmospheric conditions and include them in the air shower simulations. For the given purposes, a number of monitoring devices [Aye et al., 2003] are installed on the site (see Fig. 3.11):

- On each telescope, a *paraxial radiometer* is installed. These instruments measure the infrared emission of water molecules in the direction of telescope pointing, allowing the identification of clouds passing within the telescope field of view.
- A central *ceilometer* fires pulses of infrared light into the atmosphere and measures the backscattered light to determine the atmospheric extinction. It has an alt-az mount allowing to move it in parallel with the Cherenkov telescopes.
- The central *weather station* measures the relative humidity, temperature, air pressure, amount of rainfall, and wind velocity at ground level.
- A movable *scanning radiometer* provides cloud monitoring of the whole sky.

3.2.7 Central Data Acquisition System

The central data acquisition system has to provide the user interface for the control and monitoring of the whole array and is responsible for storing and preprocessing the data from the

Figure 3.11: *Atmospheric monitoring devices at the H.E.S.S. site.* ***L**eft: Weather station.* ***R**ight: Ceilometer.*

different hardware components. The development and maintenance of the system represents a major part of this work and therefore a detailed description is presented in Appendix A. Here, only a short overview is given.

Hardware

All data from the individual hardware components are connected to a central processing cluster of Linux workstations via a local area network (LAN, 100 MBit/s). The data from these components are distributed via a gigabit-switch to more than 20 cluster nodes, and are preprocessed and stored on a RAID-system for later analysis and archiving. The typical data rate to be processed by the system is $\sim$ 4 MByte/s which amounts to more than 500 GByte of raw data per month which is written to magnetic tape and shipped to Europe for further analysis.

Software

The software packages for the user control, data processing, and analysis are object oriented and use for inter-process communication the free implementation omniORB [Lo and Pope, 1998] of the industry standard CORBA. The data storage and analysis software uses ROOT [Rademakers and Brun, 1997], a data analysis framework used in many other high energy particle and astrophysics experiments.

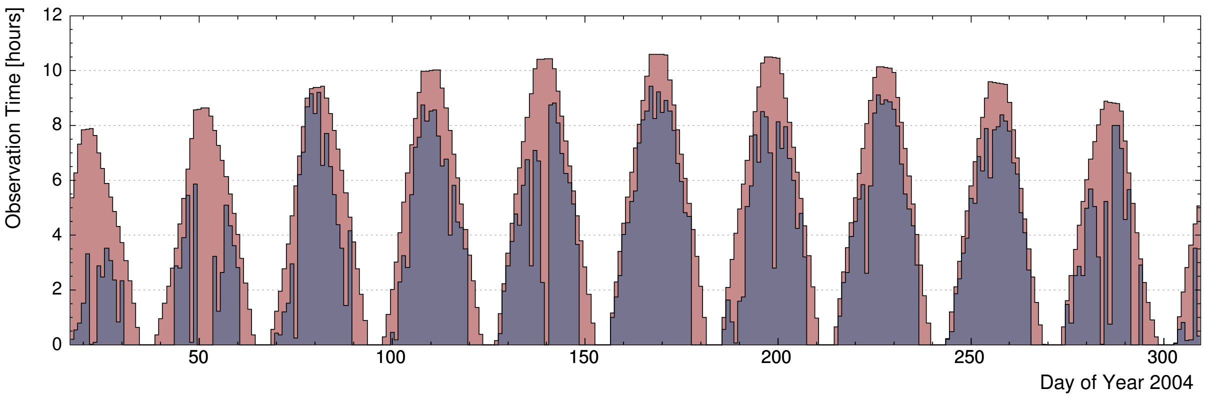

Figure 3.12: *H.E.S.S. data taking efficiency 2004. The light filled area shows the total available astronomical dark-time, when the sun is 18° and the moon just below the horizon. The dark area corresponds to the time spent on observations of H.E.S.S. targets.*

Data Taking Efficiency

Since the photon density of moonlight exceeds the density of the Cherenkov emission of air showers by several orders of magnitude, observations are only possible without the moon above the horizon. This limits the duty cycle of Cherenkov telescopes to $< 10\%$. Observations of targets are performed in *runs* of 28 minutes duration. The DAQ system needs a transition time of less than 2 minutes between two consecutive runs.

Figure 3.12 shows the total available observation time compared to the time actually spent on observations in most of the year 2004, corresponding to a data taking efficiency of 64%. Losses of observation time were caused mainly by bad weather conditions ($\sim 23\%$), the DAQ transition time between runs ($\sim 7\%$), but also due to technical problems with various detector components ($\sim 6\%$), including both, hardware and software.

3.3 Monte Carlo Simulations

Monte Carlo simulations of air showers and detector response are used for energy calibration, background suppression, and the determination of performance characteristics such as angular and energy resolution. Although these characteristics are discussed in detail in the following chapters, an overview of the principles of the simulation chain are given here.

3.3.1 Shower Simulation

For the simulation of extensive air showers induced by primary γ-rays and hadronic cosmic rays, the simulation package *CORSIKA* [Heck et al., 1998] was used. *CORSIKA* simulates the development of air showers in the atmosphere at the level of single shower particles, considering environmental parameters, such as atmospheric absorption and geomagnetic field strength, and employing various particle interaction models. The simulation of electromagnetic interactions is based on well understood QED calculations. Major uncertainties exist in the simulation of hadronic interactions, since the processes at work in air showers feature only low momentum transfers, which cannot be described by perturbative QCD. *CORSIKA* uses different phenomenological models depending on the energy of the interactions. However, these uncertainties mainly affect the cosmic ray background estimation at the upper end of the energy range of H.E.S.S.

The Cherenkov emission of the shower particles is simulated in the wavelength range between 200 and 700 nm by creating groups of photons (bunches), for which the direction, position, wavelength, and emission time is stored. The loss of photons caused by extinction in the atmosphere on the way from the emission point to the observation level is taken into account in a second step. The photon bunches which hit a virtual sphere around the detector are stored in a dedicated data format and can be used by the detector simulation program. For performance reasons, a single simulated shower is used several times by randomizing the position of the detector relative to the shower position (oversampling).

3.3.2 Detector Simulation

The Cherenkov photon data is processed by a detector simulation program, *sim_hessarray* [Bernlöhr, 2002] simulating the H.E.S.S. telescope array in detail. The simulation considers:

- ▹ the reflector layout and orientation with respect to the shower
- ▹ shadowing by the camera support structure, mirror reflectivity, and point spread function,
- ▹ the transmission of the Winston cones in front of the PMTs,
- ▹ the quantum efficiency of the PMTs,
- ▹ the electronic response of the PMTs: pulse shapes of the PMT signals for the trigger and readout channels and its evolution,
- ▹ and the telescope multiplicity requirement of the central trigger.

In order to illustrate the good agreement which is found between simulations and measurements, Fig. 3.13 shows the predicted and measured trigger rate of the H.E.S.S. array as a function of the elevation for a multiplicity n required by the central trigger (see Sec. 3.2.5). The rate decreases with the zenith angle since the Cherenkov light cone from the shower maximum is emitted at a larger distance to the array. The measured rate lies well between the curves defined by the predicted rate from simulations with different atmosphere models considered for the H.E.S.S. observation site, reflecting the current systematic uncertainty on the atmospheric transmission of Cherenkov light at this site.

3.3.3 Sample of Simulated γ-Rays Used in the Data Analysis

For the purpose of this analysis, simulated γ-ray induced air showers at zenith angles $\Theta = 30, 40, 45, 50, 55^\circ$, azimuth $\phi = 0, 180^\circ$, and with an energy spectrum $\mathrm{d}N/\mathrm{d}E \propto E^{-2}$ between 20 GeV and 100 TeV were used, commonly available within the collaboration. These showers were oversampled within a radius of 1000 m around the detector array, which is sufficient for showers with an energy of up to several 10 TeV. A sample of roughly 300 000 simulated γ-ray showers passed the detector simulation trigger. This sample was used to obtain expectation values for shower parameters, such as direction and energy, and to validate the reconstruction and analysis methods as described in the next chapters.

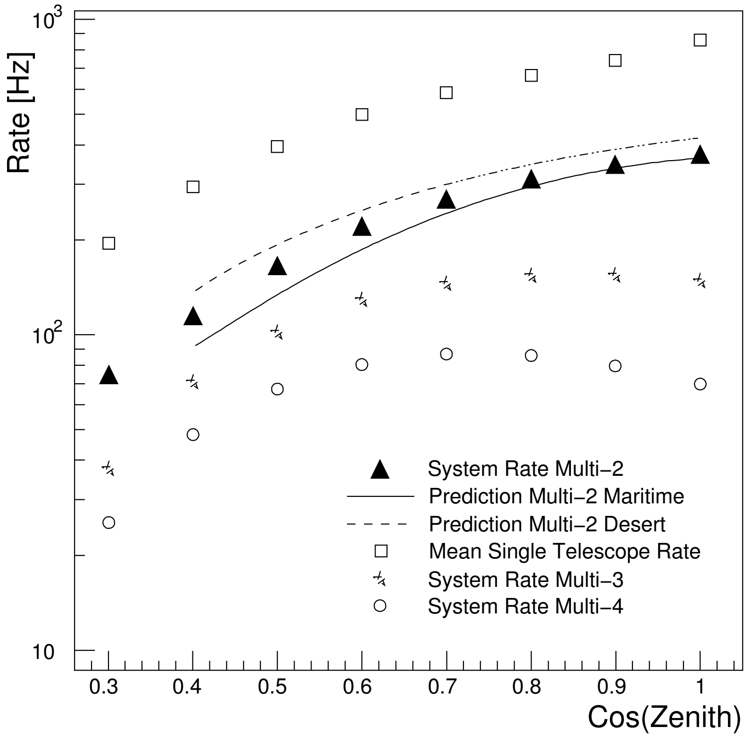

Figure 3.13: *Mean single telescope and system rate as a function of the cosine of the zenith angle for telescope multiplicities of* $n = 2, 3, 4$ *[Funk et al., 2004]. The solid and dashed lines show the rate predicted from the simulations for multiplicity 2 using two different atmospheric absorption models.*

Chapter 4

Data Selection and Reduction

The binary system of PSR B1259−63 / SS 2883 was observed by H.E.S.S. between February and June 2004 for a total of ~70 hours. This resulted in more than 200 GB of camera data from a total of 66 million air shower events and additional monitoring data from the various array components. The final aim of the data reduction routines is to reconstruct the energy and direction of a primary γ-ray. To this end, the raw ADC counts for each pixel in the camera had to be converted into Cherenkov photon intensities, the images had to be parametrized, and each air shower direction and energy had to be reconstructed, requiring a proper energy calibration and the knowledge of the exact pointing direction of each telescope. Additionally, the huge background of cosmic ray air shower events had to be reduced to a level where the detection of a γ-ray source becomes possible. Subsequently, the data had to pass several quality checks in order to minimize potential systematic errors.

In this chapter, the data set obtained by these observations of PSR B1259−63 is introduced, the applied calibration, reconstruction and background rejection procedures are described and their performance is evaluated with respect to simulated γ-rays and real data. Furthermore, the quality of the data is discussed and the data set considered for this analysis is presented.

4.1 Observations of the PSR B1259−63 System

All observation runs were carried out with the telescopes tracking sky positions with an alternating offset of ±0.5° in declination (Dec) relative to PSR B1259−63 (so-called *wobble* mode). This observation mode is designed for point sources and takes advantage of the excellent angular resolution of H.E.S.S. ($< 0.1^\circ$) and its large camera field of view, and allows to determine the background from the same field of view for γ-ray sources which are not much more extended than the angular resolution of the instrument. Using this mode, one can omit off-source observations of sky regions without γ-ray sources, normally used for the purpose of background estimation, effectively doubling the observation time and reducing possible systematic effects introduced by the off-source observation, e.g. due to a different level of diffuse NSB light or differences in the distribution of bright stars between the considered sky regions. Note, that the complete orbit of PSR B1259−63 has an extension of $\sim$ 4 milli-arcseconds at a distance of 1.5 kpc which clearly makes it a point source for H.E.S.S.

During the observation campaign, in April 2004, the analysis of the data taken before in February and March revealed another source in the same field of view, called HESS J1303-

631 [see H.E.S.S. collaboration, 2005d, and the next Chapter]. Due to this discovery, for all observations subsequent to the 14th of May 2004, the array pointing was changed to a position $\sim 0.6^\circ$ north of PSR B1259−63 and an alternating wobble offset of 0.5° in right ascension (RA) – instead of declination – was used in order to keep roughly the same angular distance to the two sources for both offsets.

Figure 4.1 shows all tracking positions used for the observation of PSR B1259−63 in the RA-Dec system. Note, that at the tracking positions, wobbling relative to PSR B1259−63 North, the angular distance to the pulsar position is slightly higher than for wobbling relative to PSR B1259−63 and therefore the sensitivity is lower compared to the standard wobble mode with 0.5° distance. The observation times obtained in the five different darkness periods, further on referred to as February, March, April, May, and June, separated by periods without observations with the moon above the horizon, are displayed in Fig. 4.2.

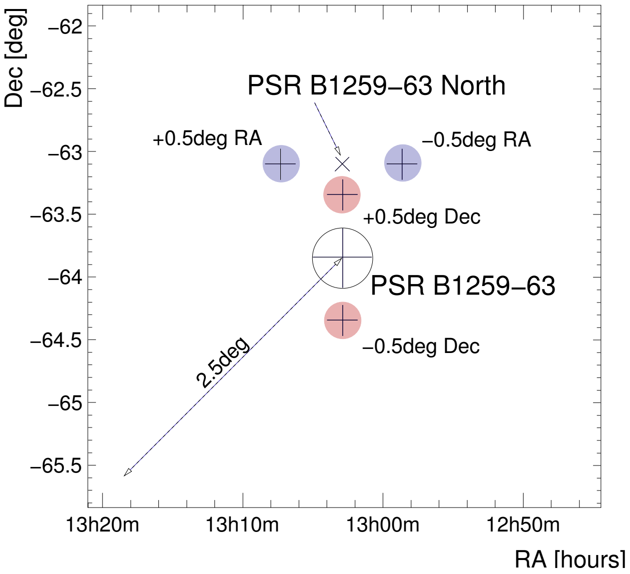

Figure 4.1: *Tracking positions used during the PSR B1259−63 observation campaign in 2004.*

The data set on PSR B1259−63 which passed the quality selections (described in Sec. 4.3) consists of 119 runs corresponding to 55 hours of observations, derived from a total of 154 runs (77 hours). A detailed run list can be found in Appendix B.

4.2 Calibration

The complete calibration of the instrument is required to provide the conversion factors between the air shower Cherenkov photons reaching the telescopes and the corresponding signal in the pixels of the cameras for each pixel separately. This requires the determination of the light

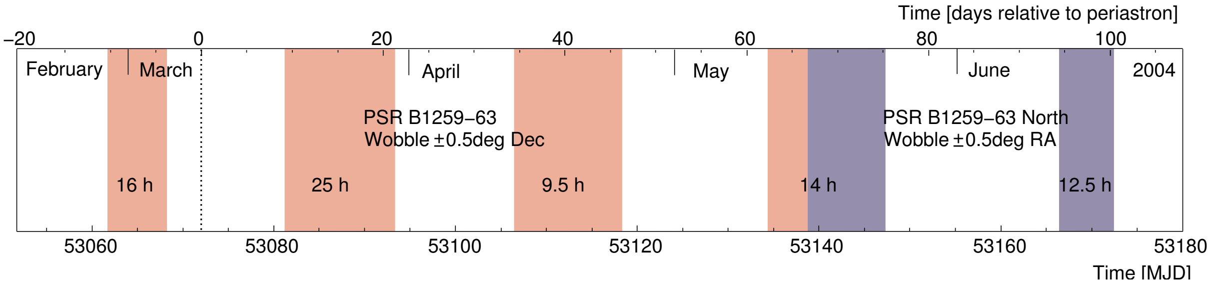

Figure 4.2: *H.E.S.S. observations of PSR B1259−63. The shaded areas represent the darkness periods where data is available. The different colors correspond to the different tracking positions which were used during the observations (see Fig. 4.1 and text).*

collection efficiency of all Winston cones, the quantum efficiency of the individual PMTs, and the conversion factors translating from the digitized signals in ADC counts and the number of photo-electrons collected by the PMTs. Several special calibration runs using dedicated calibration devices were performed, in order to determine these coefficients. A detailed description of the calibration techniques used can be found in H.E.S.S. collaboration [2004a].

Additionally, muons, produced by hadronic cosmic ray air showers, were used to determine the overall conversion efficiency from emitted Cherenkov light to camera images considering all detector components including the lower part of the atmosphere near the ground level [Bolz, 2004b].

Since the reconstruction of the shower energy and direction rely on the position of the Cherenkov images in the camera, the absolute pointing of the telescopes was calibrated as well using the camera response to stars within the field of view, measurements of the deformation of the telescope structure [Cornils et al., 2003], and monitoring of the camera position and the location of stars with dedicated CCD cameras [Gillessen, 2003].

In the following sections, the concepts of the calibration techniques are briefly described and some relevant results are given.

4.2.1 Readout Window Timing

Since the analogue ring samplers (ARS) sample continuously the PMT signal, the location of the readout window of 16 ns within the ring was optimized such that the rising edge of the PMT pulse shape in response of a single photo-electron is fully contained within the window. The window timing was determined with dedicated runs of low illumination where the PMT response was read out in individual samples of 1 ns (*sample mode*, see Fig. 4.3) instead of integrating the signal within the window (*charge mode*), and then adjusted if necessary. The timing of all cameras was re-calibrated in February 2004, continually monitored, and required no change during the observations of PSR B1259−63.

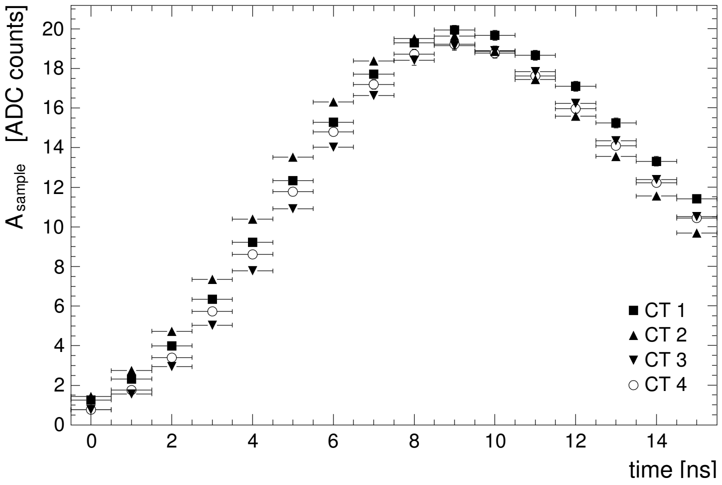

Figure 4.3: *Mean PMT signal distribution within the readout time window in all H.E.S.S. cameras for air shower events [H.E.S.S. collaboration, 2004a].*

4.2.2 Intensity Determination

For a particular camera image, the intensity I of each recorded PMT signal in units of detected photo-electrons (p.e.), used by the shower reconstruction routines, was determined from the recorded number of ADC counts A using several calibration parameters via

$$I = \gamma_{\mathrm{FF}}\, \gamma_{\mathrm{p.e.}}^{-1} \left(A - A_{\mathrm{ped}}\right).$$

A_{ped} is the PMT signal in the absence of any Cherenkov light (the *pedestal*), $\gamma_{\mathrm{p.e.}}$ is the electronic gain in units of ADC counts per p.e., and γ_{FF} is the so called flat-field coefficient. These calibration parameters are determined for each pixel separately using the methods described below. In order to reduce statistical uncertainties and systematic effects, the coefficients were merged for a particular darkness period (i.e. for one month).

Pedestal Determination

Electronic noise and NSB (e.g. star light) in a PMT and its associated readout electronics results in an increased spread of the distribution of ADC counts compared to the intrinsic signal of Cherenkov photons. The position and width of the ADC count distribution in the absence of Cherenkov photons depends on the temperature and level of NSB, respectively. Therefore, the mean pedestal position A_{ped} for each pixel was calculated directly from the air shower event data by considering pixels not containing Cherenkov light. This estimation was done frequently ($1\,\mathrm{min}^{-1}$) in order to ensure that the pedestal shift due to temperature variations was small compared to the photo-electron signal ($\Delta A_{\mathrm{ped}} \ll A(1\,\mathrm{p.e.})$). If the pedestal position was highly uncertain or very broad, the pixel was considered *unusable* (see below) and excluded from the intensity determination procedure.

PMT Gain Determination

The gain was determined on data obtained in dedicated calibration runs using an LED as light source with a faint illumination corresponding to a mean number of detected photo-electrons close to zero. These runs were performed nearly every second day during the observation campaign described here. Figure 4.4 shows the corresponding ADC count distribution for one pixel in such a run. The sharp peak at low amplitude values corresponds to the pedestal value and the secondary peaks represents the peaks for 1 and 2 p.e. The conversion factor between ADC counts and photo-electrons of each pixel – $\gamma_{\mathrm{p.e.}}$ – is determined by fitting the distribution for each pixel.

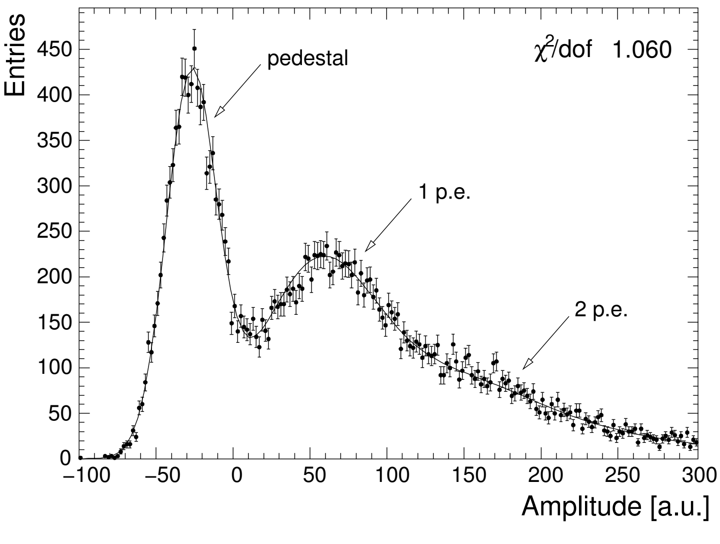

Figure 4.4: *Fit of the ADC count distribution for a single pixel illuminated at an intensity corresponding to less than 1 photo-electron [H.E.S.S. collaboration, 2004a].*

The conversion factor $\gamma_{\mathrm{p.e.}}$ was derived for the high gain channel (HG) only, for the low gain channel (LG) it was calculated using the gain ratio between both channels, $\gamma_{\mathrm{p.e.}}(\mathrm{LG}) = R^{\mathrm{HG}}_{\mathrm{LG}}\gamma_{\mathrm{p.e.}}(\mathrm{HG})$. $R^{\mathrm{HG}}_{\mathrm{LG}}$ was estimated from the ratio of pedestal subtracted ADC counts in the transition region (30-150 p.e.) of both channels using real air shower data.

Flat-Field Coefficient

Differences in photo-cathode and Winston cone efficiencies cannot be determined from such low illumination runs. Dish-mounted LEDs, providing short (5 ns) light flashes with intensities between 10 and 200 p.e. uniformly distributed over the whole camera, were used in "flat-fielding" runs in order to measure these differences. The PMT signals from these runs were calibrated without any flat-field correction and the flat-field coefficient of each pixel γ_{FF} is then defined by the ratio between the pixel signal and the mean signal of all pixels in the camera. The runs were performed as frequently as the gain determination and the maximum RMS of the coefficient distribution for the PSR B1259−63 dataset implies a spread in quantum and Winston cone efficiency of $< 13\%$ [Khélifi, 2004].

Unusable Pixels

A particular pixel was considered as *unusable* if one of the following problems was identified:

- ▹ **U**nlocked ARS. If the analogue ring sampler was not successfully synchronized, the timing of the readout window became randomized affecting all four pixels associated with the particular ARS chip.
- ▹ **I**rregular high voltage. The deviation of the monitored high voltage value from the nominal setting should not exceed a certain threshold. This includes pixels which were automatically switched off during an observation run because of too high illumination.
- ▹ **T**oo few/many large signals. The distribution of intensities has a deficit/excess at values > 30 p.e., suggesting a damaged PMT base or photo-cathode, or bit errors in the readout electronics.
- ▹ **I**ncreased noise. If the width of the pedestal distribution exceeds a certain value. This normally affects pixels with bright stars/sky regions in the field of view.

These problems can be identified for a single observation run or even for a shorter time interval. In case the merging of the calibration parameters did not succeed, and a certain pixel is lacking calibration parameters, this pixel was also considered to be unusable. Within the intensity determination procedure, all unusable pixels were treated as if they would have an intensity of zero.

The fraction of unusable pixels in each camera for the PSR B1259−63 dataset, as well as its average value, is listed in Table 4.1 and was found to be less than 10% and consistent with other observations within the galactic plane.

4.2.3 Muon Efficiencies

Atmospheric muons, produced by cosmic ray air showers and reaching the ground level, can trigger a single telescope by its Cherenkov emission. Figure 4.5 shows a typical muon image recorded by a telescope camera. The distribution of the emission detected by the camera can be modeled with a ring parametrisation which is characterized by the opening angle of the Cherenkov cone of the emitting muon and therefore its energy. The light collection efficiency ϵ_μ was determined by a χ^2 fit to the model [Leroy et al., 2003]. The efficiency $\epsilon_\mu = N_{\mathrm{pe}}/N_\gamma$ is the conversion factor between the measured pixel intensities obtained using the intensity calibration and the expected number of Cherenkov photons emitted by muons.

Since camera triggers due to muons are suppressed by the central trigger, special muon runs with telescope multiplicity $n = 1$ were performed regularly. However, the events triggered by cosmic ray air showers rarely contain muon arcs (0.1%) which additionally allow to determine ϵ_μ from regular air shower data. Figure 4.6 shows the evolution of ϵ_μ, averaged over the whole camera, for all telescopes during the PSR B1259−63 observation campaign [Bolz, 2004a]. The mean efficiency ϵ_μ for all telescopes is shown in Table 4.1, considering the PSR B1259−63 data set. The spread of the efficiency between the telescopes was found to be less than 10%.

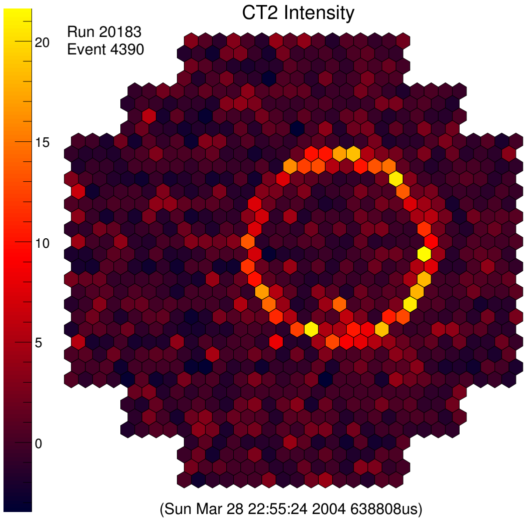

Figure 4.5: *Typical muon camera image within a run on PSR B1259−63. The color scale represents the pixel intensity in p.e. after calibration.*

Telescope	CT1	CT2	CT3	CT4	Average
ϵ_μ [%]	9.15 ± 0.23	8.84 ± 0.14	8.77 ± 0.14	9.11 ± 0.17	8.97 ± 0.09
Unusable Pixels [%]	7.1 ± 0.4	5.8 ± 0.2	7.4 ± 0.2	8.2 ± 0.2	7.14 ± 0.13

Table 4.1: *Muon efficiencies and number of unusable pixels for the H.E.S.S. PSR B1259−63 dataset after quality selections (see Sec. 4.3).*

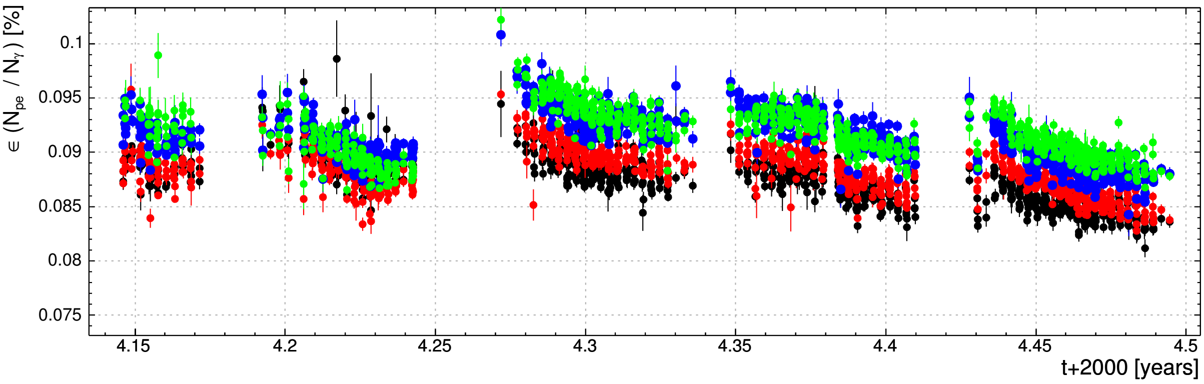

Figure 4.6: *Muon efficiencies for the darkness periods during the PSR B1259−63 observation campaign. Each color represents a different telescope.*

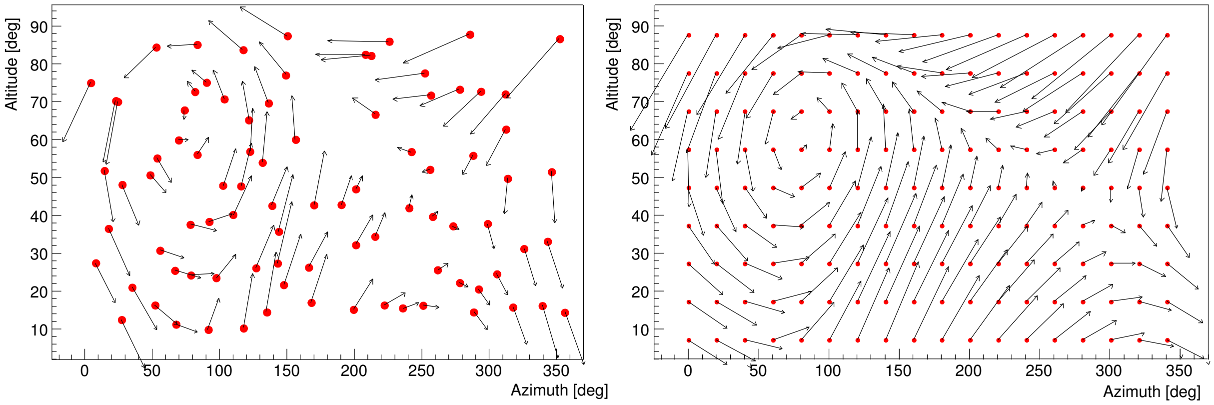

Figure 4.7: **Left**: *Measured difference between the position of a star image on the camera lid and its nominal position for a particular telescope as a function of the pointing direction in altitude and azimuth. The length of the arrows represents the mispointing in degrees multiplied by 1500.* **Right**: *Corresponding pointing correction model [Gillessen et al., 2004].*

4.2.4 Pointing Corrections

Although the angular resolution for single γ-rays is limited to $\sim 0.1°$, the position of a γ-ray point source can be determined with much higher accuracy, in principle only limited by the statistics of the signal. Therefore, with decreasing statistical errors it becomes important to keep the systematic pointing error as low as possible.

The mispointing of a H.E.S.S. telescope is dominated by deformations of the steel structure induced by gravity and – to a lesser but also less predictable extent – wind or obstacles on the drive rails. The task of any pointing correction model is to accurately determine the actual camera position at any time during an observation. Details of the methods applied for this analysis can be found in Gillessen [2003].

Mechanical Model

The mechanical deformations of the telescope structure, e.g. the bending of the camera arms, was measured using a CCD camera mounted on the dish looking onto the camera lid to record images of bright stars which were tracked by the telescope. The effect strongly depends on the azimuth and elevation of the telescope axis position and was parametrised in a *mechanical model*. The measured mispointing and the resulting model corrections of the position of the camera are shown in Fig. 4.7 and are remeasured roughly twice per year. The remaining systematic error was determined to be $\sim 20''$, dominated by the precision with which the position of the pixels is known compared to the star position [Gillessen et al., 2004].

Guide Telescope

Further reduction of the systematic error beyond the mechanical model can be accomplished using information on the mispointing obtained during observations in order to take into account variations in the pointing which are hard to predict. For this purpose, a guide telescope with a CCD camera, mounted on the telescope dish continually observes the sky region corresponding to the camera field of view. From the images, taken at a period of minutes, one can derive the actual pointing relative to stars in the field of view of the CCD camera reducing the systematic pointing error to below 5″. However, for the PSR B1259−63 dataset, a continuous CCD monitoring was not performed and therefore this correction was not applied in this analysis. Given the modest strength of the γ-ray signal of PSR B1259−63 and the unambiguous identification of the source (see Chapter 5), the achieved pointing accuracy of 20″ in each direction was considered to be sufficient.

4.2.5 Dead Time Correction

The duration of an observation run differs from the time where the instrument is actively able to record Cherenkov images. Since each camera needs time to completely read out a single air shower image, it cannot respond to any new trigger during this so-called *dead time*. The run duration was corrected for this effect to yield the live time $t_{\rm live}$.

The central trigger system (see Sec. 3.2.5) keeps track of the number of triggers received from each camera and which of these events could be read out, thus providing a direct measurement of the dead time. Figure 4.8 shows a sample distribution of time differences Δt between two consecutive camera triggers for all triggers received and those triggers for which the camera could be read out (active triggers), illustrating the dead time of the camera to be $\sim 400\,\mu$s for each event.

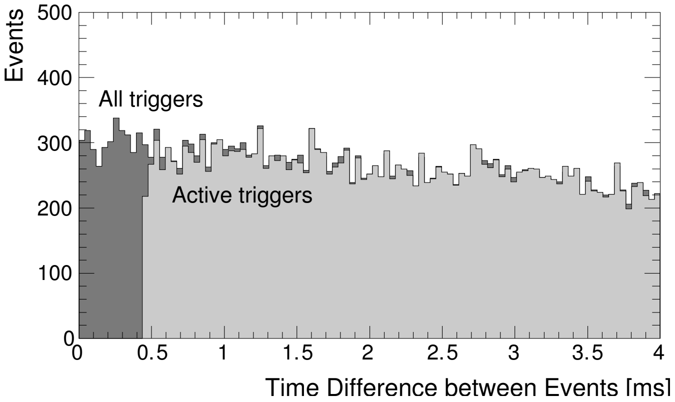

Figure 4.8: *Distribution of time differences Δt between consecutive camera triggers in a single telescope according to Funk et al. [2004]. The dark histogram shows all triggers, the light histogram shows only triggers for which the camera was read out.*

The total live time of the PSR B1259−63 data set after the quality selection described in the next section was determined accordingly to be $t_{\rm live} = 49.8$ hours with an average dead time of $\approx 9\%$.

4.3 Data Quality Selection

In order to ensure that MC simulations could be used for the reconstruction of the γ-ray characteristics in the data analysis techniques described later (see next section), data of a certain quality must be selected. For this purpose, a set of quality criteria was defined and applied to all observation runs of the PSR B1259−63 dataset. In this section the most important quality requirements are motivated.

4.3.1 Cloud Monitoring

The atmospheric transmission of Cherenkov light is influenced by several factors. Most obviously, no useful air shower images can be obtained if there are clouds within the camera field

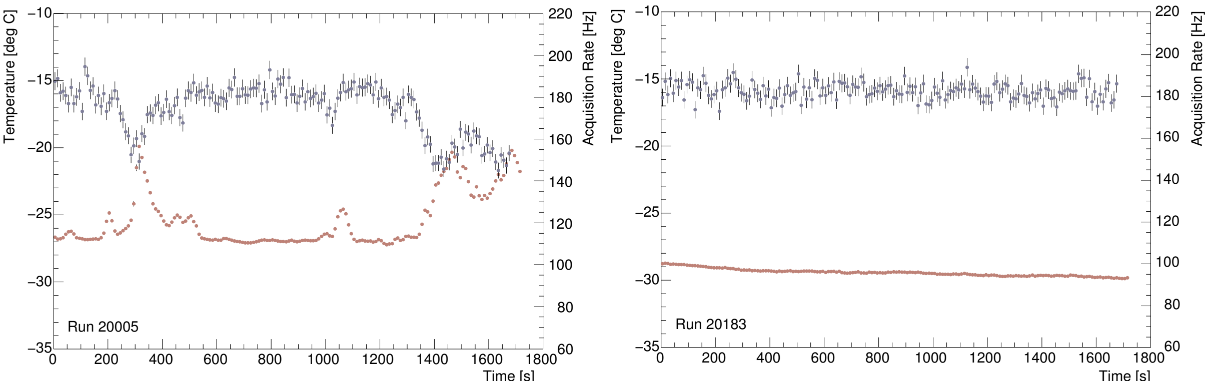

Figure 4.9: *Camera acquisition rate (upper points, right axis) and paraxial radiometer temperature (lower points, left axis) for CT4 during two observation runs with different weather conditions.* **Left***: Hazy sky partially covered with clouds. This run was rejected by the quality selection.* **R**ight*: Clear sky.*

of view. For this purpose, the temperatures measured by the paraxial radiometer were used as an indicator of cloud "activity". Additionally, if the average radiometer temperature is too high, this indicates a high level of water vapor in the atmosphere. Figure 4.9 shows two examples of the evolution of the radiometer temperature for an observation run with and without clouds.

4.3.2 Air Shower Trigger/Acquisition Rate

One of the most important quantities regarding the quality of the data obtained during a run is the camera and system trigger rate and the acquisition rate of air shower events which are directly measured using the central trigger system. Variations in the absorption of Cherenkov light in the atmosphere result directly in variations of the trigger rate. The dependence of the rate on the pointing of the array can be quantified by simulations of cosmic ray air showers. The dependence of the system rate on the zenith angle Θ (elevation $\alpha = 90^\circ - \Theta$) is shown in Fig. 3.13. Furthermore, variations of the camera and system acquisition rates could originate from possible problems during the readout process.

In order to determine variations of the rate during an observation run, a rough zenith angle correction was applied by fitting the temporal evolution of the system acquisition rate by a line, and the fractional RMS deviation from this line ΔR was calculated. All runs with a deviation exceeding a certain threshold $\Delta R_{\mathrm{run}} > \Delta R_{\mathrm{th}}$ were rejected. Figure 4.9 (left) shows the correlation of the radiometer temperatures and the camera acquisition rate during a run when clouds passed through the field of view of the system.

4.3.3 Camera Calibration – Unusable Pixels

During the calibration procedure of an observation run, problematic pixels were marked as *unusable*. In case the total number of unusable pixels exceeds 120 (12.5%) for any camera, the run was rejected. Values below this number still lead to a significant loss of image intensity, especially if these pixels are located in the inner part of the camera. Therefore, the resulting systematic effect on the energy reconstruction needs to be taken into account (see Sec. 5.3.4).

Large clusters of unusable pixels are expected to result in a bias in several reconstruction quantities such as shower direction and energy. This effect is largest in case one or more complete 16 pixel drawers are lacking intensity information and can be easily recognized in the centre of gravity (see Sec 4.4.1) distribution of all recorded shower images in a run. A flat distribution is expected to result from isotropic cosmic ray air showers. If this distribution showed more than one missing drawer seen as "holes" within a circle of 2° radius around the camera centre (see Fig. 4.10), the run was rejected.

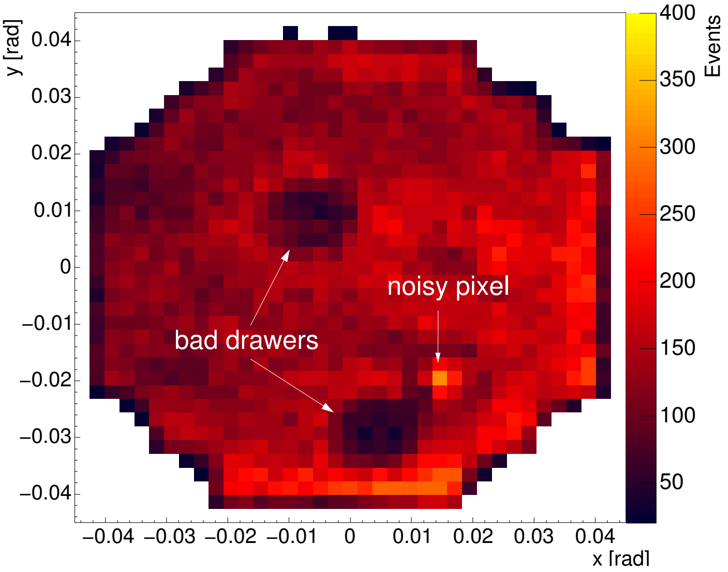

Figure 4.10: *Distribution of the centre of gravity of shower images in camera system coordinates. For this rejected run, two "holes" due to bad drawers and one noisy pixel can be seen.*

4.3.4 Pointing Accuracy

Tracking System

The pointing correction methods described in Sec. 4.2.4 rely on the accurate determination of the shaft encoder values. Therefore, these values were continuously monitored by the tracking system. The RMS of the deviation of the actual axis position from it's nominal position is required to remain below 5″. This requirement was well met for all observation runs taken on PSR B1259−63, demonstrating the reliability of the H.E.S.S. tracking system.

Star Position Determination Using PMT Currents

Stars within the field of view of a pixel cause an increase of its anode current. This current is routinely monitored and the data can be used to check the system pointing by determining the position of peaks in the current distribution in each camera and comparing them with nominal star positions for each observation run. Since the field of view rotates during an observation run because of the alt-az mount of the telescopes, the star position can be determined with higher accuracy than the pixel size of 10′, but this method is limited by the optical point spread function of the reflector, especially off-axis. Nevertheless, the method was used to check all runs considered for this analysis. Figure 4.11 shows the distribution of PMT currents for the whole PSR B1259−63 dataset and the position of stars within the field of view of a single camera.

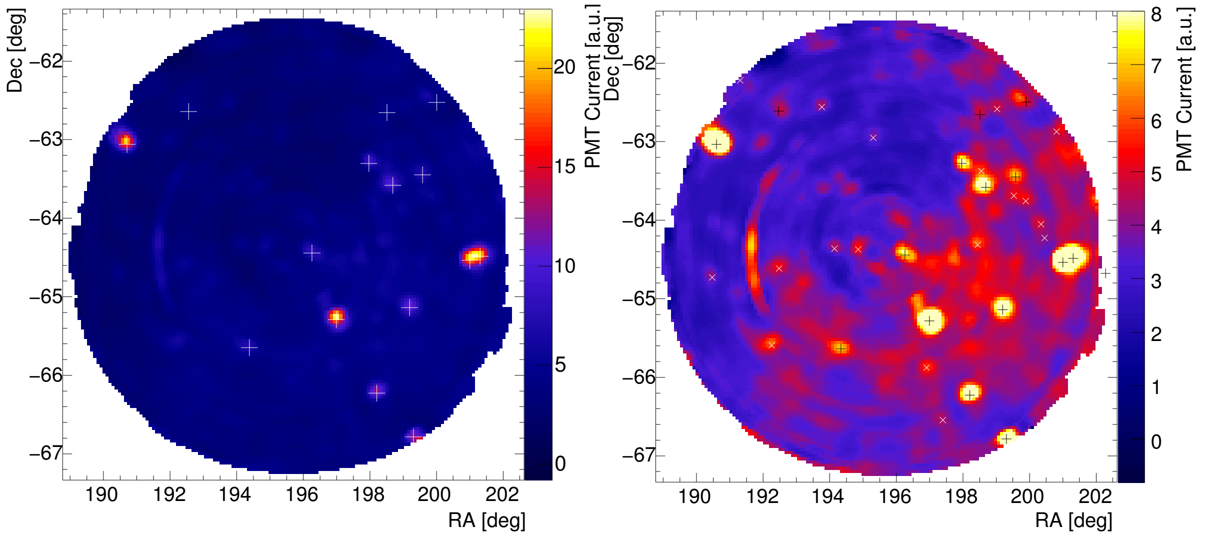

Figure 4.11: Left*: RA-Dec sky-map of PMT currents within the field of view of one camera averaged for all runs pointing to the position of PSR B1259−63 −0.5° Dec, overlaid with the nominal positions of stars (white crosses). Within this coordinate system, celestial structures have a fixed position, while the pixel positions rotate around the camera centre during the observations.* **R**ight*: The same map, but with a limited range of the current scale in order to emphasise low currents so that stars at larger magnitude become visible. The circular structures are due to unusable pixels for which the currents remained at a high level during the observations.*

4.4 Shower Reconstruction

The calibrated air shower images from the selected data set were cleaned of noise, parametrised with *Hillas* parameters, and then the shower direction and impact point were determined using a fast and simple reconstruction algorithm. The energy of the shower could only be estimated by comparison with simulated air shower images. The reconstruction methods used are based on the techniques developed in the first stereoscopic IACT project HEGRA [see e.g. Hofmann et al., 1999].

4.4.1 Image Parametrisation

Image Cleaning Using Tail Cuts

The intensity distribution of an air shower image in the telescope camera is superimposed on night sky background fluctuations in each pixel. A simple cleaning is performed with the following procedure: For each pixel, it was required that its recorded intensity exceeded a threshold of h p.e. or at least l p.e. in case it has a neighbouring pixel with an intensity exceeding h p.e. The parameters h, l (the *tail cuts*) were chosen such that the signal to noise ratio for γ-rays is optimal and at the same time insensitive to variations in the NSB level. Figure 4.12 shows a single shower image from observations on PSR B1259−63 before and after calibration (left and middle respectively), and after image cleaning (right).

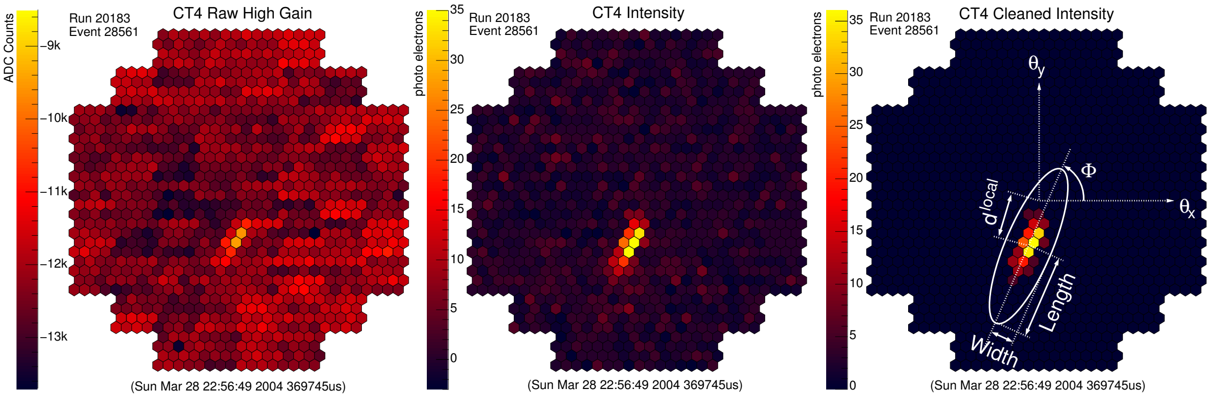

Figure 4.12: *Air shower image in a camera at different analysis stages.* **L**eft*: Raw ADC counts in the high gain channel.* **M**iddle*: Calibrated image with pixel intensities in photo-electron units.* **R**ight*: Cleaned image after tail cuts have been applied together with the image parameters. The computed ellipse is artificially enlarged by a factor of 5.*

Hillas Parameters

The cleaned images were parametrised using their first and second moments according to Hillas [1985]. The image is described as an ellipse with the parameters:

- **W**idth, **L**ength,
- **Φ**, **L**ocalDistance ($d^{\rm local}$) determining the orientation and **c**entre of gravity of the image with respect to the camera centre,
- and **S**ize, the total image intensity in p.e.,

These parameters are illustrated in Fig. 4.12, right, for a γ-ray candidate image taken from PSR B1259−63 data. The ellipse is artificially enlarged by a factor of 5.

Image Quality Cuts

In order to use only images of good quality for which the analysis methods below can be applied, two image quality cuts were applied:

- $d^{\rm local} < d^{\rm local}_{\rm max}$ was required, ensuring that the image centre of gravity was not close to the camera edge to avoid truncated images. $d^{\rm local}_{\rm max}$ was set to 80% of the camera radius (0.035 rad).
- Images were required to have a minimum image amplitude, $\text{Size} > \text{Size}_{\rm min}$. The actual cut value was derived in the cut optimisation procedure described in Sec. 4.5.3 which optimised the signal to noise ratio for γ-rays.

4.4.2 Geometric Shower Reconstruction

The geometric air shower properties relevant for this analysis are the shower direction and the position where the shower axis intersects the ground plane – the shower core position. Both quantities were calculated using a method similar to the standard reconstruction technique for a system of stereoscopic IACTs [Hofmann et al., 1999].

Shower Direction

The major axis of each recorded shower image represents a projection of the shower axis into the camera system and therefore the initial direction of the primary particle lies somewhere close to this axis. Using more than one shower image from a single event, the shower direction was determined by intersecting the major axis of the image ellipses within the camera coordinate system as shown in Fig. 4.13. If more than two telescope images were available for a particular event, the different quality of the images was considered to further increase the reconstruction accuracy. To each pair *i* of images, a weight

$$W_i = \frac{\sin(\Phi_1 - \Phi_2)}{(\mathrm{s}_1^{-1} + \mathrm{s}_2^{-1})(\mathrm{w}_1/\mathrm{l}_1 + \mathrm{w}_2/\mathrm{l}_2)}$$

was assigned, where s, w, and l are the Size, Width, and Length of the image respectively. The estimated direction is found from the weighted average of all intersection positions. The weight W_i implies that images which had a high intensity and a high aspect ratio were favoured against fainter and circular images. Pairs of images with major axes tilted towards each other have greater weights because the intersection point is much more accurately determined than for nearly parallel images. Furthermore, if one of the images did not pass the image quality selection cuts, the corresponding pair was discarded.

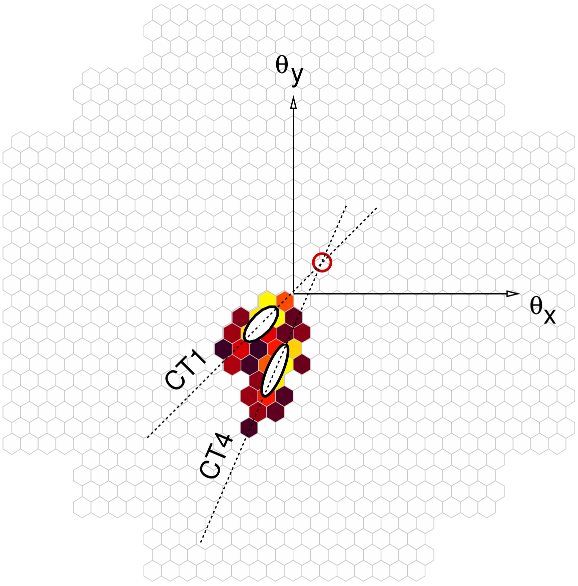

Figure 4.13: *Reconstruction of the shower direction using the image parametrisation of two telescopes for a measured γ-ray like event.*

Shower Core Position

A similar approach was used for the determination of the shower core position. Within the ground coordinate system, the major axis of the telescope image points towards the core position. Again, using the stereoscopic method with more than one image, the same algorithm as for the determination of the shower direction was applied. Since the camera plane of a telescope is only parallel if it points to zenith, a coordinate system was used which is tilted with respect to the ground and perpendicular to the telescope pointing axis (see Fig. 4.14).

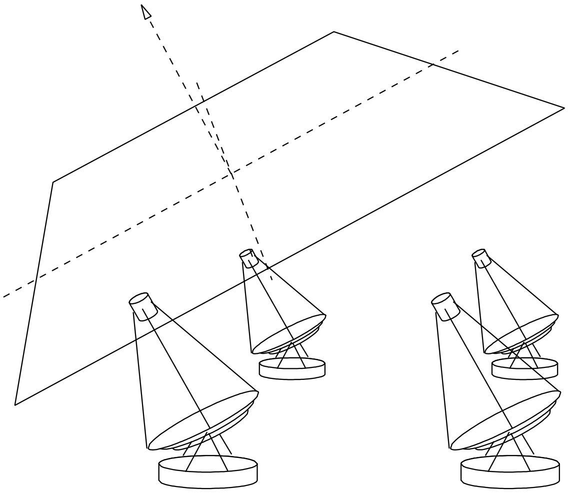

Figure 4.14: *Tilted ground system.*

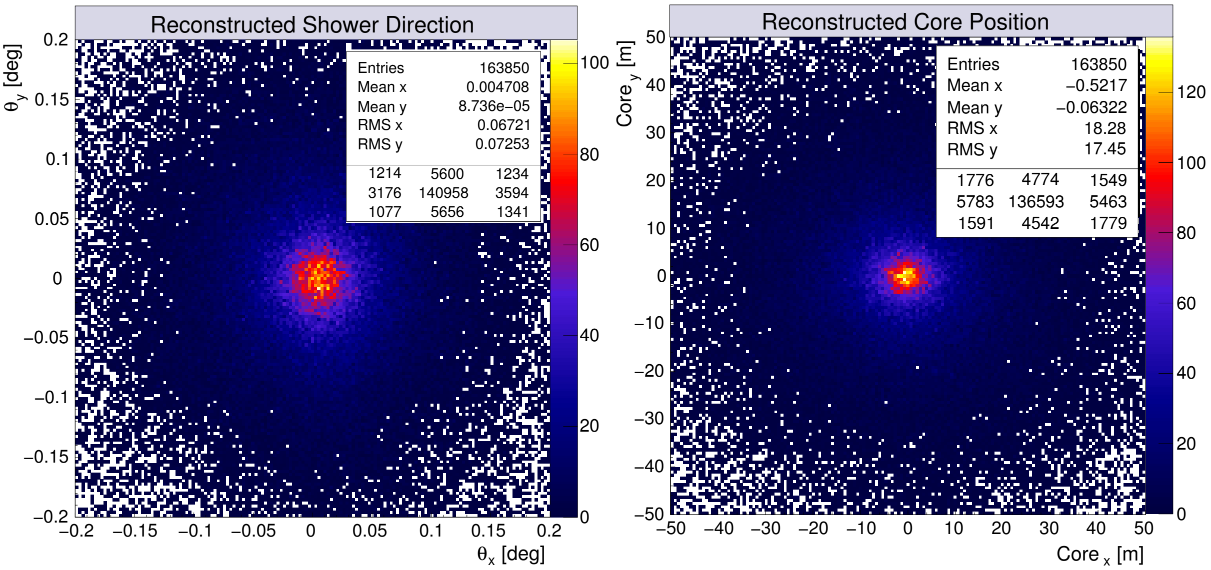

Figure 4.15: *Reconstructed shower parameters for simulated γ-rays.* **Left***: Shower direction within the camera system.* **Right***: Shower core position on the ground level.*

4.4.3 Accuracy of the Shower Reconstruction Methods

In order to quantify the accuracy of the reconstruction, the sample of simulated γ-rays at the zenith angle $\Theta = 40°$ (typical for the PSR B1259−63 dataset) was used to determine the resolution of the reconstructed direction and core position. Figure 4.15 shows the distribution of the difference between the true and reconstructed shower parameters.

Angular Resolution

For each simulated event passing the shape selection cuts (see Sec. 4.5), the angular distance θ between the true and the reconstructed shower direction was computed. Figure 4.16 (left) shows the resulting distribution of θ^2. The angular resolution can be quantified by the value $\theta_{68\%}$, for which 68% of the events have a smaller value of θ. The resulting resolution for the simulation sample is $\theta_{68\%} = 0.09°$. The distribution is significantly non-Gaussian with a long tail resulting from telescope images for which the estimation of shower orientation was bad. This distribution represents the H.E.S.S. point spread function for γ-rays, and can be parametrised by a sum of four Gaussians (see Fig 4.16, left):

$$N_\gamma(\theta) = \sum_{i=1}^{4} N_i \, e^{\theta^2/2\sigma_i^2} \tag{4.1}$$

with $\sigma_i < \sigma_{i+1}$.

Figure 4.16, right, shows the energy dependence of the angular resolution using equidistant energy bins on a logarithmic scale between 200 GeV and 50 TeV. It is obvious that the resolution improves dramatically with increasing energy. This improvement can be exploited in the determination of the position of a γ-ray excess (see Sec. 5.2).

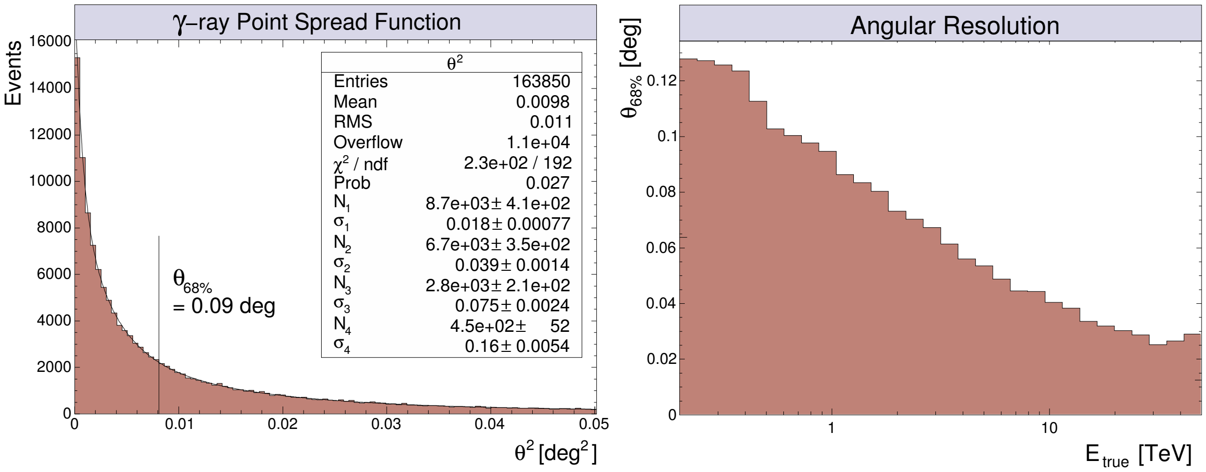

Figure 4.16: *Angular resolution for simulated γ-rays after image shape cuts.* **Left***: Distribution of the squared angular distance θ^2 between the true and reconstructed shower direction for simulated γ-rays. The vertical line shows the 68% containment radius, $\theta_{68\%}$.* **Right***: Angular resolution as a function of the true energy of the simulated shower.*

Impact Parameter Resolution

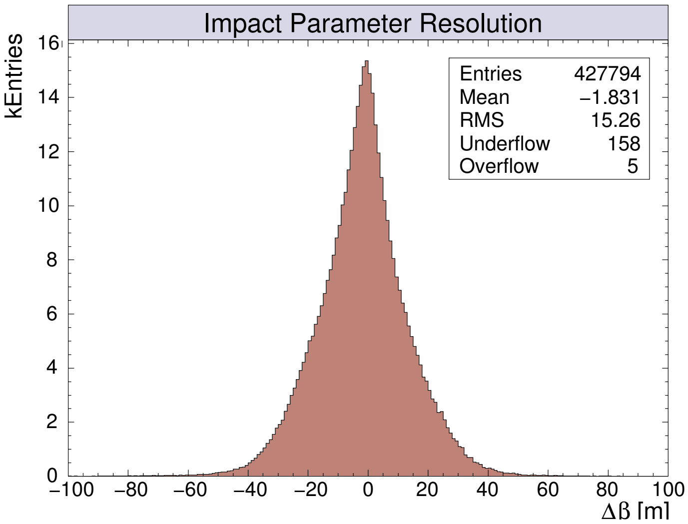

Figure 4.17: *Distribution of the difference between the true and reconstructed impact parameter $\Delta\beta = \beta - \beta_{true}$ for simulated γ-rays after all γ-ray selection cuts.*

The information of the shower core position is used in the reconstruction of the energy of primary γ-rays (as described below). For this purpose, the distance from the shower core to each telescope position, the so called impact parameter β is required. Since this shower parameter is only important for energy reconstruction, the cut on shower direction was applied as well on the simulation sample, as it was done in the spectral analysis in Sec. 5.3, in order to quantify the impact parameter resolution.

In Figure 4.17, the distribution of the difference between the true and the reconstructed impact parameter $\Delta\beta = \beta - \beta_{true}$ is shown. The mean deviates only 2 m from the nominal value, the RMS is $\sim$ 15 m, and decreases with increasing shower energy in a similar way to the angular resolution (see Fig. 4.18, left). However, the value is biased towards negative values which is an artifact of the arrangement of the telescopes in the array. The bias remains below 4 m within the considered energy range (see Fig. 4.18, right).

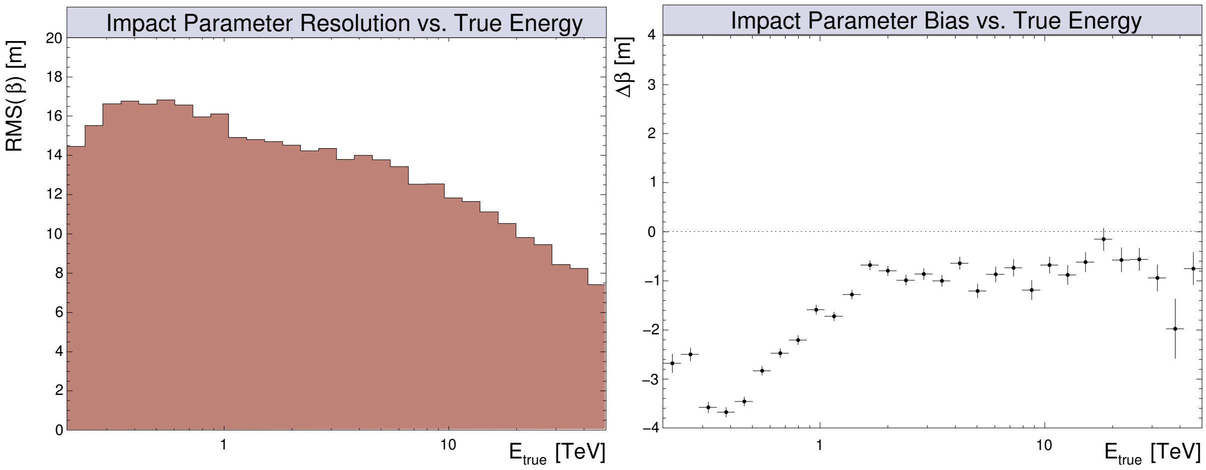

Figure 4.18: *Impact parameter resolution for simulated γ-rays. The RMS (left) and bias (right) of the $\Delta\beta$ distribution as a function of the true shower energy.*

4.4.4 Energy Reconstruction

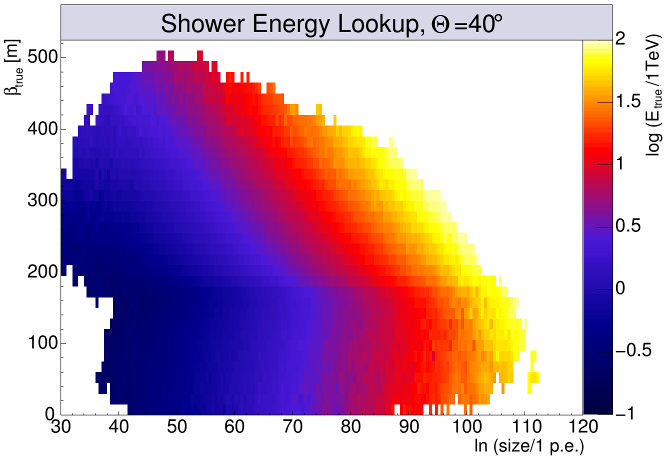

Figure 4.19: *Shower energy lookup table. The mean true energy of simulated γ-rays E_{true} is shown as a function of true shower impact distance and expected image amplitude* Size*. This distribution reflects the radial distribution of the Cherenkov light density on the ground for a given image Size.*

Assuming that a constant fraction of the energy of a primary γ-ray is converted into Cherenkov light, the intensity collected by a single telescope depends only on the extinction of this light and the distribution on the ground, the Cherenkov “light pool”. Therefore, the shower energy was estimated from the image Size in each telescope using the expectation value $\langle E\rangle$ of simulated γ-rays from a lookup table such as that shown in Fig. 4.19. The variation of the atmospheric extinction depending on the telescope pointing is accounted for by the dependence on the zenith angle Θ, and the Cherenkov light distribution on the ground is considered via the impact parameter β assuming rotational symmetry (see Fig. 3.3):

$$\langle E\rangle_{\text{MC}} = \langle E\rangle_{\text{MC}}\,(\text{Size}, \Theta, \beta).$$

Reconstruction Algorithm

The shower energy E of each γ-ray candidate event was reconstructed via:

$$E = \frac{1}{N_{\text{tels}}} \sum_{t}^{t_{\max}} \langle E\rangle_{\text{MC}}\,(\text{Size}_t, \Theta, \beta_t)$$

where N_{tels} is the number of and t the index for the individual telescopes which passed the γ-ray selection cuts, Size_t and β_t are the image amplitude and the impact parameter of the event for telescope t, respectively, and Θ is the zenith angle of the array pointing. Since γ-rays were only simulated for discrete zenith angle values Θ (see Sec. 3.3.3), $\langle E \rangle_{\text{MC}}$ was linearly interpolated in $\cos\Theta$.

Energy Resolution

Figure 4.20 shows the distribution of the difference between the reconstructed and true energy $\Delta E = E_{\text{reco}} - E_{\text{true}}$ relative to the true energy E_{true}, for the complete sample of simulated γ-rays with $\Theta = 40°$. The energy resolution was defined as the RMS of this distribution and found to be $\sim 20\%$. A Gaussian approximation of $\Delta E / E_{\text{true}}$ is not valid due to the increasing bias at low energies.

Figure 4.21 shows the energy resolution and bias as a function of the true energy. Within the range considered, the energy resolution improves with increasing shower energy. The bias in the reconstructed energy becomes greater than 10% below $\approx 400\,\text{GeV}$ of primary γ-ray energy, indicating that the reconstruction method is not efficient below this energy for observations at this zenith angle.

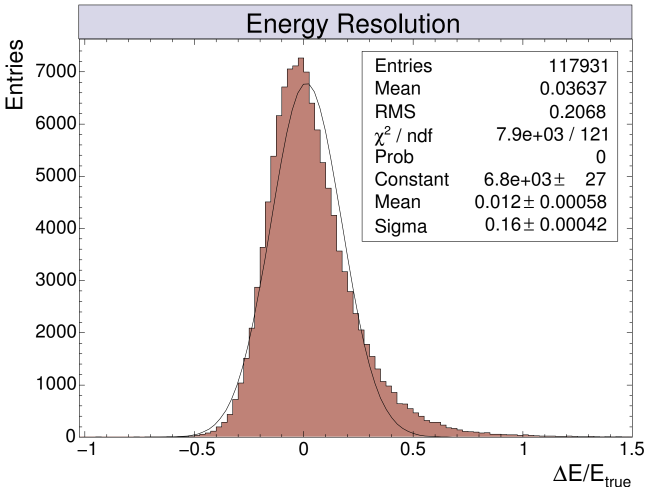

Figure 4.20: *Distribution of the relative difference between the simulated (true) and reconstructed energy* $(E_{\text{reco}} - E_{\text{true}})/E_{\text{true}}$ *for simulated γ-rays.*

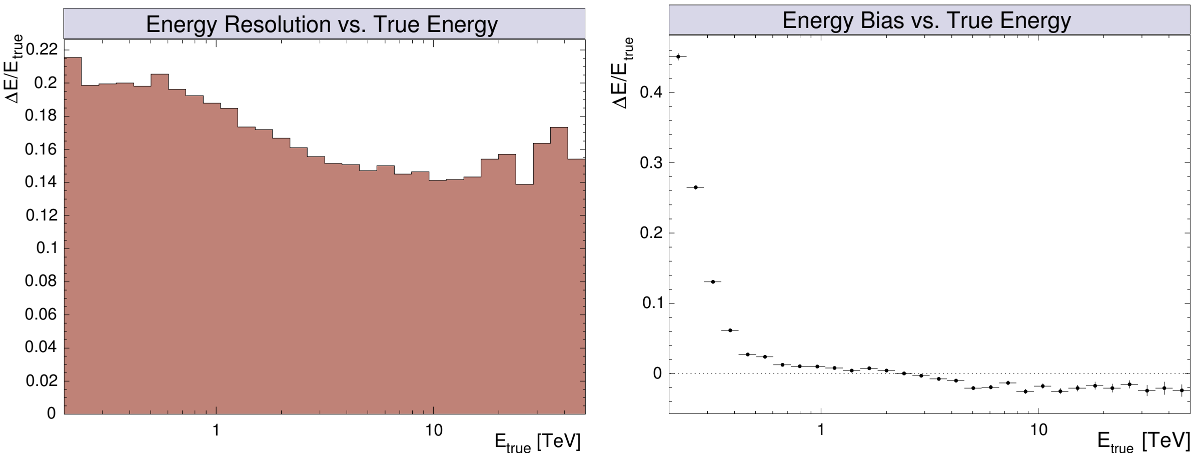

Figure 4.21: *Energy resolution and bias for simulated γ-rays after γ-ray selection cuts.* Left, Right*: RMS and mean of the distribution* $\Delta E / E_{\text{true}}$ *as a function of the true shower energy* E_{true}*, respectively.*

4.5 Background Reduction – γ-Hadron-Separation

Even for a strong VHE γ-ray source, such as the Crab Nebula, the typical H.E.S.S. event rate estimated from simulations is only $\approx 0.1\,\mathrm{Hz}$. The typical acquisition rate during observations of $\approx 300\,\mathrm{Hz}$ indicates a signal-to-noise ratio of $< 10^{-3}$ requiring an efficient background reduction method in order to detect fainter γ-ray sources. In Section 3.1.1, the characteristics of the Cherenkov emission of air showers were discussed and it was suggested that for IACTs a discrimination should be possible based on image morphology.

4.5.1 Event Selection based on Image Shape

Showers initiated by hadronic cosmic rays have a much broader lateral extent than electromagnetic showers. As a consequence, it is possible to distinguish primary γ-rays from hadrons by applying a cut on the image parameter Width. Since the image shape depends on the shower energy and impact distance, the efficiency of such a cut on the absolute image width depends on the energy and impact distance as well. In order to avoid such an effect, so-called “scaled” image parameters were introduced [based on HEGRA collaboration, 1997], scaling the shape parameters Width and Length with their expectation value derived from simulated γ-rays.

Scaling of Shape Parameters with Expectation Values

For each telescope image, the scaled image parameter p_s is defined as:

$$p_\mathrm{s} = \frac{p - \langle p \rangle_\mathrm{MC}}{\sigma_\mathrm{MC}}.$$

The expectation value and its RMS σ_MC were derived, as for the energy reconstruction procedure, as a function of impact parameter β, zenith angle Θ, and image amplitude Size, i.e. $\langle p \rangle_\mathrm{MC} = \langle p \rangle_\mathrm{MC}\,(\beta, \Theta, \mathrm{Size})$.

A scaled parameter is assigned to each shower event by averaging the parameter of each telescope passing the image quality cuts, resulting in a “Mean Reduced Scaled Parameter” (MRSP):

$$\mathrm{MRSP} = \frac{1}{N_\mathrm{tels}} \sum_{t}^{t_\mathrm{max}} p_\mathrm{s}(t).$$

The scaled image parameters corresponding to Width and Length are referred to as MRSW and MRSL, respectively, and represent the deviation of the parameters from their expectation value.

Cuts on Scaled Parameters

Figure 4.22 shows the distribution of the MRSW parameter for simulated γ-rays, simulated protons, and data from H.E.S.S. observations of a field of view containing no known γ-ray sources. The distribution for γ-rays is symmetric around zero, corresponding to the expectation value, with a width of $\approx 1\,\sigma$. The distribution for simulated protons is very similar to that measured for cosmic rays, and is much broader, with a mean $\gg 1\,\sigma$. The γ-hadron-separation was performed by rejecting all events with MRSW > $\mathrm{MRSW}_\mathrm{min}$ and MRSW < $\mathrm{MRSW}_\mathrm{max}$, and similarly for MRSL. Most rejection power is provided by the cut parameter $\mathrm{MRSW}_\mathrm{max}$.

Simulated vs. Measured γ-Rays

In order to verify that the measured γ-rays conform to expectations, the scaled parameter distributions of measured and simulated γ-ray events were compared. For this purpose, events obtained from observations of the Crab Nebula, a "standard candle" for VHE γ-ray astronomy, were used. Figure 4.23 shows the resulting distribution of MRSW for simulated γ-rays and events from the Crab data after background subtraction. The distributions are found to be in reasonable agreement.

4.5.2 Event Selection based on Shower Direction

An additional efficient background rejection – especially when searching for point sources of γ-rays – is given by selecting events based on their reconstructed shower direction. By considering only events contained within a solid angle corresponding to a circle of radius θ_{cut} around a candidate source position, it is possible to reject a large fraction of the isotropic cosmic ray background. Furthermore, γ-ray events originating from the source but with a poorly reconstructed shower direction, and thus a large energy uncertainty are also rejected.

4.5.3 Cut Optimisation and Performance

The cuts for the selection of γ-ray events were optimised using the complete sample of simulated γ-rays as signal and several off-source runs as background. The selection cuts Size_{min} (image quality), MRSW_{min}, MRSW_{max}, MRSL_{min}, MRSL_{max} (image shape), and θ_{cut} (shower direction) were varied, and for each possible combination, the number of events containing the γ-ray signal plus background $N_{\text{on}} = N_\gamma + N_{\text{data,on}}$ and background only $N_{\text{off}} = N_{\text{data,off}}$ were derived according to the "7-background" model (see Sec. 5.1.2) using a background normalisation of $\alpha = 1/7$. Subsequently, the cut values were chosen such that the significance [Li and Ma, 1983]

$$S = \sqrt{2}\left[N_{\text{on}} \ln\left(\frac{1+\alpha}{\alpha}\frac{N_{\text{on}}}{N_{\text{on}}+N_{\text{off}}}\right) + N_{\text{off}} \ln\left((1+\alpha)\frac{N_{\text{off}}}{N_{\text{on}}+N_{\text{off}}}\right)\right]^{1/2} \tag{4.2}$$

of the γ-ray excess was maximal. The excess was scaled to a source strength of 10% of the flux of the Crab Nebula in order to optimise for rather faint γ-ray sources.

Table 4.2 lists the cut values which were found in the optimisation process. These cuts retain 41.2% of the simulated γ-ray events whilst rejecting more than 99.9% of background events from data and were used for the analysis of the PSR B1259−63 dataset described in the next chapter.

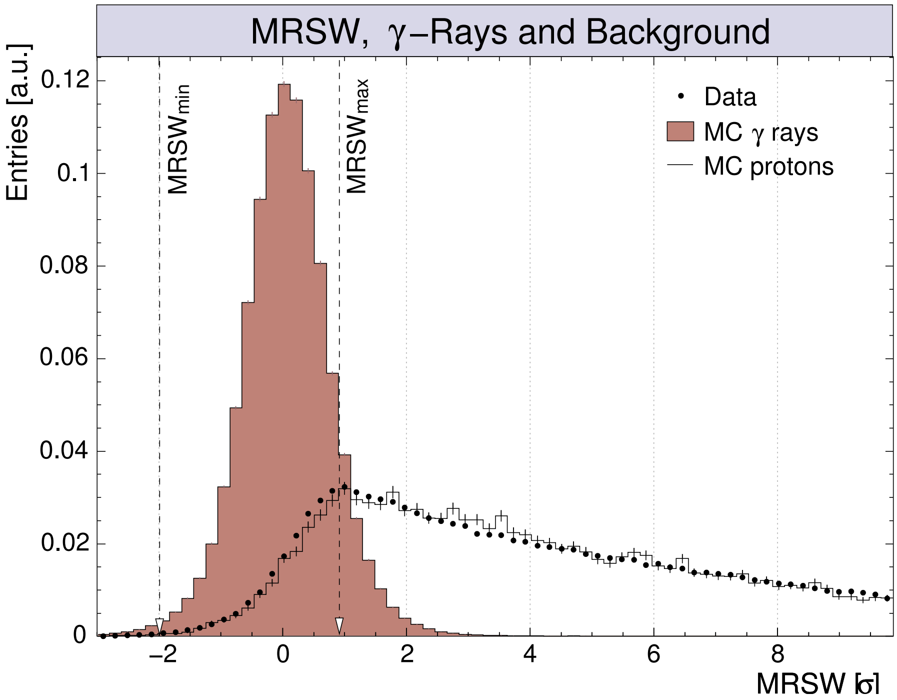

Figure 4.22: *Distribution of the mean reduced scaled width for simulated γ-rays (filled) and protons (solid line), and H.E.S.S. off-source data (points). The vertical dashed lines show the cut values used in the analysis. The distributions are normalised to unity.*

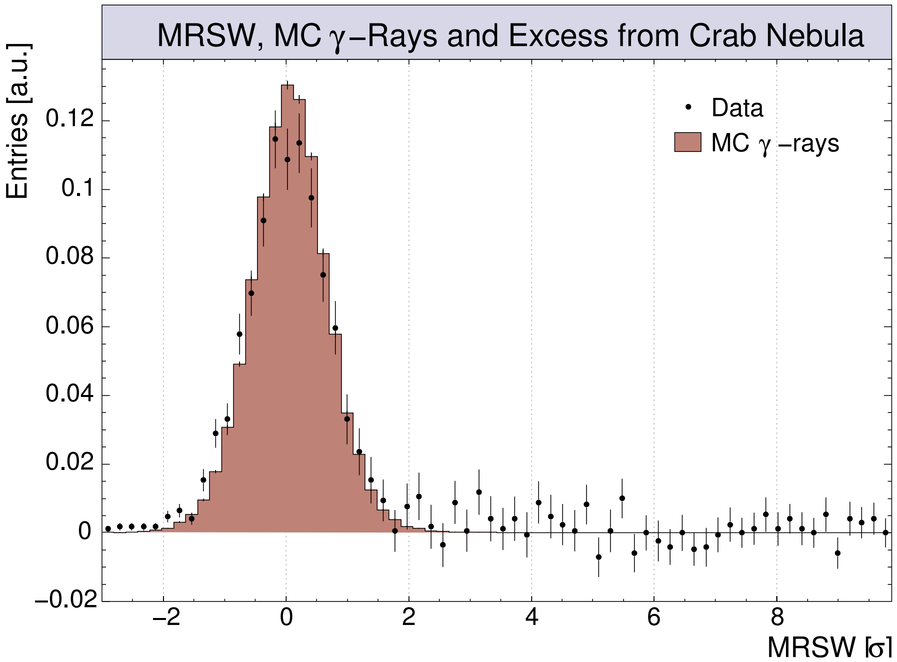

Figure 4.23: *Normalised distribution of the mean reduced scaled width for simulated γ-rays (histogram) and measured γ-rays from the Crab Nebula (points).*

Cut Category	**S**election Cut	**V**alue
image quality	$d_{\text{max}}^{\text{local}}$	0.525 m[*]
	Size_{min}	80 p.e.
image shape	MRSW_{min}	−2.0
	MRSW_{max}	0.9
	MRSL_{min}	−2.0
	MRSL_{max}	1.3
direction	θ_{cut}^2	0.02 deg^2

[*] not included in the optimisation process

Table 4.2: *Optimised γ-ray selection cuts for point sources with a flux of 0.1 Crab.*

Chapter 5

Data Analysis

In this chapter, the analysis techniques are introduced and tested with off-data and data from observations of the Crab Nebula where it was appropriate. Subsequently, the techniques are applied to the data from PSR B1259−63, and the results such as the position of the excess, the energy spectrum, and its temporal behaviour are presented.

5.1 Signal Extraction and Background Estimation

A possible γ-ray signal is detected in case the number of events N_{on} in a circle around the target position (*on-source*) significantly exceeds the number of background events. The number of background events N_{off} (*off-source*) is estimated independently and the signal, i.e. the excess N_γ, is given by:

$$N_\gamma = N_{\mathrm{on}} - \alpha N_{\mathrm{off}}. \tag{5.1}$$

The factor α is the background normalisation

$$\alpha = \frac{\int_{\mathrm{on}} \epsilon_\gamma(\theta_{\mathrm{x}}, \theta_{\mathrm{y}}, \Theta, t)\,\mathrm{d}\theta_{\mathrm{x}}\,\mathrm{d}\theta_{\mathrm{y}}\,\mathrm{d}\Theta\,\mathrm{d}t}{\int_{\mathrm{off}} \epsilon_\gamma(\theta_{\mathrm{x}}, \theta_{\mathrm{y}}, \Theta, t)\,\mathrm{d}\theta_{\mathrm{x}}\,\mathrm{d}\theta_{\mathrm{y}}\,\mathrm{d}\Theta\,\mathrm{d}t}.$$

with ϵ_γ as the acceptance for γ-ray-like showers which can vary with the position of the shower direction in the camera $\theta_{\mathrm{x}}, \theta_{\mathrm{y}}$, the zenith angle Θ, and the exposure time t.

For the wobble observation mode, the signal and background events are derived from the same field of view and thus have an identical zenith angle and exposure time. Therefore, α reduces to:

$$\alpha = \frac{\int_{\mathrm{on}} \epsilon_\gamma(\theta_{\mathrm{x}}, \theta_{\mathrm{y}})\,\mathrm{d}\theta_{\mathrm{x}}\,\mathrm{d}\theta_{\mathrm{y}}}{\int_{\mathrm{off}} \epsilon_\gamma(\theta_{\mathrm{x}}, \theta_{\mathrm{y}})\,\mathrm{d}\theta_{\mathrm{x}}\,\mathrm{d}\theta_{\mathrm{y}}}.$$

In the following sections, an acceptance model will be introduced, and two alternative methods for the background estimation are described and verified with data from a field of view containing no detectable γ-ray sources (*off-data*).

5.1.1 System Angular Acceptance

In wobble mode, used for all observations described here, the on-source region does not have a constant position within the camera plane during observations, since the camera rotates with

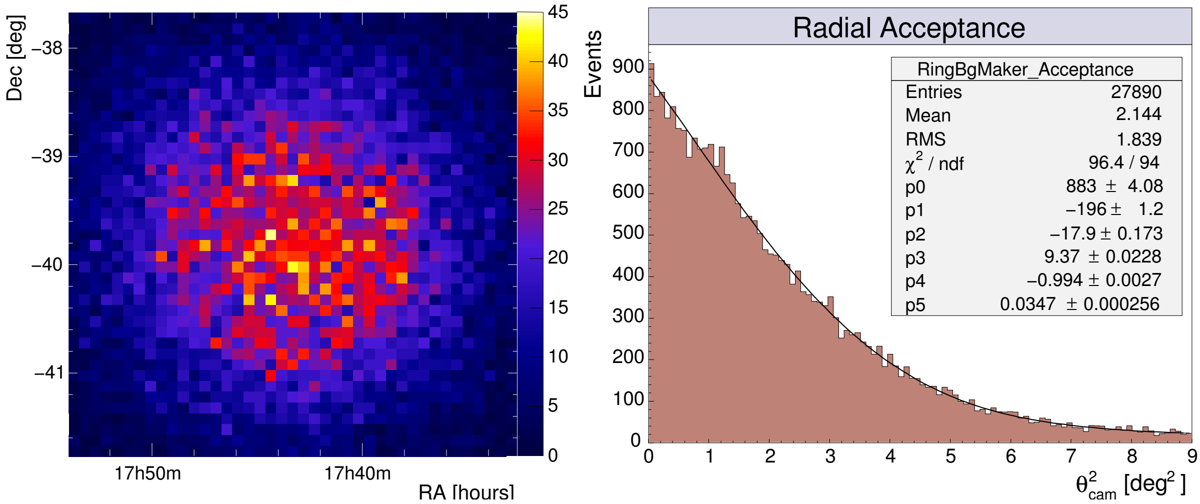

Figure 5.1: *Distributions of γ-ray-like background events within off-source data.* **L**eft: *Sky-map of the reconstructed shower direction in the RA-Dec system.* **R**ight: *Distribution of the squared angular distance with respect to the camera centre, θ^2_{cam}.*

respect to the sky. Thus, the on- and off-source regions must be considered within a celestial coordinate system such as right-ascension (ρ) and declination (δ), RA-Dec, rather than in the camera system.

Figure 5.1 (left) shows the distribution of reconstructed air shower events after image quality and shape cuts in the RA-Dec system for an off-data set. The acceptance drops radially from the camera centre towards the edge of the field of view as one would expect because the phase space for shower images pointing to a certain position in the camera decreases towards the edge.

The acceptance was assumed to be radially symmetric leading to a further simplification of the background normalisation α of

$$\alpha = \frac{\int_{\mathrm{on}} \epsilon_\gamma(\theta_{\mathrm{cam}})\,\mathrm{d}\theta_{\mathrm{cam}}}{\int_{\mathrm{off}} \epsilon_\gamma(\theta_{\mathrm{cam}})\,\mathrm{d}\theta_{\mathrm{cam}}}. \tag{5.2}$$

The acceptance was modeled by fitting the distribution of the squared angular distance between the event direction and the camera centre, θ^2_{cam}, by a polynomial function of 5th grade (see Fig. 5.1, right).

5.1.2 1D Analysis Using the 7–Background Model

Under the assumption of a rotational symmetry in the system acceptance, the most simple background estimation method would be to use an off-region which is identical to the on-region but with its position mirrored with respect to the camera centre, i.e. at $\theta_{\mathrm{cam}} = -0.5°$ in Declination in case the wobble offset of the particular run was $\theta_{\mathrm{cam}} = +0.5°$ Dec. The single off-source position would be located at the same distance to the camera centre and thus would have the same acceptance as the on-region and therefore $\alpha = 1$.

To increase the significance of a γ-ray signal (given by Eq. (4.2)), it is desirable to increase the area and exposure from which the background is estimated, and therefore reduce the normalisation α and the relative statistical error of the background counts N_{off}. This can be achieved by using, instead of a single off-region, a number n_{off} of off-regions, evenly distributed around and equidistant to the camera centre. The background normalisation in this model is given by $\alpha = 1/n_{\mathrm{off}}$. In particular, Fig. 5.2 illustrates that for an off-region with $\theta_{\mathrm{cam}} = \theta_{\mathrm{cut}}$, $n_{\mathrm{off}} = 7$ of them can be arranged at a distance of $\theta_{\mathrm{cam}} = \pm 0.5°$ around the camera centre. A safe distance from the on-region to the off-regions (defined by the γ-ray point spread function) prevents a possible background contamination by any strong γ-ray excess. Additionally, any off-regions coincident with other γ-ray sources in the field of view are excluded. This method was pioneered by the HEGRA collaboration [2001] and has the advantage that no system acceptance model is needed and any linear gradient in the acceptance cancels out in case of a symmetric distribution of wobble offsets in the data.

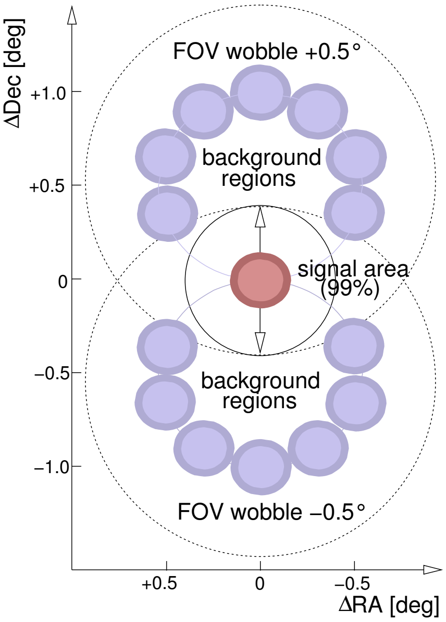

Figure 5.2: *Arrangement of on- and off-regions in the 7-background model for wobbling ±0.5° in Declination.*

The 7-background method was applied to the PSR B1259−63 data set and Fig. 5.3 (left) shows the distribution of the squared angular distance θ^2 of excess events relative to the position of PSR B1259−63. The clear excess in the direction of the pulsar has a significance of $13.8\,\sigma$. Fitting the excess distribution with the γ-ray point spread function (see Sec. 4.4.3) with the parameters $\sigma_{1...4}$ fixed yielded a $\chi^2/\mathrm{ndf} = 35.8/36$ showing that the signal is consistent with resulting from a point source. Figure 5.3 (right) displays the distribution in θ^2 for the on-source region (points) and the distribution for the off-source regions normalised by α. A uniform background results in a flat distribution in θ^2 for small values of θ. This is indeed the case for the distribution of the off-source regions.

The γ-ray signal from the direction of PSR B1259−63 was detected in most of the darkness periods when the system was observed. The results obtained with the 7-background model for each period are summarised in Table 5.1.

Darkness Period 2004	N_{tel}	t_{live} [h]	S [σ]	N_{on}	N_{off}	α	N_γ
February	3	7.9	9.8	691	2 591	0.172	246±25
March	4	17.8	7.2	1 740	8 459	0.169	307±43
April	4	5.1	7.8	644	2 705	0.167	193±25
May	4	9.9	5.2	910	4 499	0.167	160±31
June	4	9.1	1.8	722	4 027	0.167	51±28
Total		49.8	13.8	4 707	22 281	0.168	955±69

Table 5.1: *Results of H.E.S.S. observations on PSR B1259−63. For each darkness period the number of telescopes used in the analysis* N_{tel}*, the live time* t_{live}*, the significance* S*, the number of counts within the on-source (*N_{on}*) and off-source (*N_{off}*) region(s), the background normalisation* α*, and the number of detected* γ*-rays (*N_γ*) are listed.*

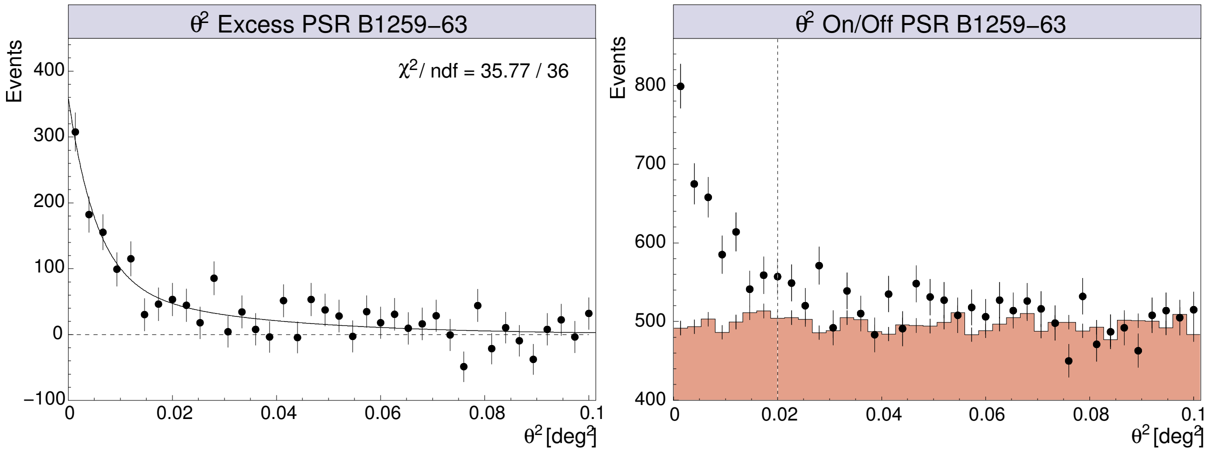

Figure 5.3: *Angular distribution of events after image shape cuts relative to the position of PSR B1259−63 for the complete data set.* **L**eft: *Distribution of background-subtracted γ-ray candidates in θ^2. The solid line indicates a fit of the γ-ray point spread function with the normalisations as the only free parameter.* **R**ight: *Distributions in θ^2 for "on-source" γ-ray candidates relative to the source position (full points) and for all background regions (histogram, scaled with the background normalisation factor α). The dashed vertical line indicates the direction cut applied ($\theta^2_{\text{cut}} = 0.02\,\text{deg}^2$).*

5.1.3 2D Analysis Using the Ring-Background Model

Ring-Background Analysis Method

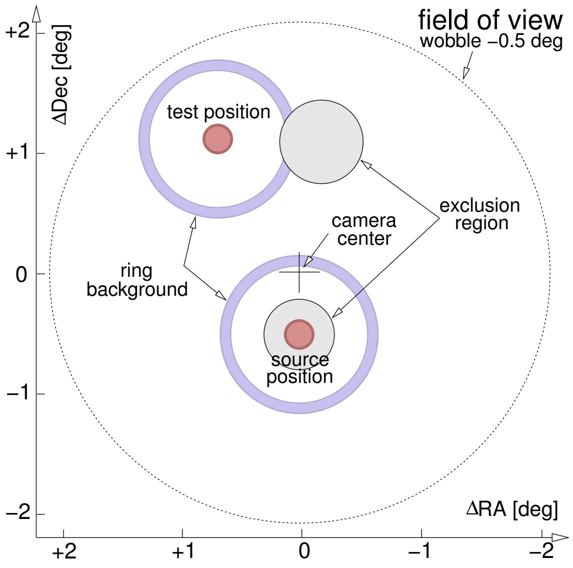

Figure 5.4: *Arrangement of signal and background regions in the ring-background model. Shown are two possible test positions, one identical to the source position and another close to a background exclusion region.*

The main disadvantage of the 7-background model is that it is only valid for source positions which have a minimum distance θ_{cam} from the camera centre determined by the value of θ_{cut}. For large distances it is sensitive to non-linear or local acceptance distortions. Therefore it is impossible to perform a 2-dimensional analysis of the complete field of view by calculating the excess for all possible source positions (test positions). In order to produce such a sky-map of γ-ray excess events and to provide a cross check for the results of the 7-background model, the so called ring-background model was applied to the data.

In this method, the 2-dimensional distribution of γ-ray candidate events $N_{\text{cand}}(\theta_{\text{RA}} = \rho, \theta_{\text{Dec}} = \delta)$ in the field of view was divided into fine bins of 0.01° × 0.01° (see Fig 5.5, left). For each bin (i, j), the number of on-events N_{on} was derived by integrating the bin content within a circle of radius θ_{cut} around the

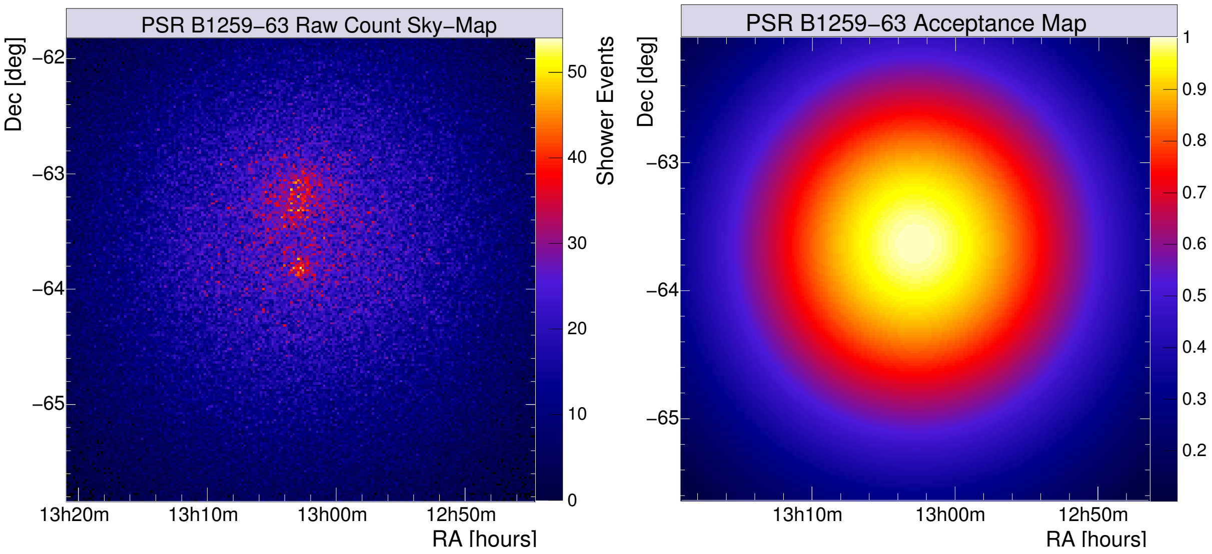

Figure 5.5: *RA-Dec sky-map of γ-ray candidates and system acceptance.* **L**eft: *γ-ray candidate events after image shape cuts for the complete PSR B1259−63 dataset.* **R**ight: *Overall system acceptance based on the acceptance model obtained for each observation run.*

bin center (the on-region C):

$$N_{\mathrm{on}}(i,j) = \sum_{k,l} N_{\mathrm{cand}}(k,l) \;\text{ with } (k,l) \in C \text{ and } \theta_{i,j} - \theta_{k,l} < \theta_{\mathrm{cut}}.$$

Since the bin size is much smaller than the integration radius, the resulting bins are correlated. In order to produce an uncorrelated excess map, each bin itself was considered as on-region.

The background was estimated from a ring $\mathcal{R}$ around the bin position with a mean radius of 0.6° and an area 7 times larger than that of the on-region (see Fig. 5.4). In order to avoid the contamination of the background with events from possible sources of γ-rays, counts within so called exclusion regions $\mathcal{R}_{\mathrm{ex}}$ were not considered (by default, at least the circle with radius 0.3° around the source position). The number of background events N_{off} is then given by:

$$N_{\mathrm{off}}(i,j) = \sum_{k,l} N_{\mathrm{cand}}(k,l) \;\text{ with } (k,l) \in \mathcal{R} \;\wedge\; (k,l) \notin \mathcal{R}_{\mathrm{ex}}.$$

Within the ring background, the acceptance cannot be assumed to be constant, and thus the normalisation α was expressed as the ratio between the integrated acceptance of the on-region and the background ring, $\alpha = \epsilon_{\mathrm{on}}/\epsilon_{\mathrm{off}}$. The acceptance ϵ was derived for each run separately by mapping the one-dimensional radial acceptance function of the particular run onto a 2d-sky-map and averaging these maps using the live time of the run as weight:

$$\epsilon(i,j) = \frac{1}{\sum_{\mathrm{runs}} t_{\mathrm{live}}} \sum_{\mathrm{runs}} t_{\mathrm{live}} \epsilon_{\mathrm{run}}(i,j).$$

Figure 5.5 (right) shows the acceptance map for the complete PSR B1259−63 data set. The integrated acceptances $\epsilon_{\mathrm{on/off}}$ for a particular bin (i,j) were determined in a similar way as the

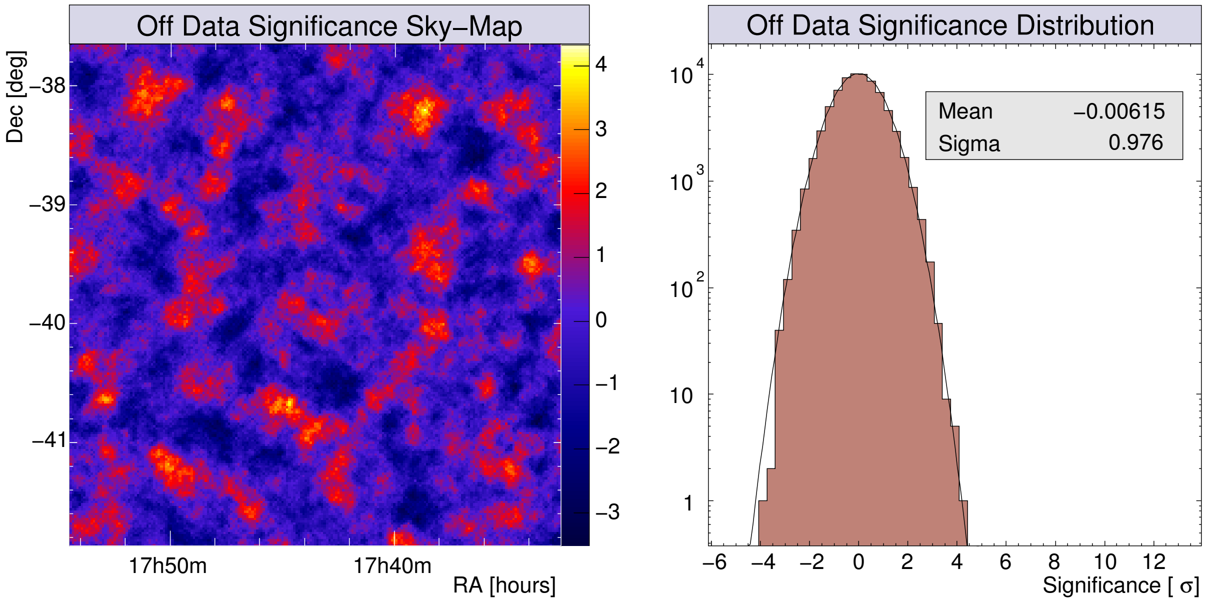

Figure 5.6: *RA-Dec significance sky-map (left) and the significance distribution of all bins (right) for off-data.*

on and off counts by integrating over the on-region and background ring and again excluding bins from the background exclusion region:

$$\begin{aligned}\epsilon_{\mathrm{on}}(i,j) &= \sum_{k,l} \epsilon(k,l) \text{ with } (k,l) \in C,\\ \epsilon_{\mathrm{off}}(i,j) &= \sum_{k,l} \epsilon(k,l) \text{ with } (k,l) \in \mathcal{R} \,\wedge\, (k,l) \notin \mathcal{R}_{\mathrm{ex}}.\end{aligned}$$

Using the above equations for N_{on}, N_{off}, and α, a significance sky-map was determined following Eq. (4.2). Fig. 5.6 (left) shows such a map for the off-data set. There is no significant excess visible as expected from this sky region and the significance distribution of all bins follows a Gaussian distribution (Fig. 5.6, right) with a mean value close to zero and an RMS of 1.0.

Sky-Map of the PSR B1259−63 Field of View

Figure 5.7 shows the significance sky-map of a region 2° × 2° around the nominal position of PSR B1259−63 for the complete data set. The excess at the pulsar position ($N_\gamma = 938 \pm 72$, $S = 13.8\,\sigma$) is consistent with the excess given in Table 5.1. The results for the individual darkness periods were verified accordingly and found to be consistent with the results of the 7-background model within the statistical errors.

The additional broad excess $\approx 0.6°$ north of the pulsar, which is visible also in the raw count map in Fig. 5.5, is the unidentified TeV source HESS J1303−631 discovered in the same field of view. An extensive study was performed, described in [H.E.S.S. collaboration, 2005d], in order to verify that the excess is indeed a source of γ-rays. The additional excess of HESS J1303−631 was considered in the analysis by an additional exclusion region with a radius of 0.4° around the centre of gravity of the excess.

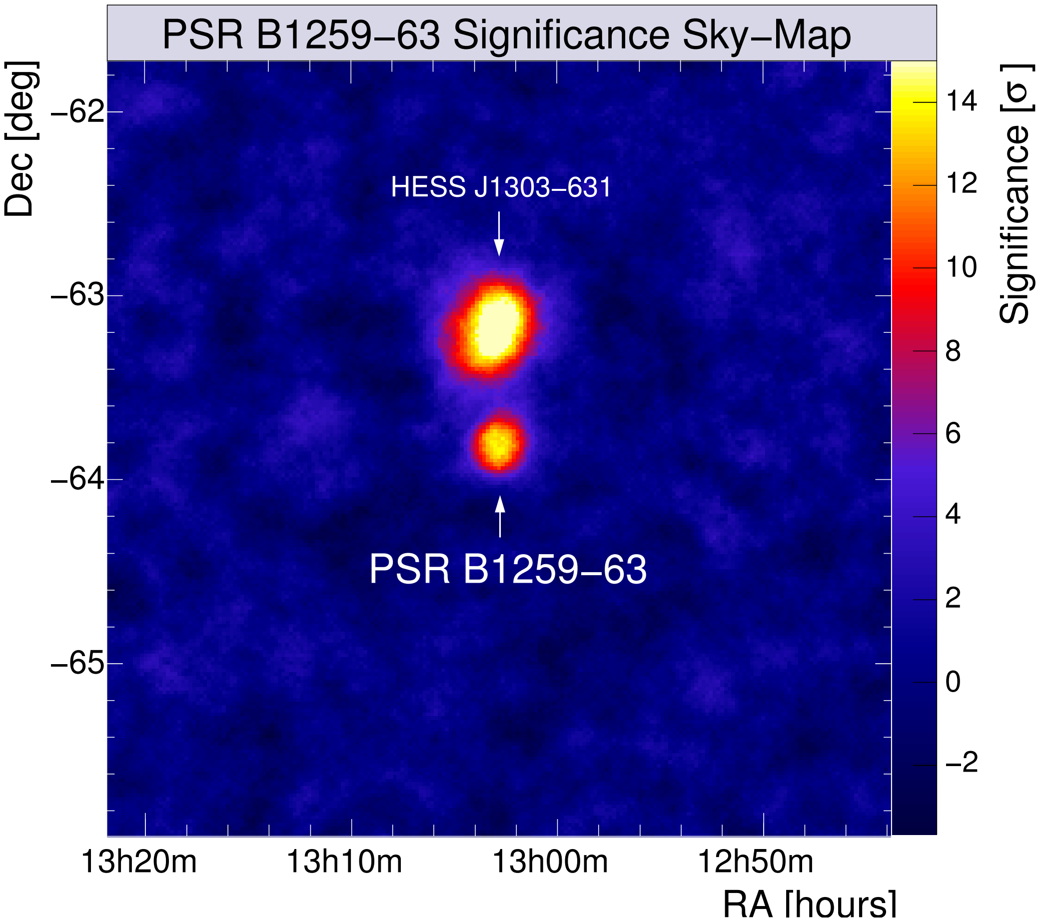

Figure 5.7: *Significance sky-map for the region* 2° × 2° *around the position of PSR B1259−63 for the H.E.S.S. 2004 data set. The excess* ≈ 0.6° *north of the pulsar is the newly discovered unidentified TeV source HESS J1303−631 [H.E.S.S. collaboration, 2005d]. The maximum of the significance scale was fixed near the peak significance of the PSR B1259−63 excess in order to emphasise the pulsar excess. The peak significance of HESS J1303−631 is* ≈ $20\,\sigma$.

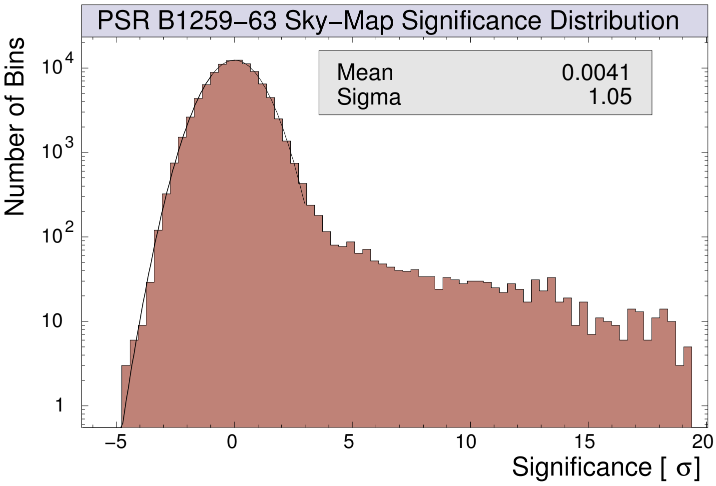

Figure 5.8: *Significance distribution for all bins of the sky-map in Fig. 5.7.*

5.2 Signal Position

In order to derive the exact position of the excess around the nominal position of PSR B1259−63 and to check for possible source extension, the data was reanalysed using hard cuts requiring a higher minimum camera image intensity $\mathrm{Size}_{\mathrm{min}} = 200$ p.e. which improves the angular resolution and reduces the cosmic ray background at the expense of a higher energy threshold of 750 GeV (see Sec. 5.3.1). This approach assumes that the centroid of the γ-ray emission is not energy dependent.

A fit to the two-dimensional count distribution obtained with the ring-background method was used to derive the signal position and size under consideration of the point spread function of the detector.

5.2.1 2D Fitting Technique

The uncorrelated two-dimensional distribution of VHE γ-ray candidate events of the whole data set was fitted within a radius of 0.2° around the nominal position of PSR B1259−63, assuming an intrinsic source intensity profile of a radially symmetric Gaussian

$$I(\theta) \propto e^{-\theta^2/2\sigma_s^2}$$

convolved with the point spread function of the detector. The point spread function for simulated γ-rays (see Sec. 4.4.3) was computed using the different cut on $\mathrm{Size}_{\mathrm{min}}$ and a double Gaussian function (instead of four Gaussians) was found to fit well the distribution in θ^2 (see Fig. 5.9).

The resulting function for the 2D-fit of the sky-map of measured γ-rays is given by:

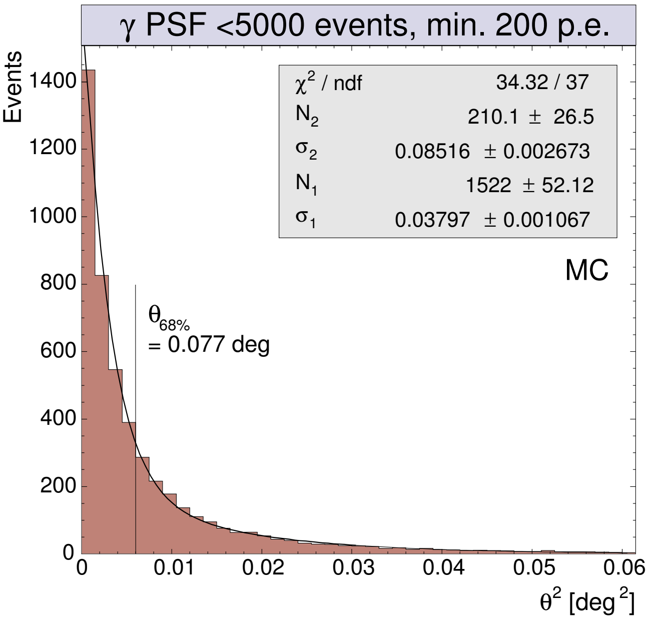

Figure 5.9: *γ-ray point spread function for an image quality cut* $\mathrm{Size}_{\mathrm{min}} = 200$ p.e. *The fit function is a sum of two Gaussians.*

$$N_\gamma(\rho = \mathrm{RA}, \delta = \mathrm{Dec}) = N_0\, e^{-\frac{\Delta\rho'^2+\Delta\delta^2}{2(\sigma_1^2+\sigma_s^2)}} + N_0 \frac{N_2}{N_1} \frac{\sigma_1^2+\sigma_s^2}{\sigma_2^2+\sigma_s^2} \frac{\sigma_2^2}{\sigma_1^2}\, e^{-\frac{\Delta\rho'^2+\Delta\delta^2}{2(\sigma_2^2+\sigma_s^2)}},$$

with

$$\Delta\rho' = \frac{\rho-\rho_0}{\cos\delta},\ \Delta\delta = \delta - \delta_0.$$

ρ_0, δ_0, N_0, and σ_s as free parameters. The scaling for the angular distance in RA results from the spherical character of the coordinate system with non-Cartesian metrics.

5.2.2 Position and Size of the PSR B1259−63 Excess

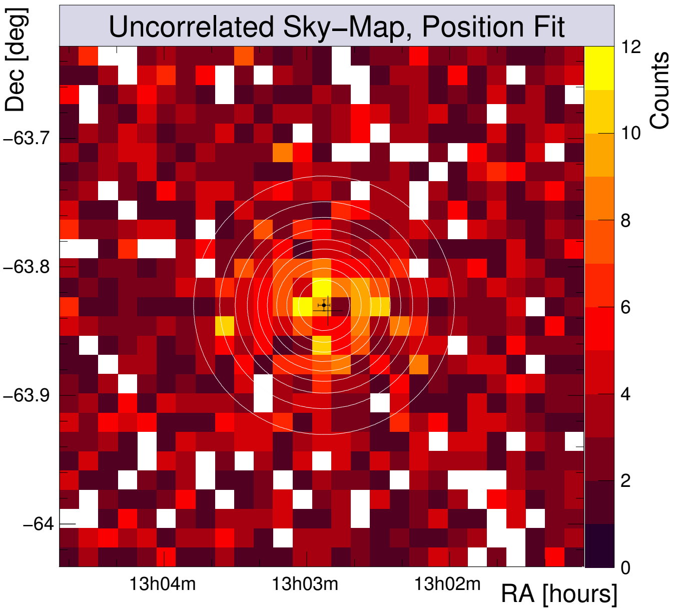

Figure 5.10: *Uncorrelated sky-map of a region 0.2° around the nominal position of PSR B1259−63 (dotted cross). Overlaid are the contours of the position fit (white circles) and the resulting excess position with 1 σ statistical error bars.*

Figure 5.10 shows an uncorrelated sky-map for the region 0.2°×0.2° using a bin size of 0.015°×0.015° around PSR B1259−63 together with contours of the performed likelihood fit. The influence of the decrease of the system acceptance, expected to be less than 5%, was neglected. The resulting position of the γ-ray signal of

$$\begin{aligned} \rho &= 13^{\mathrm{h}}2^{\mathrm{m}}49\overset{\mathrm{s}}{.}3 \pm 2\overset{\mathrm{s}}{.}3_{\mathrm{stat}} \pm 3\overset{\mathrm{s}}{.}0_{\mathrm{sys}} \\ \delta &= -63°49'53'' \pm 17''_{\mathrm{stat}} \pm 20''_{\mathrm{sys}}, \end{aligned}$$

is consistent with the position of PSR B1259−63 ($\Delta\rho = 9'' \pm 15''_{\mathrm{stat}}$, $\Delta\delta = 16'' \pm 17''_{\mathrm{stat}}$) within statistical errors. The fitted position is insensitive to changes in the bin size of the sky map.

A limit for the source extension σ_{s} was found to be $< 33''$ at 95% confidence level and thus, the excess from PSR B1259−63 was found to be consistent with a point source. This agrees with the results from the fit of the one-dimensional excess distribution in θ^2 in Fig. 5.3.

5.3 Energy Spectrum

Key information concerning the acceleration mechanisms at work in the binary system of PSR B1259−63 is contained in the energy spectrum of the detected VHE γ-ray emission. The differential energy spectrum, or differential flux of the source $F(E)$ is defined as the number of particles from the source detected per unit area, time, and energy. Thus, the spectrum can be expressed as:

$$F(E) = \frac{\mathrm{d}N_{\mathrm{source}}}{\mathrm{d}E} = \frac{1}{t_{\mathrm{live}}\,A_{\mathrm{eff}}(E)}\,\frac{\mathrm{d}N_{\gamma}}{\mathrm{d}E}, \tag{5.3}$$

where t_{live} is the live time, N_{γ} is the measured number of excess events, and A_{eff} is the effective collection area of the instrument. The latter quantity cannot be measured and must be determined using simulated γ-rays.

This section first describes the determination of the effective collection area of the detector. Subsequently, the method to reconstruct an energy spectrum is introduced and tested with data from the Crab Nebula, and finally the spectra for the PSR B1259−63 data set are given.

5.3.1 Effective Area and Energy Threshold for γ-Rays

The effective area represents that area, within which the detector could detect a flux of γ-rays assuming a detection efficiency of 100%. This quantity depends on aspects of the shower physics and the detector and cannot be derived analytically but rather must be obtained from simulations. Considering a simulated point source of γ-rays (see Sec. 3.3), the effective area is given by:

$$A_{\mathrm{eff}}(E, \Theta, \phi, \theta_{\mathrm{cam}}) = 2\pi \int_0^\infty P(E, \Theta, \phi, \theta_{\mathrm{cam}}, R)\, R\, dR, \tag{5.4}$$

where R is the distance from the shower core to the centre of the array, and P is the probability of a γ-ray shower to be detected and pass the event selection. P reflects the efficiency of the array to collect the Cherenkov emission of a shower and therefore depends on

- ▹ E, the shower energy, proportional to the intensity of the Cherenkov emission,
- ▹ Θ, the zenith angle, determining the distance between detector and shower maximum,
- ▹ ϕ, the azimuth of the telescope pointing and therefore the orientation of the shower with respect to the Earth's magnetic field,
- ▹ θ_{cam}, the distance from the shower direction to the camera centre (offset), reflecting the variation of the system acceptance.

At a large distance $R = R_0$, the corresponding detection probability becomes negligibly small and only showers with core locations within a circle of this radius R_0 need to be considered.

For a sample of simulated γ-rays, the probability P is simply the ratio of the number of simulated γ-rays to those triggering the detector, and Eq. (5.4) simplifies to:

$$A_{\mathrm{eff}}(\Delta E, \Theta, \phi, \theta_{\mathrm{cam}}) = 2\pi\, \pi R_0^2\, \frac{n(\Delta E, \Theta, \phi, \theta_{\mathrm{cam}})}{N(\Delta E, \Theta, \phi, \theta_{\mathrm{cam}})},$$

representing the effective area for an energy interval ΔE, with N as the total number of simulated γ-rays, and n the number of events remaining after the detector simulation and selection cuts.

Figure 5.11 shows the calculated effective area after selection cuts as a function of the true and reconstructed shower energy (left and right, respectively) for typical parameters regarding the observations of PSR B1259−63. The area steeply rises at low energies towards a turning point and then increases slowly until it reaches its maximum at several TeV and declines towards higher energies. At low energies A_{eff} is limited by the amount of Cherenkov light collected with the detector while at high energies, the Cherenkov images become too large to fit into the camera and are rejected by the cut on the local distance of an image.

The difference between the effective area versus the true and reconstructed energy arises from the bias in the energy reconstruction (c.f. Fig. 4.21). In order to compensate for this bias, for the energy spectrum determination method the effective area was used as a function of the reconstructed energy. Note, that this correction depends on the spectrum of simulated γ-rays (see next section).

Figure 5.12 illustrates the dependence of A_{eff} on the zenith angle (left) and the camera offset (right). For all possible combinations of $\Theta = 0, 30, 40, 45, 50, 55°$, $\phi = 0, 180°$, and $\theta_{\mathrm{cam}} = 0, 0.5, \ldots, 2.5°$, $A_{\mathrm{eff}}(\Delta E)$ was computed and fitted with an analytical function in order to reduce uncertainties resulting from the finite binning and statistical fluctuations.

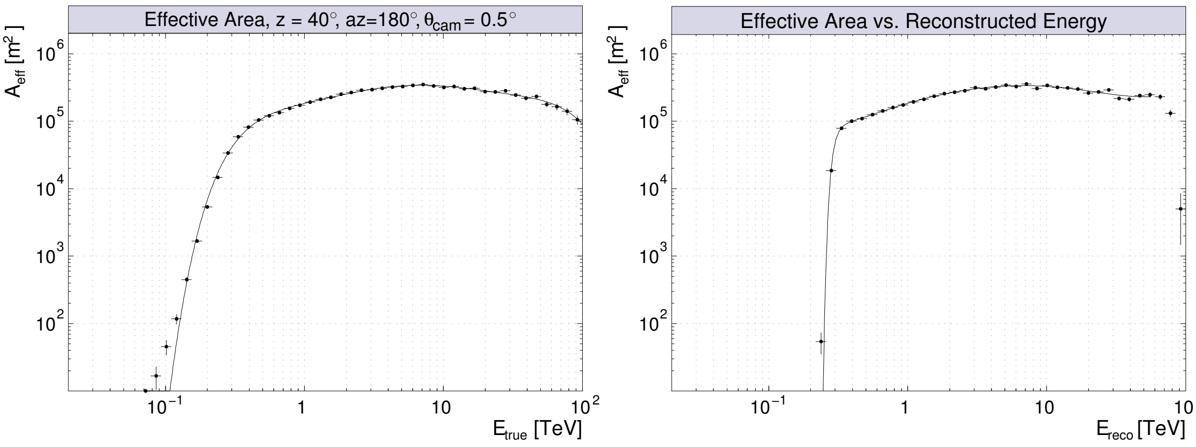

Figure 5.11: *Effective areas $A_{\rm eff}$ for simulated γ-rays for Θ = 40°, Θ = 180°, and $\theta_{\rm cam}$ = 0.5° (points) and the corresponding fitted function (solid line).* **L**eft: *Effective area as a function of simulated (true) energy.* **R**ight: *Effective area as a function of reconstructed shower energy.*

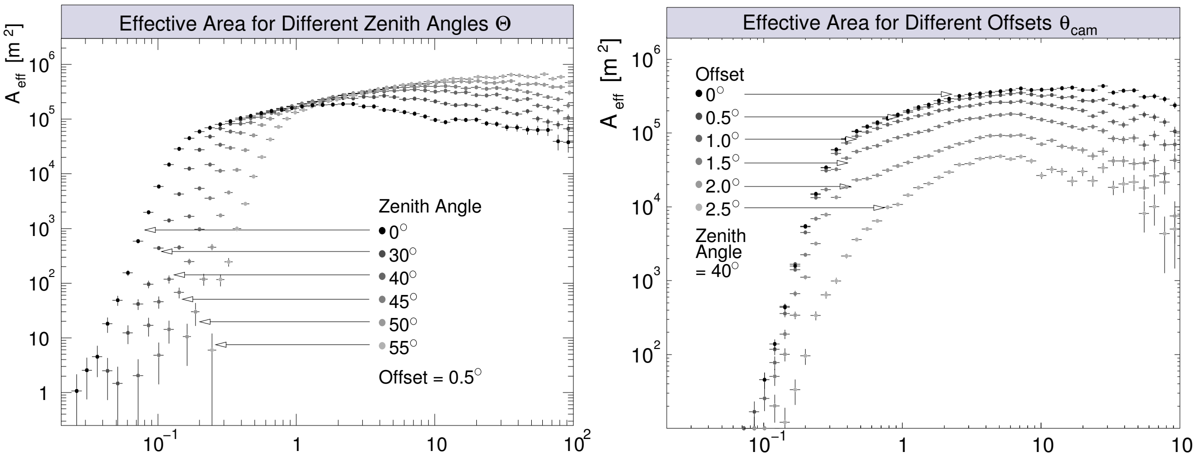

Figure 5.12: *Effective areas $A_{\rm eff}$ for simulated γ-rays for different zenith angles and offsets as a function of the true energy.* **L**eft: *$A_{\rm eff}$ for a range of zenith angle values. With increasing zenith angle, the energy threshold rises, and the collection area increases for energies above the threshold.* **R**ight: *$A_{\rm eff}$ for several camera offsets. While the area does not change significantly for offsets < 1°, the collection efficiency drops dramatically towards the camera edge.*

In order to assign an effective area to a single event, $A_{\text{eff}}(E, \Theta, \phi, \theta_{\text{cam}})$ is derived by evaluating the fit function and interpolating linearly in $\cos\Theta$ and θ_{cam}. Since the dependence on the azimuth angle ϕ is rather weak and most of the observation time of PSR B1259−63 and the Crab Nebula was spent close to their culmination, the azimuth corresponding to that of the target culmination was used.

The energy threshold E_{th} is defined as the maximum of the expected differential rate of excess events

$$\frac{\mathrm{d}R}{\mathrm{d}E} = A_{\text{eff}} \frac{\mathrm{d}N_\gamma}{\mathrm{d}E}$$

with $\mathrm{d}N_\gamma/\mathrm{d}E \propto E^{-2.62}$, as measured for the Crab Nebula by the HEGRA collaboration [2004]. Figure 5.13 shows this differential rate for the effective area curve for the mean zenith angle and camera offset of the observations of PSR B1259−63. The resulting threshold of $E_{\text{th}}^{1259} \approx 380\,\text{GeV}$ represents the mean threshold energy for this data set.

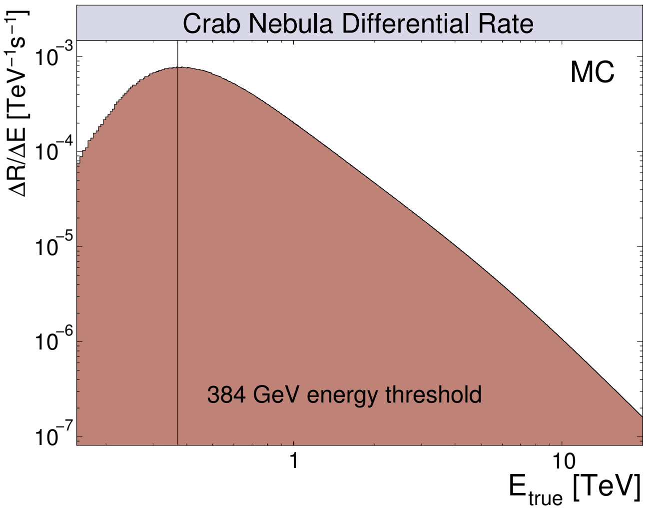

Figure 5.13: *Expected differential rate of γ-rays for a Crab-like spectrum using the effective area curve appropriate for PSR B1259−63 observations.*

5.3.2 Energy Spectrum Determination

Using Eq. (5.4), a source spectrum can be derived from the number of excess events N_γ and the effective area A_{eff} in an energy interval $\mathrm{d}E$. Since the energy of the excess events is not a directly measured quantity in the sense that the sample of events from the signal region also contains background events, the flux of the on and off events must be calculated separately and the difference yields the flux of signal events.

The considered energy range was divided into finite energy bins ΔE, and for each observation run an energy threshold E_{safe} was determined, defined as the lowest energy, for which the energy bias

$$\frac{|E_{\text{true}} - E_{\text{reco}}|}{E_{\text{true}}}(\langle\Theta\rangle, \langle\theta_{\text{cam}}\rangle),$$

dependent on the mean zenith angle and offset of the run, is below 10%. E_{safe} is typically 15–30% higher than the energy threshold E_{th}.

The flux for each energy bin was determined by using the on and off events obtained with the 7-background model. For each energy bin ΔE, the flux is given by

$$F(\Delta E) = \frac{1}{t_{\text{live}}(\Delta E)} \left\{ \sum_{i=1\ldots N_{\text{on}}}^{E_i \in \Delta E} \frac{1}{A_i} - \alpha(\Delta E) \sum_{j=1\ldots N_{\text{off}}}^{E_j \in \Delta E} \frac{1}{A_j} \right\}, \tag{5.5}$$

with

$$A = A_{\text{eff}}(E, \Theta, \theta_{\text{cam}})$$

as the effective area for the particular event. Only events for which ΔE lies above E_{safe} for the particular run were considered and thus the normalisation α and live time t_{live} can be different for a given energy bin.

In order to obtain an appropriate bin coverage within the energy range, the initial finely binned distribution was re-binned according to the signal strength. For each bin, a spectral point $(E, F(E))_{\Delta E}$ was assigned, with E as the mean energy of the energy distribution within the bin and $F(E) = F(\Delta E)/\Delta E$. All points in the spectrum were required to have a maximum relative error $\Delta F/F = 1$, and a flux above zero.

The resulting energy spectrum was fitted with a power law

$$F(E) = \mathrm{d}N/\mathrm{d}E = F_0 \left(\frac{E}{1\,\mathrm{TeV}} \right)^{-\Gamma} . \tag{5.6}$$

Since the reconstructed spectrum depends on the spectral index of the simulated γ-rays used for the determination of the effective area, A_{eff} was recalculated using the same sample of simulated γ-rays, but weighting the distribution in energy such that it resembles a power law with an index matching Γ obtained from the fit to the spectrum above. Subsequently, the spectrum was redetermined with the modified effective area A'_{eff} in a second iteration. A third iteration always yielded a result which did not change noticeably compared to the second iteration.

Validation with Data from the Crab Nebula

The method for the determination of the energy spectrum was validated with data from the Crab Nebula, since its spectrum has been measured by nearly all 1st generation IACT instruments [e.g. in Hillas et al., 1998, HEGRA collaboration, 2004] and thus the results can be compared with these measurements.

The observations of the Crab Nebula were performed in late 2003 with wobble offsets of $\pm 0.5°$ and $\pm 1°$ Dec and yielded a data set of roughly 4 hours live time after quality selection cuts (for a list of runs see Appendix B). The energy threshold of the observations is similar to that of the PSR B1259−63 data at $\approx 400\,\mathrm{GeV}$.

Although the γ-ray selection cuts were optimised for faint sources of 0.1 Crab, the cuts were not changed for the spectral analysis of the Crab data in order to test the validity of the analysis. The reconstructed spectrum should not depend on the event selection used. Figure 5.14 shows the differential energy spectrum for the Crab Nebula data set. The spectrum is well fit ($\chi^2/\mathrm{ndf} = 16.3/18$) by a power law with a photon index $\Gamma = 2.63 \pm 0.05_{\text{stat}}$ and normalisation $F_0 = (3.25 \pm 0.13_{\text{stat}}) \times 10^{-11} \mathrm{cm}^{-2} \mathrm{s}^{-1} \mathrm{TeV}^{-1}$. This result is in reasonable agreement with the results obtained by:

- Hillas et al. [1998]
  $\Gamma = 2.49 \pm 0.06_{\text{stat}} \pm 0.04_{\text{sys}}$,
  $F_0 = (3.20 \pm 0.17_{\text{stat}} \pm 0.60_{\text{sys}}) \times 10^{-12}\,\mathrm{cm}^{-2}\,\mathrm{s}^{-1}\,\mathrm{TeV}^{-1}$,
- HEGRA collaboration [2004]
  $\Gamma = 2.62 \pm 0.02_{\text{stat}} \pm 0.05_{\text{sys}}$,
  $F_0 = (2.83 \pm 0.17_{\text{stat}} \pm 0.60_{\text{sys}}) \times 10^{-11}\,\mathrm{cm}^{-2}\,\mathrm{s}^{-1}\,\mathrm{TeV}^{-1}$.

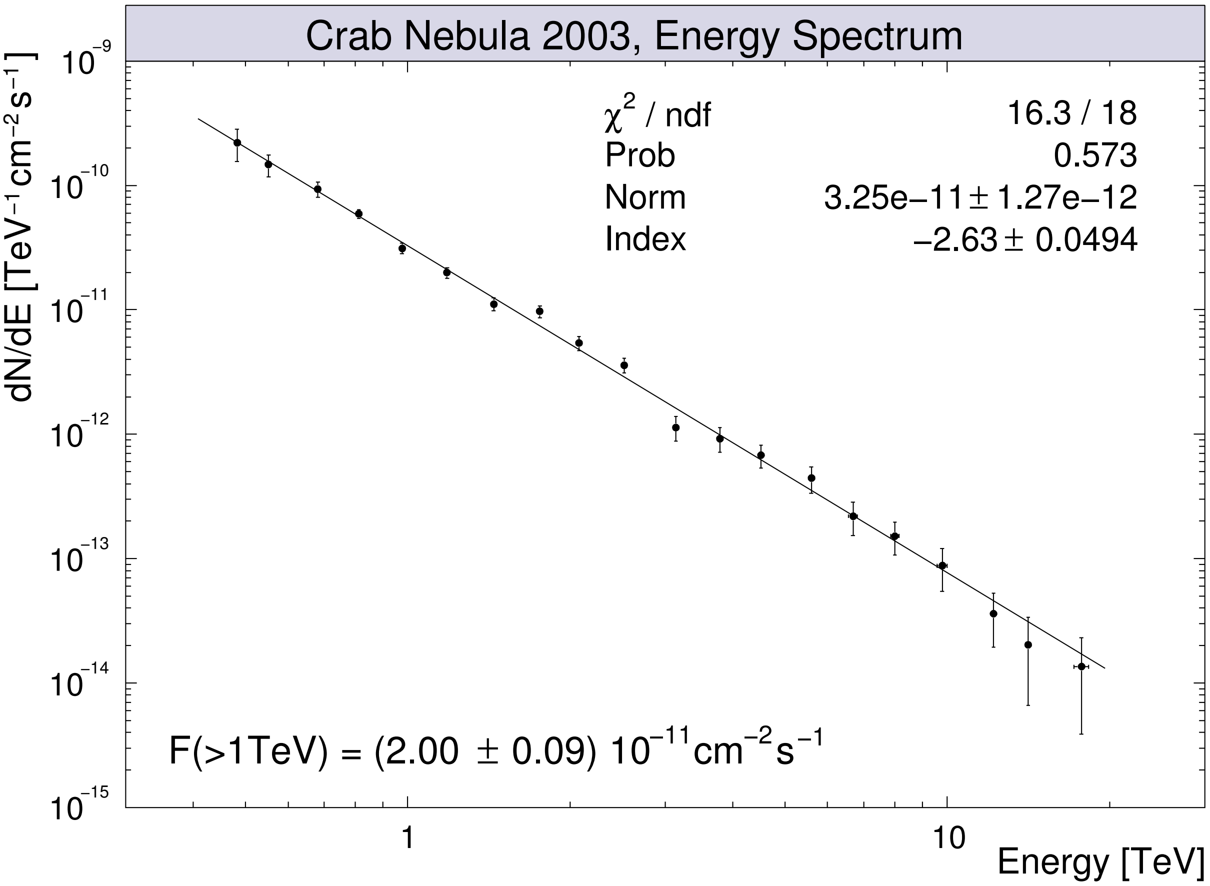

Figure 5.14: *Differential energy spectrum* $\mathrm{d}N/\mathrm{d}E$ *of* γ*-rays from the Crab Nebula using H.E.S.S. 2003 data. The solid line shows the power-law fit to the spectrum.*

5.3.3 Energy Spectra of PSR B1259−63 / SS 2883

The measured differential energy spectrum derived from all darkness periods with a significant detection of a γ-ray signal from PSR B1259−63 / SS 2883 (February to May) is shown in Fig. 5.15. The power-law fit of this time-averaged spectrum yields a photon index $\Gamma = 2.7 \pm 0.2_{\mathrm{stat}}$ and $F_0 = (1.3 \pm 0.1_{\mathrm{stat}}) \times 10^{-12}\,\mathrm{cm}^{-2}\,\mathrm{s}^{-1}\,\mathrm{TeV}^{-1}$.

The integral flux above the mean threshold energy was determined by integrating the fitted power law resulting in $F(E > 380\,\mathrm{GeV}) = (4.0 \pm 0.4_{\mathrm{stat}}) \times 10^{-12}\,\mathrm{cm}^{-2}\,\mathrm{s}^{-1}$, equivalent to 4.1% of the Crab Nebula γ-ray flux above this threshold as derived above.

For each darkness period for which the significance of the observed γ-ray excess exceeded $6\,\sigma$ (February, March, and April), a differential spectrum was derived (see Fig. 5.16) and the results of the corresponding power law fit according to Eq. (5.6) are listed in Table 5.2. Within statistical errors, there is no indication of time variability of the photon index. However, the changing flux normalisation F_0 indicates flux variability of the source which will be further quantified and discussed in Sec. 5.4.

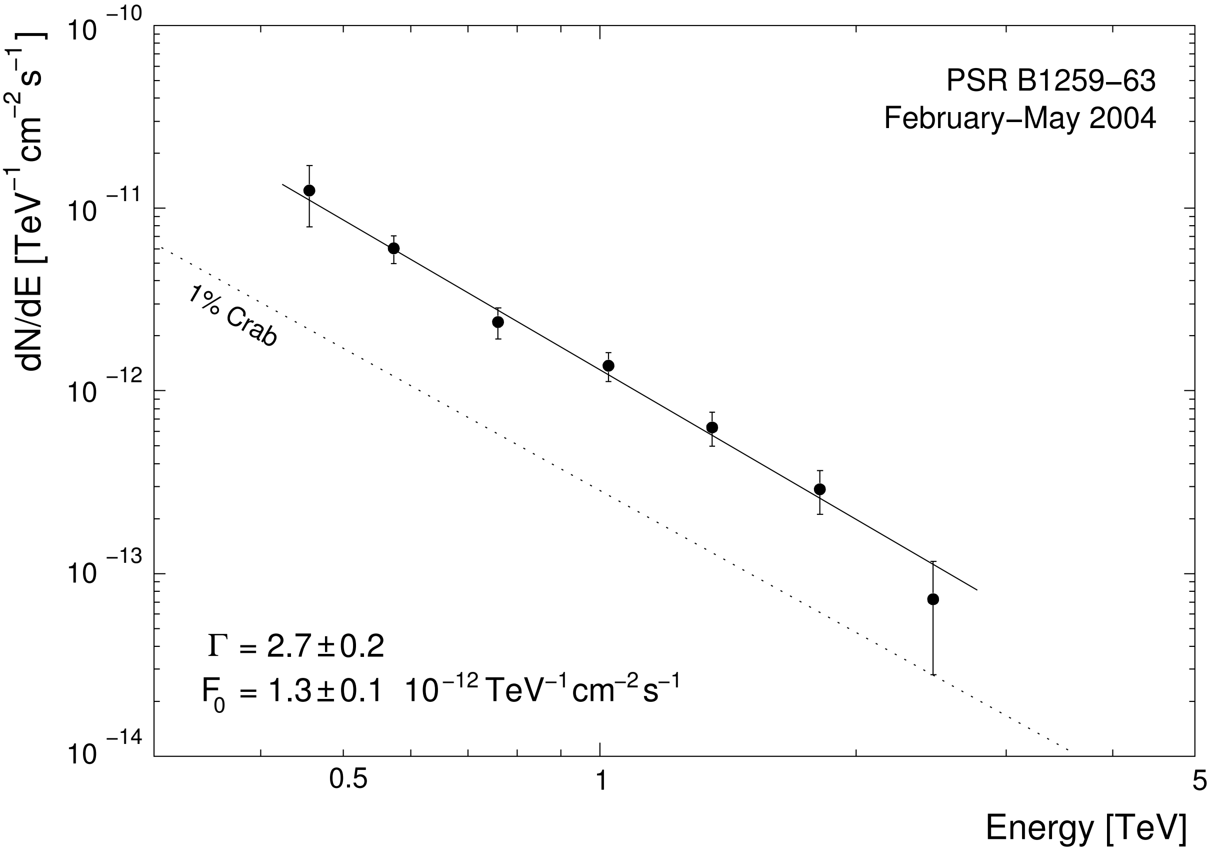

Figure 5.15: *Differential energy spectrum* $\mathrm{d}N/\mathrm{d}E$ *of* γ*-rays from PSR B1259−63 using H.E.S.S. 2004 data from the periods with significant detection of the* γ*-ray signal (February–May). The solid line shows a power-law fit to the spectrum (see also Table 5.2).*

Darkness Period 2004	Γ	F_0 [TeV^{-1} cm^{-2} s^{-1}]	χ^2/ndf	P_{χ^2}	E_{th} GeV
February	2.8 ± 0.3	$2.1 \pm 0.3 \times 10^{-12}$	1.8/4	0.77	370
March	3.0 ± 0.6	$1.0 \pm 0.2 \times 10^{-12}$	1.8/4	0.77	420
April	2.8 ± 0.4	$2.0 \pm 0.3 \times 10^{-12}$	0.4/3	0.93	350
Overall*	2.7 ± 0.2	$1.3 \pm 0.1 \times 10^{-12}$	2.3/5	0.81	380

* includes all data from February to May 2004

Table 5.2: *Parameters of the power law fit to the differential spectrum for the different darkness periods of H.E.S.S. observations on PSR B1259−63. For the periods May and June 2004, no spectrum could be derived due to insufficient statistics. Shown are the photon index* Γ *and the flux normalisation* F_0 *(with statistical error only), the* χ^2 *per number of degrees of freedom* χ^2/ndf *and the* χ^2 *probability* P_{χ^2} *for the power law fit of the spectrum, and the corresponding mean threshold energy* E_{th}.

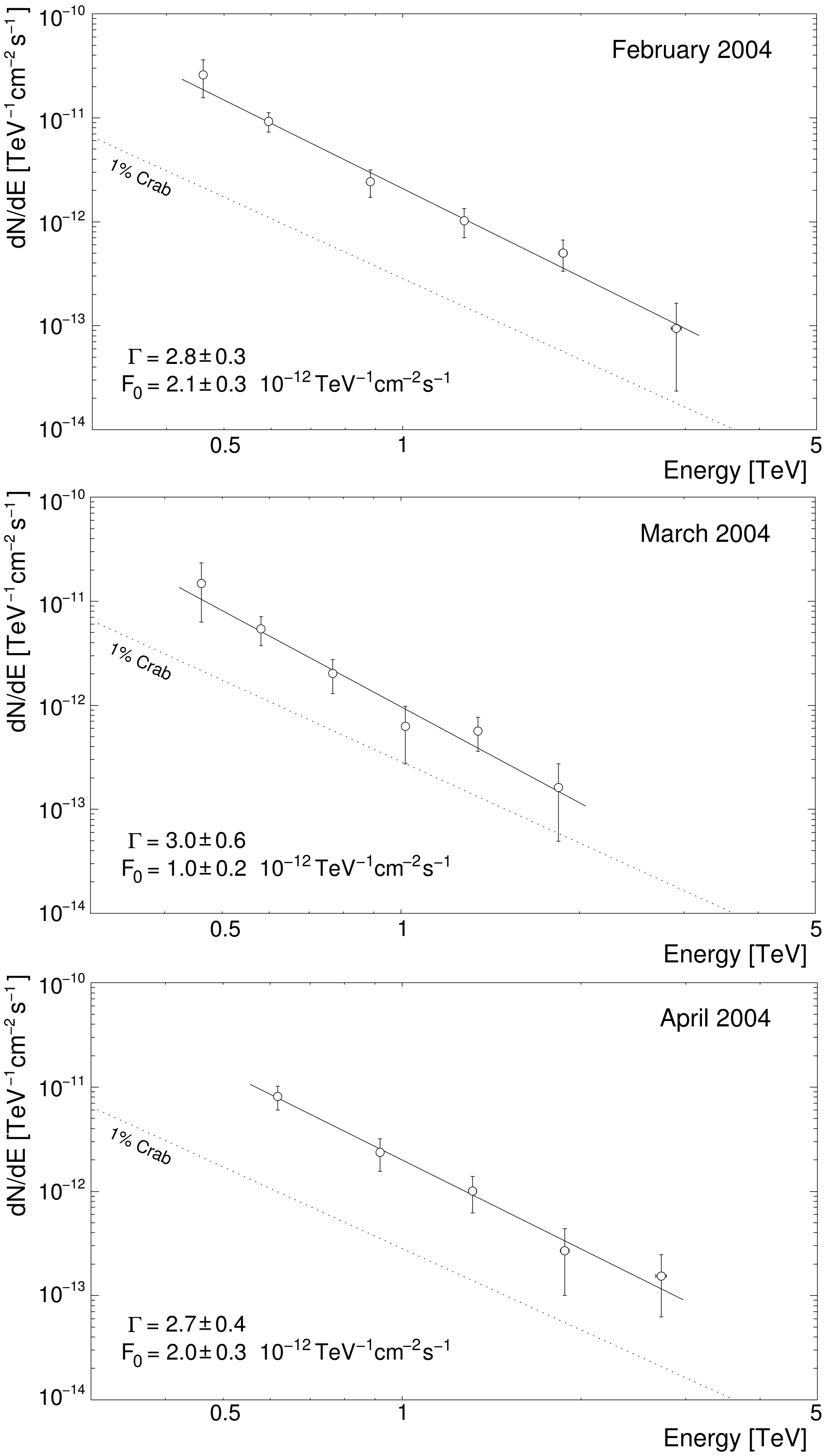

Figure 5.16: *Differential energy spectra of γ-rays from PSR B1259−63 for data of the periods February, March, and April. The solid line in each plot indicates the power-law fit to the particular spectrum for which the results are listed in Table 5.2.*

5.3.4 Systematic Errors of the Spectrum

Several components of the data analysis introduce systematic uncertainties in the reconstructed energy spectrum. In the following, the main uncertainties are discussed and the individual contributions to the measured flux normalisation F_0 and photon index Γ were estimated and summarised in Table 5.3. The individual contributions were added quadratically under the assumption that they are independent, yielding the total systematic uncertainty of $\Delta\Gamma_{\text{sys}} = \pm 0.22$ and $\Delta F/F|_{\text{sys}} = 28\%$.

Systematic Effect	$\Delta\Gamma_{\text{sys}}$	$\Delta F/F|_{\text{sys}}$ [%]
Pixel intensities after calibration	–*	±10
Reduction in image size due to unusable pixels	–*	+6
Atmosphere model for shower simulation	±0.1	±20
Flux variation of background events	–*	±12
Binning of the spectrum	±0.2	±11
Total	±0.22	±28

* effect not considered

Table 5.3: *Estimated systematic uncertainties on the photon index* Γ *and normalisation* F_0 *of the reconstructed energy spectrum.*

Pixel Intensity Calibration – Muon Efficiencies

The uncertainty on the pixel intensity calibration was tested with the measured muon efficiencies ϵ_μ (see Sec. 4.2.3). Their evolution in time was shown in Fig. 4.6 and the difference between the individual telescopes was found to be $< 10\%$ (see Table 4.1). This efficiency is directly proportional to the image amplitude. This difference was considered by a rather conservative contribution for the measured flux of $\Delta F/F|_\mu \approx \pm 10\%$.

Influence of Unusable Pixels

Unusable pixels (see Sec. 4.2.2) do not contribute anymore to any Cherenkov image and therefore reduce the mean image amplitude. In Schwanke et al. [2004] it was shown how the number of unusable pixels in a camera translates into a difference in image Size. Therein it was calculated, which fraction of simulated γ-ray images is affected by unusable pixels $A = \Delta N_{\text{bad}}/N_{\text{bad}}$ and how much of the image amplitude is lost for these images $B = \Delta\text{Size}_{\text{bad}}/\text{Size}_{\text{bad}}$ assuming different distributions of unusable pixels within the camera. Since this effect, especially its dependence on energy, was not studied in detail, it was taken as a systematic uncertainty instead of applying a correction to the Size of each image.

Using the mean number of unusable pixels for the PSR B1259−63 dataset $\Delta N_{\text{bp}}/N_{\text{bp}} \approx 8\%$ from Table 4.1, this corresponds to a mean reduction $\Delta\text{Size}/\text{Size} = A \times B \approx 0.4 \times 0.15$ and therefore $\Delta F/F|_{\text{bp}} \approx +6\%$.

Atmospheric Transmission Model

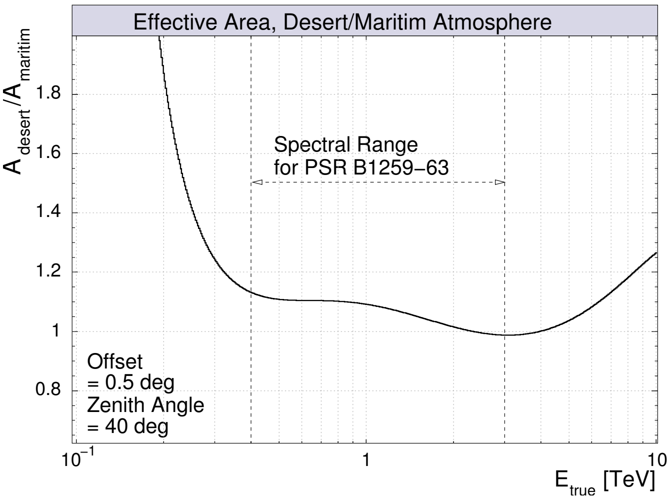

Figure 5.17: *Ratio of the effective areas calculated for simulated γ-rays using the desert and maritime atmosphere model. The dashed lines represent the energy range relevant for the PSR B1259−63 spectra.*

As already stated in Sec. 3.3 (see Fig. 3.13), the measured H.E.S.S. system trigger rate lies somewhere between the predictions made by simulations using two different atmosphere models. Figure 5.17 shows the ratio of the effective area calculated using the two models. The deviations are significant at the edges of the considered energy range, below the energy threshold and at $E > 5$ TeV. However, the PSR B1259−63 spectra cover only a limited range wherein the deviation is below 15% for the relevant zenith angle and offset. Since the effect is dependent on energy, the resulting uncertainty on F_0 and Γ cannot be easily calculated. Therefore, the deviations were determined directly by comparing the time-averaged spectrum of PSR B1259−63 for the two different atmosphere models, resulting in $\Delta F/F \approx 20\%$ and $\Delta\Gamma \approx 0.1$. These differences were considered as a symmetric systematic error $\Delta F/F|_{\mathrm{atmo}} = \pm 20\%$ and $\Delta\Gamma_{\mathrm{atmo}} = \pm 0.1$.

Variation of the Background Flux

Since all background events should originate from cosmic ray air showers, the measured flux of these events represents a probe of time-dependent variations of the collection efficiency for γ-ray events. In order to estimate the evolution of the flux of background events after all selection cuts, this quantity was calculated for each observation run according to the method described in Sec. 5.4.2. Figure 5.18 (left) shows the resulting "background light curve". The applied fit indicates a variable flux considering the statistical errors only. In Figure 5.18 (right) the distribution of the flux is plotted and it was found that it can be approximately described by a Gaussian. The relative variation $\sigma_{F,\mathrm{bg}}/\langle F_{\mathrm{bg}}\rangle = 0.12$, obtained from this fit, was used as an estimate for the systematic variation of the γ-ray flux, $\Delta F/F|_{\mathrm{bg}} = \pm 12\%$.

Background Estimation Method

The PSR B1259−63 and Crab Nebula spectra resulting from the alternative ring-background model were compared with the spectra of the default 7-background model. The differences in the spectral index and flux normalisation are $\Delta F_0/F_0 = 0.02 \pm 0.17$ and $\Delta\Gamma = 0.05 \pm 0.29$, respectively, and are small compared to the statistical error of both quantities. Given this minor differences and the fact that the two methods use different background events, the effect was considered to be negligible and no contribution to the systematic error was added.

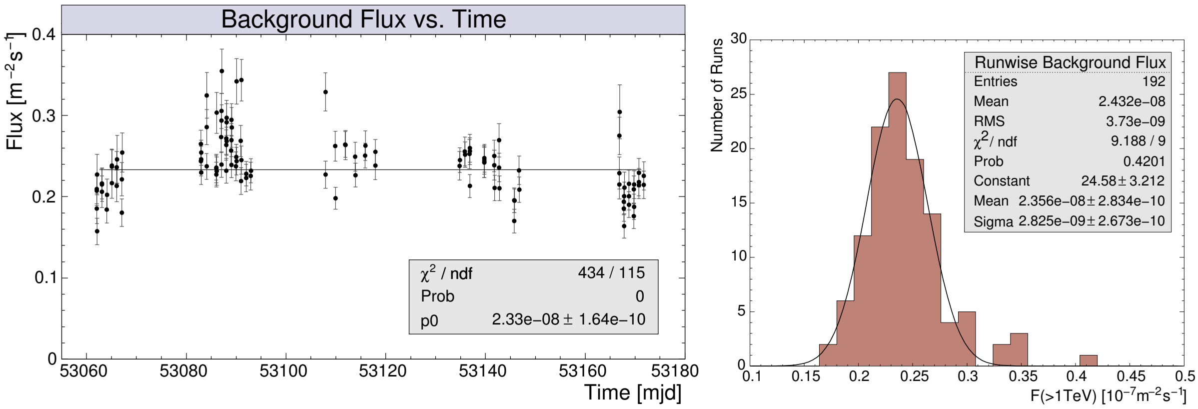

Figure 5.18: *Run-wise flux of background events within the PSR B1259−63 dataset after γ-ray selection cuts.* **L**eft: *Flux of background events for each observation run as a function of observation date. The solid line represents a fit to a constant flux.* **R**ight: *Corresponding distribution of the run-wise background flux fitted by a Gaussian (solid line).*

Binning of the Spectrum Points

The reconstructed spectrum and the power law fit depend on the binning of the considered energy range. In order to study this effect, the bin positions and widths were varied, and the time-averaged spectra for PSR B1259−63 and the Crab Nebula recalculated and fitted with a power law. The maximum resulting deviations were found to be $\Delta F/F|_{\mathrm{Crab}} = \pm 11\%$, $\Delta\Gamma|_{\mathrm{Crab}} = \pm 0.08$, and $\Delta F/F|_{1259} = \pm 5\%$, $\Delta\Gamma|_{1259} = \pm 0.2$, for the Crab Nebula and PSR B1259−63, respectively. A conservative estimate of the systematic error introduced by binning is therefore $\Delta F/F|_{\mathrm{bins}} = \pm 11\%$ and $\Delta\Gamma_{\mathrm{bins}} = \pm 0.2$.

5.4 Flux Variability – Light Curve

The observed differences in the flux of the individual darkness periods indicate variability in the γ-ray emission from PSR B1259−63. Although this variability is not unexpected, it would be the first time that a galactic object was observed to have a variable VHE γ-ray emission. Therefore, the signal was checked to be consistent with non-constant emission, and two alternative methods for deriving the evolution of the measured flux in time (light curve) were considered. These methods were again tested with data from the Crab Nebula which is known to have a VHE γ-ray flux constant on the 6% level [HEGRA collaboration, 2004].

5.4.1 Signal Stability

The evolution of a γ-ray signal can be quantified at the level of on and off counts by plotting the cumulative excess and its significance as a function of the accumulated exposure. For a stable source of γ-rays, the excess N_γ is expected to be directly proportional to the accumulated live time t_{live}. However, for a given observation run, N_γ strongly depends on the zenith angle and atmospheric absorption effects. In order to weaken this dependence, the excess can be plotted as a function of the accumulated background counts. Figure 5.19 shows the cumulated excess for data from the Crab Nebula (left) and PSR B1259−63 (right) together with a straight line fit to the data points. Figure 5.20 similarly compares the cumulative significance, which is expected to follow $S \propto \sqrt{t_{\mathrm{live}}}$ for constant emission. It is clear that the Crab excess is compatible with a stable signal whereas PSR B1259−63 data shows an unstable excess.

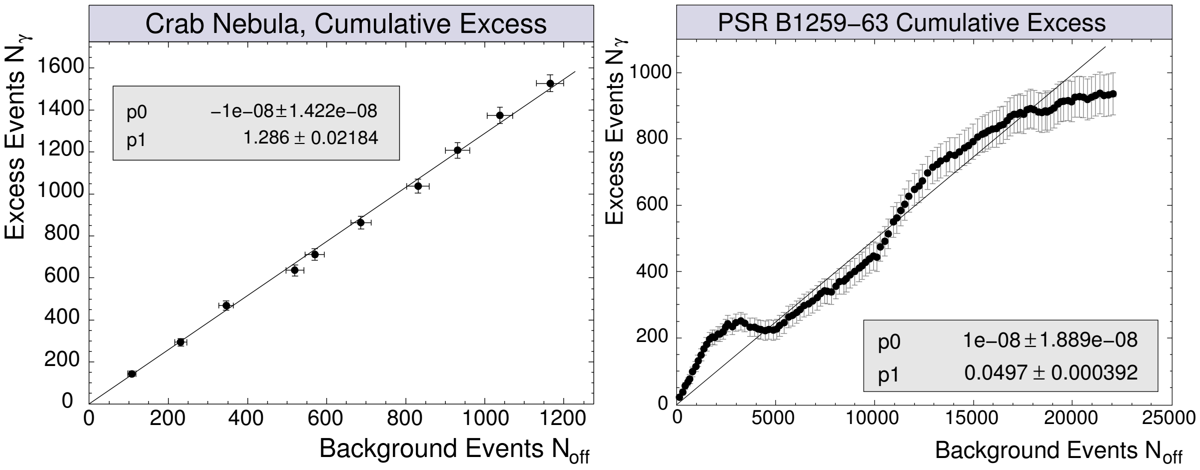

Figure 5.19: *Accumulated excess events as a function of cumulative off events for the Crab Nebula (left) and PSR B1259−63 (right) data set. The solid lines represent a fit* $N_\gamma \propto N_{\mathrm{off}}$*. A point is plotted for every observation run accumulated.*

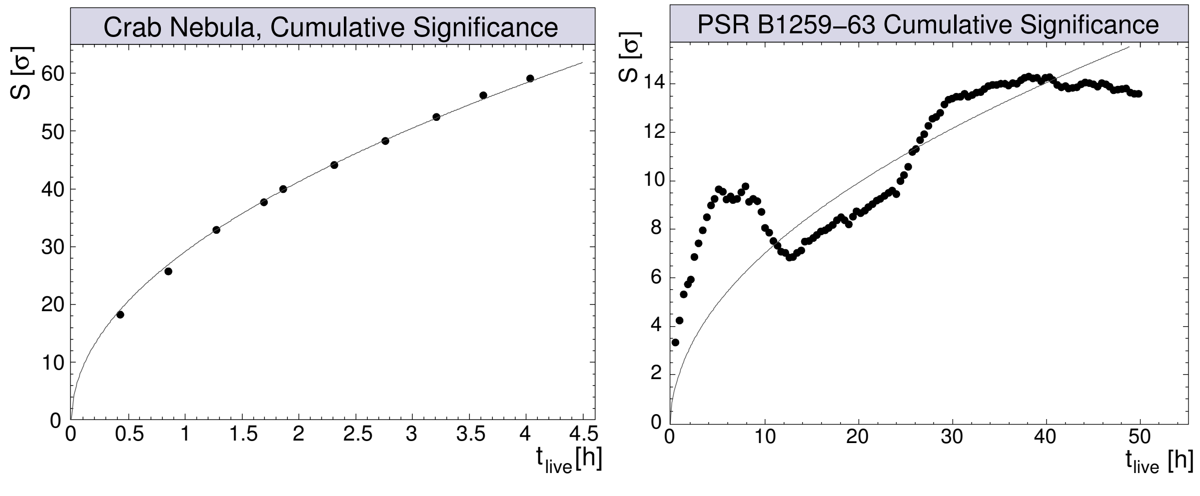

Figure 5.20: *Accumulated significance of excess events as a function of the exposure time for the Crab Nebula (left) and PSR B1259−63 (right) data set. The solid lines show a fit* $S \propto \sqrt{t_{\mathrm{live}}}$.

5.4.2 Light Curve Flux Determination

The measured rate of excess events depends on the zenith angle and camera offset of a particular exposure time. In order to derive a flux light curve, the excess rate has to be translated into an integrated flux of γ-rays above a certain γ-ray energy E_0. However, due to the limited statistics of the PSR B1259−63 signal, an energy spectrum cannot be derived for time intervals shorter than weeks. To derive a day by day flux estimate, an alternative method must be applied.

The first method considered (A) is similar to the spectrum determination technique. In Eq. (5.5), the flux for a particular energy bin ΔE was derived by summing over the inverse effective area of all on and off events. For the light curve, all events with a reconstructed energy above E_0 were used to calculate the flux:

$$F_{\mathrm{A}}(>E_0) = \frac{1}{t_{\mathrm{live}}}\left\{\sum_{i,\mathrm{on}} \frac{1}{A_{\mathrm{eff}}(E_i, \Theta_i, \theta_{\mathrm{cam},i})} - \alpha \sum_{j,\mathrm{off}} \frac{1}{A_{\mathrm{eff}}(E_j, \Theta_j, \theta_{\mathrm{cam},j})}\right\},$$

with $E_j, E_i > E_0$, i.e. considering $\Delta E = [E_0 \ldots \infty[$. The disadvantage of the method is that only a certain fraction of the total available event statistics is used depending on the choice of E_0, resulting in an increase in the statistical error on the flux. E_0 cannot be chosen arbitrarily, since it should not be significantly lower than the highest energy threshold E_{th} of all time intervals considered for the light curve, in order to avoid systematic effects resulting from the energy bias at low energies.

The second method (B) uses the measured excess N_γ to calculate the normalisation F_0 assuming a power law spectrum with a fixed photon index Γ. Starting with the differential rate of γ-rays according to Eq. (5.3)

$$\frac{\mathrm{d}R_\gamma(E, \Theta, \theta_{\mathrm{cam}})}{\mathrm{d}E} = A_{\mathrm{eff}}(E, \Theta, \theta_{\mathrm{cam}})\,\frac{\mathrm{d}N}{\mathrm{d}E},$$

with E as the true shower energy, and integrating over the energy yields

$$R_\gamma(\Theta, \theta_{\mathrm{cam}}) = \frac{N_\gamma}{t_{\mathrm{live}}}(\Theta, \theta_{\mathrm{cam}}) = \int \mathrm{d}E\; A_{\mathrm{eff}}(E, \Theta, \theta_{\mathrm{cam}})\,\frac{\mathrm{d}N}{\mathrm{d}E},$$

The live time was used to absorb the dependence on the zenith angle and camera offset $t_{\mathrm{live}} = t_{\mathrm{live}}(\Theta, \theta_{\mathrm{cam}})$, represented by distributions of the zenith angle and offset for the considered exposure. Integrating over these distributions and using a power law for the assumed source spectrum results in

$$N_\gamma = F_0 \int\!\!\int \mathrm{d}\Theta\, \mathrm{d}\theta_{\mathrm{cam}}\; t_{\mathrm{live}}(\Theta, \theta_{\mathrm{cam}}) \int \mathrm{d}E\, A_{\mathrm{eff}}(E, \Theta, \theta_{\mathrm{cam}}) \left(\frac{E}{1\,\mathrm{TeV}}\right)^{-\Gamma}. \tag{5.7}$$

Thus, the flux normalisation can be calculated with measured or known quantities, under the assumption of a constant photon index. The flux above the chosen threshold energy E_0 is then calculated by integrating the power law spectrum

$$F_{\mathrm{B}}(>E_0) = \int_{E_0}^{\infty} \mathrm{d}E\; F_0 \left(\frac{E}{1\,\mathrm{TeV}}\right)^{-\Gamma} = -\frac{F_0 E_0}{1-\Gamma}\left(\frac{E_0}{1\,\mathrm{TeV}}\right)^{1-\Gamma}.$$

This method takes advantage of the full event statistics and does not depend on the energy reconstruction. However, it is limited by the assumption of the spectral shape.

Both methods have been tested on the Crab Nebula data set and the resulting light curves are shown in Fig. 5.21, using the duration of each observation run as the integration time for each data point. The error on each flux point includes a conservative systematic error, estimated from the flux of background events, as described in Sec. 5.3.4, since all other contributions have an effect on the overall flux level but do not result in systematic variations within the time range of the light curve. The acceptable fits to a constant flux for both methods confirm the expectation of the Crab being a stable source of γ-rays within the (rather short) time range of the H.E.S.S. exposure in 2003. However, when comparing the flux obtained from both methods, a systematic difference of 10% was found between the results of the two methods.

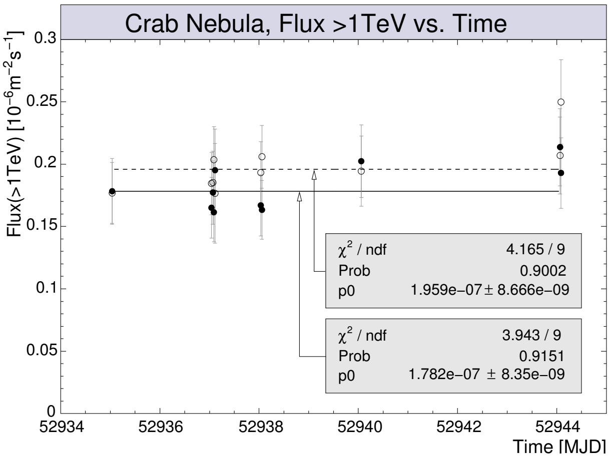

Figure 5.21: *Run-wise light curve of the Crab Nebula data from October 2003. The full (open) circles show the result from the flux calculation with method B (A) and the solid (dashed) line represent a fit to a constant flux.*

5.4.3 Light Curve of PSR B1259−63

The statistical significance for single observation runs of the PSR B1259−63 data set lies between −1 and 5 σ, with a mean value around 1.5 σ. Thus, a timescale of one day was chosen as integration time interval for the light curve in order to increase the statistical significance of each flux point and still provide a relatively short integration time since all runs within a particular night were taken within < 2 hours. Furthermore, method (B) is favoured over method (A) because of the smaller statistical error on the derived flux given the rather weak signal.

Figure 5.22 shows the light curve for the complete PSR B1259−63 data set, calculated according to method (B) using $E_0 = E_{\mathrm{th}} = 380\,\mathrm{GeV}$ and $\Gamma = 2.7$ as derived from the time-averaged spectrum. A systematic uncertainty of 12% was added to the error of each flux point (see below). The light curve clearly indicates a variable flux. This can be quantified by a fit of a constant flux to the data yielding a χ^2 of 90.9 per 35 degrees of freedom corresponding to a χ^2 probability of 1.2×10^{-7}.

The systematic error on the flux level F_{lc} of the whole light curve is composed of the systematic uncertainty on the integral flux $\Delta F(> E_0)_{\mathrm{sys}}$ (derived using the error on the flux normalisation and the photon index, see Sec. 5.3.4) and the difference between the flux obtained with the methods (A) and (B) above, yielding $\Delta F_{\mathrm{lc}}/F_{\mathrm{lc}}|_{\mathrm{sys}} \approx 25\%$.

Flux Trend for Individual Darkness Periods

In order to investigate the flux trend in each darkness period, the individual light curves were fitted separately by a straight line and the significance for an increasing or decreasing flux is listed in Table 5.4. The indication for a local flux minimum between February and middle of March is followed by a distinct rise, reaching its maximum probably between the March and

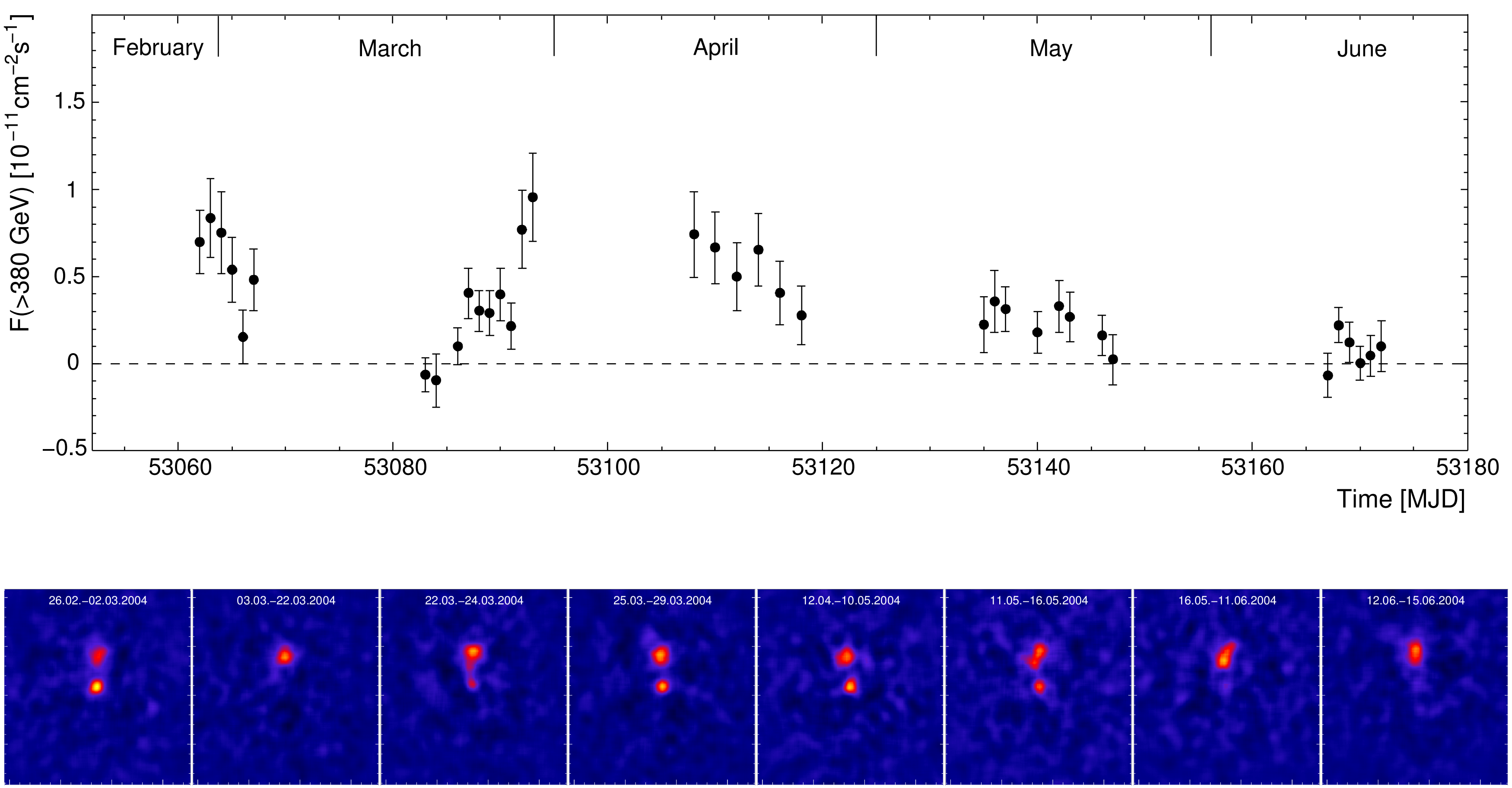

Figure 5.22: ***T**op: Daily light curve of VHE γ-rays of PSR B1259−63 using all H.E.S.S. data. The flux above 380 GeV is plotted as a function of the modified Julian date (MJD). **B**ottom: Smoothed excess sky-maps of the field of view around PSR B1259−63 based on data with the same exposure time ($\approx$ 5 h) illustrating the variability of the excess. The scale was fixed at the same value and the start and end dates are indicated for all maps.*

Period 2004	$F(> 380\,\mathrm{GeV})$ $[10^{-12}\,\mathrm{cm}^{-2}\,\mathrm{s}^{-1}]$	$\chi^2_{\mathrm{const}}/$ ndf	sign(a)	$\chi^2_{\mathrm{line}}/$ ndf	S_a $[\sigma]$
February	5.9 ± 0.6	9.4/5	-1	4.3/4	2.2
March	2.8 ± 0.4	31.9/9	$+1$	8.9/8	4.6
April	5.1 ± 0.7	4.2/5	-1	0.8/4	1.8
May	2.4 ± 0.5	4.0/7	-1	2.2/6	1.3
June	$< 2.0^*$	4.3/5	-1	4.3/4	0.2

* 99% CL, calculated according to Feldman and Cousins [1998]

Table 5.4: *Light curve properties of the H.E.S.S. 2004 data. The integrated flux* $F(> 380\,\mathrm{GeV})$ *was calculated using method (B) assuming a photon index* $\Gamma = 2.7$ *(see Sec. 5.4.2). For the daily integral flux light curve of each period the following properties are given: the* χ^2/ndf *for a fit to a constant flux, and the significance S of an increasing or declining flux* $S_a = a/\sigma_a$ *after fitting a straight line* $F(t) = at + F(0)$.

April darkness periods, and ending in a slow decrease until the observed excess is no longer significant in the June period.

Systematic Checks

The light curves of the γ-ray flux above $E_0 = 1\,\mathrm{TeV}$ were compared using the different flux determination methods (Fig. 5.23). The mean difference between the flux is $\approx 10\%$ (as found for the Crab Nebula light curve) and both methods agree within errors.

Additionally, a larger integration time interval of 2 consecutive days was considered, for which the flux was recalculated (Fig. 5.24) and found to be consistent with the flux obtained in the daily light curve above, featuring a slightly lower statistical error at the expense of a lower level of detail. However, the systematic uncertainty for each flux point did not change, and therefore the total error was not reduced significantly compared to the daily light curve.

In order to verify that the apparent variability of the measured γ-ray emission from system of PSR B1259−63 does not arise from unknown systematic effects possibly faking a flux variability, the flux of background events after selection cuts was calculated according to method B, which is not expected to show very significant variability. The corresponding "background light curve" was already introduced in Sec. 5.3.4, Fig. 5.18. Apart from the flux variation of $\approx 12\%$ already considered as systematic error, the background flux was found to be stable.

Furthermore, the source HESS J1303−631 can be utilized as a probe for additional systematic effects. The PSR B1259−63 data set was reanalysed using the ring background technique using the position of HESS J1303−631 [according to H.E.S.S. collaboration, 2005d, $\rho = 13^{\mathrm{h}}3^{\mathrm{m}}0\overset{\mathrm{s}}{.}4, \delta = -63^\circ 11' 55''$] as test position, since the 7-background method cannot be used for all wobble offsets in the data set. The derived daily light curve (obtained with method B) for the flux above 0.38 TeV is displayed in Fig. 5.25, and the flux was found to be stable over the complete period of observations. Therefore it can be concluded, that the flux variations of the PSR B1259−63 γ-ray signal do not result from time-dependent systematic effects, but rather must be intrinsic characteristics of the γ-ray emission of the source.

In summary, the checks performed above give confidence in the result of significant variability of the VHE γ-ray flux of PSR B1259−63.

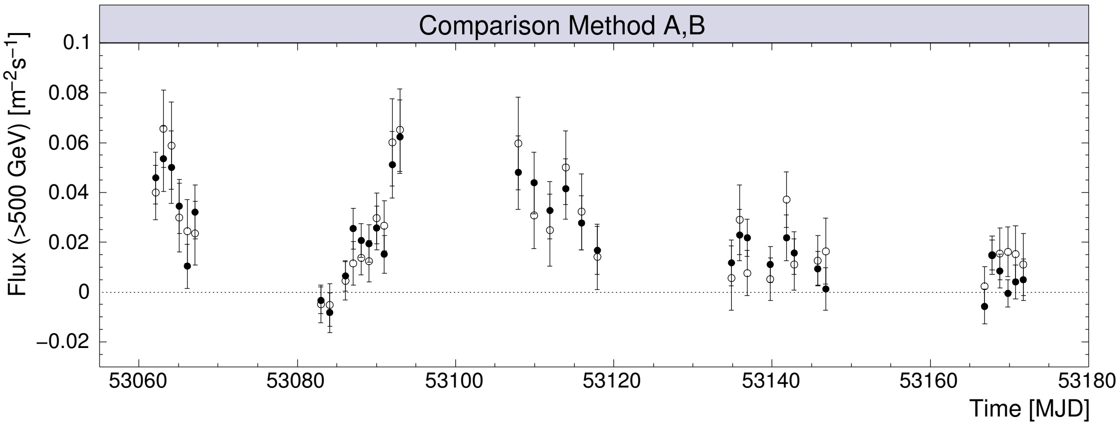

Figure 5.23: *Daily flux above 500 GeV calculated with the two considered methods (A, open circles), (B, full circles) of the flux calculation for the PSR B1259−63 data set.*

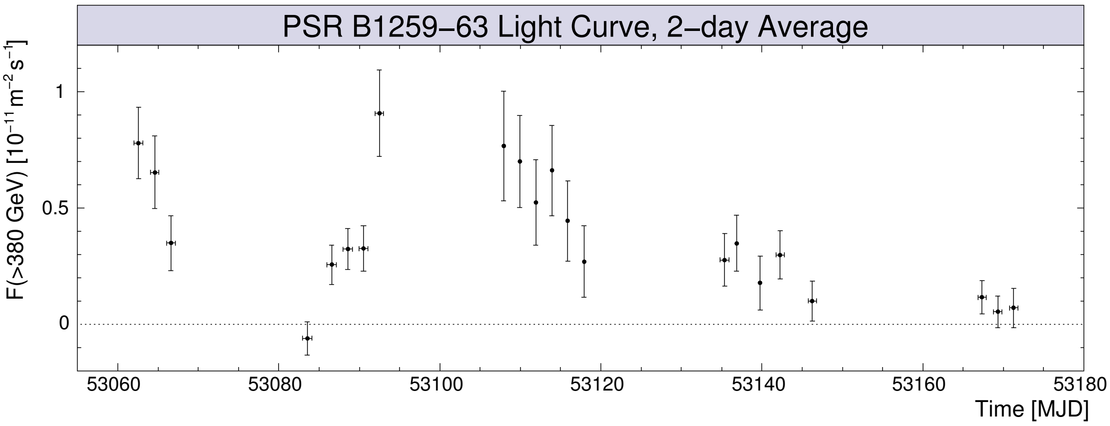

Figure 5.24: *Light curve of VHE γ-rays of PSR B1259−63 using two day binning.*

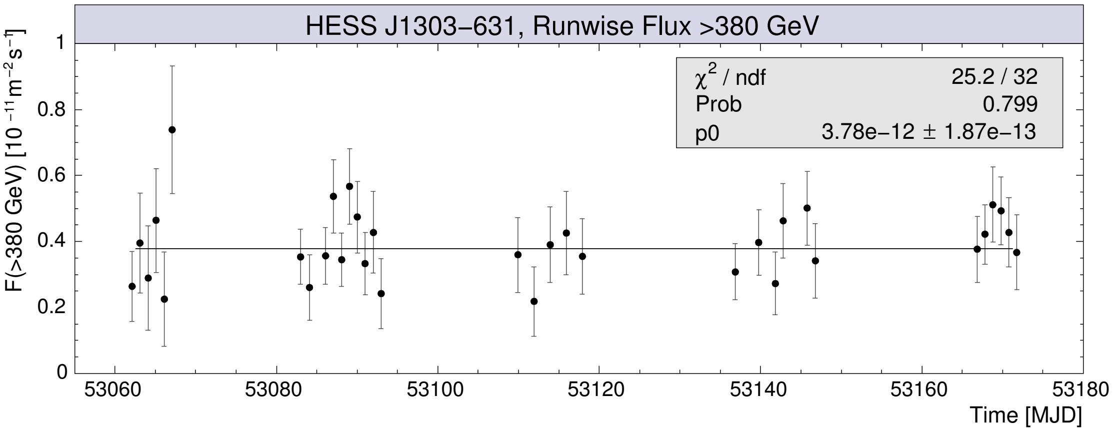

Figure 5.25: *Daily light curve obtained from the excess of VHE γ-rays from HESS J1303−631, discovered in the field of view of the PSR B1259−63 data. The flux is compatible with constant emission from this object (solid line).*

Chapter 6

Interpretation of the γ-ray Emission from PSR B1259−63 / SS 2883

The discovery of the binary system PSR B1259−63 / SS 2883 as an emitter of VHE γ-rays establishes a new type of object for high energy γ-ray astronomy. In fact, PSR B1259−63 may be a prototype of systems with a young energetic pulsar orbiting a massive main sequence star. The fact, that the system of PSR B1259−63 is the only known object of this type may be related to the exceptional eccentricity of the orbit, allowing to detect the pulsed radio emission of the pulsar at orbital phases with a large separation between both stars away from the direct proximity of SS 2883 where the pulsed emission is eclipsed. In similar systems with a more circular orbit, the pulsed radio emission of the pulsar might remain undetected, but the system may be a source of high energy radiation originating from the interaction of the strong winds of both stars.

In particular, the detection of TeV γ-ray emission from the system of PSR B1259−63 provides the first unambiguous evidence for acceleration of particles to energies above 1 TeV in this object. This immediately raises the question for the particle acceleration mechanism and whether the emission is of hadronic or leptonic origin. Additionally, the observed flux variability – although not unexpected – shows a rather complex behaviour which is not easily interpreted.

Simultaneous observations in other energy bands, especially at X-rays, are essential in order to answer the question on the origin of the non-thermal emission. Therefore, the H.E.S.S. detection of a γ-ray signal from the direction of PSR B1259−63 was immediately reported in Beilicke et al. [2004b] in order to allow for target of opportunity (ToO) observations by other instruments. In direct response, the satellites *RXTE* and *INTEGRAL* observed PSR B1259−63 at soft and hard X-ray energies in a short period post-periastron contemporaneously with H.E.S.S. [Shaw et al., 2004].

In this last chapter, the measured characteristics of the γ-ray signal from PSR B1259−63 are shortly summarised and compared to data of observations at other photon energies. Subsequently, the results are discussed with respect to the most likely γ-ray production scenarios – inverse Compton emission of electrons and π^0-decay resulting from hadronic interactions – both introduced in Chapter 1.

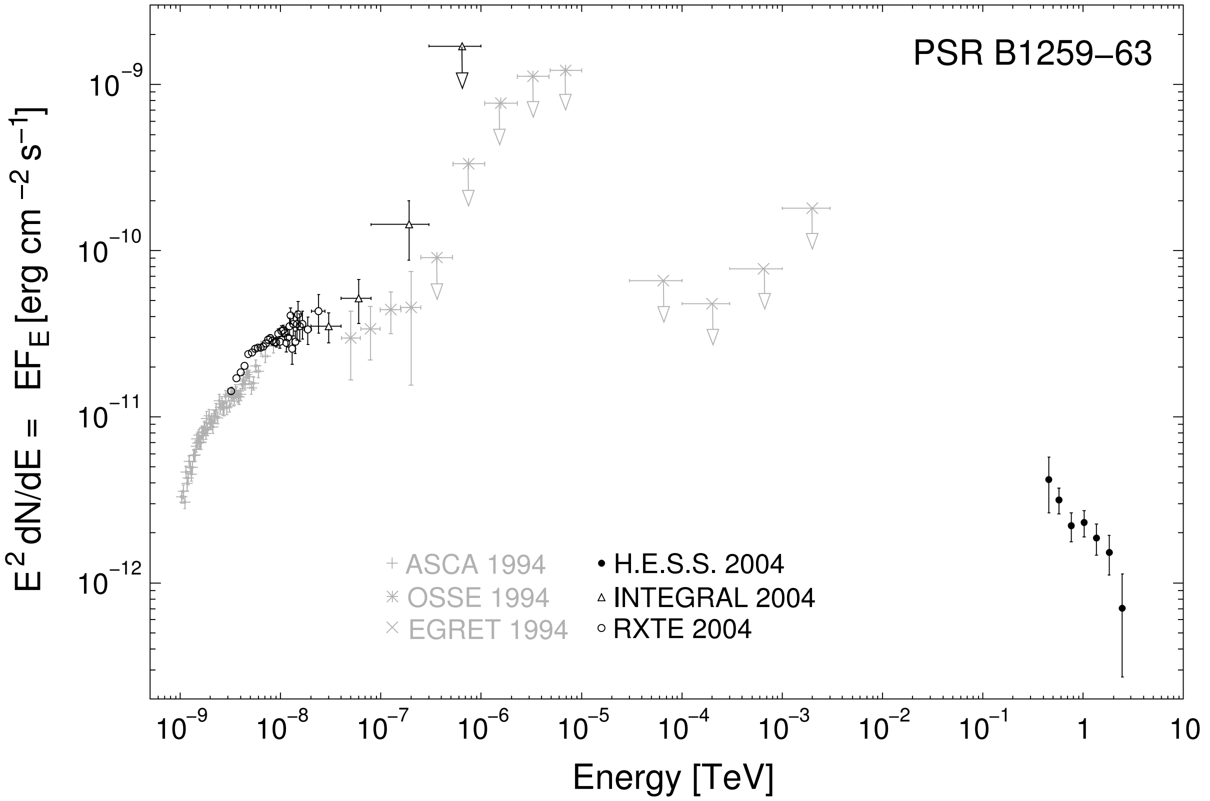

Figure 6.1: *Spectral energy distribution of the X-ray and γ-ray emission of PSR B1259−63 for data from the 2004 and 1994 periastron passage.*

6.1 Characteristics of the γ-Ray Signal

6.1.1 Position and Source Size

The measured signal position was found to be clearly coincident with the position of the binary system. However, in the vicinity of the system position exists a known variable hard X-ray source, 1RXP J130159.6−635806, found by the X-ray satellite *RXTE*, which is located 9′ southeast of the pulsar and could be an emitter or VHE γ-rays. Given the small error on the derived position of PSR B1259−63 ($\approx 30''$ in each direction), a possible source confusion can be firmly excluded.

The point source character of the detected γ-ray emission allowed to set a limit for the source extension (see Sec. 5.2). This extension, σ_s, was found to be $< 33''$ at 95% confidence level which corresponds to $0.24\,\text{pc} = 7.4 \times 10^{17}\,\text{cm}$ at an assumed distance of 1.5 kpc. The information contained in the time scale τ_{var} of the flux variability of the order of days further limits the size of the γ-ray production region to $l = c\,\tau_{\text{var}} \approx 10^{16}\,\text{cm}$.

6.1.2 Spectral Energy Distribution

Figure 6.1 shows the spectral energy distribution $E^2 \text{d}N/\text{d}E = EF_E$ of the X-ray and γ-ray emission of PSR B1259−63. The black symbols result from data taken near the 2004 periastron passage while the grey symbols are from archival data of the 1994 periastron (see Sec. 2.3.2).

The full points represent the VHE γ-ray spectrum obtained in this work. The open circles and triangles are from *RXTE* and *INTEGRAL* soft and hard X-ray measurements [Shaw et al., 2004], respectively, obtained in a rather short observation period between $\tau + 14.1$ and $\tau + 17.5$ days (see Fig. 6.3). The total energy contained in the X-ray emission, and thus the radiated luminosity, is roughly one order of magnitude higher than that of the measured VHE γ-ray emission. Additionally, the spectrum of X-rays follows a power law with photon index $\Gamma_X \approx 1.7$, while the spectrum of VHE γ-rays is softer with $\Gamma_\gamma \approx 2.7$.

The mean energy flux per energy decade contained in the VHE γ-ray emission of $EF_E \approx 3 \times 10^{-12}\,\mathrm{erg\,cm^{-2}\,s^{-1}}$ (c.f. Fig. 6.1) represents a γ-ray luminosity of $L_\gamma \approx 8 \times 10^{32}\,\mathrm{erg\,s^{-1}}$ for an assumed distance of the binary system of 1.5 kpc. This corresponds to less than 0.1% of the pulsar spin-down luminosity so that the pulsar wind emerging from PSR B1259−63 should be energetic enough to provide the main source of energy for the observed emission. Assuming that the γ-ray emission is powered by the pulsar alone, the efficiency of converting the spin-down luminosity into γ-rays is much greater than in the case of the Crab Nebula. The ratio of spin-down luminosities of both pulsars is $L_{1259}/L_{\mathrm{Crab}} \approx 2 \times 10^{-3}$ while the ratio of the squared distance from Earth is $d^2_{1259}/d^2_{\mathrm{Crab}} \approx 0.56$. The average flux level of the VHE γ-ray emission from PSR B1259−63 corresponds to $\approx 4\%$ of that of Crab and thus the γ-ray production in the system of PSR B1259−63 is one order of magnitude more efficient than in the Crab Nebula.

6.1.3 Flux Variability

The VHE γ-ray emission was found to be strongly variable with the fastest variation on a timescale of a few days close to the periastron passage of the pulsar, suggesting a radiation mechanism which is related to the interaction of the pulsar and its companion.

Figure 6.2 illustrates the VHE γ-ray flux variation with respect to the pulsar orbit and the line of sight. The light curve exhibits a characteristic shape with two high flux states before and after and an indication for a minimum at periastron, followed by a slow decrease until $\tau \sim +75$ days where the observed excess is no longer significant. Note that the orientation of the disk with respect to the orbital plane is not precisely known and no safe conclusions can be drawn about the observed time difference between the time of the post-periastron peak emission and the time of the second disk crossing assuming a disk orientation with $\omega_{\mathrm{disk}} = 90^\circ$ as indicated in the figure.

The variability pattern is quite similar to that of the transient unpulsed radio emission measured contemporaneously in radio observations [Johnston et al., 2005] as can be seen in Fig. 6.3. In fact, the observed flux rise post-periastron seems strikingly correlated between the two wavelengths on timescales of days. Additionally, the “double-bump” feature is similarly observed in the light curve of the non-thermal X-ray emission seen near periastron, however not coeval (c.f. Fig. 2.12). Unfortunately, the 2004 X-ray data provides an insufficient time coverage of only three consecutive days, indicated in Fig. 6.3, for which no significant variability could be detected.

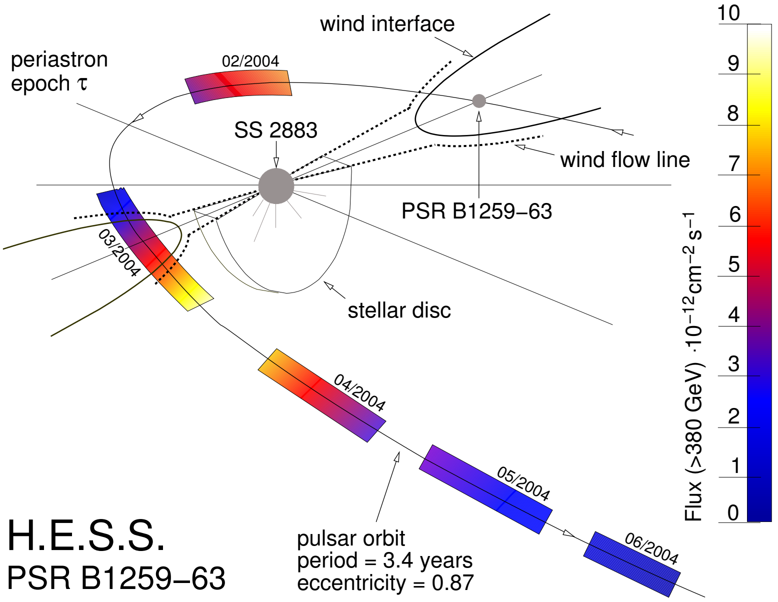

Figure 6.2: *Sketch of the orbit of PSR B1259−63 with respect to the line of sight [adapted from Johnston et al., 1999, see also Fig. 2.15]. The colour gradient bars along the orbit indicate the periods of H.E.S.S. observations and show the integral VHE γ-ray flux using a smoothed light curve based on the data points from the daily light curve.*

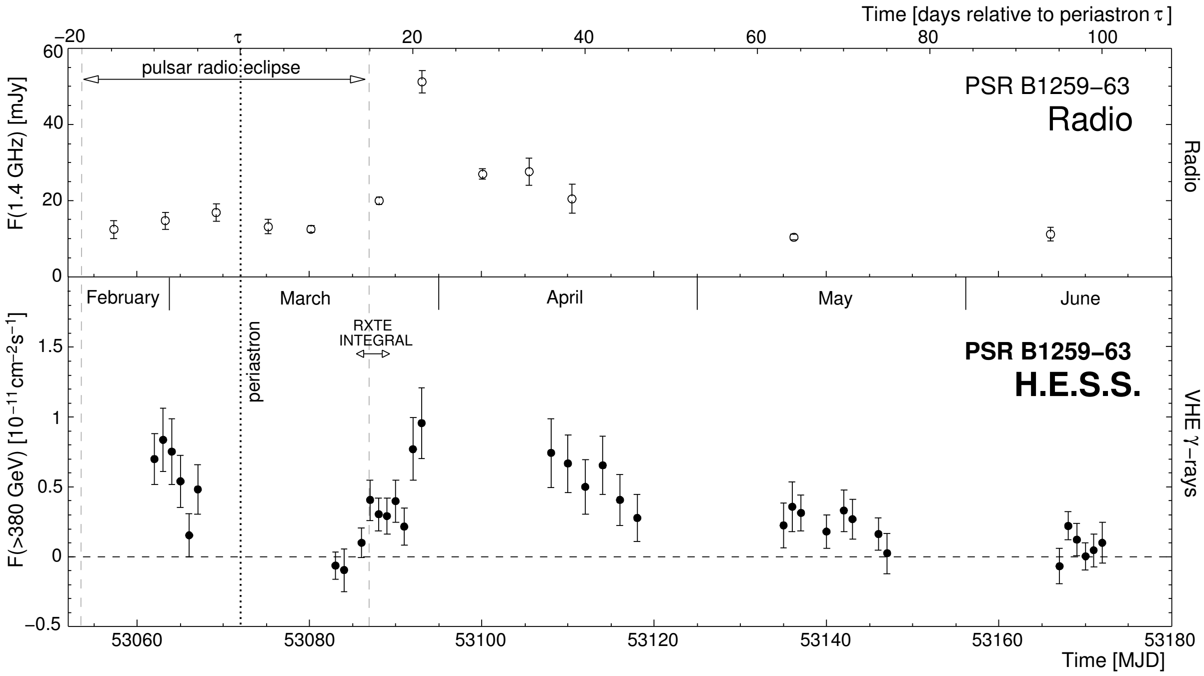

Figure 6.3: *VHE γ-ray and radio light curves of PSR B1259−63 around its periastron passage (epoch τ=0, dotted vertical line).* Upper panel, open points*: Flux density of the transient unpulsed radio emission at* 1.4 *GHz [Johnston et al., 2005]. The pulsed radio emission was eclipsed in the time interval between* $\sim \tau - 18$ *days and* $\sim \tau + 15$ *days, indicated by the two dashed vertical lines.* Lower panel, full points*: Daily integral flux above 380 GeV as measured by H.E.S.S.*

6.2 The Inverse Compton Scenario

Synchrotron radiation of shock-accelerated electrons is the most likely production mechanism for the observed non-thermal radio and X-ray emission of PSR B1259−63 / SS 2883. The high density field of thermal photons originating from SS 2883 provide an ideal target for inverse Compton scattering of the accelerated electrons which gives rise to VHE γ-ray emission. The properties of the measured VHE γ-rays – energy spectrum and variability – allow to draw several conclusions about the energy spectrum of the radiating electrons and the varying environment in this IC scenario which will be discussed in the following.

6.2.1 γ-Ray Energy Spectrum

In Section 2.4.1, two different electron populations were considered to produce IC γ-rays, the quasi-monoenergetic unshocked pulsar wind electrons and isotropically distributed electrons resulting from shock acceleration in the pulsar wind termination shock. The shape of the γ-ray spectra allows to distinguish between both populations.

Figure 6.4 shows the SED for γ-rays expected to be produced by IC scattering of the unshocked pulsar wind, as introduced in Sec. 2.4.1, and for the H.E.S.S. data. It is clear, that a spectrum with a power law shape at energies around 1 TeV is incompatible with the spectral shape of IC emission from quasi-monoenergetic pulsar wind electrons at these energies. Therefore, the “Comptonisation” of the unshocked wind by the thermal photon field of SS 2883 can be ruled out to be the dominant VHE γ-ray production mechanism in the energy range between 0.3–50 TeV for which the presented analysis is sensitive to.

This means that either: (1) the Lorentz factor of the wind electrons is out of the range $10^6 \lesssim \Gamma_{\text{wind}} \lesssim 10^8$, or (2) that the wind is terminated very close to the pulsar such that the IC drag is less dominant and the emission is much lower than that produced by an alternative γ-ray production mechanism [c.f. Ball and Kirk, 2000].

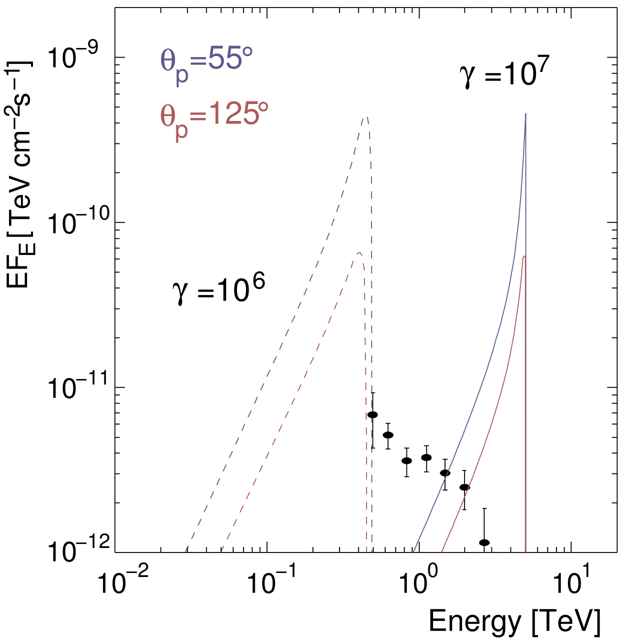

Figure 6.4: *Spectral energy distribution for γ-rays resulting from IC scattering on unshocked pulsar wind electrons [Ball and Kirk, 2000, c.f. Fig. 2.18] and the H.E.S.S. VHE γ-ray spectrum.*

In contrast, shock acceleration in the termination shock of the pulsar wind is expected to produce a power-law energy distribution of the accelerated electrons which can naturally explain the spectral shape of the observed VHE γ-rays and will be further on assumed to represent the main acceleration process.

Spectral Properties of the Radiating Electrons

The IC scattering of electrons with energies of the order of 1 TeV and the thermal photons from the star takes place in the transition region between the non-relativistic Thompson regime and the relativistic Klein-Nishina regime, since the parameter b from Eq. (2.1) is of the order of unity. The spectral index of the distribution of radiating electrons, α_e, lies in the range $\frac{1}{2}(\alpha_\mathrm{e} + 1) \leq \Gamma_\gamma \leq \alpha_\mathrm{e} + 1$, where Γ_γ is the photon index of the γ-rays, and is not easily obtained. Therefore, α_e was determined by a numerical evaluation of the scattering process.

According to Akharonian and Atoian [1981], Eq. (22–23), the spectrum $\mathrm{d}N/\mathrm{d}E$ of IC photons resulting from the scattering of isotropically distributed electrons with energy ϵ and target photons with the energy $\hbar\omega$ is given by ($\hbar = 1$):

$$\frac{\mathrm{d}N}{\mathrm{d}E} \propto \frac{1}{\omega\epsilon}\left[1 + \frac{z^2}{2(1-z)} + \frac{z}{b(1-z)} - \frac{2z^2}{b^2(1-z)^2} - \frac{z^3}{2b(1-z)^2} - \frac{2z}{b(1-z)}\ln\frac{b(1-z)}{z}\right], \quad (6.1)$$

where $z = E/\epsilon$, with

$$\frac{\omega}{\epsilon} \ll z \leq \frac{b}{1+b},$$

and $b \equiv 4\omega\epsilon$. This spectrum of IC γ-rays has to be integrated over a power law spectrum of electrons with index α_e and a Planck spectrum of target photons

$$\frac{\mathrm{d}n}{\mathrm{d}\omega} \propto \frac{(\hbar\omega)^2}{e^{\frac{\hbar\omega}{k_\mathrm{B}T}} - 1}$$

with $T = 2.3 \times 10^4$ K. The calculation was performed via Monte-Carlo integration, and the electron index α_e was determined such that the resulting IC γ-ray photon index roughly corresponds to $\Gamma_\gamma = 2.7$ – the value determined from the measured γ-ray spectrum.

Figure 6.5 shows the resulting spectrum of IC γ-rays for $\alpha_\mathrm{e} = 2.2$ and corresponding distributions of simulated target photons and power law electrons are displayed in Fig. 6.6. The photon index Γ_γ of a power-law fit to the γ-ray spectrum varies noticeably within the energy range between 0.4 and 3 TeV. In order to quantify this change, the spectrum was fit with a "parabolic power law"

$$\frac{\mathrm{d}N}{\mathrm{d}E} \propto E^{\Gamma_1 + \Gamma_2 \ln E},$$

and the resulting index $\Gamma_\gamma(E) = \Gamma_1 + \Gamma_2 \ln E$ is plotted in the inset of Fig. 6.5. This spectrum is fully compatible with the measured VHE γ-ray spectrum.

The calculation above shows, that the measured spectrum of γ-rays in the IC scenario results from an electron population with the approximate power-law index $\alpha_\mathrm{e} = 2.2 \pm 0.3$, considering the statistical and systematic error of the measurement.

Primary Electron Energy Loss Mechanism

In order to draw any conclusion about the primary injection spectrum of the shock-accelerated electrons, i.e. in order to estimate the power-law index $\alpha_\mathrm{e}^\mathrm{inj}$, the dominant energy loss mechanism has to be considered which is responsible for the spectral evolution, $\alpha_\mathrm{e}^\mathrm{inj} \rightarrow \alpha_\mathrm{e}$. For dominant adiabatic losses via plasma expansion, the shape of the injection spectrum remains unchanged, and thus $\alpha_\mathrm{e}^\mathrm{inj} \approx 2.2$ for the TeV electrons producing VHE γ-rays. In the case of dominant

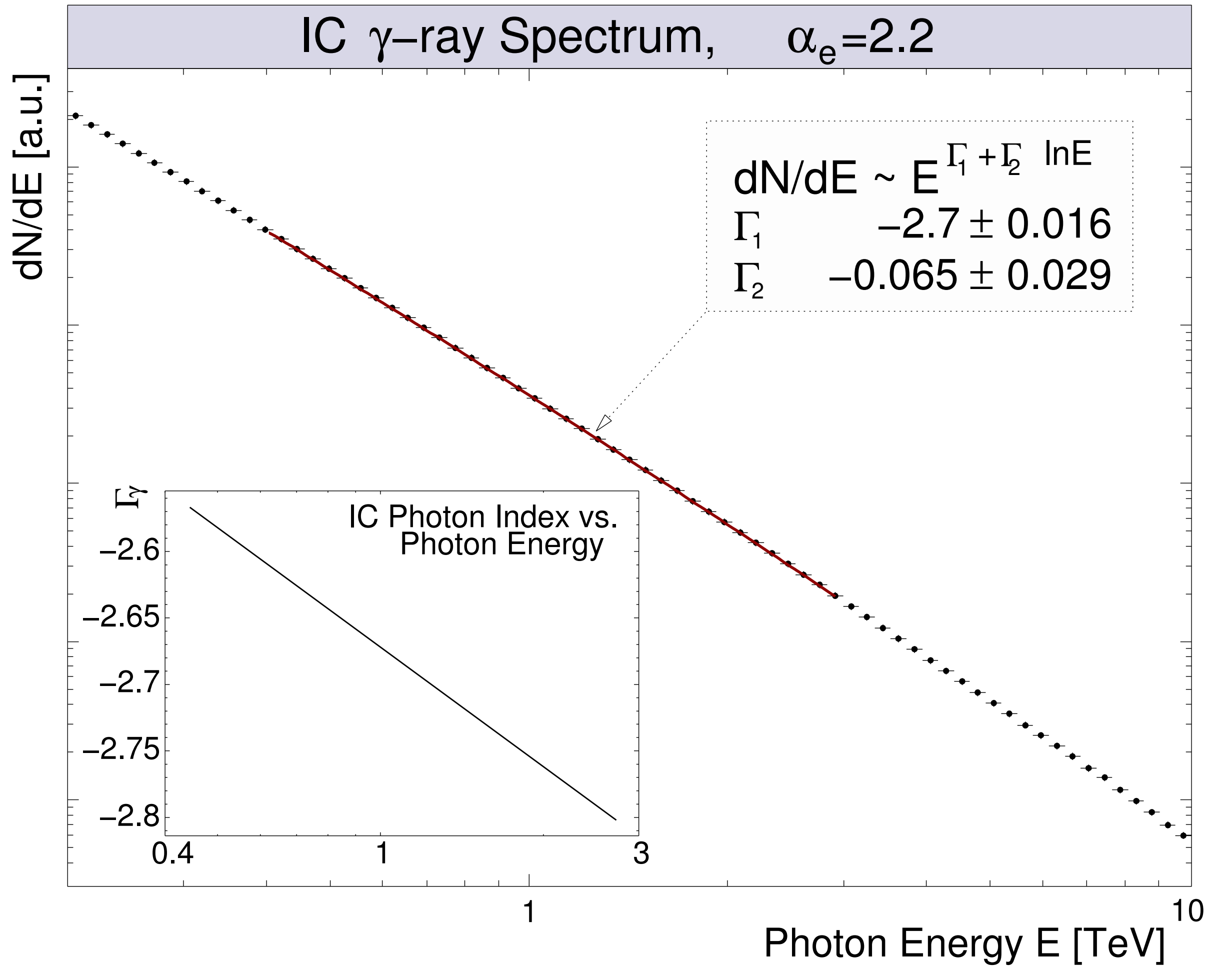

Figure 6.5: *Simulated spectrum of IC γ-rays. The solid line denotes the "parabolic power law" fit to the spectrum (see text). The inset shows the photon index Γ_γ as a function of γ-ray energy.*

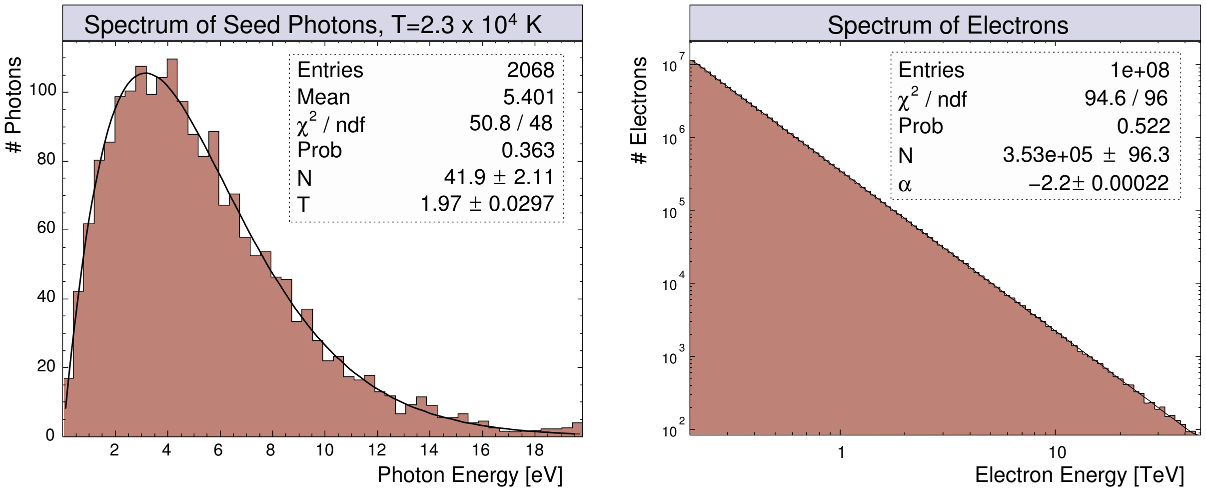

Figure 6.6: *Spectra of simulated thermal photons from SS 2883 and accelerated electrons.*

radiative losses via synchrotron or IC radiation, the injection spectrum is steepened, $\alpha_{\mathrm{e}} = \alpha_{\mathrm{e}}^{\mathrm{inj}} + 1$, and therefore an acceleration process with a much harder injection spectrum with $\alpha_{\mathrm{e}}^{\mathrm{inj}} \approx 1.2$ is needed to lead to the observed γ-ray spectrum.

The same arguments apply for the spectral shape of the X-ray emission. The X-ray photon index for all observations, either in 1994 by *ASCA* or 2004 by *RXTE* and *INTEGRAL*, was measured to lie in the range $1.6 < \Gamma_X < 1.8$ [Hirayama et al., 1996, Shaw et al., 2004, Shaw, 2004]. The resulting spectral index of the radiating electrons is given by $\alpha_{\mathrm{e}} = 2\Gamma_{\mathrm{X}} - 1 \approx 2.2 \ldots 2.6$ for the case of dominant adiabatic losses, while dominant radiative losses would again imply an injection spectrum significantly harder than $\alpha_{\mathrm{e}}^{\mathrm{inj}} = 2$.

Common shock-acceleration scenarios for pulsar wind termination shocks favour $\alpha_{\mathrm{e}}^{\mathrm{inj}} \gtrsim 2.0$ (see Sec. 2.1.3) and therefore the spectrum of the observed X- and γ-ray radiation suggests adiabatic expansion to be the dominant energy loss mechanism.

Magnetic Field in the Radiation Region

Under the assumption, that the electron population which is responsible for the synchrotron radiation in the X-ray band also emit the IC γ-rays, the magnetic field strength B in the radiating plasma can be estimated [Aharonian, 2004a].

The X-ray and γ-ray luminosities of the radiating plasma, L_γ and L_{X}, are proportional to the energy loss rate of relativistic electrons, $\dot{\epsilon} = \mathrm{d}\epsilon/\mathrm{d}\,t$, with respect to the inverse Compton scattering and synchrotron radiation processes, assuming that these processes are the only radiation mechanisms for the electrons in the considered energy range. Since the energy loss rate due to synchrotron radiation depends on the magnetic field strength, $\dot{\epsilon}_{\mathrm{sy}} = \dot{\epsilon}_{\mathrm{sy}}(B)$, the magnetic field strength can be calculated from the ratio of the observed X-ray and γ-ray luminosities:

$$\frac{L_\gamma}{L_{\mathrm{X}}} = \frac{\dot{\epsilon}_\gamma}{\dot{\epsilon}_{\mathrm{X}}} = \frac{\dot{\epsilon}_{\mathrm{IC}}}{\dot{\epsilon}_{\mathrm{sy}}(B)}. \tag{6.2}$$

For a plasma of isotropic relativistic electrons, the synchrotron energy loss rate is given by [Padmanabhan, 2000, Eq. 6.244]:

$$\dot{\epsilon}_{\mathrm{sy}}(B) = \frac{4}{3}\sigma_{\mathrm{T}} c \gamma^2 \beta^2 \frac{B^2}{8\pi} = \frac{1}{6\pi}\sigma_{\mathrm{T}} c \gamma^2 B^2, \tag{6.3}$$

where σ_{T} is the Thompson cross-section, $\epsilon = \gamma mc^2$ is the electron energy, and assuming $\beta \simeq 1$.

The IC scattering which is assumed to produce the VHE γ-rays takes place in the transition region between the Thompson and the relativistic Klein-Nishina regime (see above). Since $b \geq 1$ (c.f. Eq. 2.1), the extreme relativistic limit was considered for the IC energy loss rate, $\dot{\epsilon}_{\mathrm{IC}} = \dot{\epsilon}_{\mathrm{KN}}$. For the IC scattering of isotropic electrons with a black-body radiation field $\dot{\epsilon}_{\mathrm{KN}}$ is given by [Padmanabhan, 2000, Eq. 6.94]:

$$\dot{\epsilon}_{\mathrm{KN}} = \frac{\sigma_{\mathrm{T}}}{16} \frac{(mc\, k_{\mathrm{B}} T)^2}{\hbar^3} \left(\ln \frac{4\gamma k_{\mathrm{B}} T}{mc^2} - 1.981 \right), \tag{6.4}$$

where m is the electron rest mass, k_{B} the Boltzmann constant, and T the effective temperature of the black-body emitter. In the case of PSR B1259−63, the energy density of the target photons depends on the distance between the radiation region and SS 2883, R, and thus the energy loss rate at this distance is

$$\dot{\epsilon}_{\mathrm{KN}}(R) = \dot{\epsilon}_{\mathrm{KN}} \left(\frac{R}{R_\star}\right)^{-2} \tag{6.5}$$

Using Eqs. (6.3), (6.5), and natural units ($\hbar = c = 1$), the ratio (6.2) is determined by:

$$\frac{L_\gamma}{L_{\mathrm{X}}} = \frac{\dot{\epsilon}_{\mathrm{KN}}(R)}{\dot{\epsilon}_{\mathrm{sy}}(B)} = \frac{3\pi}{8}(k_{\mathrm{B}}T)^2 \frac{m^2}{\gamma^2} B^{-2} \left(\frac{R}{R_\star}\right)^{-2} \left(\ln \frac{4\gamma k_{\mathrm{B}} T}{m} - 1.981\right). \tag{6.6}$$

With $\epsilon_{\mathrm{TeV}} = \gamma mc^2/1\,\mathrm{TeV}$, $k_{\mathrm{B}}T \approx 2\,\mathrm{eV}$, and $m = 5.11 \times 10^5\,\mathrm{eV}$ this results in:

$$\frac{L_\gamma}{L_{\mathrm{X}}} = 0.32\,\epsilon_{\mathrm{TeV}}^{-2}\,[\ln(30.6\,\epsilon_{\mathrm{TeV}}) - 1.981] \left(\frac{B}{(\mathrm{eV})^2}\right)^{-2} \left(\frac{R}{R_\star}\right)^{-2}, \tag{6.7}$$

and therefore the magnetic field strength is determined by:

$$B_{\mathrm{G}} = 91.94\,\epsilon_{\mathrm{TeV}}^{-1}\,\sqrt{\ln(30.6\,\epsilon_{\mathrm{TeV}}) - 1.981} \left(\frac{R}{R_\star}\right)^{-1} \sqrt{\frac{L_{\mathrm{X}}}{L_\gamma}}, \tag{6.8}$$

with

$$B_{\mathrm{G}} = \frac{B}{1\,\mathrm{G}} = 51.3 \frac{B}{(\mathrm{eV})^2}.$$

The radiation luminosity L is proportional to the measured energy flux $E^2\mathrm{d}N/\mathrm{d}E = EF_{\mathrm{E}}$ at that photon energy which corresponds to the energy of the emitting electron, and thus:

$$\frac{L_{\mathrm{X}}}{L_\gamma} = \frac{E_{\mathrm{X}}^2\,\mathrm{d}N/\mathrm{d}E_{\mathrm{X}}}{E_\gamma^2\,\mathrm{d}N/\mathrm{d}E_\gamma}.$$

The measured energy flux for the VHE γ-rays around 1 TeV is

$$E_\gamma^2\,\mathrm{d}N/\mathrm{d}E_\gamma \approx 2.5 \times 10^{-12}\,\mathrm{erg\,cm^{-2}\,s^{-1}}$$

and for the X-rays between 1 and 200 keV

$$E_{\mathrm{X}}^2\,\mathrm{d}N/\mathrm{d}E_{\mathrm{X}} \approx 3 \times 10^{-11}\,\mathrm{erg\,cm^{-2}\,s^{-1}}$$

on average (c.f. Fig. 6.1). The distance R between the radiation region and the star roughly corresponds to the distance between the pulsar and its companion, i.e. 500 ls $\approx 1.5 \times 10^{13}$ cm at $\tau + 16$ days (see Fig. 2.8). Finally, using the estimates above and for an electron energy of 1 TeV, Eq. (6.8) breaks down to

$$B \approx 3.17\,\mathrm{G} = \mathcal{O}(1\,\mathrm{G}).$$

This "experimentally" estimated field strength of the order of 1 G agrees rather well with the theoretical estimate of the field derived from the MHD treatment of the pulsar wind [Tavani and Arons, 1997, Ball et al., 1999], and the value deduced from the observed unpulsed radio emission near periastron using archival data [Connors et al., 2002, c.f. Sec. 2.3.3].

The magnetic field strength in the Crab synchrotron nebula is a factor of 10^4 lower than that derived here indicating that the pulsar wind termination shock is much closer to the pulsar than in the case of Crab. This can be explained by the high pressure of the stellar mass outflow of SS 2883 terminating the pulsar wind very close to PSR B1259−63, i.e. at distances roughly four orders of magnitude lower than in the case of the Crab Nebula.

Comparison with Models

A comparison of the measured spectrum with those calculated by Kirk et al. [1999] is shown in Fig. 6.7. Since this spectrum was calculated for an orbital phase $\tau - 12$ days, only data from the February darkness period ($\tau - 10 \ldots \tau - 5$ days) was used to determine the VHE γ-ray spectrum. Reasonable agreement is found for the magnetic field strength of $B = 0.32$ G and for both, dominant inverse Compton and adiabatic energy losses of the accelerated electrons. Thus, from the spectral shape alone, no conclusion about the dominant energy loss mechanism can be drawn. Nevertheless, the case of dominant radiative cooling again is based on a hard injection spectrum with $\alpha_e^{\mathrm{inj}} < 1.4$.

Additionally, the magnetic field strength in the model agrees with the above estimate of the order of 1 G. However, the model parameters were chosen such that the synchrotron emission matches the X-ray data from 1994, while the X-ray emission for the 2004 periastron remains unknown and may differ from that of 1994.

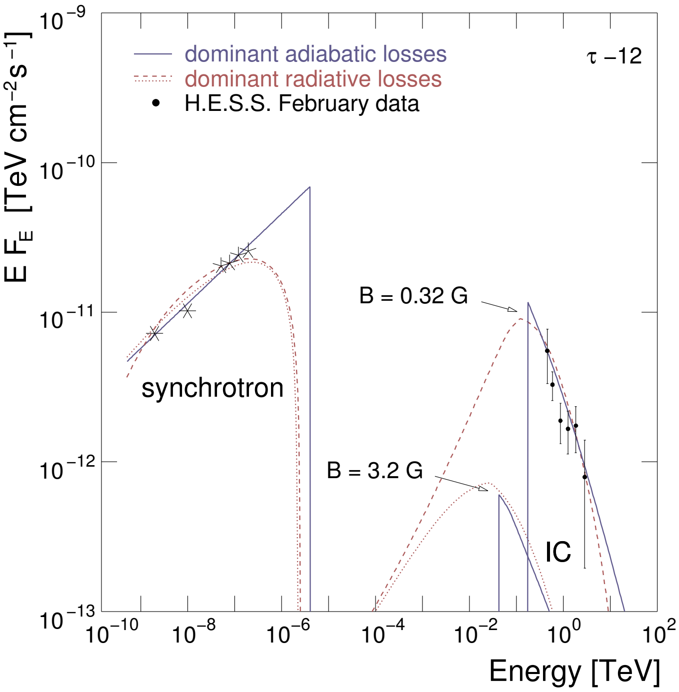

Figure 6.7: *Spectral energy distribution for γ-rays resulting from IC scattering on shock-accelerated electrons [Kirk et al., 1999, c.f. Fig. 2.19] and the measured VHE γ-ray spectrum from H.E.S.S. data of February 2004.*

Nevertheless, it seems that the spectral shape and overall flux level of the X-ray and VHE γ-ray emission are consistent with a pure leptonic origin of the radiation.

6.2.2 Temporal Variations of the VHE γ-Ray Emission

Comparison with IC Model

Figure 6.8 shows the comparison of the VHE γ-ray light curve and the IC model by Kirk et al. [1999] for dominant adiabatic and radiative (IC) losses for $B = 0.32$ G. The light curve was recalculated using a 2-day flux average in order to reduce the statistical error on each flux point at the expense loosing details. It is clear, that both model curves disagree with the measurement, in particular the indication for a flux minimum near periastron and a peak at $\approx \tau + 25$ days. Nevertheless, the disagreement is not surprising since the variability pattern indicates an enhanced VHE γ-ray flux during the epochs of the interaction of the pulsar wind and the stellar disk which was neglected in the model.

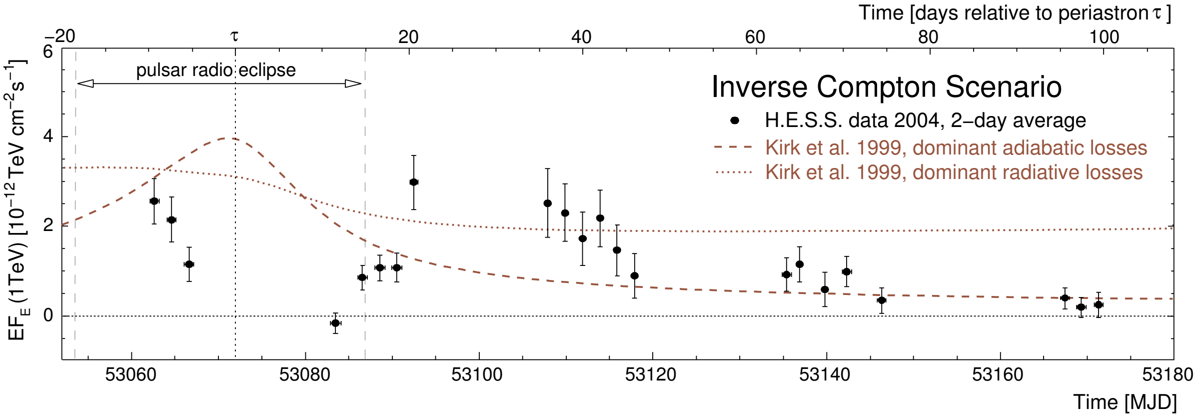

Figure 6.8: *Model light curves of the VHE γ-ray energy flux according to Kirk et al. [1999] for dominant adiabatic and radiative losses (dashed and dotted line, respectively). The full points represent the flux measured by H.E.S.S. averaged over a time period of two days for each point.*

Inverse Compton Drag Near Periastron

The indication of a low flux level at the periastron passage suggests that the shock-accelerated electrons are less efficiently produced or loose their energy much faster than during the phases of high flux before and after periastron.

Firstly, the high density of thermal photons from SS 2883 near periastron might decelerate the pulsar wind before it is terminated by the stellar mass outflow and much less electrons with the nominal Lorentz factor are available for shock acceleration. This scenario of the γ-ray emission from the unshocked wind was excluded from the measured spectrum in the range of wind Lorentz factors between $\gamma_{\mathrm{wind}} \approx 10^6 \ldots 10^8$ to be responsible for the observed VHE γ-rays. However, since the energy threshold for the observations of PSR B1259−63 is higher than 300 GeV, the emission from the unshocked wind with Lorentz factors below the threshold and above the maximum energy of ≈ 10 TeV the analysis was sensitive to would remain undetected by the H.E.S.S. observations.

Thus, the unshocked wind scenario might account for the observed flux decrease of VHE γ-rays and non-thermal X-rays a few days around periastron. However, the observed asymmetry of the γ-ray flux with respect to periastron cannot be explained by the inverse Compton drag alone.

Interaction of the Pulsar Wind with the Stellar Disk Outflow

The indication of two flux maxima, several days pre- and post-periastron suggest a connection between the high flux states and the crossings of the pulsar through the regions of enhanced mass outflow in the stellar disk of SS 2883.

The fact that both the X-ray and VHE γ-ray fluxes have a minimum during periastron excludes that radiative losses via synchrotron or IC emission of the accelerated electrons dominate. On the other hand, if adiabatic energy losses of the shock-accelerated electrons dominate, as suggested by the spectral shape of the γ-ray emission, the variability pattern can be explained with a varying confinement of the pulsar wind by the stellar outflow [Aharonian and Völk, 2004] illustrated in Fig. 6.9.

During the interaction of the pulsar wind with the disk, the down-stream regions of the shocks are relatively compact and close to the pulsar with a relatively slow post-shock plasma flow along the contact discontinuity away from SS 2883. In the regions where the pulsar wind interacts with the less dense polar component of the stellar outflow, the shock occurs less close to PSR B1259−63 and the heated plasma can rapidly expand in the down-stream region. This scenario can qualitatively explain the two high flux states at the pulsar disk crossings and a flux minimum near periastron for all radiation components produced in the down-stream regions of both wind termination shocks.

Stellar Disk Orientation

The general connection of the radiation flux level with the stellar wind density is supported by the correlation between the γ-ray light curve and that of the X-ray and unpulsed radio emission near periastron.

The variability pattern of the X-ray emission near periastron also showed two flux maxima near periastron with a minimum at periastron which was modeled by Tavani and Arons [1997] to be compatible with an inclined disk with $\omega_{\mathrm{disk}} \approx 120°$. The calculated timescales of the shock-acceleration and dominant energy loss processes of the order of hundreds of seconds (c.f. Fig. 2.17) require the peak emission to occur at the time of the disk crossing. Since the VHE γ-ray production is assumed to originate from the same electron population as the X-ray emission, the VHE γ-ray flux maxima can be interpreted to correspond as well to the times of the disk crossings. Using the post-periastron maximum of the γ-ray flux at around $\tau + 25 \pm 5$ days as a reference time for the disk crossing, the corresponding disk orientation would be $\omega_{\mathrm{disk}} \approx 105°$ as it is illustrated in Fig. 6.10 with the dashed line. The expected peak of the pre-periastron disk crossing would lie in this case at $\tau - 12$ days which is compatible with the VHE γ-ray light curve.

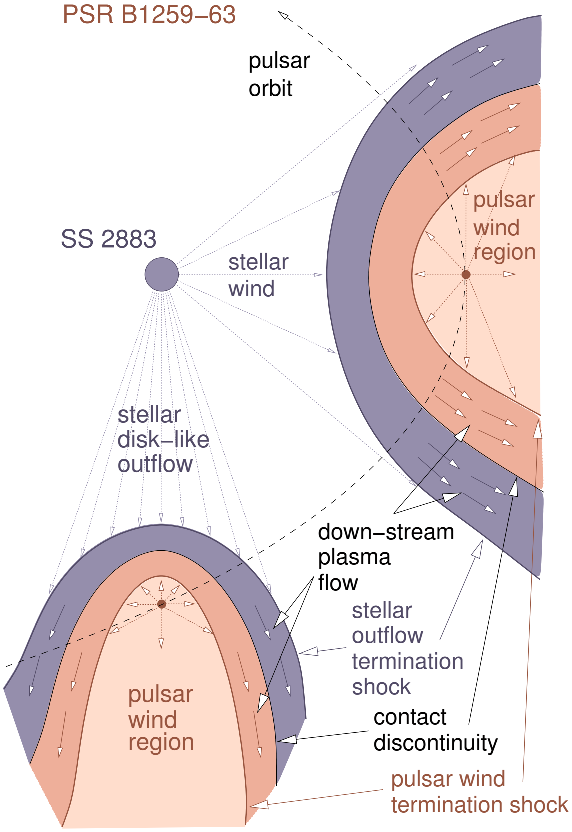

Figure 6.9: *Schematic geometry of the interaction between the pulsar and stellar winds near periastron. The down-stream shock regions are compressed during the phase of pulsar wind – disk interaction while at periastron, these regions are less compact allowing a more rapid expansion of the plasma.*

In contrast, the peaks of the unpulsed radio emission (see Fig. 6.3) were interpreted by Ball et al. [1999] in the case of an inclined disk as synchrotron radiation from electrons shock-accelerated on the Be star side shock of the pulsar wind "bubble" (c.f. Sec. 2.3.3). In this model, the bubble decays slowly by synchrotron losses only and thus shows a peak flux a few days after the assumed disk crossings of the pulsar for a disk orientation with $\omega_{\mathrm{disk}} \approx 90°$. Since the VHE γ-ray emission shows a correlated flux enhancement one could assume the same mechanism to be responsible for the γ-ray emission. This would be contrary to the case above, where dynamical flow effects on timescales of minutes were considered to be important, and the peak emission would directly correspond to the phases of the crossings.

Alternatively, the electrons responsible for the radio emission could be accelerated in the Be star side shock as required by Ball et al. [1999] but could evolve similarly to the pulsar wind shock electrons, i.e. rapidly loosing their energy by dominant adiabatic expansion instead of slow synchrotron cooling, and thus the observed radiation would be correlated at all photon energies.

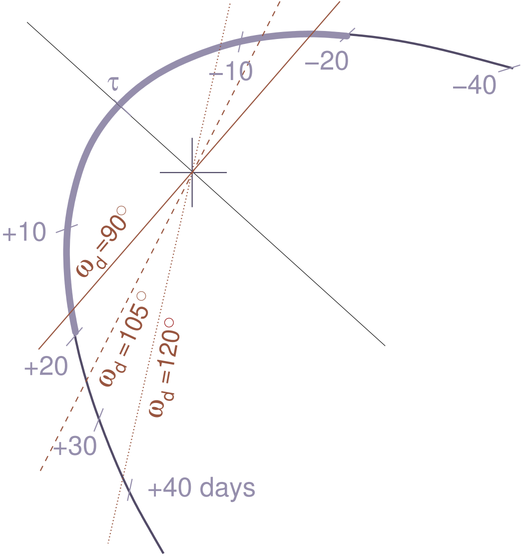

Figure 6.10: *Orbit of PSR B1259−63 near periastron (c.f. Fig. 2.8). The solid, dashed and dotted straight line illustrate different orientations of the stellar disk.*

Flux Level Differences Between the Disk Crossings

In the case, where the γ-ray flux peaks correspond to the times of the pulsar disk passages, the question remains why the flux near the post-periastron passage seems enhanced with respect to the first passage, although the peak flux pre-periastron was not covered by the H.E.S.S. observations.

Firstly, if the disk crossings are not symmetrical with respect to periastron, i.e. $\omega_{\text{disk}} > 90°$, the pulsar wind would be terminated closer to the pulsar during the first crossing and thus the magnetic field strength in the plasma would be higher (c.f. Fig. 2.17), resulting in a suppression of the γ-ray flux by enhanced synchrotron losses compared to the second crossing, while the X-ray flux level would show the opposite behaviour (c.f. Fig. 2.16). Secondly, the γ-rays produced during the first crossing have to travel through a region with a higher density of thermal photons from SS 2883 compared to the second crossing and thus may be more strongly absorbed by $e^{\pm}$ pair production [Kirk et al., 1999]. Finally, since the down-stream flow of accelerated particles proceeds along the contact discontinuity between the pulsar and stellar wind shocks along the "comet tail" mainly in the direction away from the pulsar and its companion, one could expect a modulation of the γ-ray light curve by the Doppler shift with respect to the line of sight [de Jager, 2004]. The γ-ray flux F at a given pulsar orbital phase then depends on the angle $\theta_{\text{p}} \equiv \theta$ between the line of sight and the line pulsar/Be-star and is suppressed by a factor of

$$\frac{F}{F_0} = \left(\frac{1 + \beta \cos\theta}{1 + \beta \cos\theta_0} \right)^{\Gamma_\gamma + 1}$$

compared to a point of the orbit where this angle is minimal, $\theta = \theta_0 \approx 55°$ with a corresponding flux F_0. The key parameter is the flow velocity of the plasma β which might be even supersonic with $\beta > c/\sqrt{3}$. Using $\Gamma_\gamma = 2.7$, the angle θ and the resulting flux ratio for different values of β are shown in Fig. 6.11 bottom and top, respectively, as a function of time for the epochs of the H.E.S.S. observations.

The Doppler shift could account for a reduction of the flux at the first compared to the second disk crossing. Note however, that the suppression due to the Doppler effect will only be applicable as long as a cometary tail exists: If the ram pressure due to the stellar wind is

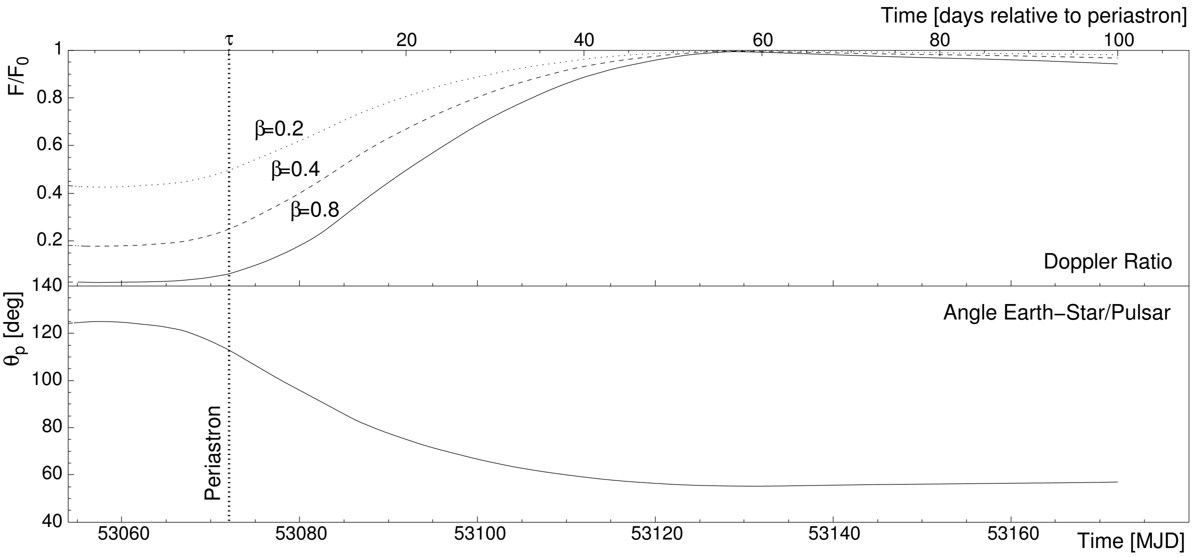

Figure 6.11: ***T**op: Relative γ-ray flux suppression due to Doppler shifting (see text) for different down-stream plasma flow velocities β as a function of time for the time range of H.E.S.S. observations of PSR B1259−63. **B**ottom: Angle between the line of sight and the line between the pulsar and its companion θ_p as a function of time.*

unable to produce a well collimated cometary tail outside the two epochs of the disk crossing no Doppler suppression is expected. Interestingly, in the case of a disk orientation symmetric with respect to periastron (with $\omega_\mathrm{disk} = 90°$) the suppression of the TeV flux could explain a delayed flux maximum which occurs several days after the second disk crossing associated with a minimal θ as stated above. Long after the periastron passage, the ram pressure in the stellar wind will again be too small to support a cometary tail, resulting in an interpretation in terms of a weakly collimated cometary tail, where Doppler effects would be less pronounced.

6.3 The Hadronic Interaction Scenario

An alternative to the leptonic origin of the observed γ-rays is provided by hadronic interactions of shock-accelerated ions. The leptonic scenario, where the observed X- and γ-rays can be interpreted as synchrotron and IC emission from a single population of shock-accelerated electrons, seems to be rather self-consistent in terms of the estimated magnetic field strength in the radiating plasma and the corresponding flux level and spectral shape of the radiation. However, a hadronic origin of the γ-rays cannot be ruled out by the data.

There are two possibilities for the origin of shock-accelerated ions: (1) a significant fraction of the pulsar wind kinetic energy is carried by ions which are accelerated in the pulsar wind termination shock, or (2) ions from the stellar mass outflow accelerated in the Be star side shock front. The correlation between the flux variability pattern of the unpulsed radio emission and the γ-ray light curve could be interpreted as indication for case (2) if one follows the argumentation of Ball et al. [1999] about the Be star shock origin of the radio emission.

In Section 2.4.2, the model from Kawachi et al. [2004] was introduced, wherein protons are modeled to be shock-accelerated in the Be star side shock producing γ-rays via proton-proton interactions. The expected flux level was found to be proportional to the parameter x of the stellar mass outflow in Kawachi et al. [2004], $F_\gamma \propto x^2$ and the γ-ray spectral shape reflects that of the distribution of accelerated protons which was assumed to be a power law.

Figure 6.12 shows the model spectrum for the epoch of periastron together with the time-averaged spectrum of γ-rays obtained from the H.E.S.S. data. Obviously, neither the photon index nor the flux level is in good agreement. Nevertheless, the flux level depends on the choice of the outflow parameter x and the spectral shape of the shock-accelerated protons in the model was assumed to be $\alpha_\mathrm{p} = 2$. A shock-acceleration process which is able to produce a proton spectrum with $n(\epsilon_\mathrm{p}) \propto \epsilon_\mathrm{p}^{-2.7\pm0.3}$ could account for the observed shape of the γ-ray spectrum, although this is incompatible with first order Fermi acceleration. Since the flux is expected to be variable and the periastron passage was not covered by the H.E.S.S. observations, the flux normalisation from the model spectrum cannot be compared with that of the H.E.S.S. spectrum.

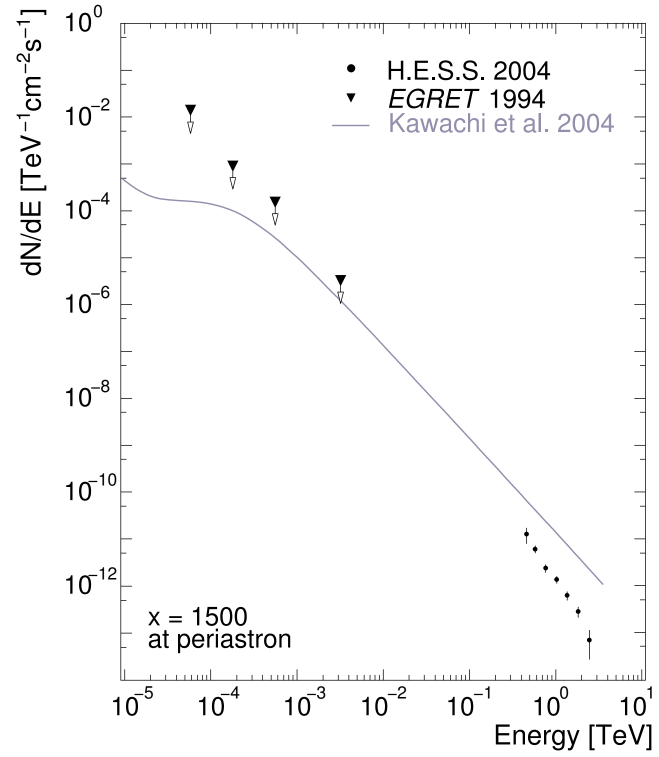

Figure 6.12: *Comparison of the γ-ray spectrum in the hadronic interaction model by Kawachi et al. [2004] (c.f. Fig. 2.21) for the epoch of periastron and the H.E.S.S. time averaged spectrum (full circles).*

Several cases for the alignment of the stellar disk of SS 2883 were considered in the model resulting in different flux variability patterns. Figure 6.13 shows the comparison of the expected and measured energy flux at 1 TeV γ-ray energy for the case of a misaligned disk with two associated crossings of the pulsar through the disk. The model light curve seems to be qualitatively similar to that of the measurement, although the epochs of the high flux states do not match. The peaks of the emission could be shifted due to the same reasons as discussed in the last section: by a Doppler-shift of the down-stream plasma flow in case of a "cometary tail" or by a different orientation of the stellar disk with respect to periastron. However, in the latter case where an orientation angle $\omega_\mathrm{disk} > 90^\circ$ was discussed, the first flux peak would be shifted further towards periastron which might be inconsistent with the data. The model light curve for an outflow parameter $x = 1500$ was scaled by a factor 0.3 in order to roughly match the flux level of the data. Thus, the outflow parameter in this model can be constrained to be $x \approx 800$.

6.4 Outlook

With the H.E.S.S. detection of VHE γ-ray emission from PSR B1259−63 / SS 2883 and the measurement of the energy spectrum and variability pattern, an important step in the understanding

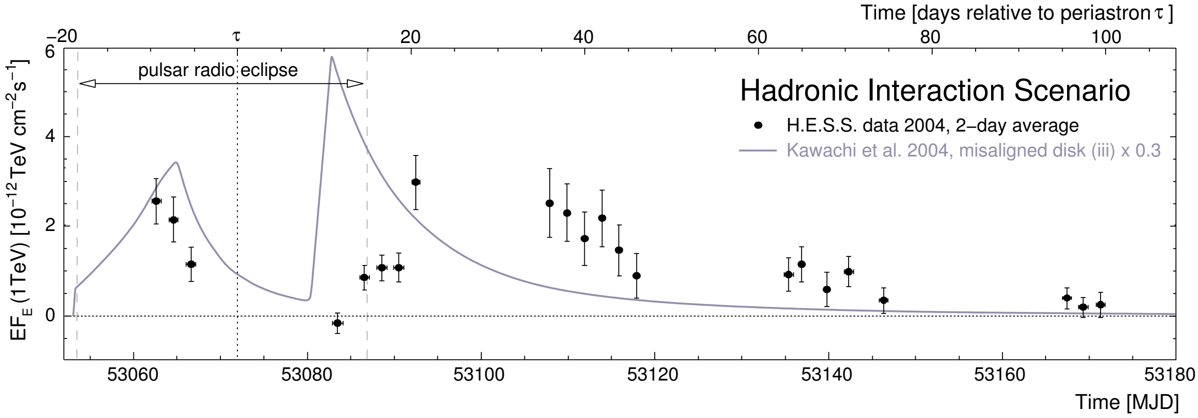

Figure 6.13: *Comparison of the VHE γ-ray light curve (energy flux at 1 TeV) in the hadronic interaction model by Kawachi et al. [2004] (c.f. Fig. 2.21) for the case of a misaligned disk and the H.E.S.S. data using flux points with a 2-day average.*

of the high energy emission from this object was achieved. Nevertheless, many open questions remain to be answered by either detailed theoretical modeling of the data presented or future observations.

Further monitoring of the source in the VHE γ-ray energy band, also far away from periastron, seems desirable for two reasons: Firstly, the distance of the pulsar wind termination shock is expected to drastically increase while the pulsar travels away from its companion and this would result in a lower magnetic field strength in the down-stream region of the shock. PSR B1259−63 was detected in X-rays near apastron at a flux level roughly one order of magnitude lower than near periastron. In the scenario of IC emission from shock-accelerated electrons, the low magnetic field would result in a higher γ-ray emission in relation to the synchrotron X-ray emission, enabling H.E.S.S. to detect the source at apastron. Secondly, VHE γ-ray observations during future periastron passages with deep exposures of H.E.S.S. and other existing or even with more sensitive instruments would be useful in order to improve the time coverage of the observations and derive γ-ray spectra on a daily basis providing further constrains on the particle acceleration and radiation mechanisms at work.

Furthermore, the question of the leptonic or hadronic origin of the the VHE γ-rays emitted near periastron could be answered by sensitive detectors covering the energy range between several MeV and 100 GeV, like satellite detectors and IACT experiments with a low energy threshold. The shape of the spectral energy distribution in this energy range has to be resolved, where either a local minimum between the peak of the synchrotron and IC radiation of electrons or a rather flat distribution due to the emission resulting from hadronic interactions is expected. Additionally, with these instruments it may be possible to see the IC γ-ray emission from electrons in the unshocked pulsar wind.

The high variability of the emission near periastron in all energy bands will require more simultaneous observations in dedicated multi-wavelength campaigns, especially near periastron where many instruments provide a sufficient sensitivity in order to detect the high flux states induced by the interaction of the highly energetic winds of PSR B1259−63 and SS 2883.

Chapter 7

Summary

This work represents the first comprehensive analysis of VHE γ-rays discovered to be emitted from the binary system of PSR B1259−63 / SS 2883 using data obtained with the H.E.S.S. array of imaging atmospheric Cherenkov telescopes.

In the experimental part of the work, firstly an overview of the detector components was given with special emphasis on the design and implementation of the H.E.S.S. central data acquisition system (DAQ). The DAQ hardware is represented by a distributed computer cluster connected via a local area network on which a system of distributed processes controls and monitors all detector components. The processes are implemented using an object oriented software design which can be easily configured to control additional detector components such as new telescopes.

Subsequently, the data analysis was described in detail and the results were presented. The detector calibration, data reduction, and γ-ray reconstruction are well understood, which was demonstrated by the good agreement between γ-ray simulations and data. It was shown that H.E.S.S. is able to reconstruct γ-ray air showers with an angular resolution of better than 0.1° and an energy resolution of $< 20\%$. The analysis routines used for the extraction of the characteristics of a VHE γ-ray signal such as energy spectrum and light curve were tested with the data from the Crab Nebula – the standard candle of VHE γ-ray astronomy – and the results were found to be in good agreement with results from earlier IACT instruments.

Finally, the results from the analysis of the data set recorded in the observations from February to June 2004 near the periastron passage of PSR B1259−63 were presented. The VHE γ-ray signal measured at the direction of the system was found to have a total significance of more than 13 standard deviations for the complete data set. It was shown, that the center of gravity of the emission coincides with the position of PSR B1259−63 within errors and that the source has a point source character allowing to constrain the intrinsic source size to $< 33''$ at 95% confidence level.

The time averaged γ-ray spectrum can be described by a power law $\mathrm{d}N/\mathrm{d}E = F_0 E^{-\Gamma}$ with the photon index $\Gamma = 2.7 \pm 0.2_{\mathrm{stat}} \pm 0.2_{\mathrm{sys}}$ and the flux normalisation $F_0 = (1.3 \pm 0.1_{\mathrm{stat}} \pm 0.4_{\mathrm{sys}}) \times 10^{-12}\,\mathrm{cm}^{-2}\,\mathrm{s}^{-1}\,\mathrm{TeV}^{-1}$ in the γ-ray energy range between 0.4 TeV and 3 TeV corresponding to an average of roughly 4% of the flux of the Crab Nebula. Within statistical errors, no variation of the photon index was seen in the data set.

The observed flux was found to vary significantly on timescales of days. The measured light curve shows strong signals to be emitted in pre- and post-periastron phases with a flux minimum around periastron, followed by a gradual flux decrease in the months after. The analysis of the variability was cross-checked using two independent methods for which a good agreement was found giving confidence in the obtained result. The observed flux variability makes PSR B1259−63 / SS 2883 the first variable galactic source of VHE γ-rays observed so far.

The experimental results were discussed and interpreted within the context of the current theoretical understanding of the astrophysical processes associated with the production of VHE γ-rays in this source and were compared to several existing γ-ray emission models.

First of all, the discovery of VHE γ-rays from the binary system PSR B1259−63 / SS 2883 by H.E.S.S. provides the first unambiguous evidence for acceleration of particles to energies above 1 TeV in this object.

The γ-ray spectrum was found to be consistent with expectations for the γ-ray emission from a pulsar wind nebula formed due to the interaction of the pulsar wind of PSR B1259−63 with the stellar outflows of its companion. In this case, the γ-ray emission is produced by particles accelerated in the termination shocks of the colliding winds. Assuming that the γ-rays originate from inverse Compton scattering of shock-accelerated electrons with the intense thermal photon field of SS 2883, several conclusions can be drawn from the γ-ray spectrum. The assumed power-law energy spectrum of the radiating electrons was constrained to have a spectral index $\alpha_\mathrm{e} = 2.2\pm0.3$. Since the acceleration spectrum is expected to have a similar shape, adiabatic expansion of the electrons in the down-stream region of the shock was concluded to be the dominant energy loss mechanism. Furthermore, under the assumption that the observed X-ray emission of the system results from synchrotron emission of the same electrons, the magnetic field strength in the radiating plasma was estimated to be of the order of 1 G. Indeed, the measured pre-periastron spectrum agrees well with that of the model of Kirk et al. [1999] which was matched to archival X-ray data for a similar magnetic field strength.

A hadronic origin of the γ-ray emission cannot be excluded, but would require a soft acceleration spectrum with a spectral index of $\alpha_\mathrm{p} = 2.7 \pm 0.3$ which is incompatible with first order Fermi acceleration.

The measured light curve does not agree with any of the considered theoretical models which may be a result of the high level of simplifications which where made. The observed variability pattern strongly suggests the γ-ray flux to be enhanced near the orbital phases where PSR B1259−63 is thought to cross the equatorial disk of SS 2883. This would imply that the disk is inclined with respect to the orbital plane as suggested by several other measurements at various wavelengths. This indication is confirmed by the correlation found between the flux evolution of the detected γ-ray emission and that of the transient unpulsed radio emission of PSR B1259−63 / SS 2883 near periastron. However, the indicated post-periastron flux maximum occurs several days after the expected disk crossing, which was discussed to be possibly related to a Doppler boost of the accelerated particles or a slightly different disk orientation with respect to periastron.

In the IC scenario and considering dominant adiabatic cooling of the shocked plasma as indicated by the measured spectrum, the observed variability pattern can be qualitatively explained by a varying confinement of the pulsar wind by the stellar mass outflow which results in different plasma flow velocities and therefore variable energy loss rates of the accelerated electrons. An alternative explanation, especially for the low flux state around periastron, is the deceleration of the unshocked pulsar wind by the increased rate of IC scattering near periastron. However, since the observed VHE γ-rays can be excluded to originate from the unshocked pulsar wind, the wind particles would have to have Lorentz factors below 10^6 or above 10^8 such that the resulting IC γ-rays are emitted at energies undetectable by H.E.S.S.

A leptonic origin of the emission should be favoured against a possible hadronic origin since it provides a rather consistent picture considering the broad band non-thermal emission of the source, especially at X-ray energies. Nevertheless, a detailed theoretical modeling of the presented results is needed and may provide further answers on the origin of the high energy emission of PSR B1259−63 / SS 2883. With the detection of PSR B1259−63 / SS 2883 as an emitter of VHE γ-rays, a new type of object is established in VHE γ-ray astronomy. The results clearly demonstrate the power of γ-ray observations for the study of the properties and the nature of high energy processes in this unique cosmic accelerator.

Appendix A

Central Data Acquisition System

Each telescope in the H.E.S.S. array is a heterogeneous system with several subsystems, as described in Chapter 2, that must be controlled and read out. The central DAQ system provides the connectivity and readout of all these systems. It takes over run control, the recording of event and slow control data, error handling, and monitoring of all subsystems.

A.1 Central DAQ Software

The H.E.S.S. central DAQ system is designed as a network of distributed C++ and *Python* objects, living in approximately 100 multi-threaded processes for the H.E.S.S. Phase I configuration. For inter-process communication the *omniORB* implementation [Lo and Pope, 1998] of the CORBA protocol standard is used which provides language bindings for C++ and Python. CORBA allows to call methods of objects in remote processes and to pass data objects. The transport and storage of objects needs a serialization mechanism which is provided by the *ROOT Data Analysis Framework* [Rademakers and Brun, 1997]. Both the ROOT-based H.E.S.S. data format and the ROOT graphics and histogram classes are used online and offline allowing a seamless integration of data analysis code and hence fast feedback.

A.1.1 The `StateController`

The base classes for all DAQ applications are provided by a central library. Derived classes, implementing the base class interfaces, control for example a hardware component or handle different types of data streams.

The data taking has to be performed in an ordered way using of the order of one hundred processes and considering dependencies between different tasks to be performed. E.g. the camera has to have the lid opened before the trigger can be started for the recording of camera data. Therefore, each DAQ process contains a `StateController` object which implements inter-process communication, states, and state transitions. Figure A.1 shows all possible states of a `StateController` and the transition allowed between the states. The states signalize the status of each process:

- *Safe*: The process and its possibly associated hardware is in a safe state where no damaging of or through the component can arise, e.g. during day time when no observations are

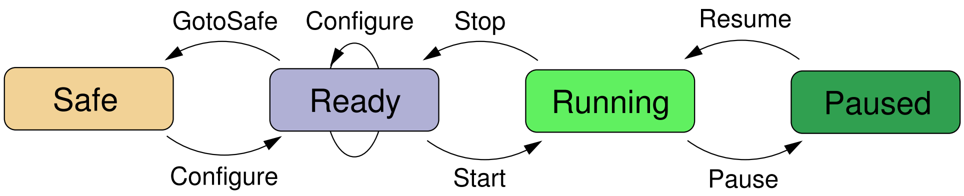

Figure A.1: *States and their transition of the* `StateController`*.*

performed and the telescopes have to be in a secure position, and the camera HV is off.

- *Ready*: The process is configured and ready for data taking, e.g. the camera lid is open and the telescope tracks the target position. Also, the process can take part in exchanging monitoring data, either by sending or receiving it.
- *Running*: The actual data taking is being performed.
- *Paused*: The data taking is suspended but can be resumed without reconfiguration.

In order to switch to a certain state, one or several tasks have to be performed implemented in state transitions. Only certain transitions are allowed between two individual states as illustrated in Fig. A.1:

- *Configure*: The process is brought from the *Safe* to the *Ready* state, e.g. positioning the telescopes, raise the HV of the camera to a low value, and opening the lid. A process has to be able to be reconfigured, e.g. due to a hardware failure, without being sent to a safe state before. Therefore, *Configure* is allowed to be invoked in the *Ready* state as well and represents the only transition for which the state may not change.
- *Start*: Start the data taking. This e.g. raises the HV to a nominal value and starts the camera trigger, and opens files for storing the data.
- *Pause, Resume*: Suspend and resume the data taking by e.g. disabling and re-enabling the camera trigger, respectively.
- *Stop*: Stop the data taking and bring the processes back to the *Ready* state, e.g. lowering the HV and close the data files.
- *GotoSafe*: Send the process to the *Safe* state, e.g. closing the camera lid and disable any telescope movement.

Any state transition is able to be interrupted by sending an *Interrupt* signal which resets the process to the pre-transition state.

A.1.2 Process Types

The DAQ system distinguishes four different process categories as shown in Fig. A.2. The *Controllers* directly interact with the hardware and read out the data. Each hardware component is controlled by one Controller process. The Controllers push the data to intermediate *Receivers*, which perform further processing and store the data. The Receivers also provide an interface that allows other processes to sample processed data. *Readers* actively request data from the Receivers at a rate different from the actual data-taking rate. The data or derived quantities are then available for display and monitoring purposes. *Manager* processes are not involved in the data transport but control the data-taking.

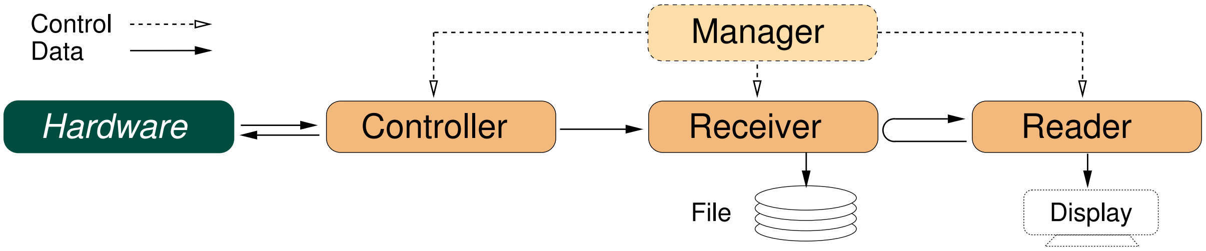

Figure A.2: *Types of processes in the DAQ system.*

Controllers

Each controller has an associated piece of hardware for which the states and transitions are implemented. Furthermore, most of the controllers produce data which have to be sent to one or more receivers. The data is filled into an object of a particular event class. Any external process which wants to receive this data has to *Subscribe* and *Unsubscribe* itself to the controller as a data receiver. For each subscriber, one or more data objects are packed into `Folders` which are written into a buffer on the controllers host machine. Each buffer is connected to the respective subscriber by a CORBA connection and the sending of the data occurs asynchronously in a separate thread.

Table A.1 lists some example controllers in the H.E.S.S. DAQ system with their function, states, and data types they produce together with their approximate event rates.

Receivers

The main data stream is produced by the cameras which generate events with a size of 1.5 kB. At the maximum system trigger rate of 400 Hz, this yields a maximum data rate of 2.4 MB/s for four telescopes, resulting in roughly 50 GB of data per observation night. The data rates from the other subsystems are significantly smaller.

The data Receivers have to store the data sent by Controllers in the local memory in order to allow other processes to fetch the data at a slower rate for monitoring purposes, and write the data to a file for archiving. This mechanism is implemented in a single generic process – the `Receiver` – which is able to receive and process any given H.E.S.S. data event. In the *Configure* transition, the `Receiver` reads its assigned Controller from the database, subscribes itself as a data receiver at the controller, and establishes a buffered CORBA connection. When *Start*ing, the receiver opens a file and sequentially processes all events in its input buffer until it is *Stop*ped and the files are being closed. This mechanism works well for all data with an input rate up to 100 Hz.

Since the camera data is sent as an unbuffered raw byte stream at a high data rate, there is a dedicated Receiver for this data – the `CameraReader`. This process has to provide an event buffer for the data of each telescope camera. The individual telescope events have to be merged into a single shower event using a unique event number provided by the central trigger. This event-building is performed online and the data is directly stored in the ROOT-format which is

Controller Name	**F**unction	**D**ata Types	*Safe*	*Ready*	*Running*
1 process per telescope					
Tracking	Drive system	Tracking 3 Hz, Monitoring 1 Hz	halted	positioning / tracking	tracking
CameraTrigger	Camera trigger / acquisition	Raw pixel data 400 Hz, Monitoring < 1 Hz	off	off	on
CameraHV	Camera high voltage control	Monitoring	disabled	400 V	1 kV
CameraLid	Camera lid		closed	open	open
Flatfield	Flatfield LED near the dish centre	Pulse rate monitoring 1 Hz	off	off	on
Radiometer	Paraxial radiometer	Temperature 1 Hz	off	connected	measuring
unique process					
CentralTrigger	Central trigger	Trigger bunch 0.2 Hz	off	VME board initialized	Check VME status
Meteo	Meteo station	Meteo event 1 Hz	off	connected	measuring

Table A.1: *Examples of hardware* Controllers *in the DAQ system with a brief description of their types and rates of data output, and the meaning of their states.*

used for later offline analysis. Since the rate at which the data is processed is lower than the data rate coming from the telescope cameras, many instances of the `CameraReader` – Nodes – distributed over different machines are required. The cameras send the data to one Node for a period of 5 s and then switch to another Node. The states *Running* and *Paused* are used to indicate the status of each Node, busy with data processing or available to receive new data, respectively. For observations with the full array of four telescopes, 20 Nodes are used routinely, providing a sufficient safety margin in order to avoid data loss in case of an unexpected increase of the data rate from the cameras.

Readers

Data readers fetch the data objects in `Folders` from the receivers for either duplicating a data stream, e.g. in order to store meteo data associated to an observation run, or for displaying purposes in the slow control of the array status. The first case is implemented by copying the object and writing it to a file.

The task of displaying the data is performed by a generic process using the ROOT graphics engine. This process – the `Displayer` – is solely configured by a database entry containing the type of the event which it has to fetch from a Receiver, the type of quantity contained in the event, the refresh rate, and the way in which the quantity should be displayed. During the *Configure* step, the `Displayer` reads its assigned database entries and opens dedicated graphics canvases. In the *Running* state it fetches the data from the assigned Receiver and draws the relevant quantities. Figure A.3 shows some examples of the various possibilities to configure the `Displayer`.

An intuitive and functional visualisation of the current state of the drive system cannot be easily implemented with the generic `Displayer` since it involves many different quantities in a rather complex interplay. Therefore, a dedicated *Tracking Display* was developed, conceptually similar to the other Reader processes with respect to the underlying data transfer and at the same time providing a compact display of the relevant status information of all telescopes in the array. Figure A.4 shows the tracking display during an observation run.

Managers

Managers are used for the state control of groups of processes in the central DAQ system. Furthermore, they serve as cross points in the message passing system. The functionality of Managers will be discussed in the next section.

A.1.3 Run Configuration

Different data-taking configurations of the array correspond to different *run types*. A run type is defined by a set of required Controllers, Receivers, Readers, and Managers. Examples for run types are the observation run type using most of the available subsystems, various calibration run types for the cameras, and dedicated run types for testing and data-taking with specific subsystems, e.g. the tracking system. An actual run is given by its type and a set of parameters, including a unique run number. All run type definitions, run parameters, the configuration of the DAQ system, and observation schedules are stored in a MySQL database acting as central information source and logging facility for the DAQ system.

An user-friendly way of creating a run schedule is provided by a graphical user interface (GUI) – the *Schedule Editor* – shown in Fig. A.5. It allows to choose a certain run type and to modify its parameters, such as the telescopes which will take part in the run, the target of observations, and the run duration etc.

A.1.4 Contexts & Sub-Arrays

Setting up the required processes for a specific run type is simplified by combining related processes in groups that are called *contexts*. An example for a context is `CT1` which comprises all Controllers accessing the hardware of telescope number 1. Thus, for example the CT1 context contains the processes `CT1/Tracking, CT1/CameraHV, CT1/Radiometer` etc. Every context contains one Manager, e.g. the `CT1/Manager` that is responsible to control the state transitions of all processes in its context (see Fig. A.6, left).

The status of all hardware components needs to be routinely monitored at any time. Therefore, a set of Receivers and Readers is grouped in the `SlowControl` context. The Receivers for all types of monitoring data are contained in the `SlowControl/Receiver` context, while the Readers, all of which are `Displayer` instances used for monitoring purposes, reside in the `SlowControl/Display` context. The Managers of these sub-contexts are controlled by the higher ranked `SlowControl/Manager` and all state transitions are recursively passed to the processes in the sub-contexts via their Managers.

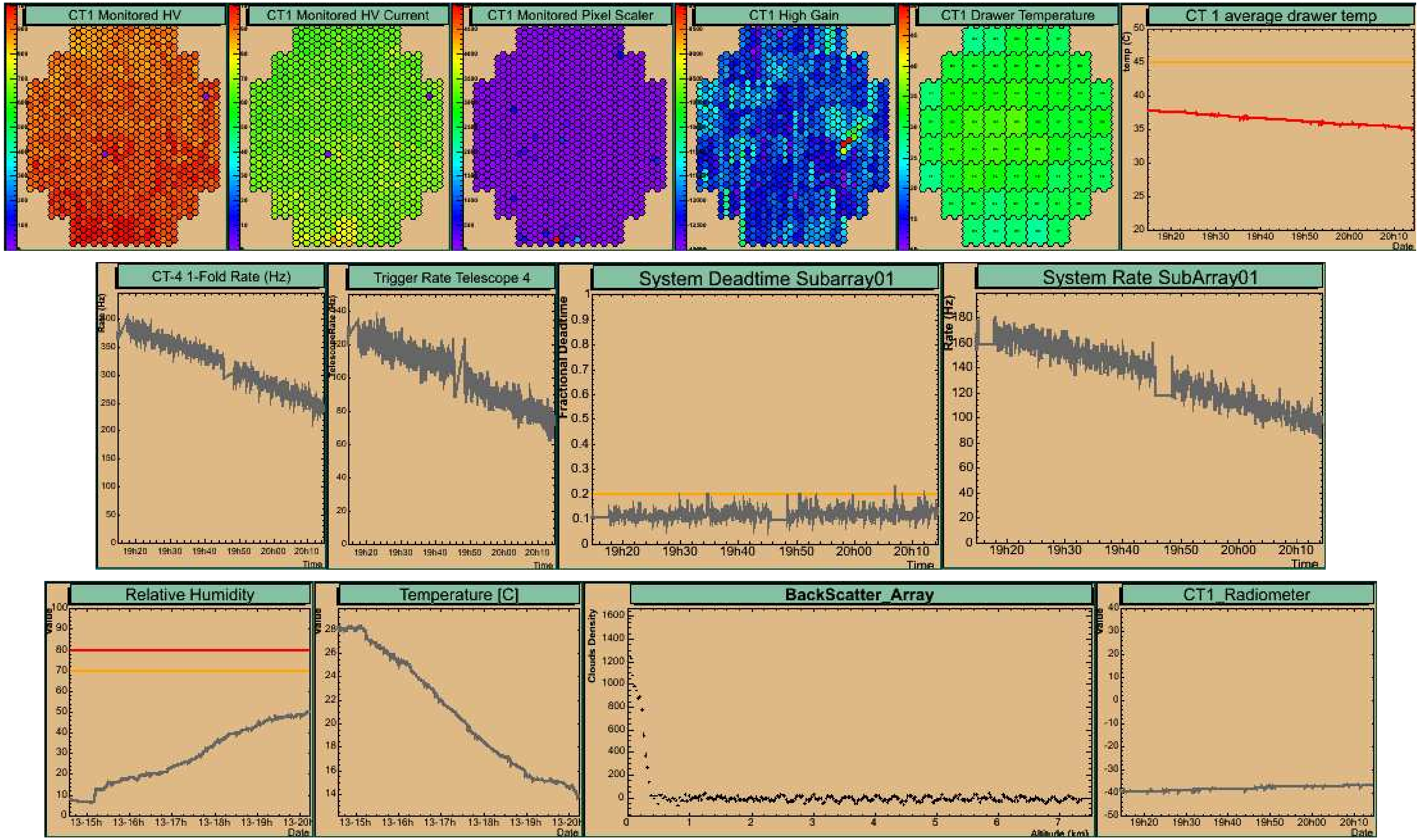

Figure A.3: *Examples of different configurations of the generic* `Displayer`*. Shown are some monitoring values during an observation run with an exceptional level of dust in the lower atmosphere.* ***T****op: Monitoring values in a single camera (from left to right): pixel HV, pixel HV current, pixel trigger activity (scalers), pixel intensity in ADC counts (with a typical shower image), drawer temperatures, and history of the mean drawer temperature in the camera.* ***M****iddle: History of trigger monitoring values: rate of multiplicity 1 triggers of one telescope, telescope trigger rate, mean fractional system dead time, and system trigger rate (multiplicity 2).* ***B****ottom: Weather monitoring: history of the relative humidity and temperature on the ground, amount of backscattered light measured by the ceilometer as a function of atmospheric height above the ground level, and the sky temperature in the field of view of one telescope as measured by the paraxial radiometer.*

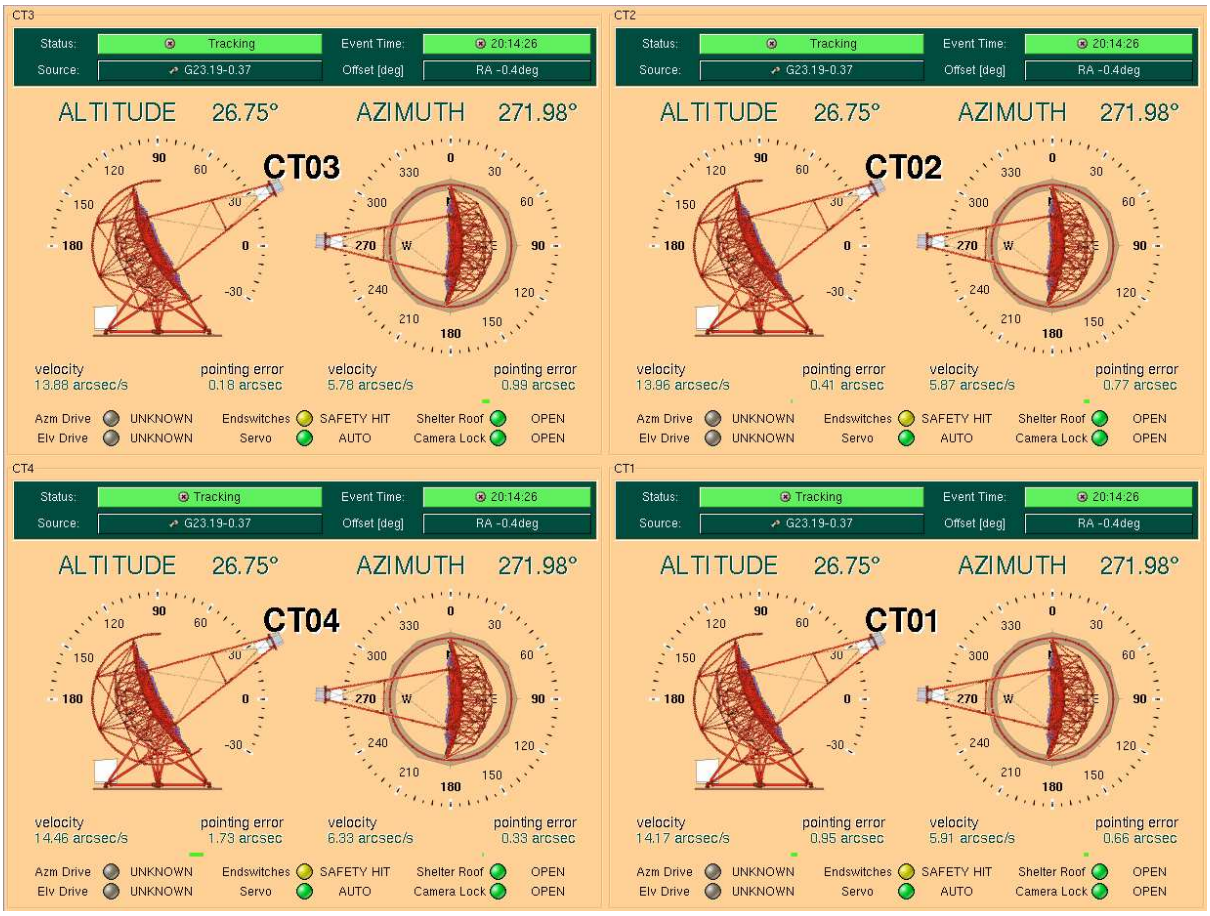

CT3
Status: Tracking
Event Time: 20:14:26
Source: G23.19-0.37
Offset [deg]: RA -0.4deg
ALTITUDE 26.75°
AZIMUTH 271.98°
velocity 13.88 arcsec/s
pointing error 0.18 arcsec
velocity 5.78 arcsec/s
pointing error 0.99 arcsec
Azm Drive UNKNOWN
Elv Drive UNKNOWN
Endswitches SAFETY HIT
Servo AUTO
Shelter Roof OPEN
Camera Lock OPEN

CT2
Status: Tracking
Event Time: 20:14:26
Source: G23.19-0.37
Offset [deg]: RA -0.4deg
ALTITUDE 26.75°
AZIMUTH 271.98°
velocity 13.96 arcsec/s
pointing error 0.41 arcsec
velocity 5.87 arcsec/s
pointing error 0.77 arcsec
Azm Drive UNKNOWN
Elv Drive UNKNOWN
Endswitches SAFETY HIT
Servo AUTO
Shelter Roof OPEN
Camera Lock OPEN

CT4
Status: Tracking
Event Time: 20:14:26
Source: G23.19-0.37
Offset [deg]: RA -0.4deg
ALTITUDE 26.75°
AZIMUTH 271.98°
velocity 14.46 arcsec/s
pointing error 1.73 arcsec
velocity 6.33 arcsec/s
pointing error 0.33 arcsec
Azm Drive UNKNOWN
Elv Drive UNKNOWN
Endswitches SAFETY HIT
Servo AUTO
Shelter Roof OPEN
Camera Lock OPEN

CT1
Status: Tracking
Event Time: 20:14:26
Source: G23.19-0.37
Offset [deg]: RA -0.4deg
ALTITUDE 26.75°
AZIMUTH 271.98°
velocity 14.17 arcsec/s
pointing error 0.95 arcsec
velocity 5.91 arcsec/s
pointing error 0.66 arcsec
Azm Drive UNKNOWN
Elv Drive UNKNOWN
Endswitches SAFETY HIT
Servo AUTO
Shelter Roof OPEN
Camera Lock OPEN

Figure A.4: *The tracking display.*

In order to be able to observe multiple targets at the same time with groups of telescopes or to perform test runs in parallel with observation, the array can be divided into subunits called *SubArrays* labeled by an increasing number, SubArray01 etc. Since the data recorded during regular observation has to be written separately for each SubArray, the corresponding Readers and Receivers are grouped into sub-contexts of each SubArray context, e.g. Receivers of the first SubArray are grouped in the `SubArray01/Receiver` context.

The Nodes are put into contexts with increasing number, `Node01...NodeNN`, and are named `NodeXX/Receiver`. This allows for a flexible assignment of the available Nodes to one particular SubArray.

A.1.5 Process Handling

At startup of the DAQ system, a central `ResourceHandler` and one `HostHandler` is launched on each host of the computer cluster (see Sec. A.2). The `ResourceHandler` reads the information about the process hierarchy from the database, connects to the corresponding `HostHandler` of each process, and asks it to launch the process. Furthermore, the `ResourceHandler` brings the `SlowControl` context to the *Running* state by issuing a *Configure* and *Start* transition of the `SlowControl/Manager` which is propagated to all processes in this context via the Managers

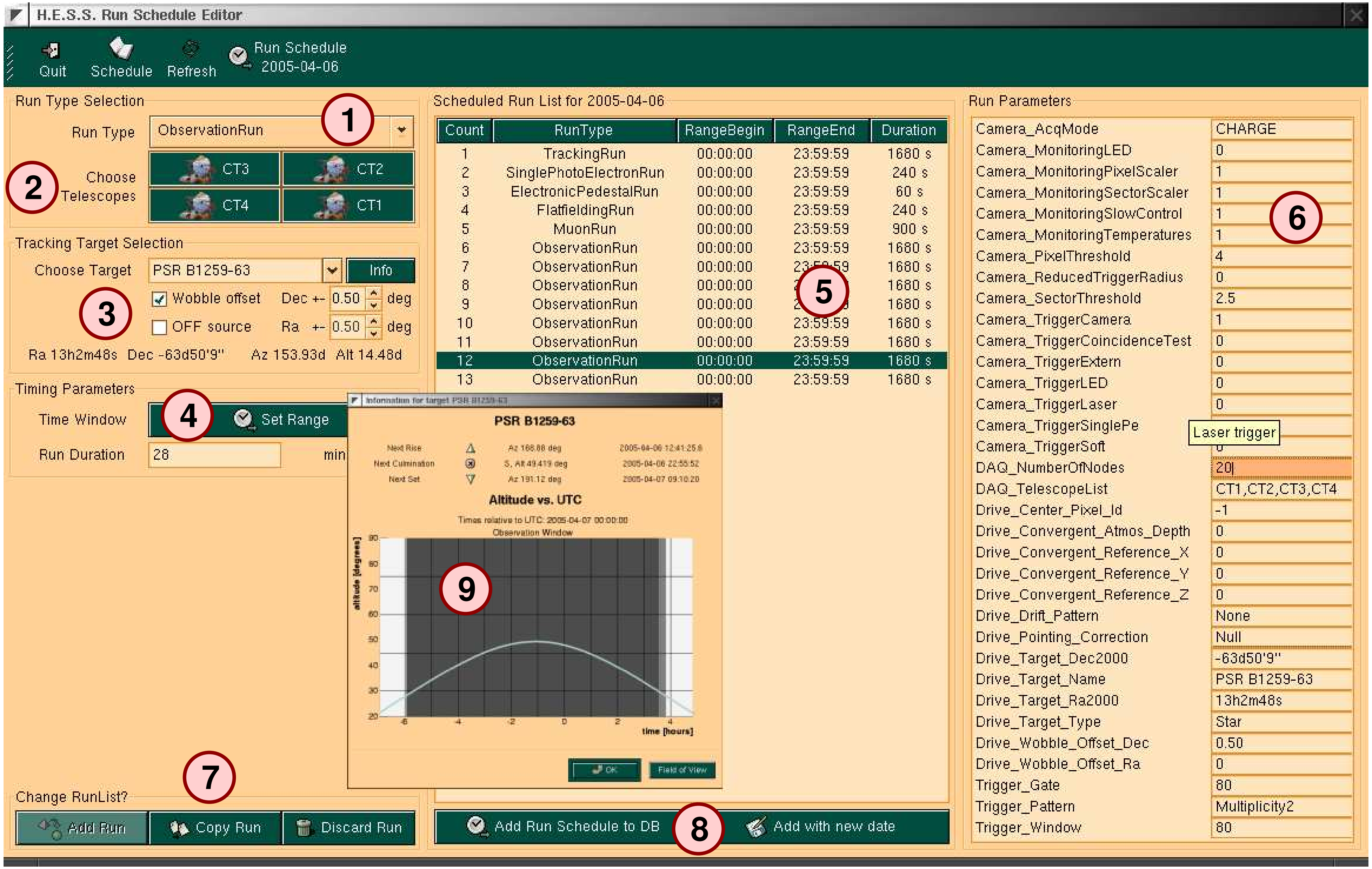

Run Type: ObservationRun

Choose Target: PSR B1259-63

☑ Wobble offset Dec +- 0.50 deg

☐ OFF source Ra +- 0.50 deg

Ra 13h2m48s Dec -63d50'9'' Az 153.93d Alt 14.48d

Run Duration: 28 min

Scheduled Run List for 2005-04-06

Count	RunType	RangeBegin	RangeEnd	Duration
1	TrackingRun	00:00:00	23:59:59	1680 s
2	SinglePhotoElectronRun	00:00:00	23:59:59	240 s
3	ElectronicPedestalRun	00:00:00	23:59:59	60 s
4	FlatfieldingRun	00:00:00	23:59:59	240 s
5	MuonRun	00:00:00	23:59:59	900 s
6	ObservationRun	00:00:00	23:59:59	1680 s
7	ObservationRun	00:00:00	23:59:59	1680 s
8	ObservationRun	00:00:00	[illegible]	1680 s
9	ObservationRun	00:00:00	[illegible]	1680 s
10	ObservationRun	00:00:00	23:59:59	1680 s
11	ObservationRun	00:00:00	23:59:59	1680 s
12	ObservationRun	00:00:00	23:59:59	1680 s
13	ObservationRun	00:00:00	23:59:59	1680 s

Run Parameters

Camera_AcqMode	CHARGE
Camera_MonitoringLED	0
Camera_MonitoringPixelScaler	1
Camera_MonitoringSectorScaler	1
Camera_MonitoringSlowControl	1
Camera_MonitoringTemperatures	1
Camera_PixelThreshold	4
Camera_ReducedTriggerRadius	0
Camera_SectorThreshold	2.5
Camera_TriggerCamera	1
Camera_TriggerCoincidenceTest	0
Camera_TriggerExtern	0
Camera_TriggerLED	0
Camera_TriggerLaser	0
Camera_TriggerSinglePe	[illegible]
Camera_TriggerSoft	0
DAQ_NumberOfNodes	20
DAQ_TelescopeList	CT1,CT2,CT3,CT4
Drive_Center_Pixel_Id	-1
Drive_Convergent_Atmos_Depth	0
Drive_Convergent_Reference_X	0
Drive_Convergent_Reference_Y	0
Drive_Convergent_Reference_Z	0
Drive_Drift_Pattern	None
Drive_Pointing_Correction	Null
Drive_Target_Dec2000	-63d50'9''
Drive_Target_Name	PSR B1259-63
Drive_Target_Ra2000	13h2m48s
Drive_Target_Type	Star
Drive_Wobble_Offset_Dec	0.50
Drive_Wobble_Offset_Ra	0
Trigger_Gate	80
Trigger_Pattern	Multiplicity2
Trigger_Window	80

PSR B1259-63

Next Rise	△	Az 166.88 deg	2005-04-06 12:41:25.8
Next Culmination	⊗	S, Alt 49.419 deg	2005-04-06 22:55:52
Next Set	▽	Az 191.12 deg	2005-04-07 09:10:20

Times relative to UTC: 2005-04-07 00:00:00

Figure A.5: *The Schedule Editor. Short descriptions of the elements: 1. Run type selector, 2. Telescope selector, 3. Tracking target field, the target name can be entered or selected from a pre-defined list and the wobble offsets can be altered, 4. Run timing, 5. List of all scheduled runs for the selected date, 6. List of all run parameters and their values which can be changed, 7. Buttons for run list alteration, 8. Button for saving the run list in the database, 9. Optional target information window.*

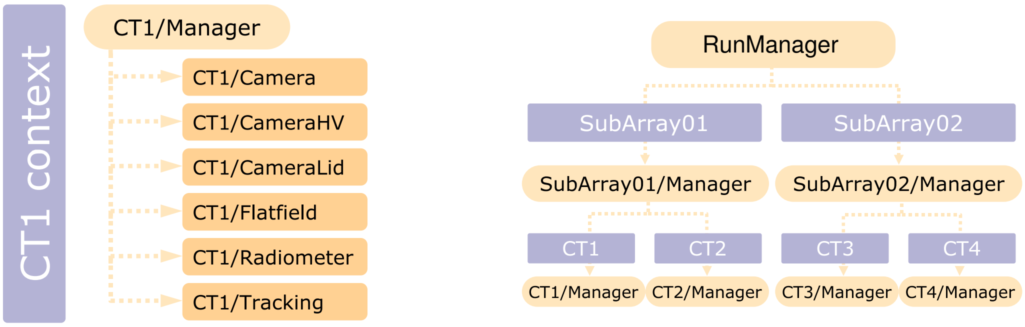

Figure A.6: *Examples of contexts and their usage.* ***L****eft: Context containing all Controllers of telescope 1.* ***R****ight: Concept of SubArrays and the Manager hierarchy.*

of the sub-contexts.

After startup, the `ResourceHandler` checks every second that all processes are alive and restarts a process, in case it was terminated for any reason. Additionally, the `ResourceHandler` keeps track of the assignment of the hardware resources, namely the Controllers and Nodes, to a certain SubArray, prohibiting all attempts from any Manager to access a certain resource more than once.

A.1.6 Run Control

For data-taking, a central *RunManager* reads the observation schedule from the database and determines the actual sequence of runs according to the availability of contexts and passes the run configuration to the Manager of the SubArray context – the `SubArray/Manager` (see Fig. A.6, right). This Manager gains the control of all participating contexts, e.g. for an observation run these are the `CTX` contexts of the participating telescopes, a number of `NodeXX` contexts, and all sub-contexts in the `SubArray` context, and signalises the `ResourceHandler` to make these contexts unavailable (lock). The state of the `SubArray/Manager` reflects the state of all child processes taking part in the run and state transitions are performed for all of these child processes in parallel.

For some of the processes taking part in one run, the state transition has to be performed consecutively, e.g. the file of the `Node/Receiver` has to be opened before the camera trigger `CTX/CameraTrigger` is started, both of which is done in the *Start* transition. These dependencies are handled by the context Managers. The Managers keep a list of the processes on which their child processes depend on, which they read from the database. Upon the *Start* transition in the example above, the `CTX/Manager` contacts the `NodeXX/Manager` and waits until the `NodeXX/Receiver` finished its transition. If this is the case, it invokes *Start* on `CTX/CameraTrigger`.

A certain run is finished, if the `SubArray/Manager` successfully performed a sequence of state transitions: *Configure*, *Start*, and *Stop*. After run stop, the Manager unlocks its associated contexts at the `ResourceHandler` and they are free to be used in a subsequent run.

A.1.7 Message Passing and Error Handling

In order to provide some feedback to the shift crew and handle possible errors, a message passing system is implemented for each DAQ process. Each message produced by a process is passed via its context Manager to the assigned `SubArray/Manager` (see Fig. A.7). Several messages types are defined:

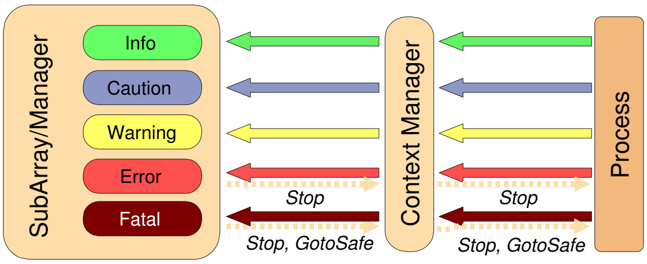

Figure A.7: *Message passing in the central DAQ.*

- *Info*: This is used for notifying and has no further implications. The message is added to the DAQ log as all other message types.
- *Caution*: The process has noted an unusual behaviour. A single occurrence is unproblematic but a massive number of Cautions should be noted by the shift crew, and thus a muted audio signal is played. No automatic action is taken by the DAQ.
- *Warning*: A problem occurred which has to be investigated but does not directly prevent data taking. A notification window is raised containing the message and a sound is played. No automatic action is taken by the DAQ.
- *Error*: An error has occurred which prevents taking useful data. Besides a similar notification as for the Warning, the `SubArray/Manager` initiates the *Stop* transition, stopping any ongoing data taking. If the Error occurs during a state transition, the transition is interrupted before.
- *Fatal*: A serious error has occurred which makes it necessary to take further action to avoid damage of any detector components. In addition to the steps performed for the Error message, the `SubArray/Manager` initiates the *GotoSafe* transition after the data taking has been stopped.

Whenever a DAQ process issues an *Error*, it depends on the actual run type if this error prevents taking useful data. E.g. during regular observations, if the `CT1/Radiometer` issues an Error there is no need to stop the data taking, while during a dedicated run for testing the radiometer or measuring the quality of the atmosphere, the run can be stopped since the radiometer is the primary source of data. In order to take this into account, each context Manager keeps a list of *required* and *optional* processes depending on the run type. If a *required* process issues an Error, this is passed on to the `SubArray/Manager`, in case of an *optional* process the Error is converted into a Warning.

A.1.8 Array Control Interface

The shift crew interacts with the DAQ system via a central control GUI providing an access point to the system and direct monitoring of the states of the different processes. A screen shot of the GUI during regular data taking is shown in Fig. A.8.

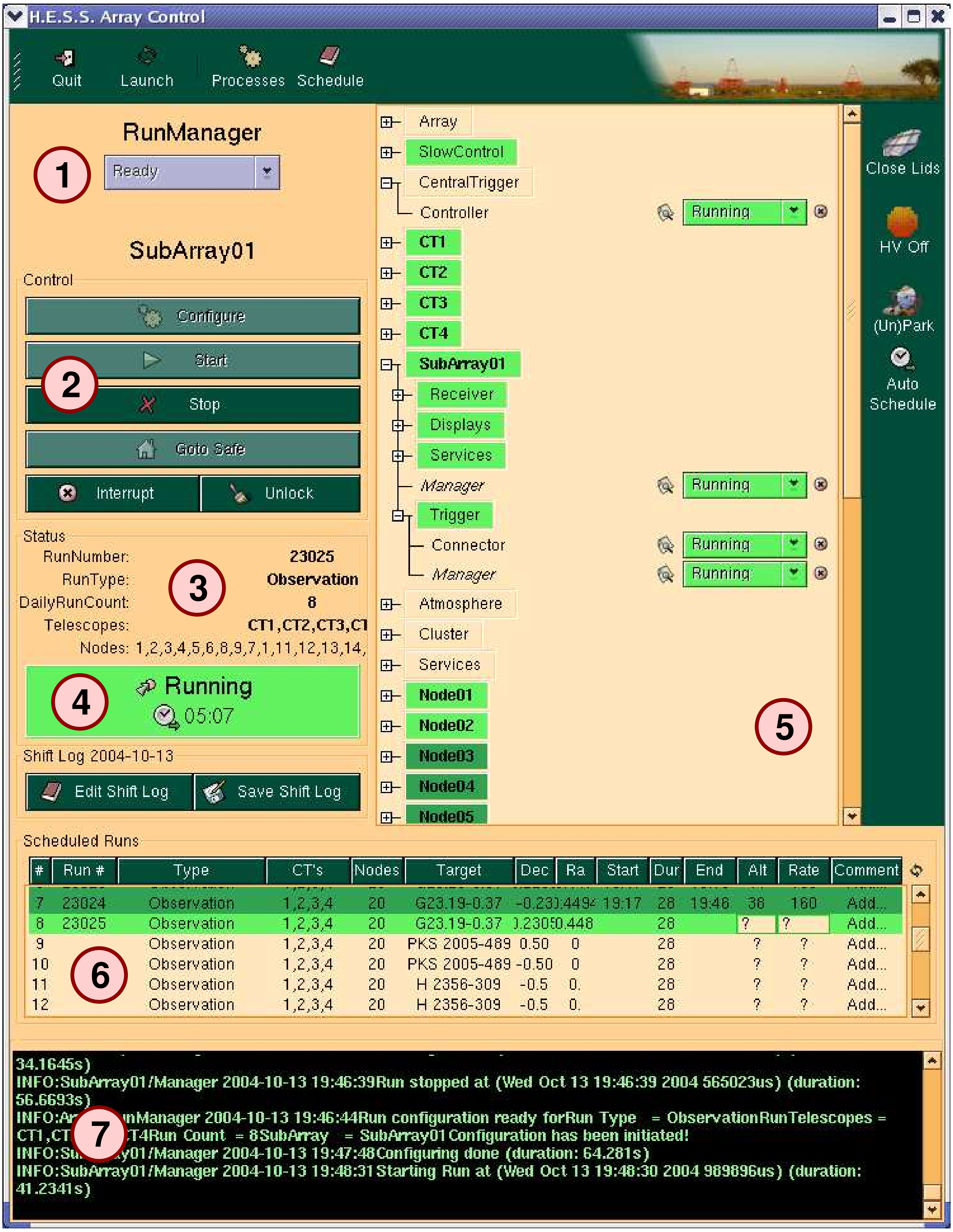

RunManager: Ready

Status
RunNumber: 23025
RunType: Observation
DailyRunCount: 8
Telescopes: CT1,CT2,CT3,C1
Nodes: 1,2,3,4,5,6,8,9,7,1,11,12,13,14,

Running 05:07

Scheduled Runs

#	Run #	Type	CT's	Nodes	Target	Dec	Ra	Start	Dur	End	Alt	Rate	Comment
7	23024	Observation	1,2,3,4	20	G23.19-0.37	-0.23	):4494	19:17	28	19:46	38	160	Add...
8	23025	Observation	1,2,3,4	20	G23.19-0.37	).2305	0.448		28		?	?	Add...
9		Observation	1,2,3,4	20	PKS 2005-489	0.50	0		28		?	?	Add...
10		Observation	1,2,3,4	20	PKS 2005-489	-0.50	0		28		?	?	Add...
11		Observation	1,2,3,4	20	H 2356-309	-0.5	0.		28		?	?	Add...
12		Observation	1,2,3,4	20	H 2356-309	-0.5	0.		28		?	?	Add...

```
34.1645s)
INFO:SubArray01/Manager 2004-10-13 19:46:39Run stopped at (Wed Oct 13 19:46:39 2004 565023us) (duration:
56.6693s)
INFO:Ar      nManager 2004-10-13 19:46:44Run configuration ready forRun Type   = ObservationRunTelescopes =
CT1,CT      T4Run Count  = 8SubArray   = SubArray01 Configuration has been initiated!
INFO:Su      y01/Manager 2004-10-13 19:47:48Configuring done (duration: 64.281s)
INFO:SubArray01/Manager 2004-10-13 19:48:31 Starting Run at (Wed Oct 13 19:48:30 2004 989896us) (duration:
41.2341s)
```

Figure A.8: *The central DAQ GUI. The different elements are shortly described: 1.* `RunManager` *state control, 2.* `SubArray/Manager` *state control, 3. Main parameters of the current run. 4. SubArray state and remaining run time, 5. List of all running DAQ processes and their states ordered in the context hierarchy, 6. List of processed, ongoing, and scheduled runs along with a selection of important run parameters. 7. Logging window of DAQ messages.*

A.2 Central DAQ Hardware

The central DAQ computing hardware has to supply the resources for the different DAQ processes, provide the connectivity between the individual hardware components, and allow the shift crew to control and monitor the array using the interfaces introduced in the last section. Figure A.9 shows a schematic view of the hardware used and the connections between the different components.

The telescope camera trigger signals are sent via glass fibre links to the central trigger system, which is located in the central control building. The main data stream of the telescope cameras is also transferred via independent fibre cables to a computing farm in the control building containing currently 24 individual rack-mounted computers (see Fig. A.10). The data is routed via a GBit switch to the cluster of *Data Nodes* which process the data and write them onto an array of hard disks hosted by a *Storage Server*. On each Data Node, two `Node/Receivers` are running, each of them exclusively using one CPU of the dual processor machine for data processing. This data acquisition chain was tested to operate stably for system event rates up to 2 kHz.

Two *Server* machines containing the database, the CORBA name service, the user file system, and hosting two tape drives used for data archiving are additionally connected to the main switch. A second, fast Ethernet switch (100 kBit/s) connects ordinary *Nodes* to the main switch, on which the other DAQ processes are running. A global positioning system (GPS) time server provides accurate timing for all farm machines.

At the telescopes, a *CCD Server* provides the connection to the Sky- and Lid-CCDs. This machine and the other hardware components of the telescope such as the tracking system, radiometer, and flatfield LEDs are connected to a small switch, which is also linked to the control building via a fibre cable.

The shift crew works on desktop machines in a dedicated control room within the control building. A special PC with four screens is used for a coherent monitoring of the array status using the various instances of the `Displayer` process. All machines inside the control building are connected to an uninterruptable power supply (UPS) which provides power for roughly 20 minutes in case of a generator breakdown (occurring quite regularly).

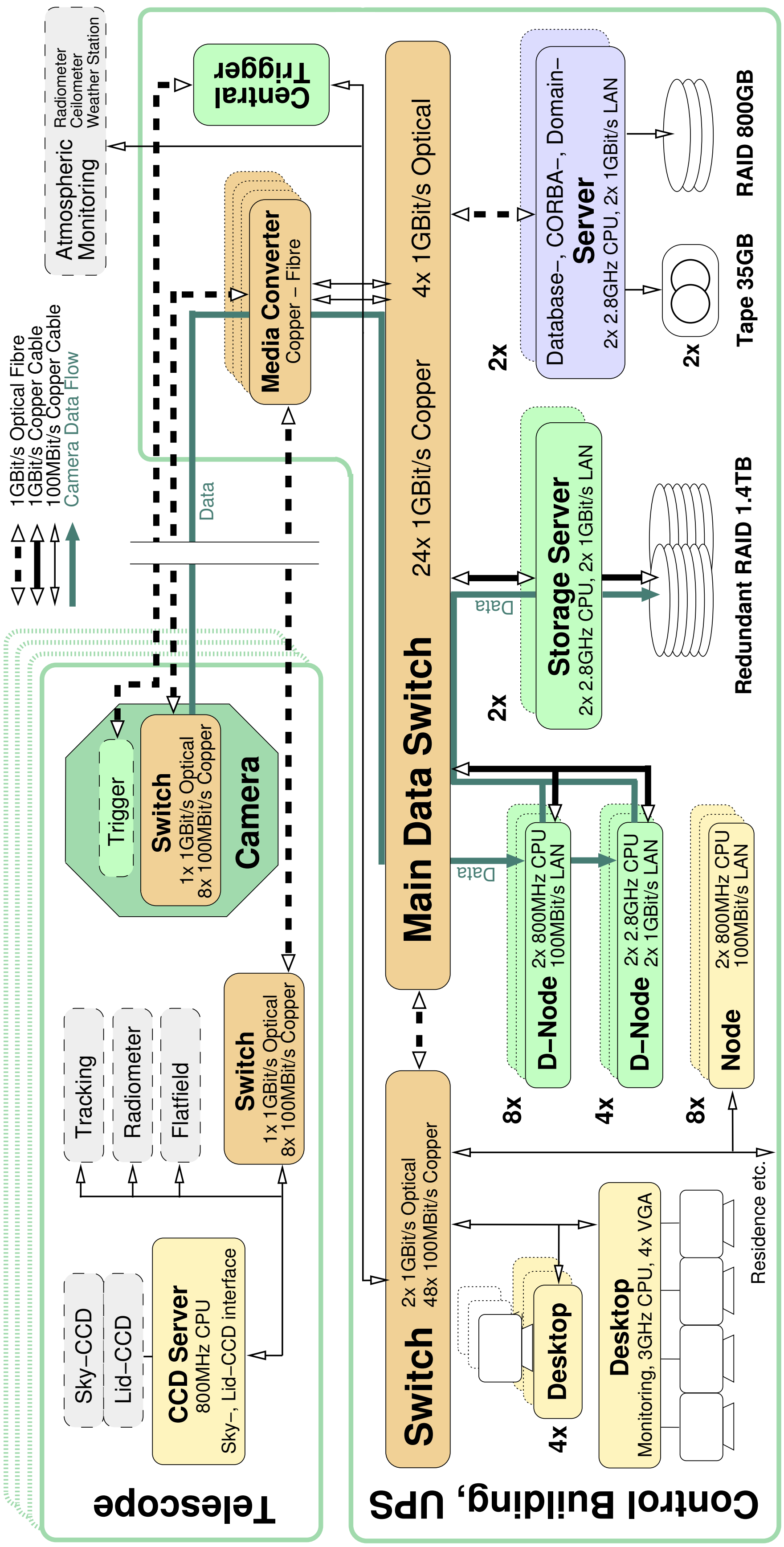

Figure A.9: *Schematic view of the H.E.S.S. DAQ system hardware which is described in the text.*

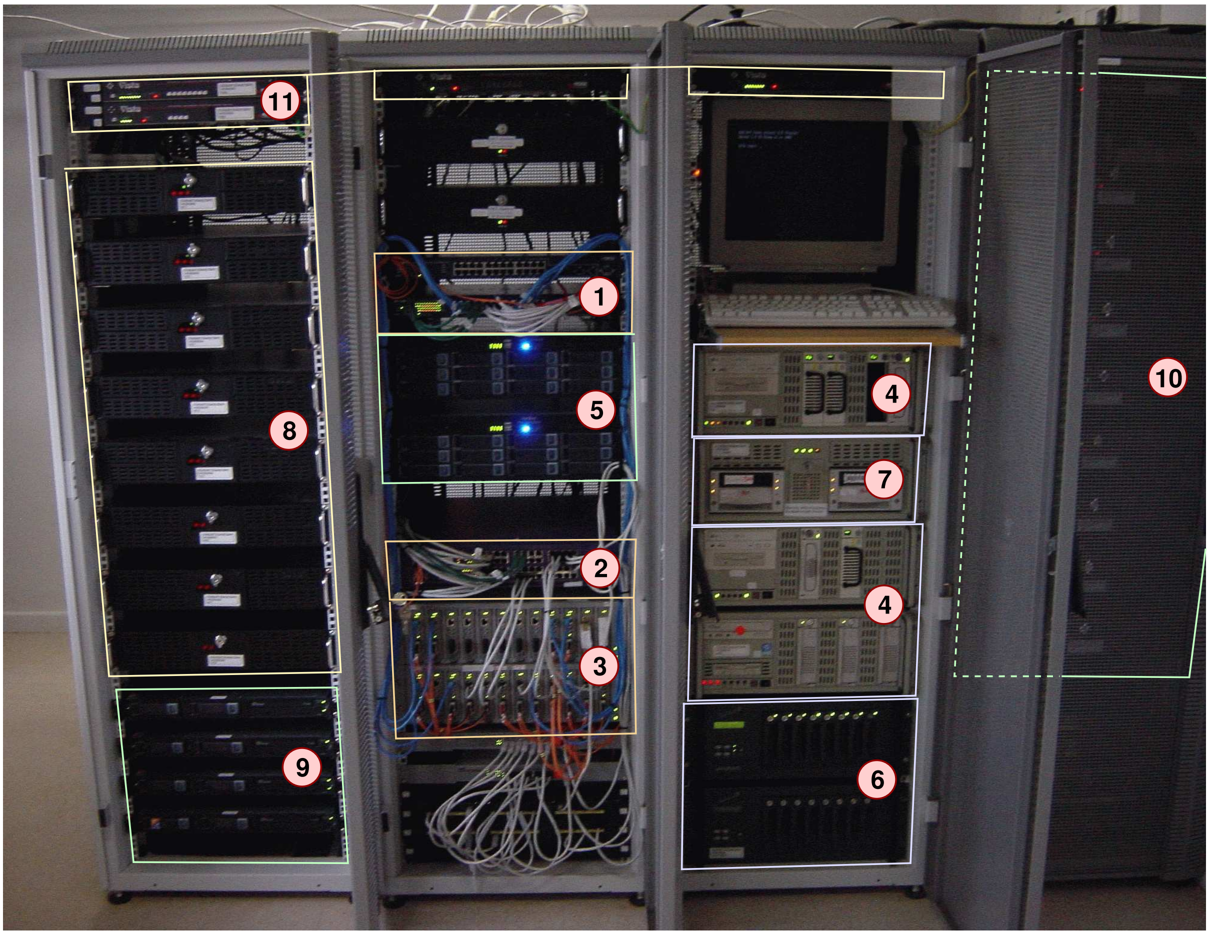

Figure A.10: *Main computing cluster of the DAQ system. The individual components in Fig. A.9 correspond to: 1 - Main data switch (+spare). 2 - 48 port switch. 3 - Media converters. 4 - Servers (2+spare). 5 - Storage servers (2×1.4 GB). 6 - RAID system (0.8 GB+spare). 7 - Tape drives. 8 - Data nodes (8×0.8 GHz). 9 - Data nodes (4×2.8 GHz). 10 - Nodes (8×0.8 GHz). 11 - Keyboard switches.*

Appendix B

Run Lists of the PSR B1259−63 and Crab Nebula Datasets

The following table shows the run lists of the data sets from observations of PSR B1259−63 in 2004 and the Crab Nebula in 2003, which passed the quality selection and was considered in the analysis of this work. Listed for each observation run of 28 minutes is the H.E.S.S. internal run number, the name of the target of the observation, the wobble offset in RA and Dec, the number of telescopes with valid shower data, the start time, and the total number of shower events recorded.

Run **N**umber	**T**arget Name	**O**ffset [°]		N_{tel}	**S**tart Time [y-m-d h:m:s]	**E**vents 10^3
		RA	**D**ec			
19140	PSR B1259-63	0.0	0.5	3	2004-02-27 00:39:33	512
19141	PSR B1259-63	0.0	-0.5	3	2004-02-27 01:13:07	509
19142	PSR B1259-63	0.0	0.5	3	2004-02-27 01:45:08	518
19143	PSR B1259-63	0.0	-0.5	3	2004-02-27 02:17:05	498
19147	PSR B1259-63	0.0	0.5	3	2004-02-27 03:03:06	361
19179	PSR B1259-63	0.0	0.5	3	2004-02-28 01:27:00	523
19180	PSR B1259-63	0.0	-0.5	3	2004-02-28 02:00:19	514
19181	PSR B1259-63	0.0	0.5	3	2004-02-28 02:32:20	514
19208	PSR B1259-63	0.0	-0.5	3	2004-02-29 01:45:06	515
19209	PSR B1259-63	0.0	0.5	3	2004-02-29 02:21:09	524
19237	PSR B1259-63	0.0	0.5	3	2004-03-01 01:04:18	545
19238	PSR B1259-63	0.0	-0.5	3	2004-03-01 01:37:28	530
19239	PSR B1259-63	0.0	0.5	3	2004-03-01 02:11:12	528
19271	PSR B1259-63	0.0	0.5	3	2004-03-02 00:51:01	524
19272	PSR B1259-63	0.0	-0.5	3	2004-03-02 01:24:36	512
19277	PSR B1259-63	0.0	0.5	3	2004-03-02 03:09:12	297
19312	PSR B1259-63	0.0	-0.5	3	2004-03-03 01:16:03	542
19313	PSR B1259-63	0.0	0.5	3	2004-03-03 01:48:11	533
19319	PSR B1259-63	0.5	0.5	3	2004-03-03 02:55:39	508
19868	PSR B1259-63	0.0	-0.5	4	2004-03-18 21:05:07	472
19869	PSR B1259-63	0.0	0.5	4	2004-03-18 21:05:07	487
19870	PSR B1259-63	0.0	-0.5	4	2004-03-18 21:05:07	488

Run	**T**arget Name	**O**ffset [°]		N_{tel}	**S**tart Time	**E**vents
Number		**R**A	**D**ec		[y-m-d h:m:s]	10^3
19871	PSR B1259-63	0.0	0.5	4	2004-03-18 21:05:07	489
19872	PSR B1259-63	0.0	-0.5	4	2004-03-18 21:05:07	483
19928	PSR B1259-63	0.0	-0.5	4	2004-03-20 00:49:35	455
19929	PSR B1259-63	0.0	0.5	4	2004-03-20 00:49:35	442
19931	PSR B1259-63	0.0	0.5	4	2004-03-20 00:49:35	389
20004	PSR B1259-63	0.0	-0.5	4	2004-03-21 18:21:21	478
20005	PSR B1259-63	0.0	0.5	4	2004-03-21 18:21:21	470
20006	PSR B1259-63	0.0	-0.5	4	2004-03-21 18:21:21	449
20008	PSR B1259-63	0.0	-0.5	4	2004-03-21 18:21:21	437
20009	PSR B1259-63	0.0	0.5	4	2004-03-21 18:21:21	425
20052	PSR B1259-63	0.0	0.5	4	2004-03-22 18:24:40	511
20053	PSR B1259-63	0.0	-0.5	4	2004-03-22 18:24:40	491
20054	PSR B1259-63	0.0	0.5	4	2004-03-22 18:24:40	482
20055	PSR B1259-63	0.0	-0.5	4	2004-03-22 18:24:40	456
20056	PSR B1259-63	0.0	0.5	4	2004-03-22 18:24:40	438
20081	PSR B1259-63	0.0	0.5	4	2004-03-23 18:42:06	520
20082	PSR B1259-63	0.0	-0.5	4	2004-03-23 18:42:06	510
20083	PSR B1259-63	0.0	0.5	4	2004-03-23 18:42:06	517
20084	PSR B1259-63	0.0	-0.5	4	2004-03-23 18:42:06	494
20085	PSR B1259-63	0.0	0.5	4	2004-03-23 18:42:06	476
20086	PSR B1259-63	0.0	-0.5	4	2004-03-23 18:42:06	447
20087	PSR B1259-63	0.0	0.5	4	2004-03-23 18:42:06	415
20109	PSR B1259-63	0.0	0.5	4	2004-03-25 00:14:48	501
20110	PSR B1259-63	0.0	-0.5	4	2004-03-25 00:50:21	480
20111	PSR B1259-63	0.0	0.5	4	2004-03-25 01:20:38	471
20112	PSR B1259-63	0.0	-0.5	4	2004-03-25 01:50:52	454
20113	PSR B1259-63	0.0	0.5	4	2004-03-25 02:21:14	434
20129	PSR B1259-63	0.0	0.5	4	2004-03-25 22:25:26	490
20131	PSR B1259-63	0.0	-0.5	4	2004-03-26 00:00:54	493
20133	PSR B1259-63	0.0	-0.5	4	2004-03-26 01:18:13	459
20135	PSR B1259-63	0.0	0.5	4	2004-03-26 02:25:10	431
20143	PSR B1259-63	0.0	0.5	4	2004-03-26 22:00:45	480
20145	PSR B1259-63	0.0	0.5	4	2004-03-26 23:04:55	497
20149	PSR B1259-63	0.0	-0.5	4	2004-03-27 01:26:05	442
20150	PSR B1259-63	0.0	0.5	4	2004-03-27 01:56:16	434
20167	PSR B1259-63	0.0	0.5	4	2004-03-27 23:38:14	480
20168	PSR B1259-63	0.0	-0.5	4	2004-03-28 00:08:46	462
20182	PSR B1259-63	0.0	0.5	4	2004-03-28 22:24:12	487
20183	PSR B1259-63	0.0	-0.5	4	2004-03-28 22:54:46	481
20237	PSR B1259-63	0.0	0.5	3	2004-04-12 21:40:29	484
20239	PSR B1259-63	0.0	-0.5	3	2004-04-12 22:14:55	473
20278	PSR B1259-63	0.0	0.5	4	2004-04-14 21:24:04	448
20279	PSR B1259-63	0.0	-0.5	4	2004-04-14 21:54:28	442

Run **N**umber	**T**arget Name	**O**ffset [°] **R**A	 **D**ec	N_{tel}	**S**tart Time [y-m-d h:m:s]	**E**vents 10^3
20318	PSR B1259-63	0.0	-0.5	4	2004-04-16 21:25:18	540
20319	PSR B1259-63	0.0	0.5	4	2004-04-16 21:55:32	544
20361	PSR B1259-63	0.0	0.5	4	2004-04-18 21:18:29	458
20362	PSR B1259-63	0.0	-0.5	4	2004-04-18 21:48:47	441
20411	PSR B1259-63	0.0	-0.5	4	2004-04-20 21:05:19	489
20412	PSR B1259-63	0.0	0.5	4	2004-04-20 21:35:34	500
20483	PSR B1259-63	0.0	0.5	4	2004-04-22 21:27:02	476
20484	PSR B1259-63	0.0	-0.5	4	2004-04-22 21:57:14	468
20667	PSR B1259-63	0.0	0.5	4	2004-05-09 19:44:31	469
20668	PSR B1259-63	0.0	-0.5	4	2004-05-09 20:14:41	463
20681	PSR B1259-63	0.0	0.5	4	2004-05-10 20:45:04	469
20682	PSR B1259-63	0.0	-0.5	4	2004-05-10 21:15:18	455
20694	PSR B1259-63	0.0	0.5	4	2004-05-11 19:46:39	469
20695	PSR B1259-63	0.0	-0.5	4	2004-05-11 20:16:43	470
20696	PSR B1259-63	0.5	0.0	4	2004-05-11 20:46:55	471
20697	PSR B1259-63	-0.5	0.0	4	2004-05-11 21:17:17	453
20752	PSR B1259-63 North	-0.5	0.0	4	2004-05-14 17:40:11	417
20753	PSR B1259-63 North	0.5	0.0	4	2004-05-14 18:10:17	418
20754	PSR B1259-63 North	-0.5	0.0	4	2004-05-14 18:40:24	433
20755	PSR B1259-63 North	0.5	0.0	4	2004-05-14 19:10:33	445
20799	PSR B1259-63 North	-0.5	0.0	4	2004-05-16 17:39:22	437
20800	PSR B1259-63 North	0.5	0.0	4	2004-05-16 18:09:29	447
20805	PSR B1259-63 North	-0.5	0.0	4	2004-05-16 20:44:19	456
20827	PSR B1259-63 North	0.5	0.0	4	2004-05-17 17:39:15	359
20828	PSR B1259-63 North	-0.5	0.0	4	2004-05-17 18:09:24	386
20830	PSR B1259-63 North	-0.5	0.0	4	2004-05-17 19:09:45	403
20864	PSR B1259-63 North	-0.5	0.0	4	2004-05-20 18:05:35	376
20865	PSR B1259-63 North	0.5	0.0	4	2004-05-20 18:35:51	386
20866	PSR B1259-63 North	-0.5	0.0	4	2004-05-20 19:06:07	396
20889	PSR B1259-63 North	0.5	0.0	4	2004-05-21 17:57:03	399
20890	PSR B1259-63 North	-0.5	0.0	4	2004-05-21 18:27:17	410
21102	PSR B1259-63 North	0.5	0.0	4	2004-06-10 19:53:47	432
21103	PSR B1259-63 North	-0.5	0.0	4	2004-06-10 20:23:55	407
21104	PSR B1259-63 North	0.5	0.0	4	2004-06-10 20:53:58	397
21106	PSR B1259-63 North	-0.5	0.0	4	2004-06-10 21:38:37	255
21115	PSR B1259-63 North	-0.5	0.0	4	2004-06-11 17:52:06	390
21117	PSR B1259-63 North	0.5	0.0	4	2004-06-11 18:26:19	390
21119	PSR B1259-63 North	0.5	0.0	4	2004-06-11 19:28:15	380
21120	PSR B1259-63 North	-0.5	0.0	4	2004-06-11 20:00:19	356
21121	PSR B1259-63 North	0.5	0.0	4	2004-06-11 20:30:26	347
21137	PSR B1259-63 North	-0.5	0.0	4	2004-06-12 18:11:09	407
21138	PSR B1259-63 North	0.5	0.0	4	2004-06-12 18:41:15	416
21139	PSR B1259-63 North	-0.5	0.0	4	2004-06-12 19:11:26	412

Run **N**umber	**T**arget Name	**O**ffset [°] **R**A	**D**ec	N_{tel}	**S**tart Time [y-m-d h:m:s]	**E**vents 10^3
21155	PSR B1259-63 North	-0.5	0.0	4	2004-06-13 17:37:02	402
21156	PSR B1259-63 North	0.5	0.0	4	2004-06-13 18:07:10	416
21157	PSR B1259-63 North	-0.5	0.0	4	2004-06-13 18:37:17	417
21158	PSR B1259-63 North	0.5	0.0	4	2004-06-13 19:07:24	424
21177	PSR B1259-63 North	0.5	0.0	4	2004-06-14 17:40:40	455
21178	PSR B1259-63 North	-0.5	0.0	4	2004-06-14 18:10:52	448
21179	PSR B1259-63 North	0.5	0.0	4	2004-06-14 18:41:06	450
21180	PSR B1259-63 North	-0.5	0.0	4	2004-06-14 19:11:13	437
21204	PSR B1259-63 North	-0.5	0.0	4	2004-06-15 17:55:00	428
21205	PSR B1259-63 North	0.5	0.0	4	2004-06-15 18:25:10	439
16266	Crab Nebula	0.0	0.5	3	2003-10-23 00:48:22	352
16357	Crab Nebula	0.0	-0.5	3	2003-10-25 00:56:43	424
16358	Crab Nebula	0.0	0.5	3	2003-10-25 01:33:30	434
16359	Crab Nebula	0.0	-0.5	3	2003-10-25 02:04:36	441
16360	Crab Nebula	0.0	0.5	3	2003-10-25 02:35:39	175
16403	Crab Nebula	0.0	0.5	3	2003-10-26 00:47:02	388
16404	Crab Nebula	0.0	-0.5	3	2003-10-26 01:19:18	423
16480	Crab Nebula	0.0	1.0	3	2003-10-28 01:24:15	383
16646	Crab Nebula	0.0	1.0	3	2003-11-01 01:32:15	379
16647	Crab Nebula	0.0	-1.0	3	2003-11-01 02:03:23	388

Bibliography

F. A. Aharonian. 2004a. private communication.

F. A. Aharonian. *Very High Energy Cosmic Gamma Radiation : A Crucial Window on the Extreme Universe*. River Edge, NJ: World Scientific Publishing, 2004, 2004b.

F. A. Aharonian and S. V. Bogovalov. Exploring physics of rotation powered pulsars with sub-10 GeV imaging atmospheric Cherenkov telescopes. *New Astronomy*, 8:85–103, Feb. 2003.

F. A. Aharonian and H. Völk. 2004. private communications.

F. A. Akharonian and A. M. Atoian. Compton scattering of relativistic electrons in compact X-ray sources. *Ap&SS*, 79:321–336, Oct. 1981.

K.-M. Aye, P. M. Chadwick, C. Hadjichristidis, M. K. Daniel, I. J. Latham, R. Le Gallou, J. C. Mansfield, T. J. L. McComb, J. M. McKenny, A. Noutsos, K. J. Orford, J. L. Osborne, and S. M. Rayner. In *Proc. 28th ICRC, Tsukuba*, page 2879. Univ. Academy Press, Tokyo, 2003.

L. Ball and J. Dodd. Shock Geometry and Inverse Compton Emission from the Wind of a Binary Pulsar. *Publications of the Astronomical Society of Australia*, 18:98–104, 2001.

L. Ball and J. G. Kirk. Probing pulsar winds using inverse compton scattering. *Astroparticle Physics*, 12:335–349, Jan. 2000.

L. Ball, A. Melatos, S. Johnston, and O. Skjæraasen. Origin of the Transient, Unpulsed Radio Emission from the PSR B1259-63 Binary System. *ApJ*, 514:L39–L42, Mar. 1999.

M. Beilicke, B. Khelifi, C. Masterson, M. de Naurois, M. Raue, L. Rolland, and Schlenker, S., for the H.E.S.S. collaboration. Investigation of the PSR B1259−63 field of view with H.E.S.S. – discovery of HESS 1303−63. In *Int. Symp. High-Energy Gamma-Ray Astronomy, Heidelberg, Germany*, page p? American Institute of Physics, 2004a.

M. Beilicke, M. Ouchrif, G. Rowell, and S. Schlenker. *IAU Cir.*, 8300, 2004b.

A. R. Bell. The acceleration of cosmic rays in shock fronts. I. *MNRAS*, 182:147–156, Jan. 1978.

Benbow, W. for the H.E.S.S. collaboration. Status and Performance of H.E.S.S. In *Int. Symp. High-Energy Gamma-Ray Astronomy, Heidelberg, Germany*, page 611. American Institute of Physics, 2004.

K. Bernlöhr, O. Carrol, R. Cornils, S. Elfahem, P. Espigat, S. Gillessen, G. Heinzelmann, G. Hermann, W. Hofmann, D. Horns, I. Jung, R. Kankanyan, A. Katona, B. Khelifi, H. Krawczynski, M. Panter, M. Punch, S. Rayner, G. Rowell, M. Tluczykont, and R. van Staa. The optical system of the H.E.S.S. imaging atmospheric Cherenkov telescopes. Part I: layout and components of the system. *Astropart. Phys.*, 20:111–128, Nov. 2003.

K. Bernlöhr. MC images of air showers. `http://www.mpi-hd.mpg.de/hfm/~bernlohr/HESS/`, 2000.

K. Bernlöhr. Corsika and sim hessarray - simulation of the imaging atmospheric cherenkov technique for the h.e.s.s. experiment. *unpublished, H.E.S.S. internal note*, 2002.

R. D. Blandford and J. P. Ostriker. Particle acceleration by astrophysical shocks. *ApJ*, 221: L29–L32, Apr. 1978.

G. Blumenthal and R. Gould. *Rev. Mod. Phys.*, 42:237, 1970.

S. V. Bogovalov and F. A. Aharonian. *MNRAS*, 313:504, 2000.

O. Bolz. private communications, 2004a.

O. Bolz. *Absolute Energiekalibration der Abbildenden Cherenkov-Teleskope des H.E.S.S. Experiments und Ergebnisse erster Beobachtungen des Supernova-Überrests RX J1713−3946*. PhD thesis, Universität Heidelberg, 2004b.

M. A. Chernyakova and A. F. Illarionov. Non-pulsed gamma radiation from a binary system with a pulsar. *MNRAS*, 304:359–366, Apr. 1999.

L. Cominsky, M. Roberts, and S. Johnston. Detection of X-ray emission from the PSR 1259-63/SS 2883 binary system. *ApJ*, 427:978–983, June 1994.

T. W. Connors, S. Johnston, R. N. Manchester, and D. McConnell. The 2000 periastron passage of PSR B1259-63. *MNRAS*, 336:1201–1208, Nov. 2002.

R. Cornils, S. Gillessen, I. Jung, W. Hofmann, M. Beilicke, K. Bernlöhr, O. Carrol, S. Elfahem, G. Heinzelmann, G. Hermann, D. Horns, R. Kankanyan, A. Katona, H. Krawczynski, M. Panter, S. Rayner, G. Rowell, M. Tluczykont, and R. van Staa. The optical system of the H.E.S.S. imaging atmospheric Cherenkov telescopes. Part II: mirror alignment and point spread function. *Astroparticle Physics*, 20:129–143, Nov. 2003.

F. V. Coroniti. Magnetically striped relativistic magnetohydrodynamic winds - The Crab Nebula revisited. *ApJ*, 349:538–545, Feb. 1990.

J. M. Davies and E. S. Cotton. Design of the quartermaster solar furnace. *J. Solar Energy Sci. Eng.*, 1:16, 1957.

O. C. de Jager. 2004. private communication.

G. J. Feldman and R. D. Cousins. Unified approach to the classical statistical analysis of small signals. *Phys. Rev.*, D 57:3873, 1998.

E. Fermi. *Phys. Rev.*, 75:1169, 1949.

S. Funk, G. Hermann, J. Hinton, D. Berge, K. Bernloehr, W. Hofmann, P. Nayman, F. Toussenel, and P. Vincent. The trigger system of the H.E.S.S. telescope array. *Astropart. Phys.*, 22/3-4: 285, 2004.

S. Gillessen. Arcsecond-Level Pointing of the H.E.S.S. Telescopes. In *Proc. 28th ICRC, Tsukuba*, page 2899. Univ. Academy Press, Tokyo, 2003.

S. Gillessen, J. Hinton, and S. Funk for the H.E.S.S. collaboration. Locating the TeV-excess from the Galactic Centre region. In *Int. Symp. High-Energy Gamma-Ray Astronomy, Heidelberg, Germany*, page 758. American Institute of Physics, 2004.

P. Goldreich and W. H. Julian. Pulsar Electrodynamics. *ApJ*, 157:869–+, Aug. 1969.

J. R. I. Gott. Studies Concerning the Existence of Runaway Stars with Collapsed Companions. *ApJ*, 173:227–+, Apr. 1972.

K. Greisen. *Prog. Elem. Part. Cosmic Ray Physics*, 3:1, 1956.

J. E. Grove, M. Tavani, W. R. Purcell, W. N. Johnson, J. D. Kurfess, M. S. Strickman, and J. Arons. Evidence for Shock Acceleration in the Binary Pulsar System PSR B1259-63. *ApJ*, 447:L113+, July 1995.

D. Heck, J. Knapp, J. Capdevielle, G. Schatz, and T. Thouw. CORSIKA: A Monte Carlo Code to Simulate Extensive Air Showers. *FZKA*, page 6019, 1998.

HEGRA collaboration. First results on the performance of the HEGRA IACT array. *Astroparticle Physics*, 8:1–2, Dec. 1997.

HEGRA collaboration. *A&A*, 349:11, 1999.

HEGRA collaboration. Evidence for TeV gamma-ray emission from Cassiopeia A. *A&A*, 370: 112–120, 2001.

HEGRA collaboration. The Crab Nebula and Pulsar between 500 GeV and 80 TeV: Observations with the HEGRA Stereoscopic Air Cerenkov Telescopes. *ApJ*, 614:897–913, Oct. 2004.

O. Helene. *NIM*, 212:319, 1983.

V. F. Hess. *Phys. Z.*, 13:1084, 1913.

H.E.S.S. collaboration. Calibration of cameras of the H.E.S.S. detector. *Astropart. Phys.*, 22: 109–125, 2004a.

H.E.S.S. collaboration. High-Energy Particle Acceleration in the Shell of a Supernova Remnant. *Nature*, 432:75, 2004b.

H.E.S.S. collaboration. Very high energy gamma rays from the direction of Sagittarius A*. *A&A*, 425:L13–L17, 2004c.

H.E.S.S. collaboration. A New Population of Very High Energy Gamma-Ray Sources in the Milky Way. *Science*, 307:1938, 2005a.

H.E.S.S. collaboration. H.E.S.S. observations of PKS 2155-304. *A&A*, 430:865–875, Feb. 2005b.

H.E.S.S. collaboration. H.E.S.S. observations of the Crab Nebula. *in preparation, to be submitted to A&A*, 2005c.

H.E.S.S. collaboration. Serendipitous discovery of the unidentified extended TeV γ-ray source HESS 1303−631 with the H.E.S.S. Cherenkov telescopes. *A&A, in press*, 2005d.

H.E.S.S. collaboration, S. Johnston, J. G. Kirk, and O. Skjæraasen. Discovery of the Binary Pulsar PSR B1259-63 in Very-High-Energy Gamma-Rays around periastron with H.E.S.S. *A&A, in press*, 2005.

J. J. Hester, K. Mori, D. Burrows, J. S. Gallagher, J. R. Graham, M. Halverson, A. Kader, F. C. Michel, and P. Scowen. Hubble Space Telescope and Chandra Monitoring of the Crab Synchrotron Nebula. *ApJ*, 577:L49–L52, Sept. 2002.

A. Hewish, S. J. Bell, J. D. Pilkington, P. F. Scott, and R. A. Collins. Observation of a Rapidly Pulsating Radio Source. *Nature*, 217:709–+, 1968.

A. Hillas. In *Proc. 19th ICRC, La Jolla*, page 445, 1985.

A. M. Hillas. Differences between Gamma-Ray and Hadronic Showers. *Space Science Reviews*, 75:17–30, Jan. 1996.

A. M. Hillas, C. W. Akerlof, S. D. Biller, J. H. Buckley, D. A. Carter-Lewis, M. Catanese, M. F. Cawley, D. J. Fegan, J. P. Finley, J. A. Gaidos, F. Krennrich, R. C. Lamb, M. J. Lang, G. Mohanty, M. Punch, P. T. Reynolds, A. J. Rodgers, H. J. Rose, A. C. Rovero, M. S. Schubnell, G. H. Sembroski, G. Vacanti, T. C. Weekes, M. West, and J. Zweerink. The Spectrum of TeV Gamma Rays from the Crab Nebula. *ApJ*, 503:744–+, Aug. 1998.

J. A. Hinton. The status of the HESS project. *New Astronomy Review*, 48:331–337, Apr. 2004.

M. Hirayama, L. R. Cominsky, V. M. Kaspi, F. Nagase, M. Tavani, N. Kawai, and J. E. Grove. X-Ray/Gamma-Ray Observations of the PSR B1259-63-SS 2883 System near Apastron. *ApJ*, 521:718–722, Aug. 1999.

M. Hirayama, F. Nagase, M. Tavani, V. M. Kaspi, N. Kawai, and J. Arons. Post-Periastron ASCA Observation of the PSR B1259-63 System. *PASJ*, 48:833–840, Dec. 1996.

C. M. Hoffman, C. Sinnis, P. Fleury, and M. Punch. Gamma-ray astronomy at high energies. *Reviews of Modern Physics*, 71:897–936, July 1999.

W. Hofmann, I. Jung, A. Konopelko, H. Krawczynski, H. Lampeitl, and G. Pühlhofer. Comparison of techniques to reconstruct VHE gamma-ray showers from multiple stereoscopic Cherenkov images. *Astroparticle Physics*, 12:135–143, Nov. 1999.

M. Hoshino, J. Arons, Y. A. Gallant, and A. B. Langdon. Relativistic magnetosonic shock waves in synchrotron sources - Shock structure and nonthermal acceleration of positrons. *ApJ*, 390:454–479, May 1992.

J. Jelley. Cherenkov radiation and its application. *"Cherenkov Radiation and its Application", Pergamon*, 1958.

S. Johnston, L. Ball, N. Wang, and R. N. Manchester. Radio observations of psr b1259-63 through the 2004 periastron passage. 2005.

S. Johnston, L. Ball, N. Wang, and R. N. Manchester. Radio observations of PSR B1259-63 through the 2004 periastron passage. *MNRAS*, 358:1069–1075, Apr. 2005.

S. Johnston, A. G. Lyne, R. N. Manchester, D. A. Kniffen, N. D'Amico, J. Lim, and M. Ashworth. A high-frequency survey of the southern Galactic plane for pulsars. *MNRAS*, 255: 401–411, Apr. 1992a.

S. Johnston, R. N. Manchester, A. G. Lyne, M. Bailes, V. M. Kaspi, G. Qiao, and N. D'Amico. PSR 1259-63 - A binary radio pulsar with a Be star companion. *ApJ*, 387:L37–L41, Mar. 1992b.

S. Johnston, R. N. Manchester, A. G. Lyne, L. Nicastro, and J. Spyromilio. Radio and Optical Observations of the PSR:B1259-63 / SS:2883 Be-Star Binary System. *MNRAS*, 268:430–+, May 1994.

S. Johnston, R. N. Manchester, D. McConnell, and D. Campbell-Wilson. Transient radio emission from the PSR B1259-63 system near periastron. *MNRAS*, 302:277–287, Jan. 1999.

S. Johnston, N. Wex, L. Nicastro, R. N. Manchester, and A. G. Lyne. The 1997 periastron passage of the binary pulsar PSR B1259-63. *MNRAS*, 326:643–648, 2001.

V. M. Kaspi, M. Tavani, F. Nagase, M. Hirayama, M. Hoshino, T. Aoki, N. Kawai, and J. Arons. X-Ray Detection of PSR B1259-63 at Periastron. *ApJ*, 453:424–+, Nov. 1995.

K. Katama and J. Nishimura. *Prog. Theor. Phys. Suppl.*, 6:93, 1958.

A. Kawachi, T. Naito, J. R. Patterson, P. G. Edwards, A. Asahara, G. V. Bicknell, R. W. Clay, R. Enomoto, S. Gunji, S. Hara, T. Hara, T. Hattori, S. Hayashi, S. Hayashi, C. Itoh, S. Kabuki, F. Kajino, H. Katagiri, T. Kifune, L. Ksenofontov, H. Kubo, J. Kushida, Y. Matsubara, Y. Mizumoto, M. Mori, H. Moro, H. Muraishi, Y. Muraki, T. Nakase, D. Nishida, K. Nishijima, M. Ohishi, K. Okumura, R. J. Protheroe, K. Sakurazawa, D. L. Swaby, T. Tanimori, F. Tokanai, K. Tsuchiya, H. Tsunoo, T. Uchida, A. Watanabe, S. Watanabe, S. Yanagita, T. Yoshida, and T. Yoshikoshi. A Search for TeV Gamma-Ray Emission from the PSR B1259-63/SS 2883 Binary System with the CANGAROO-II 10 Meter Telescope. *ApJ*, 607: 949–958, June 2004.

C. F. Kennel and F. V. Coroniti. *ApJ*, 283:694, 1984.

B. Khélifi. private communications, 2004.

J. G. Kirk, L. Ball, and O. Skjæraasen. Inverse Compton emission of TeV gamma rays from PSR B1259-63. *Astroparticle Physics*, 10:31–45, Jan. 1999.

J. G. Kirk and O. Skjæraasen. Dissipation in Poynting-Flux-dominated Flows: The σ-Problem of the Crab Pulsar Wind. *ApJ*, 591:366–379, July 2003.

S. S. Komissarov and Y. E. Lyubarsky. The origin of peculiar jet-torus structure in the Crab nebula. *MNRAS*, 344:L93–L96, Oct. 2003.

N. Leroy, O.Bolz, J. Guy, I. J. and. I. Redondo, L. Rolland, J.-P. Tavernet, K.-M. Aye, P. Berghaus, K. Bernl¨ohr, P. M. Chadwick, V. Chitnis, M. de Naurois, A. Djannati-Ata¨, P. Espigat, G. Hermann, J. Hinton, B. Khelifi, A. Kohnle, R. Le Gallou, C. Masterson, S. Pita, T. Saitoh, C. Theoret, and P.Vincent. In *Proc. 28th ICRC, Tsukuba*, page 2895. Univ. Academy Press, Tokyo, 2003.

T.-P. Li and Y.-Q. Ma. Analysis methods for results in gamma-ray astronomy. *ApJ*, 272:317–324, Sept. 1983.

S. L. Lo and S. Pope. The implementation of a high performance orb over multiple network transports. *Distributed Systems Engineering Journal*, See also `http://omniorb.sourceforge.net`, 1998.

A. G. Lyne and F. Graham-Smith. *Pulsar Astronomy*. Cambridge University Press, ISBN 0521594138, 1998.

A. G. Lyne, R. N. Manchester, and J. H. Taylor. The galactic population of pulsars. *MNRAS*, 213:613–639, Apr. 1985.

A. Melatos, S. Johnston, and D. B. Melrose. Stellar wind and stellar disc models of dispersion and rotation measure variations in the PSR B1259 - 63/SS2883 binary system. *MNRAS*, 275: 381–397, July 1995.

G. Mohanty, S. Biller, D. A. Carter-Lewis, D. J. Fegan, A. M. Hillas, R. C. Lamb, T. C. Weekes, M. West, and J. Zweerink. Measurement of TeV gamma-ray spectra with the Cherenkov imaging technique. *Astroparticle Physics*, 9:15–43, June 1998.

K. Murata, H. Tamaki, H. Maki, and N. Shibazaki. X-ray and γ-ray emission from the PSR B1259-63/Be star system. *Advances in Space Research*, 33:601–604, 2004.

T. Padmanabhan. *Theoretical Astrophysics, Volume 1: Astrophysical Processes*. Cambridge University Press, 601 pp., 2000.

T. Padmanabhan. *Theoretical Astrophysics, Volume 2: Stars and Stellar Systems*. Cambridge University Press, 594 pp., 2001.

P. Podsiadlowski, N. Langer, A. J. T. Poelarends, S. Rappaport, A. Heger, and E. Pfahl. The Effects of Binary Evolution on the Dynamics of Core Collapse and Neutron Star Kicks. *ApJ*, 612:1044–1051, Sept. 2004.

F. Rademakers and R. Brun. Root: An object-oriented data analysis framework. *Nucl. Inst. & Meth. in Phys. Res. A*, 389:81–86, 1997.

M. J. Rees and J. E. Gunn. The origin of the magnetic field and relativistic particles in the Crab Nebula. *MNRAS*, 167:1–12, Apr. 1974.

G. P. Rowell. *A&A*, 410:389, 2003.

S. Schlenker. Simulation Study of the H.E.S.S. Single Telescope Trigger Rate. *Diploma thesis, Humboldt–Universität zu Berlin*, 2001.

U. Schwanke, N. Komin, T. Lohse, and S. Schlenker. Recovering the intensities of broken pixels using interpolation and fitting techniques. *unpublished, H.E.S.S. internal note*, 2004.

S. Shaw. 2004. private communication.

S. E. Shaw, M. Chernyakova, J. Rodriguez, R. Walter, P. Kretschmar, and S. Mereghetti. INTEGRAL observations of the PSR B1259-63/SS2883 system after the 2004 periastron passage. *A&A*, 426:L33–L36, Nov. 2004.

I. H. Stairs. Pulsars in Binary Systems: Probing Binary Stellar Evolution and General Relativity. *Science*, 304:547–552, Apr. 2004.

C. B. Stephenson and N. Sanduleak. Luminous stars in the Southern Milky Way. *Publications of the Warner & Swasey Observatory*, 1:1–+, 1971.

M. Tavani and J. Arons. Theory of High-Energy Emission from the Pulsar/Be Star System PSR 1259-63. I. Radiation Mechanisms and Interaction Geometry. *ApJ*, 477:439–+, Mar. 1997.

M. Tavani, J. E. Grove, W. Purcell, W. Hermsen, L. Kuiper, P. Kaaret, E. Ford, R. B. Wilson, M. Finger, B. A. Harmon, S. N. Zhang, J. Mattox, D. Thompson, and J. Arons. High-energy emission from the PSR B1259-63 system near periastron. *A&AS*, 120:C221+, Dec. 1996.

P. Vincent, J.-P. Denance, and Huppert, J.-F. et al. Performance of the H.E.S.S. cameras. In *Proc. 28th ICRC, Tsukuba*, page 2887. Univ. Academy Press, Tokyo, 2003.

N. Wang, S. Johnston, and R. N. Manchester. 13 years of timing of psr b1259-63. *MNRAS*, 351:599, 2004.

L. B. F. M. Waters, E. P. J. van den Heuvel, A. R. Taylor, G. M. H. J. Habets, and P. Persi. Evidence for low-velocity winds in Be/X-ray binaries. *A&A*, 198:200–210, June 1988.

T. C. Weekes. *Very high energy gamma-ray astronomy*. IoP Series in astronomy and astrophysics, ISBN 0750306580. Bristol, UK: The Institute of Physics Publishing, 2003, 2003.

N. Wex, S. Johnston, R. N. Manchester, A. G. Lyne, B. W. Stappers, and M. Bailes. Timing models for the long orbital period binary pulsar PSR B1259-63. *MNRAS*, 298:997–1004, Aug. 1998.

C. A. Wiedner. Site aspects of the HESS project: astronomical and visibility conditions. *unpublished, H.E.S.S. internal note*, 1998.

Acknowledgments

I would like to thank the following people supporting this work:

- first of all Thomas and Christian, who made it possible for me to work within H.E.S.S. and were competent advisors. Thanx a lot for your support!
- all other current and past members of the Berlin H.E.S.S. group, especially Nukri for his presence on the other side of the desk, Christoph for his exceptional C++ support, and Ulli for some valuable discussions.
- the whole Heidelberg and Hamburg H.E.S.S. groups, and especially Stefan Funk, David Berge, Jim Hinton, Oliver Bolz, Conor Masterson, Wystan Benbow, Gavin Rowell, Stefan Gillessen, Bruno Khélifi, and Konrad Bernlöhr for the good team-work.
- Jean-Paul, Loic, Mathieu, Nicolas, Pascal, and many others from the French H.E.S.S. groups.
- Felix Aharonian, Götz Heinzelmann, Werner Hofmann, Heinz Völk, and Okkie de Jager, for the interesting discussions and ideas about the binary pulsar.
- my parents (all four of them) for supporting me during the whole time.
- and finally my dear Rike for making my day all the time!

Erklärung

Hiermit erkläre ich, die vorliegende Arbeit ohne fremde Hilfe verfasst und nur die angegebene Literatur und erlaubte Hilfsmittel verwendet zu haben.

Berlin, den 18. April 2005

Stefan Schlenker